

Università degli studi di Roma “Tor Vergata”
Facoltà di Scienze Matematiche, Fisiche e Naturali
Dottorato di Ricerca in Astronomia
XVII ciclo (A. A. 2001/2002–2003/2004)

DETAILED CHEMICAL ABUNDANCES IN THE Sgr AND CMa DWARF GALAXIES

Luca Sbordone

Coordinatore

PROF. ROBERTO BUONANNO

Relatori esterni

DOTT. PIERCARLO BONIFACIO
DOTT. GIANNI MARCONI

Relatore interno

PROF. ROBERTO BUONANNO

Abstract

Detailed chemical abundances for up to 23 elements from Oxygen to Europium have been obtained from VLT-UVES spectra for 12 giants in the Sagittarius Dwarf Spheroidal galaxy (Sgr dSph), 5 in the associated globular cluster Terzan 7, and 3 in the direction of the newly discovered and still controversial CMA overdensity. The analysis has been accomplished by means of a GNU-Linux ported version of R. L. Kurucz's codes for atmosphere modeling (ATLAS), abundance determination (WIDTH) and spectral synthesis (SYNTHE). The porting details are discussed in the thesis, the ported codes are freely available on line.

Sgr dSph is the nearest *confirmed* dwarf spheroidal galaxy. Moving along a short period, quasi-polar orbit around the Milky Way (MW) it is undergoing tidal disruption inside the Halo. It is, consequently, an ideal test case for studying the role of tidal merging in shaping our Galaxy. In this study we evidence the presence of a metal rich (from $[\text{Fe}/\text{H}] \sim -0.8$ up to slightly over-solar) young (about 1 GYr) population in Sgr dSph, also displaying a very characteristics overall chemical signature, including sub-solar $[\alpha/\text{Fe}]$ ratio, low Na, Al, Sc, Ni, Cu and Zn ratios over iron, and strongly enhanced La, Ce and Nd. These highly characteristic abundances are also shared by the MW globular cluster Palomar 12, thus demonstrating definitively that it originated inside the Sgr dSph system, and was consequently stripped from it. We also report some results from an ongoing FLAMES study aiming to obtaining spectroscopic metallicities for a large sample of Sgr dSph stars, indicating that a very metal poor population also exist in the galaxy, down to $[\text{Fe}/\text{H}] \sim -3$. All together, these findings suggest a very long and slow star formation history for Sgr dSph (the metallicity spread being comparable with the one encountered inside the MW), thus leading to infer that a large quantity of gas should have been present in the galaxy. Such gas is also necessary to explain the formation of at least five globulars. We also looked for interstellar absorption systems at high radial velocities (compatible with the one of Sgr dSph stars, $V_{rad} \sim 140 \text{ kms}^{-1}$ in the spectra of our targets, finding them superimposed to two stars only. This enforces the previous results (from radio surveys) indicating that very little gas survived inside Sgr dSph, adding an hint that it should likely have a spotty distribution.

We also observed 5 cool, low gravity giants in Terzan 7, which showed a mean metallicity of $[\text{Fe}/\text{H}]=-0.57$, and an abundance pattern coherent with the one identified in the Sgr dSph main body stars. On three of these stars, we were able to accomplish the first Sulphur abundance measurement in an extragalactic star.

Finally, we present the results of a first FLAMES exploratory study of the CMa overdensity, suspected to be the residual of an in-plane accretion event, associated with the Galactic Anticenter Stellar Structure (GASS). We concentrate on the analysis of the three (out of seven) UVES targets which radial velocity is compatible with the one of the overdensity. One of them is likely a MW interloper, one appears of uncertain origin, the third one appears to be of extragalactic origin due to its peculiar chemical abundances. It is a subgiant ($\log g$ 3.5, T_{eff} 5337 K) showing over-solar iron content, α elements depletion, La, Ce and Nd enhancement and a significant Cu enhancement ($[\text{Cu}/\text{Fe}]=+0.25$). It is worth noticing that, while some of these anomalies are coherent with the ones found in Sgr dSph and in other dSph (the α elements depletion and the Lanthanides enhancement), others are significantly at odd with them. We also describe the results of the first metallicity and radial velocity analysis in the GIRAFFE sample, showing that an overdensity appears to exist in phase space, with respect to the previsions of the Besançon MW model, in the observed area. All in all, our findings support the claimed detection of a tidal accretion remain in CMa, but the size of this first sample is way too small to provide conclusive results.

Keywords: Stars: abundances, Stars: atmospheres, ISM: general, Galaxies: abundances, Galaxies: dwarf, Galaxies: evolution, Galaxies: stellar content, Galaxies: individual: Sgr dSph, Galaxy: globular clusters: individual: Terzan 7

Sommario

Abbondanze chimiche dettagliate (fino a 23 elementi, dall'Ossigeno all'Europio) sono state ottenute, da spettri VLT-UVES, per 12 stelle giganti nella Galassia Nana Sferoidale del Sagittario (Sgr dSph), 5 nell'ammasso globulare Terzan 7, ad essa associato, e 3 nella direzione della recentemente scoperta (ed ancora controversa) Sovradensità del Cane Maggiore. L'analisi è stata compiuta per mezzo di una versione da noi portata sotto GNU-Linux dei codici di R. L. Kurucz per il calcolo di modelli di atmosfera (ATLAS), la determinazione delle abbondanze (WIDTH) e la spettrosintesi (SYNTHE). I dettagli del porting sono discussi nella tesi, i codici sono scaricabili gratuitamente dalla rete.

Sgr dSph è la più vicina nana sferoidale *accertata*. In moto lungo un'orbita quasi polare di corto periodo attorno alla Via Lattea (MW), sta venendo dissolta nell'Alone a causa dell'interazione mareale con la Galassia. Di conseguenza, costituisce un test ideale per studiare il ruolo rivestito dall'accrescimento mareale nella formazione della Galassia. In questa tesi evidenziamo la presenza di una popolazione *metal rich* (da $[Fe/H] \sim -0.8$ fino a valori lievemente sovrasolari) e giovane (circa 1 GYr) all'interno della Sgr dSph. Tale popolazione inoltre presenta una "firma" chimica complessiva molto caratteristica, che comprende $[\alpha/Fe]$ sub-solare, basse abbondanze di Na, Al, Sc, Ni, Cu e Zn, e forti sovrabbondanze di La, Ce e Nd. Simili peculiarità chimiche sono state osservate anche nell'ammasso globulare galattico Palomar 12, il che dimostra definitivamente come esso abbia avuto origine entro la Sgr dSph, e sia stato successivamente acquisito dalla Via Lattea. Inoltre, riportiamo i primi risultati di uno studio FLAMES (attualmente in corso) mirato ad ottenere velocità radiali e metallicità per un vasto campione di stelle della Sgr dSph, indicanti la presenza di una popolazione estremamente povera di metalli, fino a $[Fe/H] \sim -3$. Presi congiuntamente, questi risultati suggeriscono che la formazione stellare in Sgr dSph debba essere stata molto prolungata (l'intervallo di metallicità osservate essendo comparabile con quello caratteristico della Via Lattea) e lenta, il che permette di inferire che una grande quantità di gas dovesse essere presente nella galassia. Ciò è anche necessario per giustificare la formazione di almeno 5 ammassi globulari. Abbiamo anche

compiuto una ricerca di sistemi di assorbimento interstellari ad alta velocità radiale (compatibili con una appartenenza alla Sgr dSph, $V_{rad} \sim 140 \text{ kms}^{-1}$) negli spettri delle stelle da noi osservate, trovandone negli spettri di sole due stelle. Ciò conferma i precedenti risultati (da *survey* radio) indicanti che ben poco gas deve essere sopravvissuto entro Sgr dSph, e suggerisce inoltre che esso sia distribuito sotto forma di piccole nubi locali.

Abbiamo anche osservato 5 giganti di bassa temperatura e gravità nell'ammasso globulare Terzan 7, che ha mostrato una metallicità media di $[\text{Fe}/\text{H}] = -0.57$, ed abbondanze coerenti con quelle osservate nel corpo principale della Sgr dSph. Per tre di queste stelle è stato possibile (per la prima volta in oggetti al di fuori della Via Lattea) misurare l'abbondanza di Zolfo.

Infine, presentiamo i risultati di un primo studio esplorativo FLAMES della Sovradensità del Cane Maggiore (CMA), sospettata essere il residuo di una galassia nana, distrutta in seguito ad un'interazione lungo il piano della Via Lattea, ed associata alla cosiddetta *Galactic Anticenter Stellar Structure* (GASS). In questa tesi ci concentriamo sull'analisi delle tre (di sette totali) stelle osservate con UVES le cui velocità radiali sono compatibili con un'appartenenza alla Sovradensità. Una di esse appartiene probabilmente alla Via Lattea, una appare avere origine incerta, la terza è quasi sicuramente di origine extragalattica a causa delle sue peculiari abbondanze chimiche. Si tratta di una subgigante ($\log g$ 3.5, T_{eff} 5337 K) caratterizzata da un'abbondanza di ferro sovrasolare, povertà di elementi α , sovrabbondanza in La, Ce e Nd, e una significativa sovrabbondanza di Cu ($[\text{Cu}/\text{Fe}] = +0.25$). È interessante notare che, mentre alcune di tali anomalie sono coerenti con quanto riscontrato in Sgr dSph ed in altre nane sferoidali (il basso contenuto di elementi α e la sovrabbondanza di Lantanoidi), altre sono significativamente in contrasto con esse. Descriviamo anche i risultati delle prime analisi di velocità radiali e metallicità del campione di stelle GIRAFFE, indicanti che, rispetto alle previsioni del modello di Besançon della Via Lattea, una sovradensità nello spazio delle fasi appare effettivamente esistere nell'area osservata. Complessivamente, i nostri risultati supportano la teoria che la Sovradensità sia il residuo di un accrescimento mareale, ma la dimensione di questo primo campione è decisamente troppo limitata per permettere di affermare alcunché di conclusivo.

Contents

1	Introduction	21
1.1	Abundance analysis in dwarf galaxies with high resolution spectroscopy	22
1.2	Production channels for different elements	23
1.2.1	Light odd elements	23
1.2.2	α elements	24
1.2.3	Iron peak elements	25
1.2.4	Heavy neutron capture elements	25
1.3	Observed abundance ratios in Dwarf Galaxies	26
1.3.1	α elements	26
1.3.2	Neutron capture elements	31
1.3.3	Undesirable building blocks	32
2	Atlas model atmospheres	33
2.1	Overview of the model structure	35
2.2	Some examples of model atmospheres	36
3	Porting the ATLAS suite to GNU Linux	57
3.1	Porting Issues and solutions	58
3.1.1	Execution scripts	63
3.1.2	Linelists, opacities and similar input data	64
3.2	Results, performance and availability	64
4	Abundances in Sgr dSph	71
4.1	Introduction	71
4.2	Observations and data reduction	74
4.3	Abundance analysis	75
4.4	Results: the signature of an exotic chemistry	78

4.4.1	Iron: a young population	79
4.4.2	α elements	85
4.4.3	Light odd elements	88
4.4.4	Iron peak elements	88
4.4.5	Heavy neutron capture elements	91
4.4.6	Palomar 12, the lost son	91
4.4.7	Comparison with other studies	92
4.5	Widening the view: an ongoing FLAMES study	94
4.6	Looking for gas in Sgr dSph	96
4.7	On the star formation in Sgr dSph	98
5	Abundances in Terzan 7	127
5.1	Introduction	127
5.2	Observations and data reduction	129
5.3	Abundance analysis	130
5.3.1	Sulphur abundances	135
5.4	Results	140
5.5	Conclusions	146
6	The Canis Major overdensity	149
6.1	Introduction	149
6.2	Observations and data reduction	150
6.3	UVES stars abundance analysis	151
6.4	GIRAFFE results: metallicity and V_{rad}	154
6.5	Discussion	155

List of Figures

1.1	The $[\text{Fe}/\text{H}]$, $[\alpha/\text{Fe}]$ diagram for stars in the Local Group dwarf spheroidals, Draco, Ursa Minor, Sextans from Shetrone, Côté, & Sargent (2001), Carina, Sculptor, Fornax and Leo from Shetrone, Venn, Tolstoy, Primas, Hill, & Kaufer (2003) Sagittarius from Bonifacio, Sbordone, Marconi, Pasquini, & Hill (2004) (open circles), Galactic stars from Gratton, Carretta, Claudi, Lucatello, & Barbieri (2003) (triangles) and for DLAs from Centurión et al. (2003) (\times symbols). For the stars $[\alpha/\text{Fe}]$, in this plot, is defined as $0.5 \times ([\text{Mg}/\text{Fe}] + [\text{Ca}/\text{Fe}])$, for the DLAs $[\text{Si}/\text{Zn}]$ is used as a proxy for $[\alpha/\text{Fe}]$ and $[\text{Zn}/\text{H}]$ as a proxy for $[\text{Fe}/\text{H}]$	27
1.2	Same symbols as in as Fig.1.1, except that $[\text{Mg}/\text{Fe}]$ and $[\text{Ca}/\text{Fe}]$ are shown separately.	29
1.3	The $[\text{Mg}/\text{Ca}]$ ratio as a function of metallicity for stars in LG dSph galaxies (circles) and Galactic stars (triangles, Gratton et al. (2003))	30
2.1	Graphics for a model with $T=4932$ K, $\log(g) = 3$, and composition scale factor of 0.31623. See text for details	38
2.2	For the same model in fig. 2.1 Temperature, pressure and thermal gradient against $\log(\tau_{ross})$	39
2.3	Same as in fig. 2.1, but with mass density and metric depth of the model in the two upper panels.	40
2.4	For the same model in fig. 2.1, the percent error over flux and flux derivative constancy and the thermal gradient are plotted against $\log(\tau_{ross})$	41
2.5	Comparison between the thermal gradients of the four models, plotted against $\log(\tau_{ross})$	42

2.6	Confrontation between the <i>adiabatic</i> thermal gradients for the four models, against $\log(\tau_{ross})$	44
2.7	Confrontation between the thermal gradients of the four models, plotted against ρ_x	45
2.8	Confrontation between the thermal gradients of the four models, plotted against the depth in kilometers from the outermost layer of the model.	46
2.9	Confrontation between the electronic numeric densities of the four models, plotted against $\log(\tau_{ross})$	48
2.10	Confrontation between the mass densities of the four models, plotted against $\log(\tau_{ross})$	49
2.11	Confrontation between the Rosseland mean opacities of the four models, plotted against $\log(\tau_{ross})$	50
2.12	Confrontation between the fraction of fluxes transported by convection in the four models, plotted against $\log(\tau_{ross})$	51
2.13	Confrontation between the metric depths in the four models, plotted against $\log(\tau_{ross})$	52
2.14	Confrontation between the temperatures in the four models, plotted against $\log(\tau_{ross})$	53
2.15	Same plots as in fig. 2.1, but for a model with T_{eff} 4932 K, $\log(g) = 3$ and <i>overshooting</i>	54
2.16	Same plots as in fig. 2.3, but for a model with T_{eff} 4932 K, $\log(g) = 3$ and <i>overshooting</i>	55
3.1	Plot of T against $\log(\tau_{Ross})$ along the atmosphere of a star of $T_{eff} = 5000$ K, $\log g = 2.5$, $[Fe/H]=-0.5$, as produced by the Linux ported code (solid line) and the original VMS code (triangles).	66
3.2	Synthetic spectrum for the above mentioned star around the Mg b triplet. Open squares is VMS original code, solid line Linux code. The resolution of the calculation is 600000, then a gaussian broadening (7 km/s FWHM) has been added to simulate the output of a spectrometer with resolution of about 43000. An example of line label: 518360 = 518.360 nm; 1200 = Mg (12 atomic number) neutral (00); 2 = 2% residual intensity at line center (unbroadened spectrum); AZ is a code for the line $\log(gf)$ source.	67

- 3.3 Same as in fig. 3.1, but now comparing electron number densities. 68
- 4.1 Sample from the Mg b triplet region for the 12 stars of Sgr dSph. Spectra are normalized to one on the continuum, but shifted vertically to make the figure readable. Each spectrum is shifted of 1.5 with respect to the one below it, such as the continuum of Sgr 432 is at residual intensity of 1, for Sgr 867 is at 2.5, for Sgr 635 is at 4 and so on. Spectra are ordered such that metallicity increases *ascending* in the plot, every one is labeled with the star number and the $[\text{Fe}/\text{H}]$ of the star. . . . 76
- 4.2 The overall plot of the chemical “signature” of the analyzed population in Sgr dSph. $[\text{X}/\text{Fe}]$ ratios are here plotted against atomic number. Blue symbols represent neutral elements for which $[\text{X}/\text{FeI}]$ is plotted, while red symbols represent ionized elements, for which $[\text{X}/\text{FeII}]$ is displayed. 80
- 4.3 CMD of the Marconi et al. (1998) photometry of Field 1, with superimposed the program stars (filled dots) and three isochrones from the Padova series (Girardi et al., 2002) for the metallicities found in the sampled population. Adopted reddening $E(V-I)=0.22$, $A_V=0.55$, and distance modulus ($m-M$)= 16.95 from Marconi et al. (1998). 86
- 4.4 Distribution of metallicity for the 12 UVES stars in Sgr dSph. 87
- 4.5 Updated version of fig. 1.1. Here the new Sgr dSph α elements values here presented (black filled dots). Blue open circles refer again to stars in the Local Group dwarf spheroidals, Draco, Ursa Minor, Sextans from Shetrone, Côté, & Sargent (2001), Carina, Sculptor, Fornax and Leo from Shetrone, Venn, Tolstoy, Primas, Hill, & Kaufer (2003). Red open triangles represent the MW sample of Venn et al. (2004), comprising the Gratton et al. (2003) sample already presented in fig. 1.1. . . . 103
- 4.6 In top-left panel, $[\alpha/\text{Fe}]$ for the 12 Sgr dSph stars, plotted against $[\text{Fe}/\text{H}]$. Here we define $[\alpha/\text{Fe}]$ as the weighted mean of $[\text{Mg}/\text{Fe}]$, $[\text{Si}/\text{Fe}]$ and $[\text{Ca}/\text{Fe}]$, which are plotted, again versus $[\text{Fe}/\text{H}]$ in the remaining three panels. $[\alpha/\text{Fe}]$ appear to have a decreasing trend with increasing metallicity, and remains sub-solar or solar down to almost $[\text{Fe}/\text{H}]=-0.8$ 104

4.7	[O/Fe] and [Ti/Fe] ratios for the 12 stars of Sgr dSph plotted against [Fe/H].	105
4.8	Spectral syntheses for the Cu I 510.5 nm line in stars 628 and 635.	105
4.9	[Mg/Ca] ratio for Sgr dSph, after the new measurements (black filled dots with error bars), for stars in the other LG dwarf spheroidals (blue open circles, same sample used in fig. 1.1 and 4.5, and for the sample of MW stars from Venn et al. (2004) (red open triangles).	106
4.10	Na, Al and Sc ratios with Iron, against [Fe/H], in the Sgr dSph sample. For Na and Al ratios against Fe I are plotted against [FeI/H] while for Sc we plot [ScII/FeII] vs. [FeII/H]. Notice the [Fe/H] range is larger for the Sc plot.	107
4.11	[X/Fe] vs.[Fe/H] for V, Cr, Mn and Co in the sampled stars. V, Mn and Co are neutral, Cr is ionized, so Fe II is used instead of Fe I and the [Fe/H] range is different.	108
4.12	Same than in fig. 4.11, for Ni, Cu and Zn.	109
4.13	[X/FeII] vs. [FeII/H] for species Y II, Ba II and La II in Sgr dSph.	110
4.14	[X/FeII] vs. [FeII/H] for species Ce II, Nd II and Eu II in Sgr dSph.	111
4.15	Comparison of Sgr dSph and Pal 12 on the [X/Fe] vs. [Fe/H] for light odd elements Na and Sc. Big star symbol is the mean value for four Pal12 giants from Cohen (2004).	112
4.16	Like in fig. 4.15, but now for α elements Mg, Si and Ca.	113
4.17	Like in fig. 4.15, but now for Fe-peak elements Ni, Cu and Zn.	114
4.18	Like in fig. 4.15, but now for heavy n-capture elements Y, La, Eu.	115
4.19	Selection of the targets for the FLAMES analysis. Dark dots represent the targets considered Sgr dSph members, light dots the ones that resulted to be non members.	116
4.20	Histogram of the entire FLAMES sample presented in Zaggia et al. (2004). The peak of the distribution is around [Fe/H]=-0.5, the secondary peak around [Fe/H]=-1.5 is due to M54 stars. Separate histograms are presented for stars within and outside 7.5 arcmin from the M54 center.	117

- 4.21 Spectra of stars showing high velocity Na I D absorptions. The dashed-dotted line is the synthetic IS fit whereas the continuous line is the synthetic stellar spectrum. The local components in star # 635 are severely contaminated by telluric lines and the fit was not reliable. 118
- 4.22 A map of the position in the sky of the 12 Sgr dSph main body stars, with indicated the two stars along which line of sight high velocity interstellar absorption components have been identified. The coordinates of the field center are indicated. 119
- 5.1 A sample of the spectra of the five stars in the wavelength range 601 to 605 nm, where many used Fe I features are. For star # 1282 the DIC1 spectrum is shown. 128
- 5.2 Atmospheric models for star # 1665. All models correspond to $T_{eff} = 3945$ K $\log g = 0.70$. The solid lines refer to an opacity sampling ATLAS 12 model with abundances as provided in table 5.5. The dashed lines refer to an ATLAS 9 model computed with a solar-scaled ODF with $[M/H] = -0.5$ and a microturbulence of 1 km s^{-1} . The dash-dotted lines refer to the ionization structure of the above ATLAS 9 model computed by WIDTH when the abundances of table 5.5 are provided as input. The top panel shows the Fe I and Fe II ions, the middle panel the Mg I and Mg II ions, while the bottom panel displays the temperature structure of the model. The neutral ions show a peak in number densities around $\log \tau_{ross} \sim -1.5$. 136
- 5.3 On the left, $[S/Fe]$ vs. $[Fe/H]$ for the three stars of Terzan 7 and the sample of galactic stars of Ecuillon et al. (2004). The three stars are indicated by letters: # 1665 is D, # 1282 is E and # 1708 is F. On the right, S/O vs. Oxygen content for the three Terzan 7 stars and for the galactic and extragalactic HII regions from the samples of Garnett (1989) and Izotov & Thuan (1999). The solid line represents the solar value, where $A(S)_{\odot} = 7.21$ (Lodders, 2003) and $A(O)_{\odot} = 8.72$ (Asplund et al., 2004a). 138
- 5.4 Best fit of the 922.8 nm S I line for the stars # 1665, # 1282 and # 1708 (top to bottom). This is the only of the three line to be not contaminated by telluric or CN features. 139

5.5	[X/Fe] against [Fe/H] for the light odd atomic number elements in Terzan 7 (filled dots), compared to the ones presented in chapter 4 for Sgr dSph main body (open dots). Also, for comparison we include the mean value of the three stars from Tautvaišienė et al. (2004) (large open star). As usual, ratios against Fe I are presented for neutral species, while for ionized species the comparison is made against Fe II.	141
5.6	As in figure 5.5 but now for mean α elements and Mg, Si and Ca: this figure resembles directly fig. 4.6.	142
5.7	As in figure 5.5 but now for Fe-peak elements Ni, Cu and Zn.	143
5.8	As in figure 5.5 but now for heavy n-capture elements Y, La, Nd and Eu.	144
5.9	Comparison of our measured EWs with the ones of Tautvaišienė et al. (2004), for Fe, Mg, Si and Ca lines. Open hexagons refer to star 1282, crosses to star 1665, asterisks star 1708. The line is not a fit, but simply the bisector.	147
6.1	The EIS CMD of NGC 2477 inside which Bellazzini et al. (2004) identified the CMa population. The selected FLAMES targets are indicated by large dots, the three likely CMa members UVES stars (see 6.3) are indicated by open stars.	158
6.2	Spectra of the three most probable CMa stars, in the region of the Mg b triplet. [Fe/H], $\log(g)$ and T_{eff} all increase from bottom to top. The spectra are normalized to one, stars 30077 and 6631 are shifted vertically for display purposes (continuum is at 2.5 for 30077 and at 4 for 6631).	159
6.3	Abundance ratios against iron plotted vs. [Fe/H] for the light odd elements Na, Al and Sc in the three possible CMa members.	160
6.4	Like in fig. 6.3, for mean α elements abundance and Mg, Si and Ca. Here we use a single figure due to the small number of stars. The filled circles with error bars represent the mean α elements abundance similar to the one in the up-left panel of fig. 4.6, while triangles, squares and open circles represent Mg, Si and Ca respectively. Error bars for the single elements removed for clarity.	161
6.5	Like in fig. 6.3, for Fe-peak elements Ni and Cu.	162

- 6.6 Like in fig. 6.3, for heavy n-capture elements Ba, La, Ce and Nd. 163
- 6.7 Synthesis for the Cu I 510.5 nm line in EIS 6631 (thick line) with superimposed the observed spectrum. Hyperfine splitting is taken into account, $[\text{Cu}/\text{Fe}] = +0.25$ in the synthesis. 164
- 6.8 Metallicity distribution of the giants in the GIRAFFE sample (red shaded histogram). The green histogram is a realization of the Besançon model of the Galaxy, rescaled to the observed number of objects. 165
- 6.9 Radial velocity distribution of the sample giant stars (red shaded histogram), of the predicted stars of the Besançon model (green) and of the sample dwarf stars (blue). 166
- 6.10 The $[\text{Fe}/\text{H}]$ vs. V_{rad} distribution of the observed FLAMES giants. The red dots are the GIRAFFE targets, the three stars represent the UVES candidate CMa members, the green contour lines are the isodensity curves of the Besançon MW model. The two vertical dashed lines include the radial velocities within which we estimate that MW contamination to the CMa population should be below 30%. 167
- 6.11 Radial velocity vs. galactic longitude plot for different objects of interest. Open dots mark open clusters, asterisks are globular clusters, crosses mark the velocity measurements for the recently discovered H I outer spiral arm (McClure-Griffiths et al., 2004); magenta squares represent the Yanny et al. (2003) measurements of the Monoceros Ring, the blue star is the last CMa measurements by Martin et al. (2004b), the red dot is our possible CMa component. The green lines show the expected velocity for a component in circular motion at 220 km s^{-1} at 15 Kpc from the center of the Galaxy. 168

List of Tables

3.1	Execution time comparison for ATLAS 9, calculated on 135 iterations of a 72 layers model (time per iteration within parentheses), and for the calculation of a 5 nm synthetic spectrum at resolution 600000 with SYNTHE. Systems are: VMS: AlphaServer 800 5-500; Pentium 4: 1.9 GHz 768 Mb RAM kernel 2.4.18-3 (Red Hat 7.3) IFC 7.0; Pentium M: 1.6 GHz, 512 Mb RAM kernel 2.4.22-1.2115.nptl (Fedora Core 1) IFC 8.0. All times in seconds.	65
4.1	Position, photometry, S/N ratios 580 nm and atmosphere parameters for the 12 Sgr dSph stars.	75
4.2	Abundances for the first 6 Sgr dSph stars.	81
4.3	Abundances for the other 6 Sgr dSph stars.	82
4.4	Ratios against Iron for the first 6 stars. [X/FeI] is used for neutral ions, [X/FeII] for the ionized ones. For Fe I and Fe II [Fe/H] is displayed instead.	83
4.5	Ratios against Iron for the other 6 stars. [X/FeI] is used for neutral ions, [X/FeII] for the ionized ones. For Fe I and Fe II [Fe/H] is displayed instead.	84
4.6	Atomic data, measured EWs, sources of the atomic data and derived abundances for the measured lines, for stars 439, 628, 635 and 656. “Syn” means that the line has been measured by synthesis (no EW provided), “HFS” that hyperfine splitting has been taken into account in the synthesis, so no EW is given, and the log gf is of limited significance. For the meaning of the log gf source references see table 4.12.	120
4.7	Continued from table 4.6.	121
4.8	As in table 4.6 for stars 709, 716, 717, and 772	122

4.9	Continued from table 4.9	123
4.10	As in table 4.6 for stars 867, 879 894 and 927	124
4.11	Continued from table 4.10	125
4.12	Bibliographic reference for the log gf sources cited in tables 4.6 through 4.11, 5.2 through 5.4 and 6.5 through 6.7.	126
5.1	Photometry and physical parameters for the five stars.	129
5.2	Iron lines for the five Terzan 7 stars. For other elements see tables 5.3 and 5.4, please refer to table 4.12 for the reference of the log gf sources.	131
5.3	Other elements lines for the five stars (see also tab. 5.2, 5.4). For the three Sulphur lines, in each star equal abundances are given for all the lines, since they have been fitted together (see 5.3.1).	132
5.4	Other elements lines for the five stars (see also tab. 5.2, 5.3) .	133
5.5	Abundances for the Terzan 7 stars, and assumed solar abun- dances.	145
5.6	Ratios against Iron for the Terzan 7 stars. $[X/FeI]$ is used for neutral ions, $[X/FeII]$ for the ionized ones. For Fe I and Fe II $[FeI/H]$ and $[FeII/H]$ is presented.	146
6.1	Photometry and physical parameters for the three stars.	150
6.2	Abundances and assumed solar abundances for the three likely CMA members.	151
6.3	Abundance ratios for the three stars. $[X/Fe I]$ is used for neutral elements, $[X/Fe II]$ for ionized species, and $[Fe/H]$ for Fe I and Fe II. For Fe I and Fe II, $[FeI/H]$ and $[FeII/H]$ are presented.	152
6.4	Abundance ratios in different Galactic components, from Venn et al. (2004).	155
6.5	Employed iron lines, atomic data, EWs and resulting abun- dances for the three likely CMA overdensity members. Other ions, see tables 6.6 and 6.7. For the log gf references see table 4.12.	169
6.6	Employed lines, atomic data, EWs and resulting abundances for ions from Na I to Mn I, for the three likely CMA overdensity members. For iron lines see table 6.5, for ions between Co I and Eu II see table 6.7.	170

6.7 Employed lines, atomic data, EWs and resulting abundances
for the three likely CMa overdensity members, for ions between
Co I and Eu II. See also tables 6.5 and 6.6. 171

Chapter 1

Introduction

Up to a few years ago while the Milky Way could be studied in great detail, on a star by star basis, our knowledge of external galaxies had to be desumed mainly from integrated light properties. The advent of 8m class telescopes has changed the situation dramatically, at least for Local Group (LG) galaxies, which can now be studied on a star by star basis with the same methods previously applicable only to Galactic stars.

Dwarf galaxies in the LG are interesting objects to study for a number of reasons. The most trivial is that they are our nearest neighbors, i.e. the ones which we may study more easily. More important they constitute a natural laboratory where to study the galaxy-satellite interaction. In particular, they have been considered, since the formulation of the hierarchical galaxy formation scenarios (White & Frenk, 1991; Navarro et al., 1995), as the most likely “building blocks” out of which larger galaxies, like the Milky Way, have been assembled. We will see later on how, nowadays, this interpretation should be (at least partly) rejected, since clear signs exist that present day dwarf galaxies have significantly evolved from the time of the merging phase that, in the cited scenario, built the giant galaxies. As a consequence, they may now retain only part of the characteristics of the aforementioned “building blocks”. Nevertheless, some of them have likely contributed to the formation of the Galactic Halo, and, as the case of the Sagittarius dwarf Spheroidal galaxy (Sgr dSph) strikingly shows (Majewski et al., 2003), they are still heavily contributing to shape it.

Dwarf galaxies seem also to dominate the luminosity functions, at least by numbers, both in the field (Zucca et al., 1997) and in galaxy clusters (Trentham (1998)). Moreover, their actual contribution to the cluster pop-

ulation may still be underestimated, as suggested by the recent discovery of important populations of Ultra Compact Dwarf (UCD) galaxies inside some rich nearby clusters (Like Virgo and Fornax, see Drinkwater et al. 2003). These objects are likely the residuals of nucleated dwarf galaxies that lost their envelope in the strong gravitational fields of the central parts of these rich clusters (Bekki et al., 2003), a mechanism invoked, in the LG, also to explain the genesis of ω Centauri (Tsuchiya et al., 2004).

Finally, we will see that there is an intriguing resemblance between LG dwarf spheroidals and the Damped Ly- α systems.

1.1 Abundance analysis in dwarf galaxies with high resolution spectroscopy

The topic of this thesis is the chemical abundance analysis in stars of the Sgr dSph and of the recently discovered Canis Major Dwarf galaxy (CMa). High resolution studies are the only ones able to produce abundance ratios for a large number of ions, far more rich in information than a mean “metallicity” (see 1.2). Just to cast an example, only detailed abundance analysis can determine the $[\alpha/\text{Fe}]$ ratio of a given population, which can significantly affect color magnitude diagram (Cassisi et al., 2004).

Shetrone et al. (1998) should be credited for initiating this field; with a bold leap they used the Keck telescope and the HIRES spectrograph to observe four giants in Draco. The spectroscopic metallicities confirmed what was suspected from photometry, namely a large spread in $[\text{Fe}/\text{H}]$ ranging roughly from -3.0 to -1.4. One of the most exciting results of these pioneering observations was the discovery that the ratio $[\text{Ca}/\text{Fe}]$ was almost solar even at very low metallicities, in stark contrast with what observed in Galactic stars.

Right from its commissioning also UVES (Dekker et al., 2000) at the VLT began to provide its contribution, by observing two giants in Sagittarius (Bonifacio et al. (2000a)). Also in this case the results were quite exciting, unveiling the existence of a rather metal-rich population ($[\text{Fe}/\text{H}] \sim -0.25$) which was not at all expected from the photometric studies.

It was thus clear from the beginning that the use of high resolution spectroscopy was providing new insight into these galaxies and the time investment in 8m telescopes was really quite fruitful. We now have available abun-

dances based on high resolution spectra for 8 LG dwarf spheroidals: Draco (Shetrone et al. (1998, 2001)), Sextans, Ursa Minor (Shetrone et al. (2001)), Sagittarius (Bonifacio et al. (2000a); McWilliam et al. (2003); Bonifacio et al. (2004)), Sculptor, Fornax, Carina and Leo I (Shetrone et al. (2003)). The strategy of the various groups has been different, while Shetrone and collaborators tried to observe a few stars in as many galaxies as possible, the groups working on Sagittarius, probably driven by the complexity of this galaxy, tried to obtain data for large samples of stars in one galaxy. It is clear that both approaches have their merits and drawbacks and are highly complementary. Hopefully in a few years time we shall have large samples of stars in each of a large number of galaxies, however already the presently available data allows to draw an interesting picture of the chemistry of LG dwarf spheroidals.

1.2 Production channels for different elements

In order to interpret the evolutionary meaning of the abundances (and abundance ratios) we observe in dwarf galaxies, it may be useful to briefly resume the physical mechanisms through which the different elements are formed in the stellar interior, and released in the interstellar gas. We will not enter in detail of all the nucleosynthesis process, but will instead limit us to the species that are more easily and typically measured in giant stars, the main targets of high resolution spectroscopy in the dwarf galaxies.

1.2.1 Light odd elements

Among them, the most easily measured in giants are Na ($Z=11$), Al ($Z=13$) and Sc ($Z=21$). Their production channels are diverse, and still open to debate. They are produced mainly in both hydrostatic and explosive burning inside massive stars exploding as SN II: Na is produced mainly in the C-burning shell, by balancing $^{12}\text{C}(^{12}\text{C},\text{p})^{23}\text{Na}$ with $^{23}\text{Na}(\text{p},\alpha)^{20}\text{Ne}$, Al in the same site, where it is created from Mg ($^{26}\text{Mg}(\text{p},\gamma)^{27}\text{Al}$) and partially converted in Si ($^{27}\text{Al}(\text{p},\gamma)^{28}\text{Si}$) (Limongi & Chieffi, 2003; Chieffi & Limongi, 2003, 2004). Nevertheless, some impact from proton capture processes (e.g. NeNa cycle) may influence their abundances, thus leading possibly to explain the Na-O anticorrelation observed in the Globular Clusters (GC).

1.2.2 α elements

The even atomic number elements from 8 (Oxygen) to 22 (Titanium), are generally referred to as “ α elements”, since their dominant isotopes are always multiples of ${}^4\text{He}$ nuclei. By far the easiest to measure in giant stars spectra are Mg, Si Ca and Ti. O presents consistent observative challenges, due to the fact that its only two optical lines are forbidden and extremely weak.

In general, α elements are produced inside massive, short lived stars (with a maximum impact on the chemical enrichment due to $\sim 25M_{\odot}$ stars, see Limongi & Chieffi 2003), and then released during the successive SN II explosion. As a consequence, α elements enrichment is considered to be an extremely fast process inside a stellar population, since the lifetime of such massive stars is negligible compared to the one, e.g., of a $\sim 1M_{\odot}$ star. For the same reason, α elements enrichment rate drops quickly if the star formation stops in the population.

The production channels are somewhat diverse: O ($Z=8$) and Mg ($Z=12$) are produced during hydrostatic ${}^4\text{He}$ (for O) and ${}^{12}\text{C}$ and ${}^{20}\text{Ne}$ (for Mg) core burning in the late stages of massive stars (Limongi & Chieffi, 2003; Chieffi & Limongi, 2003); In fact, since O burning subsequently reprocesses the Ne-burning shell, almost all the Mg produced during hydrostatic Ne burning gets destroyed. Significant quantities of Mg are also produced during explosive Ne burning, especially in low mass SN II. At the same time, both may be affected by other production/destruction channels (ON cycle, MgAl cycle, see Sneden 2004). The bulk of Si ($Z=14$) Ca ($Z=20$) and Ti ($Z=22$) is instead produced *probably* by the so-called “ α -process”, or “ α -rich freeze out”, taking place during the actual SN II explosion, when the α -particle density is particularly high (Nakamura et al., 2001). As a consequence, although tracing the same stellar types, and consequently an overall similar evolution with time, some discrepancy may exist between different α elements (see 1.3) evolution rates. In particular, the presence or absence of hypernovae in dwarf galaxy may lead to significant changes in the [Mg/Ti] and [Mg/Ca] ratios (Venn et al., 2004, and references therein). Also, there’s the possibility that some amount of Ti and Ca may be produced by He white dwarfs exploding as SN Ia (Venn et al., 2004, and references therein). Since SN Ia are the product of slowly evolving star systems, the correlation between α elements and short lived, massive population would be weakened.

1.2.3 Iron peak elements

The elements with $Z=23$ (Vanadium) to 30 (Zinc) are generally defined Fe-peak elements. All of them can be measured in giant stars. They are mainly released in the interstellar medium (ISM) by type Ia and type II supernovae, but the variety of possible SN Ia scenarios, as well as the uncertainties in the SN II models do not allow to put too much weight in the ratios between these elements.

SN II produce important quantities of Fe peak during complete and incomplete explosive burning of ^{28}Si and ^{30}Si (V, Cr, Mn, Co, Ni and obviously Fe) but the entire complete Si burning shell is believed to fall back on the compact core, and the produced elements do not pollute the ISM (Limongi & Chieffi, 2003; Chieffi & Limongi, 2004).

The simplest (and most significant) effect involving both Fe-peak and α elements is related to the fact that SN Ia do not seem to produce significant quantities of α elements (Tsujimoto et al., 1995, but see the caveat about Ca and Ti in 1.2.2). Since they enrich the ISM in Fe-peak elements, and do it on a time scale much longer than the one needed by the original α elements enrichment, the $[\alpha/\text{Fe}]$ ratio is seen to generally decrease with increasing $[\text{Fe}/\text{H}]$. As we will see later, the main factors actually determining the *rate* of this decrease are star formation efficiency and, in the case of dwarf galaxies, the strength of the galactic wind (Lanfranchi & Matteucci, 2004).

Another interesting effect expected to take place is the Na-Ni correlation (Venn et al., 2004, and references therein). Basically, it is due to the fact that during the SN II explosion, ^{58}Ni production is favored by a neutron rich medium. The most common neutron rich nucleus produced by pre-SN hydrostatic burning is ^{23}Na . As a consequence, Na and Ni yields from SN II are expected to correlate.

1.2.4 Heavy neutron capture elements

Elements above Zn ($Z>30$) are generally produced by n-capture processes on lighter nuclei. The most frequently observed in giant stars are Yttrium ($Z=39$), Barium ($Z=56$), Lanthanum ($Z=57$), Cerium ($Z=58$), Neodymium ($Z=60$) and Europium ($Z=63$).

Two main production channels exist for these elements. The so-called *r-process* (or *rapid* process) requires a high density of neutrons, and is believed to take place in the exploding envelopes of SN II. It's interesting to notice

how the mechanism of production of the elements beyond Zinc at very low metallicity is still unclear, since an heavy yield cutoff exist above $Z=30$ for metallicities below $Z \sim 10^{-3}$ (Chieffi & Limongi, 2004). At increasing metallicity, the r-process starts to enrich the ISM in n-capture elements. While the r-process remains the main source for some of these elements (namely Eu), at higher metallicities the s-process becomes available.

The *s-process* (or *slow process* Busso et al., 1999) is particularly efficient (among the better observable elements) for Ba, and rather efficient for Y, La, Ce and Nd. The main places where this process is believed to take place are the envelopes of low to intermediate mass AGB stars experiencing the thermal pulse phase. An alternate form (the so-called *weak s-process*) should take place during the hydrostatic burnings of high mass stars, but it could possibly affect only elements up to Yttrium.

At solar metallicity, almost all the Ba is produced via s-process, while 95% of Eu is still produced by r-process. As a consequence, [Ba/Eu] ratio is another signature heavily dependent on the ration between high and low-mass, short and long lived stars. Nevertheless, strong uncertainties on the actual yields and s vs. r contribution to many heavy elements make this signature less easy to interpret than the $[\alpha/\text{Fe}]$ ratio.

1.3 Observed abundance ratios in Dwarf Galaxies

1.3.1 α elements

In Fig. 1.1 we show the run of $[\alpha/\text{Fe}]$ versus $[\text{Fe}/\text{H}]$ for the dwarf spheroidals for which data are available; α has been defined as a mean of Mg and Ca, both elements have been measured for all the observed stars. In the plot these are compared with similar data for Galactic stars (Gratton et al., 2003) and for Damped Ly- α systems (DLAs, Centuri3n et al., 2003).

From Fig.1.1 it can be readily seen that the locus occupied by stars in dwarf spheroidal galaxies is different from that occupied by Galactic stars. On the other hand the majority of DLAs seem to fall precisely on the locus defined by dSph galaxies. The early results of Shetrone et al. (1998) and Bonifacio et al. (2000a) now appear to be a general feature of dSph galaxies: the α/Fe ratio is smaller than in Galactic stars at any given metallicity. This result was theoretically expected in galaxies which are characterized by a star

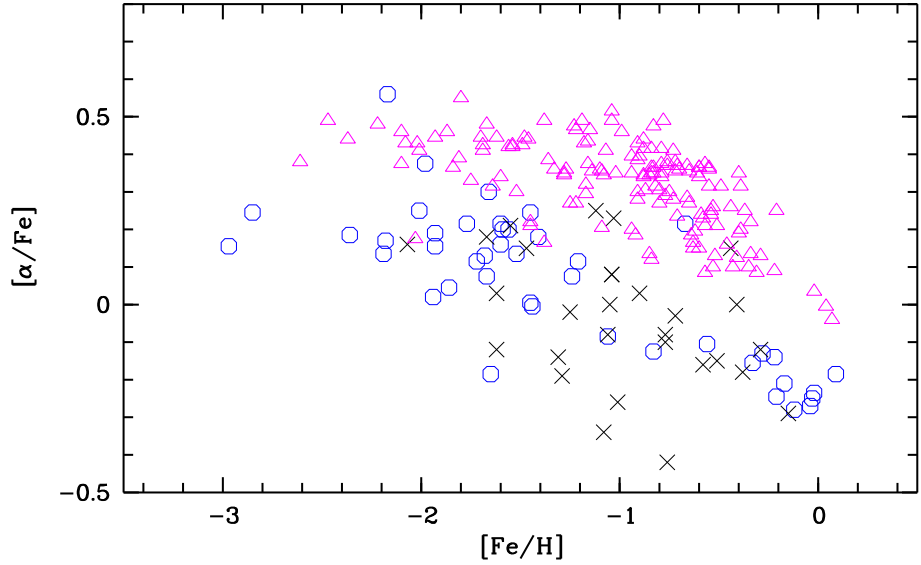


Figure 1.1: The $[\text{Fe}/\text{H}]$, $[\alpha/\text{Fe}]$ diagram for stars in the Local Group dwarf spheroidals, Draco, Ursa Minor, Sextans from Shetrone, Côté, & Sargent (2001), Carina, Sculptor, Fornax and Leo from Shetrone, Venn, Tolstoy, Primas, Hill, & Kaufer (2003) Sagittarius from Bonifacio, Sbordone, Marconi, Pasquini, & Hill (2004) (open circles), Galactic stars from Gratton, Carretta, Claudi, Lucatello, & Barbieri (2003) (triangles) and for DLAs from Centurión et al. (2003) (\times symbols). For the stars $[\alpha/\text{Fe}]$, in this plot, is defined as $0.5 \times ([\text{Mg}/\text{Fe}] + [\text{Ca}/\text{Fe}])$, for the DLAs $[\text{Si}/\text{Zn}]$ is used as a proxy for $[\alpha/\text{Fe}]$ and $[\text{Zn}/\text{H}]$ as a proxy for $[\text{Fe}/\text{H}]$.

formation which is either slow or bursting (Gilmore & Wyse, 1991; Marconi et al., 1994; Lanfranchi & Matteucci, 2003). If, as proposed for the first time by Tinsley (1979), the pattern of α/Fe in Galactic stars is essentially due to the time delay between Type II and Type Ia supernovae, the low α/Fe values in galaxies with a slow star formation rate can be easily understood. In the Galaxy metal-poor stars are enriched mainly by Type II supernovae, while more metal-rich stars have a contribution from Type Ia supernovae, which produce large amounts of iron-peak elements, but little or no oxygen and α elements, but have longer lifetimes. When the star-formation is slow, or bursting, Type Ia supernovae have time to explode, thus pushing down the α/Fe ratio in the interstellar gas, *before* the next generation of stars

are formed. Thus such a galaxy should show a lower α/Fe ratio, at any metallicity, when compared to a galaxy with a continuous and rather fast star formation, like the Milky Way.

DLAs are observed as line absorption systems against the background of distant QSOs, which are characterized by large hydrogen column densities ($\log N > 10^{2.3} \text{cm}^{-2}$, Wolfe et al., 1986). These column densities are characteristic of the disc of a spiral galaxy. It is generally accepted that the majority of the DLAs are in fact associated with galaxies of some sort, in fact they are often referred to as DLA galaxies, although, in absence of other information, one cannot exclude that any given DLA may be associated with intracluster gas or large scale filaments. Imaging studies have been able to identify the galaxies responsible for the DLA (Rao & Turnshek, 1998; Le Brun et al., 1997). For the purpose of the present discussion we shall therefore assume that DLAs are indeed galaxies. What makes DLAs very interesting is that they are observed also at high redshift ($z > 3$.) and it is possible to derive an accurate chemical composition, metallic lines are observed at all redshifts; no metal-free DLA has been observed to date. The lookback-time attainable through the observations of DLAs is comparable to that of old Galactic stars.

The similarity of the chemical properties of most DLAs and dSphs is intriguing. One cannot conclude that most DLAs are dSphs because we know that the latter galaxies are gas-poor, while DLAs, by definition, have significant amounts of gas. One could argue that DLAs are dSphs caught in a gas-rich phase, but this is highly speculative. Instead there are two considerations which I think are fairly robust:

1. all LG dwarf spheroidals follow a similar path of chemical evolution;
2. this path is similar to that followed by DLAs.

The key to this similarity could be indeed the presence of a slow, or bursting, star formation, as suggested above. Note however that there are alternative explanations. If one admits that the initial mass function (IMF) is not the same at all times and in all places, then the increase of α/Fe with the decrease of metallicity may be interpreted as an effect of a metallicity-dependent IMF which produces more massive stars at lower metallicities. In this framework the low α/Fe in dSphs and DLAs would be the signature of an IMF which, at any metallicity, produces less high-mass stars than the Galactic IMF.

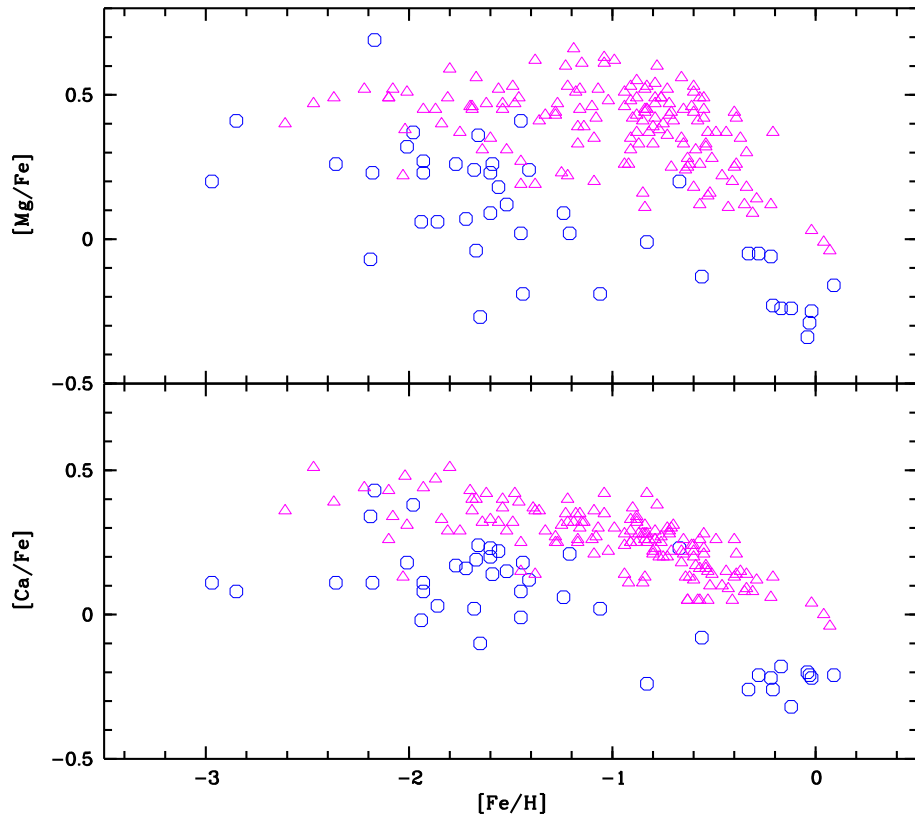


Figure 1.2: Same symbols as in as Fig.1.1, except that $[Mg/Fe]$ and $[Ca/Fe]$ are shown separately.

Another interesting proposal is the idea that Type Ia supernovae cannot be produced at metallicities below, roughly, $[Fe/H] = -1$ (Kobayashi et al., 1998, 2000). Type Ia supernovae arise in binary systems, in which a white dwarf accretes matter so as to increase its mass above the Chandrasekhar limit, thus leading to contraction and an explosion. The most popular models involve a white dwarf plus a red giant companion. In such models at low metallicities the wind of the red giants are too weak to accrete a substantial mass on the white dwarf thus the explosion stage is never reached. This scenario explains neatly the evolution of α/Fe in the Galaxy, however is unable to explain the low α/Fe ratios at low metallicities observed in dwarf spheroidals and in DLAs. Kobayashi (2003) invoked for these galaxies an IMF

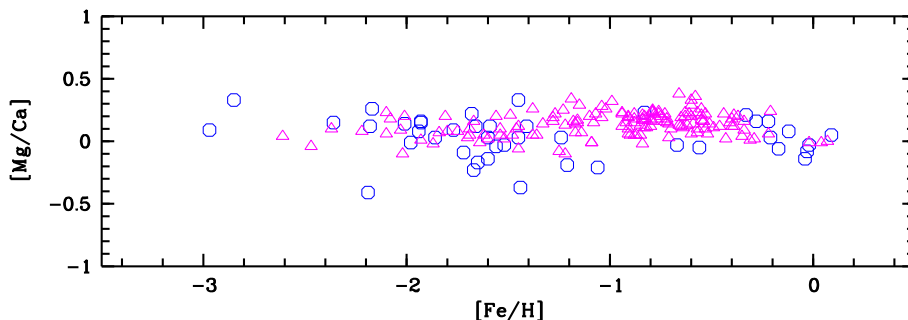


Figure 1.3: The $[Mg/Ca]$ ratio as a function of metallicity for stars in LG dSph galaxies (circles) and Galactic stars (triangles, Gratton et al. (2003))

which privileges low-mass Type II supernovae ($13-15 M_{\odot}$), which produce low α/Fe ratios. This provides a viable solution, however one should be aware that so far in all the models of Type II supernovae the *mass-cut*, i.e. the mass in the SN model above which all the material is ejected and below which all material falls back on the SN remnant, cannot be determined from first principles and is therefore assumed as a free parameter (Chieffi & Limongi, 2004). A suitable choice of mass-cut may produce low α/Fe for stars of all masses. Therefore the model of Kobayashi (2003) is valid for a particular choice of (arbitrary) mass-cut.

Recently Venn, Irwin, Shetrone, Tout, Hill, & Tolstoy (2004) produced a very extensive comparison of the abundances of dwarf spheroidals with Galactic stars. On the basis of this comparison they claim that the $[Mg/Fe]$ ratio seems to lie below $[Ca/Fe]$ in dwarf spheroidals, while this does not seem to be the case in Galactic stars. This could be a very interesting finding, and there could be several ways to explain such behavior. The two elements Ca and Mg are produced in different sites: Mg is mainly produced by carbon burning on rather long time scales ($\sim 10^3$ yr) in rather deep layers, while Ca is produced by oxygen burning on much shorter time scales (~ 0.3 yr) in much more superficial layers (Limongi & Chieffi, 2003). Depending on the mass-cut the ratio Mg/Ca may change. As usual also different IMFs result in different Mg/Ca ratios. The chemical evolution models of Lanfranchi & Matteucci (2004), show Ca/Fe ratios lower than Mg/Fe ratios, due to the fact that Ca and Ti are produced by Type Ia SNe more than O or Mg, thus the decrease in Ca/Fe with increasing metallicity is smaller than for Mg/Fe.

Although there are several theoretical reasons to expect this behavior, one should be cautioned that the evidence supporting this claim is still marginal. In Fig.1.2 we show the data for dwarf spheroidals and for Galactic stars, with the same symbols as in Fig.1.1. Quite obviously the scatter in $[\text{Mg}/\text{Fe}]$ is much larger than in $[\text{Ca}/\text{Fe}]$ however this simply reflects the observational fact that few Mg lines are measurable, while usually a larger number of Ca lines is available. If one considers all observed dSphs, except Sgr, which cover a metallicity range in which Galactic stars show a rather uniform value of $[\text{Mg}/\text{Fe}]$ and $[\text{Ca}/\text{Fe}]$, the mean $[\text{Mg}/\text{Fe}]$ is 0.16 with a standard deviation of 0.2, while the mean $[\text{Ca}/\text{Fe}]$ is 0.14 with a standard deviation of 0.11, by comparison all the Galactic stars of Gratton et al. (2003) which cover the same metallicity range (103 stars) show a mean $[\text{Mg}/\text{Fe}]$ of 0.43 with a standard deviation of 0.11 and a mean $[\text{Ca}/\text{Fe}]$ of 0.30 with a standard deviation of 0.08. Thus the claim that both these ratios are *lower* in LG galaxies than they are in Galactic stars is fairly robust, however the claim that $[\text{Ca}/\text{Fe}]$ is lower than $[\text{Mg}/\text{Fe}]$ among LG galaxies than in Galactic stars, is weak. This is more obvious if we look directly at the $[\text{Mg}/\text{Ca}]$ ratio (Fig. 1.3), a larger scatter is observed, but there does not appear to be a significant difference between LG galaxies and Galactic stars.

1.3.2 Neutron capture elements

The two Sgr giants observed by Bonifacio et al. (2000a) displayed a puzzling pattern of neutron capture elements: Y appeared to be overdeficient with respect to iron, while Ba, La, Ce, Nd and Eu appeared to be overabundant. Shetrone et al. (2001) for Draco, Sextans and Ursa Minor found a similar situation: Y/Fe lower than in Galactic stars, and Ba/Fe compatible with that of Galactic stars. Now thanks to the larger data set accumulated and the precious work of Venn et al. (2004) it appears that a high $[\text{Ba}/\text{Y}]$ and low $[\text{Y}/\text{Fe}]$, compared to Galactic stars, is a general feature of dSphs.

There is yet no totally satisfactory explanation of this pattern, however such a behavior could be expected when neutron capture elements are produced by metal-poor AGB stars, in which, due to the large neutron-to-seed ratio, the heavier elements are favored: Ba is favored over Y and Pb is favored over Ba (Busso et al. (1999)).

This cannot be the whole story, of course, because most of these stars also show $[\text{Eu}/\text{Fe}]$ ratios which are similar or larger than those observed in Galactic stars, implying that the r -process is in operation at a level equal

or larger than what occurring in the Galaxy.

1.3.3 Undesirable building blocks

There are other elements which seem to display, at least in the case of Sagittarius, abundance patterns different from the Galactic ones, like Na (Bonifacio et al., 2000a), Mn (McWilliam et al., 2003) and Ni (Bonifacio et al., 2000a, , this work). The bottom line is that these chemical signatures make LG dSphs *undesirable building blocks* for the Galactic Halo. It is not possible to assemble the Galactic Halo from dSphs with the characteristic of the present day ones. If one assumes that hierarchical galaxy formation applies to the Milky Way, one has to conclude that the dwarf galaxies which acted as building blocks were very different from present-day ones. In particular, assuming that the low α/Fe in present-day dSphs is caused by a low star formation, it can be argued the building blocks of the Milky Way were characterized by a vigorous star formation. In some sense the new information we have on LG dSphs poses more new questions than it answers old ones.

Chapter 2

Atlas model atmospheres

The use of a model of the stellar atmosphere is a key step in the process of interpreting stellar spectra. We call atmosphere the outermost layers of the stellar envelope, where all the spectral features (continuum and lines) originate. Here, detailed calculations are required in order to deal with the radiation transport in a optically thin, partially ionized mixture of gas. The ATLAS code simulates a one dimensional, plane parallel atmosphere under the hypothesis of flux conservation through the atmosphere. This means neglecting any effect related to “horizontal” motions in the atmosphere (stellar rotation, for instance). The depth of the atmosphere is also assumed to be small with respect to the stellar radius, so that the curvature of the atmospheric layers may be neglected, and any non-radiative heating process is set to zero: the constancy of flux through the atmosphere is assumed, no heat sources or sinks are allowed. This last limit is probably the most restrictive, because this “energetic equilibrium” is well known to fall off in the outer solar atmosphere (the so-called *transition zone* to the corona) where a steep temperature increase occurs due to heating processes probably driven by seismic and magnetic waves. Another limit of such models comes from the assumption of local thermodynamic equilibrium (LTE) under which the level populations are computed¹. In fact, there is a complex interplay between these phenomena in the outer atmosphere of solar-like stars: NLTE processes *under radiative equilibrium* are partly responsible of the observed temperature rise at the bottom of the corona. Several strong spectral fea-

¹In the codes are in fact implemented (as optional) non-LTE (NLTE) calculations for some specific hydrogen transitions, but this is considered mainly an experimental feature, and is used only in very hot atmospheres: see Castelli (1988).

tures are produced in such zones, like the Ca H-K doublet core, the H α core and the Lyman continuum. A last caveat must be made: as we will see in detail later, in ATLAS convection is treated with a “classical” mixing length approximation. In the model we shall use, overshooting is neglected, giving way to a temperature profile that is somewhat unphysical at the boundaries of the convective zone. The upper boundary of the convective layer is placed at $\tau_{ross} > 1$, so this problem will not affect strong spectral features, but will be rather important for most weak spectral lines.

Despite of these limits, Kurucz’s models have proved to be very effective as a base for spectral analysis; their main strengths are the very detailed treatment of the bound-bound and bound-free opacity, and the very large database of atomic and molecular transition devoted to this purpose. It actually amounts to several millions of transitions, even if the physical parameters are not well known for all of them, and the ones used are sometimes affected by large uncertainties. The task to deal with such a huge body of transitions is essentially impossible to address analytically, and so two main ways have been developed to practically calculate the opacity. The *Opacity Distribution Functions* (ODF) method calculates explicitly the opacity for given physical conditions, and then gives its results in a particular functional form, which allows to describe the opacity with sufficient high accuracy using a rather small dataset. The computation requires a long time, and cannot be performed during the actual model iterative calculation, so ODF are pre-calculated in a grid of different conditions, between which the values for the present model step are interpolated. The *Opacity Sampling* (OS) method relies on statistical methods in order to determine a sub-sample of the entire transition database adequate to derive the main features of the opacity. The advantage of this procedure lies in its (relative) rapidity, which allows to perform it inside the atmosphere model calculation². The models used as examples here have been obtained using ATLAS9, the version of ATLAS code using the ODF.

²A description of the actual structure of both ODF and OS along with their strengths and limits are out of the scope of the present work. A good review has been given by Carbon (1979), a detailed description of the ODF is provided by Kurucz (1979), while OS is well described, for example, by Sneden et al. (1976).

2.1 Overview of the model structure

As previously stated, ATLAS calculates plane parallel, one dimensional atmosphere models under the hypothesis of flux conservation. The last condition, actually, gives the convergence parameter: the model is supposed to have converged when constancy in flux and flux derivative is assured (to a chosen cutoff) over the entire depth of the calculated atmosphere structure. The code proceeds via iterative recalculation of the physical parameters over a maximum of 72 mesh points along the atmosphere. Radiative and convective energy transport are taken into account, input data to be passed to the model are effective temperature of the star, surface gravity³, and chemical composition of the gas. Usually, solar rescaled abundances are used, eventually taking into account alpha elements enhancement. Additionally, a mixing length parameter must be set to evaluate convective flux. ATLAS may take into account convective overshooting in its calculations (we will show later a model in which overshooting is employed) but not semi-convection. It must be stressed that atmospheric convection is much more sensitive to the mixing length approximation faults than core convection, since the lower opacity and viscosity enhances superadiabaticity and overshooting. A physical model of the overshooting scale, however, would require complex (and not so robust) hydro-dynamical considerations, so, if overshooting is introduced, ATLAS simply makes a smoothing of the boundaries of the convective zone on a scale of the order of the pressure scale height. This is pretty unphysical, although an abruptly ending convective layer is not much better from this point of view. Many people, anyway, prefer not to use overshooting when using ATLAS (see Castelli et al. (1997)).

Finally, a so called *micro-turbulence* parameter (which is dimensionally a velocity of the order of a few km/s) must be chosen, in order to adequately account of the non-thermal doppler broadening of the lines due to local (“turbulent”) motions in the stellar atmosphere. This last parameter, which obviously affects the opacity, is considerably important in order to derive chemical abundances from observed equivalent width of the spectral lines.

³In the so called “log g” form, i.e. the logarithm of the gravity acceleration in the atmosphere: its small depth and mass compared to the whole star allow usually to consider the gravity constant along the entire model. $\text{Log}(g) = 4$ is typical of dwarf stars, while $\text{log}(g) = 2 \div 3$ are the values for stars along the RGB. The gravity acceleration g is here taken in CGS system.

A starting model must be provided, and it can also be initially calculated by the program. If a database of already calculated models is available, however, is customary (and generally preferable to fasten the model convergence) to start from an existent model with parameters near to the ones desired. In this hypothesis 45 to 60 model iterations are usually sufficient to reach convergence conditions not exceeding 1% maximum error in flux constancy and 10% in flux derivative constancy. The final model provides, along the 72 mesh points, the thermodynamical parameters of the gas (temperature, mass density, pressure) the ionization degree for all the elements considered in the model, electronic density, Rosseland mean opacity, convective flux fraction, depth in kilometers and so on. The program uses, as “natural” variable defining each mesh, the column density:

$$\rho_x = \int_0^x \rho(x) dx.$$

2.2 Some examples of model atmospheres

Here we present a little collection of models calculated for stars of rather low mass and metallicity, in ZAMS and RGB phases. These atmospheres have been chosen to be roughly similar to the ones we will actually encounter in our target stars, in order to give some ideas both on the way ATLAS code works and on the physics involved in such objects.

We start from a model calculated for $T_{eff} = 4932$ K, $\log(g) = 3$ and a solar chemical composition rescaled to 0.31623, i.e. $[M/H] = -0.5$ ⁴. The graphs are shown in fig. 2.1. Starting from upper left panel, are shown the fraction of the flux that is transported by convection, the contributions to the total electron density due to several elements ionization (ordered by maximum contribution: the H is the solid line, the Mg the dotted line and so on), the logarithm of the mean Rosseland opacity, the so called “thermal gradient” $\frac{d \log(T)}{d \log(P)}$, the temperature and the logarithm of the electronic density, all plotted with respect to the logarithm of the Rosseland mean optical depth. The choice of this abscissa comes from its direct dependence from the opacity and, consequently, its correlation with the energy transport mechanism.

At the first glance, a steep change may be seen in all the graphs around $\tau = 1$. Starting from the interior of the star we can see that, in the innermost

⁴ $[M/H] \equiv \log(\frac{M}{H}) - \log(\frac{M}{H})_{\odot}$, where M and H are the metal and H fractions, respectively.

layers, about all the flux is transported by convection. The opacity is at its maximum, almost all the electrons are contributed by the ionization of the hydrogen. It must be stressed that the temperature in this layer is still rather low: only roughly 10% of the H is ionized, but its high abundance makes it by far the first source of free electrons in the gas (He is essentially neutral at such temperatures). Moving outward, the efficiency of the convection decreases steeply with the optical depth of the gas and the thermal gradient increases until a maximum is reached around $\tau = 3$. This can be seen as the point where the low opacity of the convective cells makes the convective transport essentially ineffective. Almost the entire flux is then transported by radiation, a mechanism far less efficient at such opacities. Still outward, the density and ionization continue to decrease, the atmosphere becomes essentially optically thin and the heat may be transported with higher efficiency; consequently, the thermal gradient falls off to near zero values, as the temperature decreases much more slowly than the pressure (see fig. 2.2).

Is important to stress that the outer zone (roughly for $\tau_{ross} < 10^{-4}$) is not correctly modeled by ATLAS: here, as said before, the radiative equilibrium falls off and a steep temperature increase leads to the corona. All the strong spectral features at visible wavelength come from the region of (essentially flat) temperature decrease between $\tau_{ross} = 1$ and $\tau_{ross} = 10^{-4}$. In this region, almost all the free electrons are contributed by metallic ionization. The principal opacity source is here constituted by H^- ionization.

The steep decrease of the convective efficiency at $\tau_{ross} \approx 3$ has to be attributed mainly to the variation of the opacity due to a change in its source between H^- (outward) and H ionization (inward). This may be clearly seen in fig. 2.3: the density, indeed, remains high and about constant until the convective flux has reached zero. Another interesting fact can be seen in fig. 2.3. The convective layer appear to be very thin, entirely contained in the last 2000 km.

Last, in fig. 2.4 we show the two errors used by ATLAS as a convergence check. Here we have plotted the (percent) deviation of the flux from the constancy, the deviation of the flux derivative from zero and the thermal gradient against $\log(\tau_{ross})$. It is evident that the code encounters the biggest problems around the peak in the thermal gradient. All the models plotted here are calculated with 60 iterations.

We will now compare this model with three others, calculated with T_{eff} augmented and diminished by 500 K and with temperature unchanged, but with $\log(g) = 4$, typical of a ZAMS star.

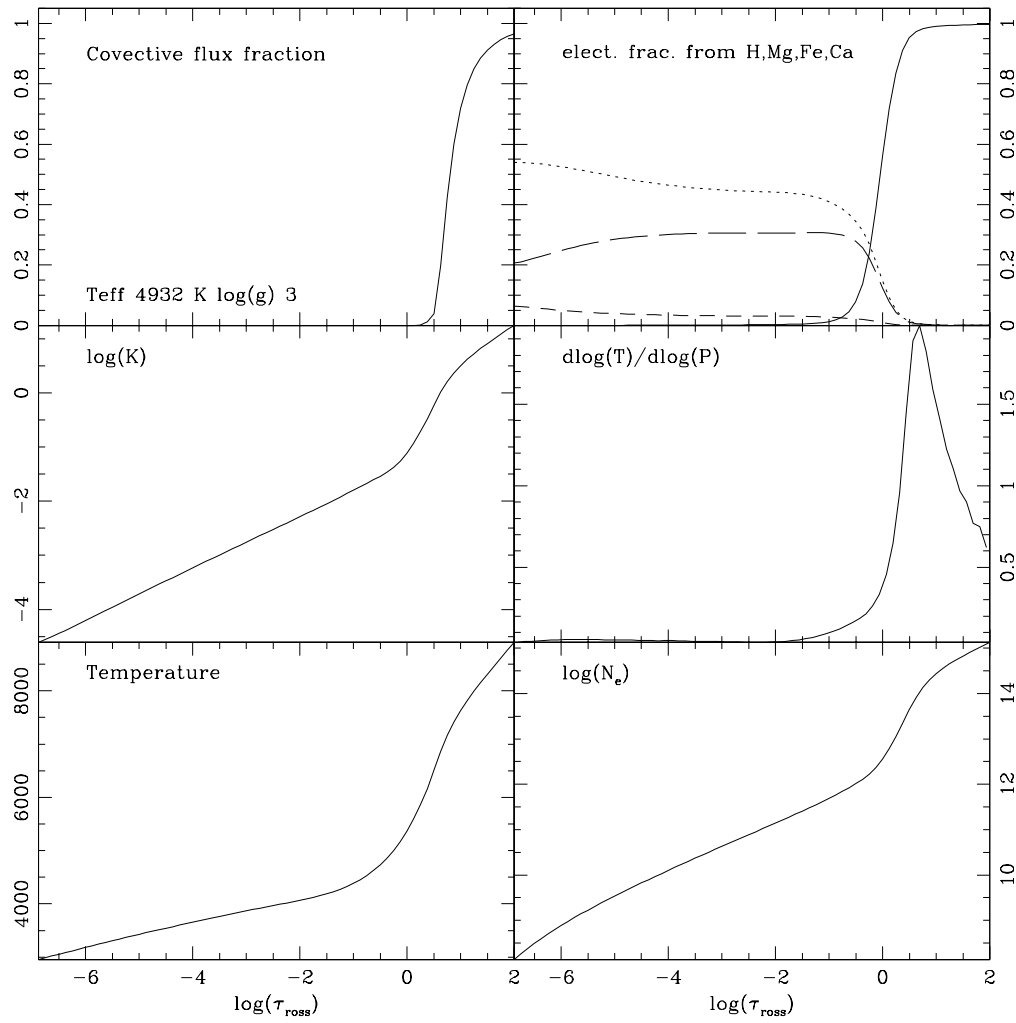


Figure 2.1: Graphics for a model with $T=4932$ K, $\log(g) = 3$, and composition scale factor of 0.31623. See text for details

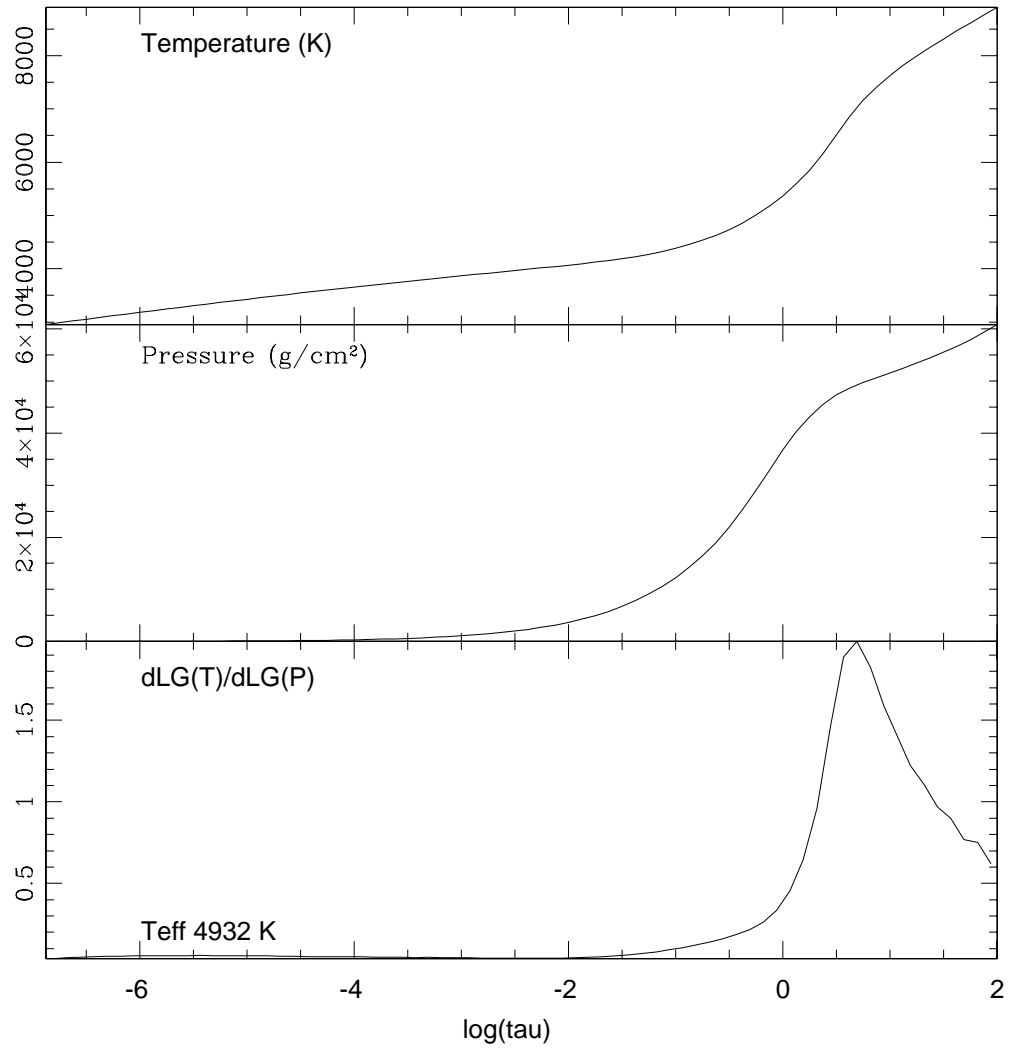


Figure 2.2: For the same model in fig. 2.1 Temperature, pressure and thermal gradient against $\log(\tau_{\text{ross}})$.

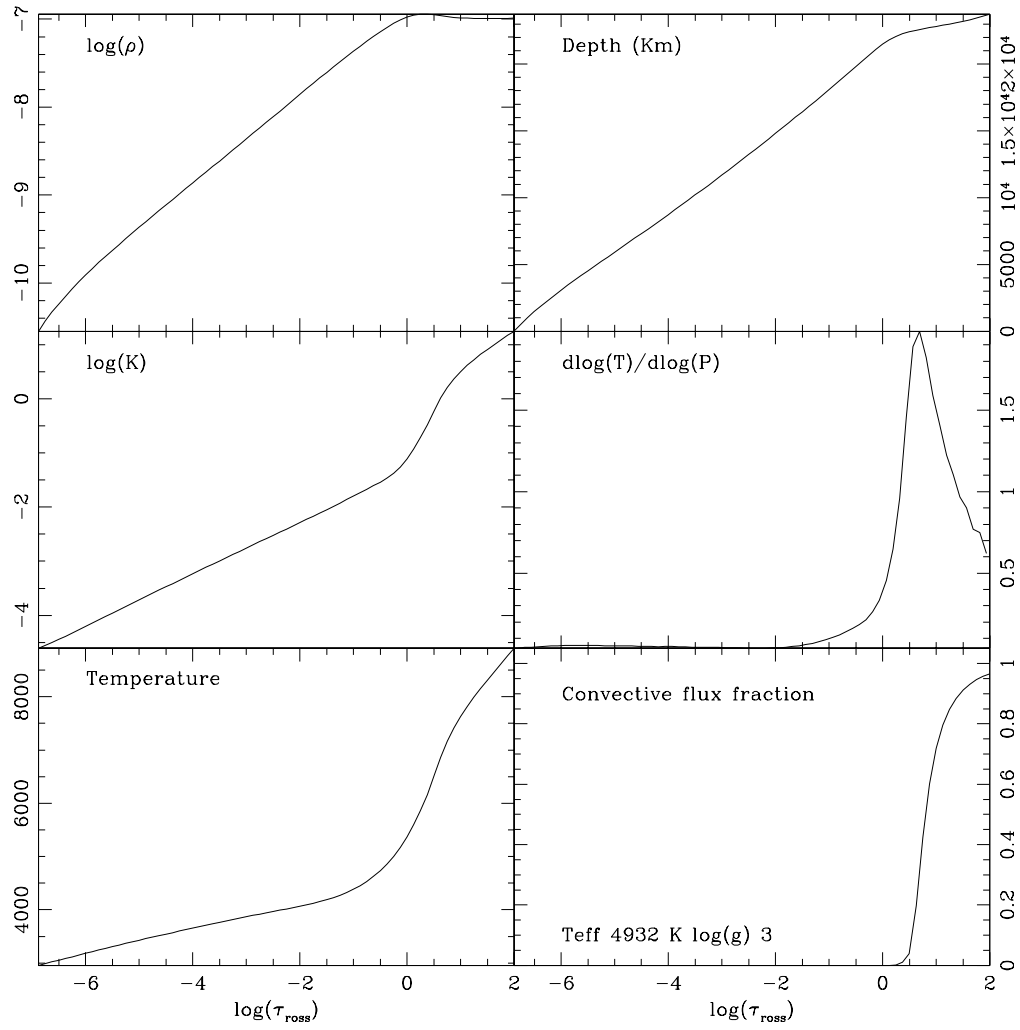


Figure 2.3: Same as in fig. 2.1, but with mass density and metric depth of the model in the two upper panels.

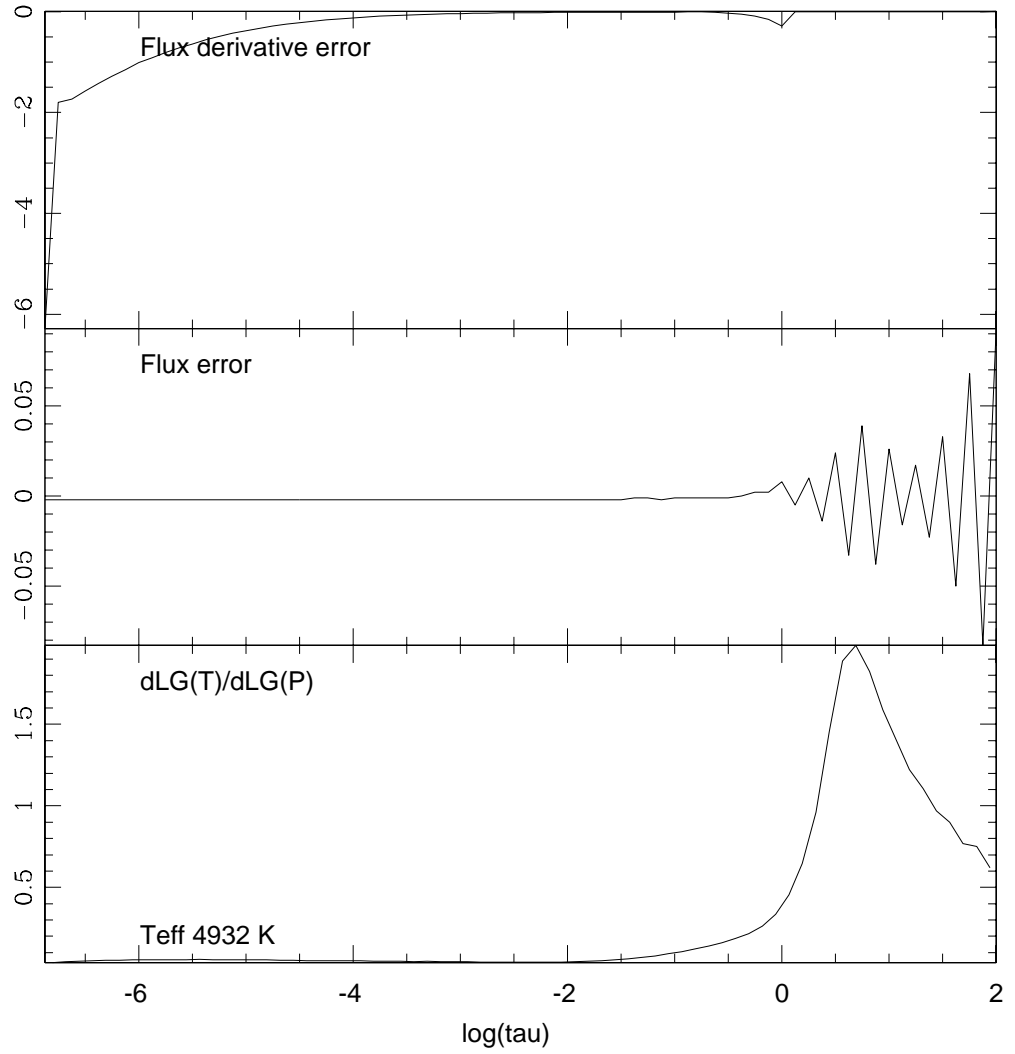


Figure 2.4: For the same model in fig. 2.1, the percent error over flux and flux derivative constancy and the thermal gradient are plotted against $\log(\tau_{ross})$.

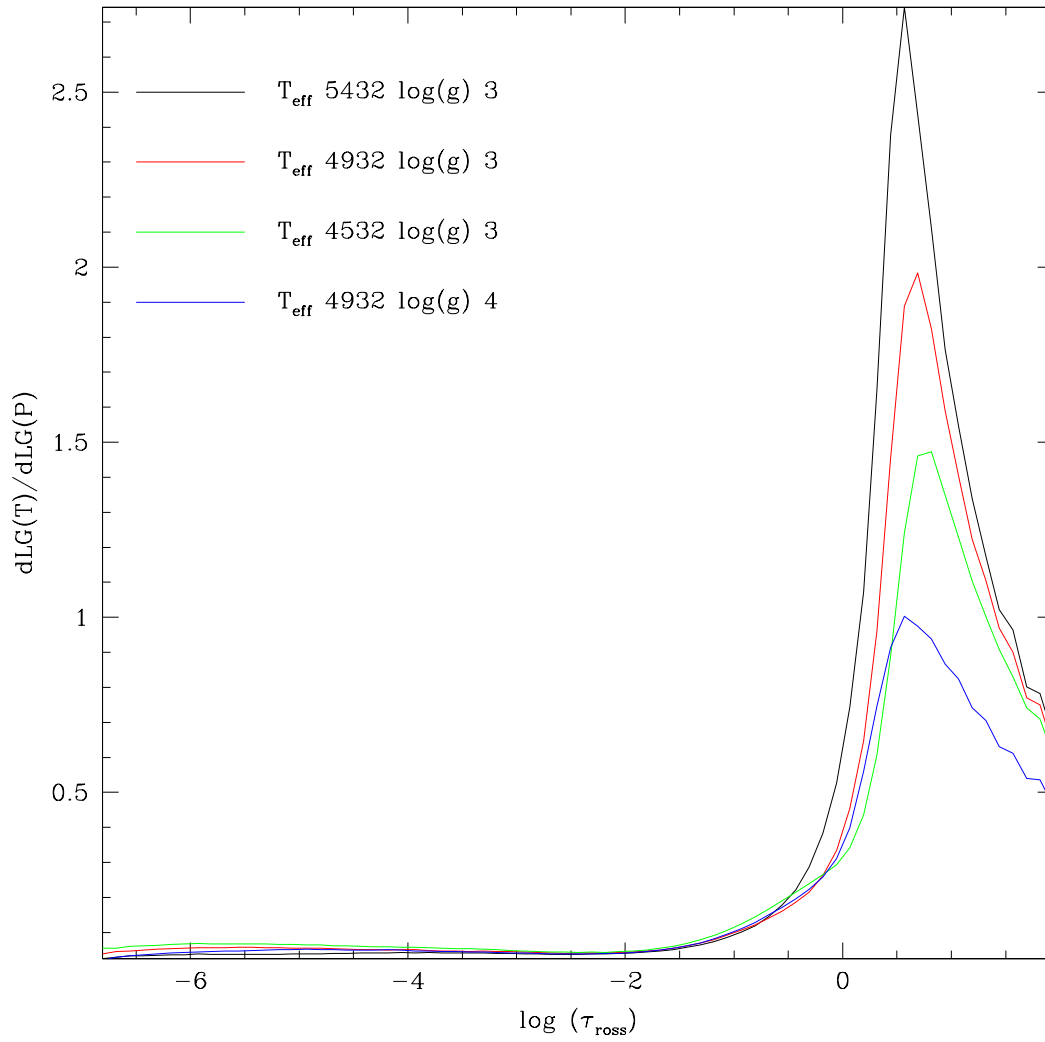


Figure 2.5: Comparison between the thermal gradients of the four models, plotted against $\log(\tau_{ross})$.

First we look at the thermal gradient. Its shape appear to be very similar in all the four model, but various “scaling” differences are present. In fig. 2.5 they are plotted against $\log(\tau_{ross})$; not surprisingly, the peak occurs at very similar optical depth: the onset of convection is strictly related to the opacity. Lower temperature and higher gravity both reduce the height of the peak. Note, in fig. 2.6, the confrontation between the *adiabatic* thermal gradients. Formally, the so called *adiabatic gradient* is defined as:

$$\nabla_{ad} = \left(\frac{d \log T}{d \log P} \right)_{ad} = \frac{P \delta}{T \rho c_P}$$

where c_P is the specific heat at constant pressure and

$$\delta = \left(\frac{d \log \rho}{d \log T} \right)_P.$$

This means that its value is sensitive mainly to equation of state, chemical composition and degree of ionization of the gas. Anyway, if a perfect monoatomic gas is assumed and any composition and ionization gradient is excluded, it can be seen that the quantity assumes a constant value, $\nabla_{ad} = 0.4$. The main cause of departure from this value is, in stellar atmospheres, the ionization gradients in the gas mixture: the hotter model in figure 2.6 approaches better to the perfect gas in the outer layers, but it shows higher deviations in the inner zones, where H ionization becomes significant. It can be seen that, when the actual thermal gradient in the gas exceeds ∇_{ad} , the layer become unstable and convection sets on. In the innermost layers, a consistent depression in the adiabatic gradient contributes along with the increasing opacity to set on the convection. Note that the high gravity model differs here significantly from the low gravity model of same temperature, being very similar to the colder one. This can be correlated to the peaks in the thermal gradient: they are higher for the models with deeper adiabatic gradient sinks; even here, the high gravity model shows a peak much lower than the one of its low gravity “brother”, and more similar to the one of the 4532 K model.

Plotting the gradients against the column density ρ_x (fig. 2.7) shows grater differences: hotter atmospheres are less dense, so, along the model, ρ_x reaches smaller values. Finally, fig. 2.8 shows the gradients plotted against the metric depth of the atmosphere: the higher gravity of the fourth model leads to a far thinner atmosphere; the other three models become thicker as temperature increases, tending to “inflate” the atmosphere.

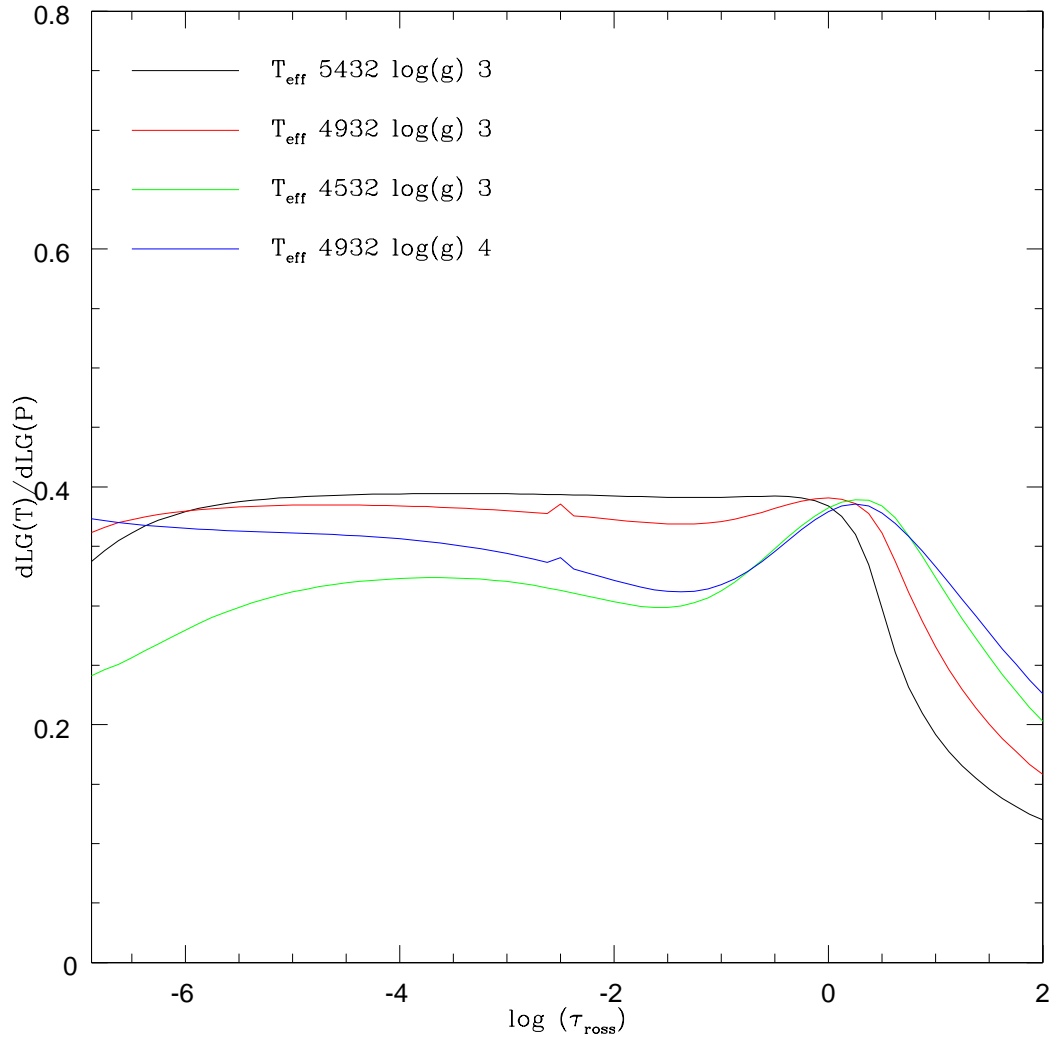


Figure 2.6: Confrontation between the *adiabatic* thermal gradients for the four models, against $\log(\tau_{ross})$

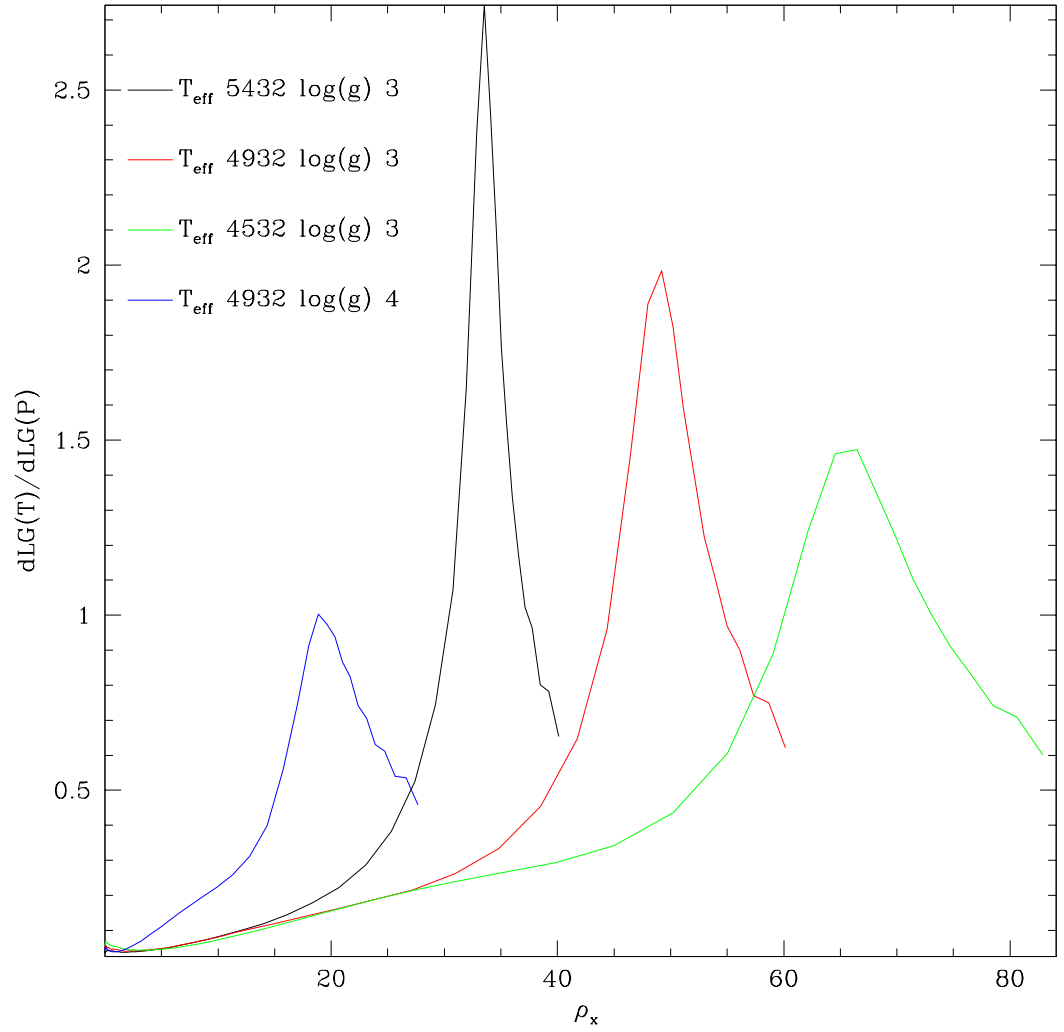


Figure 2.7: Confrontation between the thermal gradients of the four models, plotted against ρ_x .

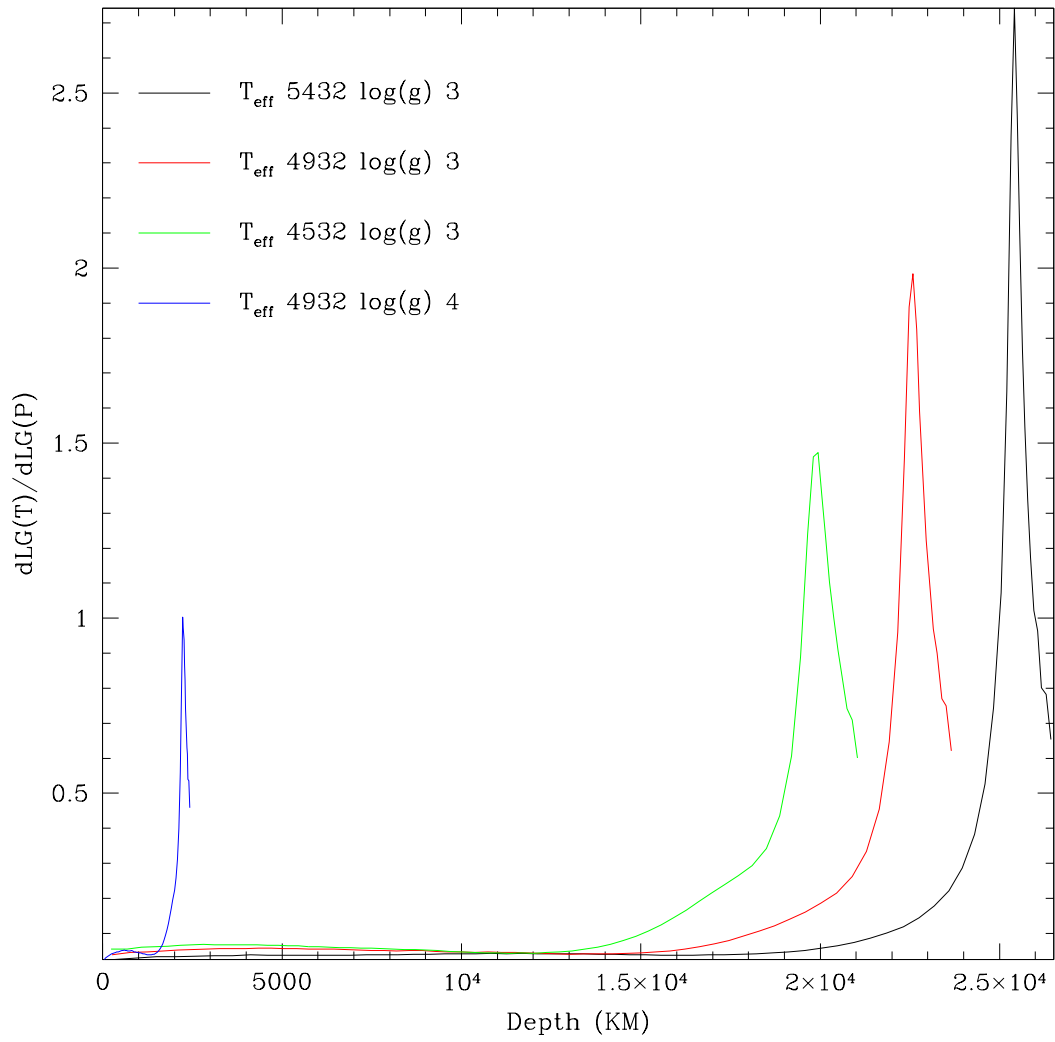


Figure 2.8: Confrontation between the thermal gradients of the four models, plotted against the depth in kilometers from the outermost layer of the model.

Then, we have plotted together for the four models most of the quantities already seen in figs 2.1 and 2.3. It's worth to consider together the figures 2.10, 2.11 and 2.13. For example, the high-gravity model has, for $\tau_{ross} < 1$, the highest opacity and highest mass density for any given optical depth. Its metric depth is, however, by far the smallest, due to the gravity. So, for this model, one must reach higher densities and opacities in order to have the same optical depth.

Some other things can be seen, much of them rather obvious: in fig. 2.10 one can see that, at the same gravity, the mass density decreases with increasing temperature. In fig. 2.11 the opacity appear very similar at low optical depth (for the same gravity), but becomes very different when H becomes significantly ionized.

The temperatures are shown in fig. 2.14: the shape of the four models appear very similar, and the dependence from the gravity is very slight. This is interesting, considering the great differences in the physical dimensions of the various models. This is consistent with the similar shape of the thermal gradient. In the same way can be read the extreme similarity of the graphs (fig. 2.12) showing the convective flux fractions.

Finally, in fig. 2.15 and 2.16, are shown the same graphs for a model equal to the one showed in fig. 2.1 and 2.3 but where convective overshooting is considered. The effect of the overshooting can be clearly seen around $\tau_{ross} = 1$: a clear "bump" appears in the convective flux fraction, and its effect influences mainly the temperature, opacity and thermal gradient graphs. As said before, this modification, occurring around $\tau_{ross} = 1$ would alter significantly any not too strong spectral feature.

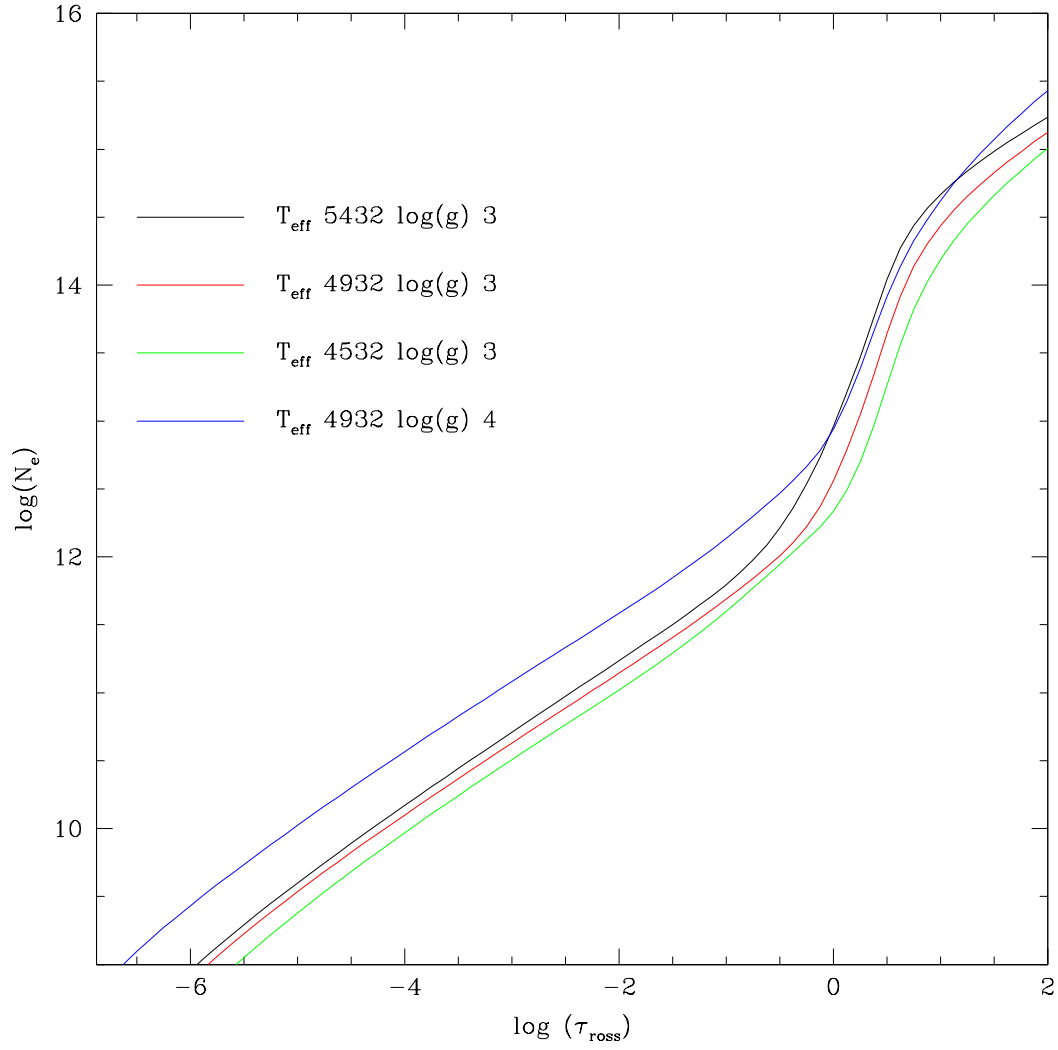


Figure 2.9: Confrontation between the electronic numeric densities of the four models, plotted against $\log(\tau_{ross})$.

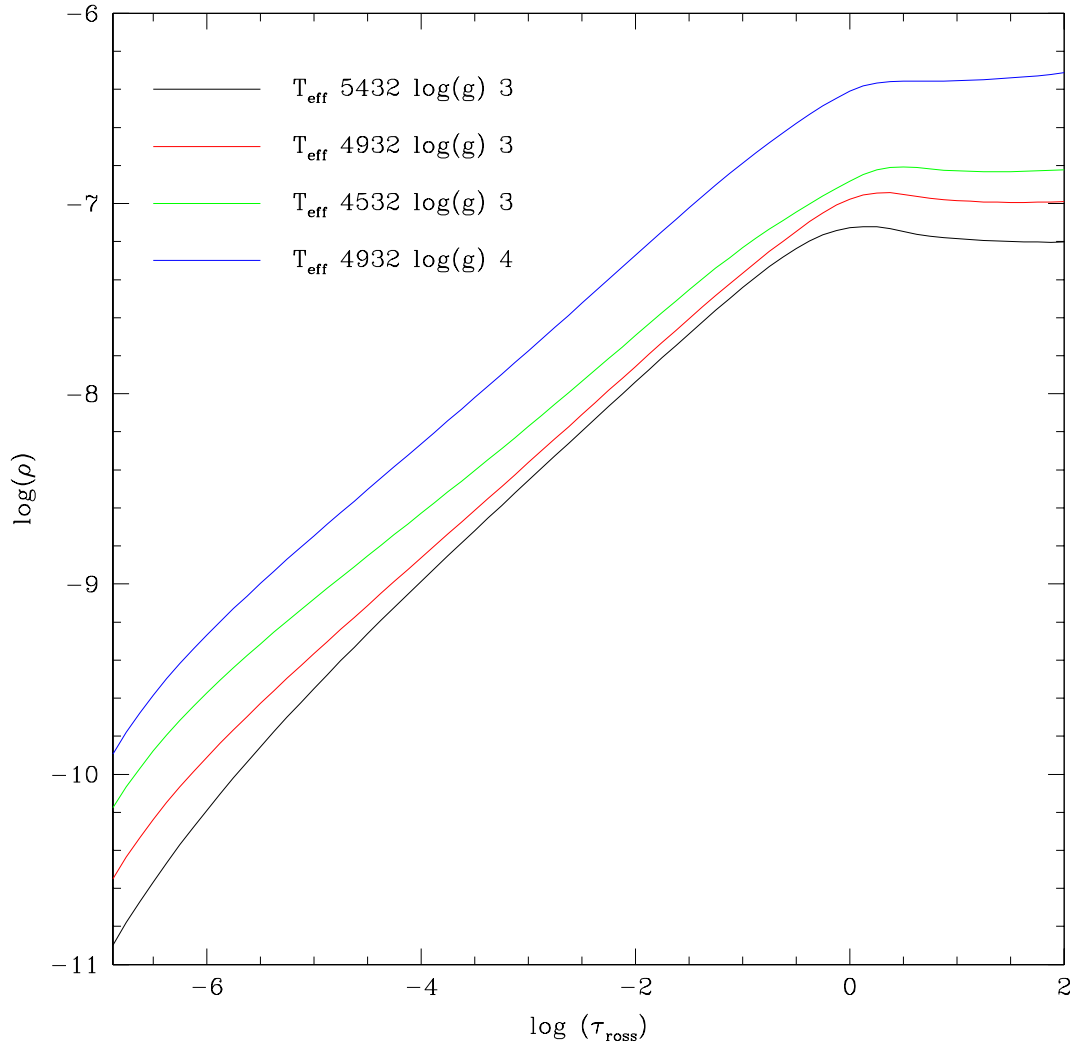


Figure 2.10: Confrontation between the mass densities of the four models, plotted against $\log(\tau_{ross})$.

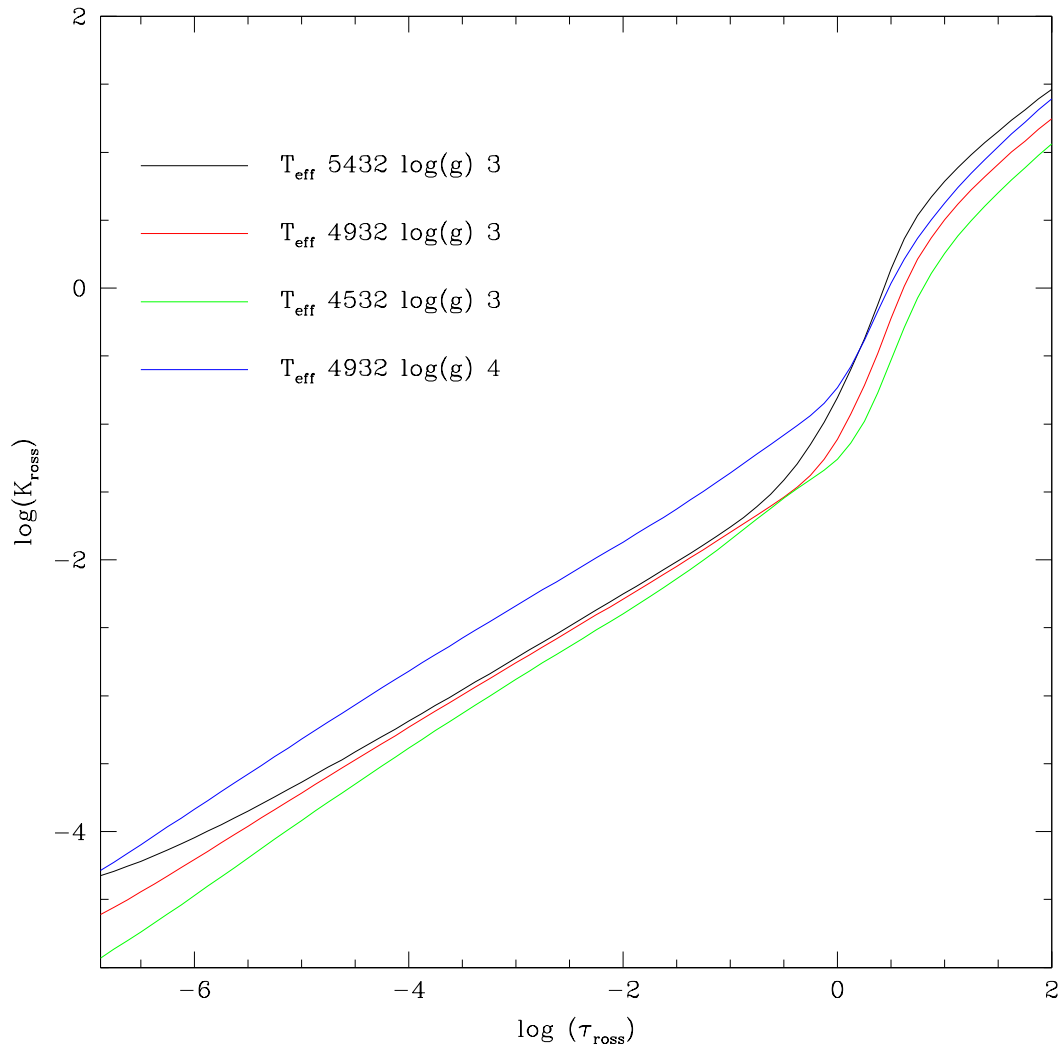


Figure 2.11: Confrontation between the Rosseland mean opacities of the four models, plotted against $\log(\tau_{\text{ross}})$.

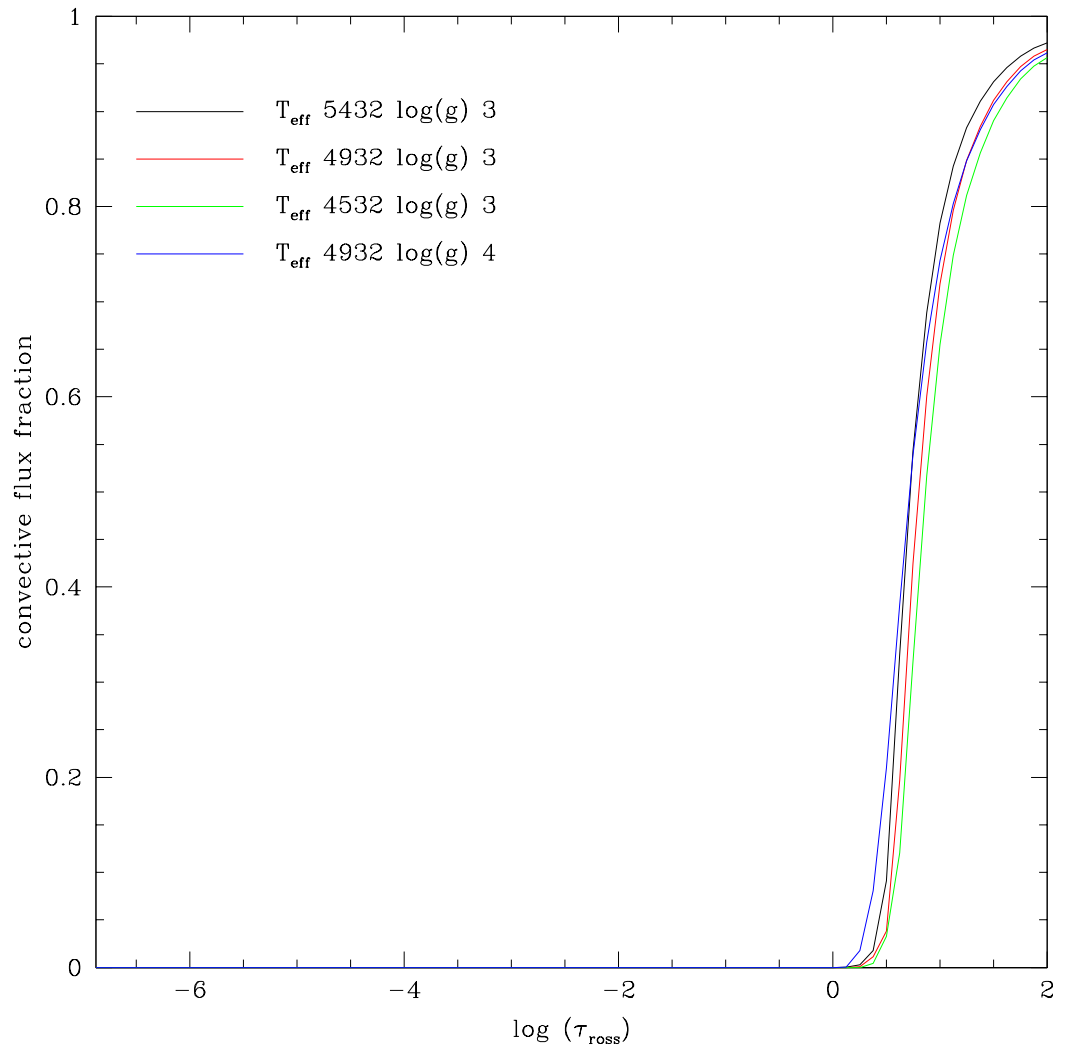


Figure 2.12: Confrontation between the fraction of fluxes transported by convection in the four models, plotted against $\log(\tau_{ross})$.

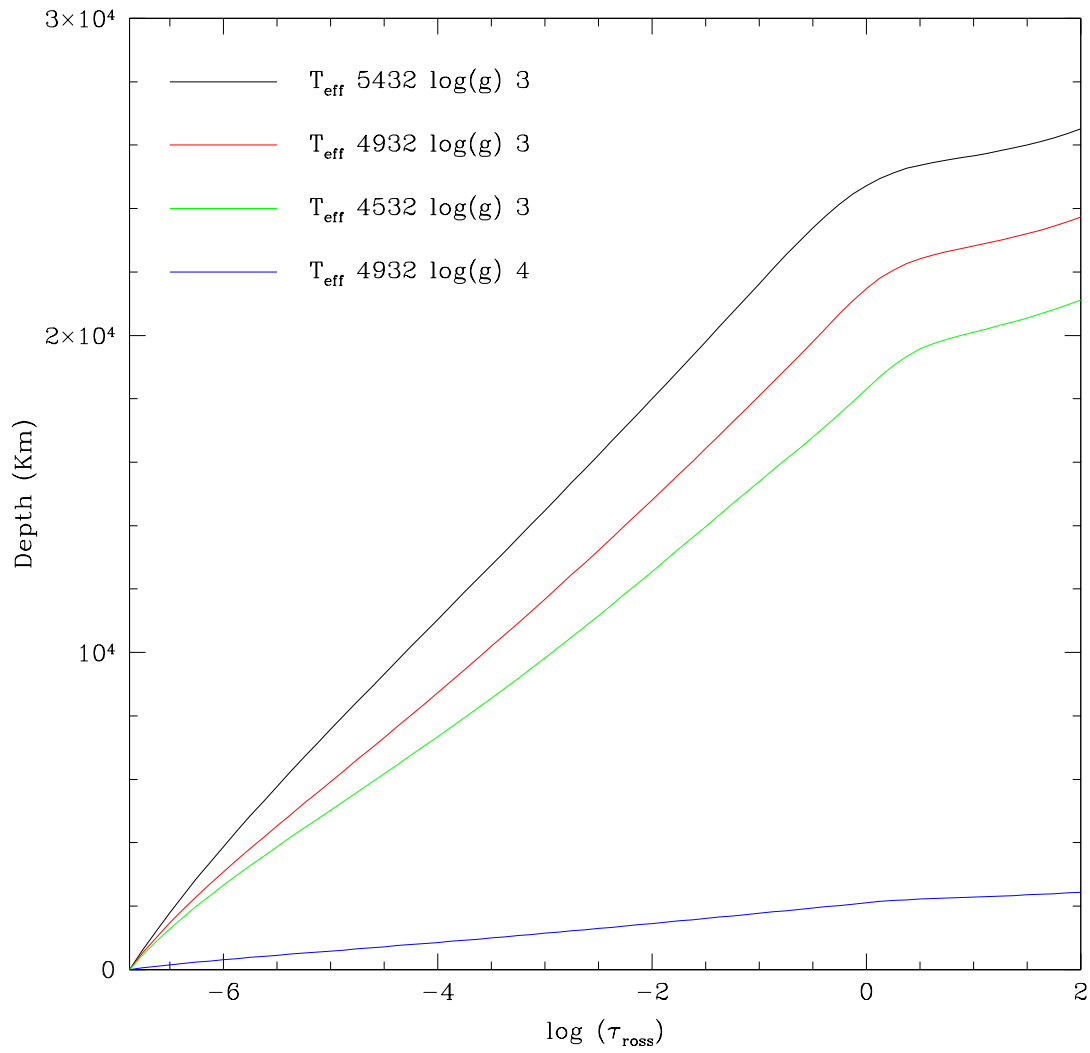


Figure 2.13: Confrontation between the metric depths in the four models, plotted against $\log(\tau_{ross})$.

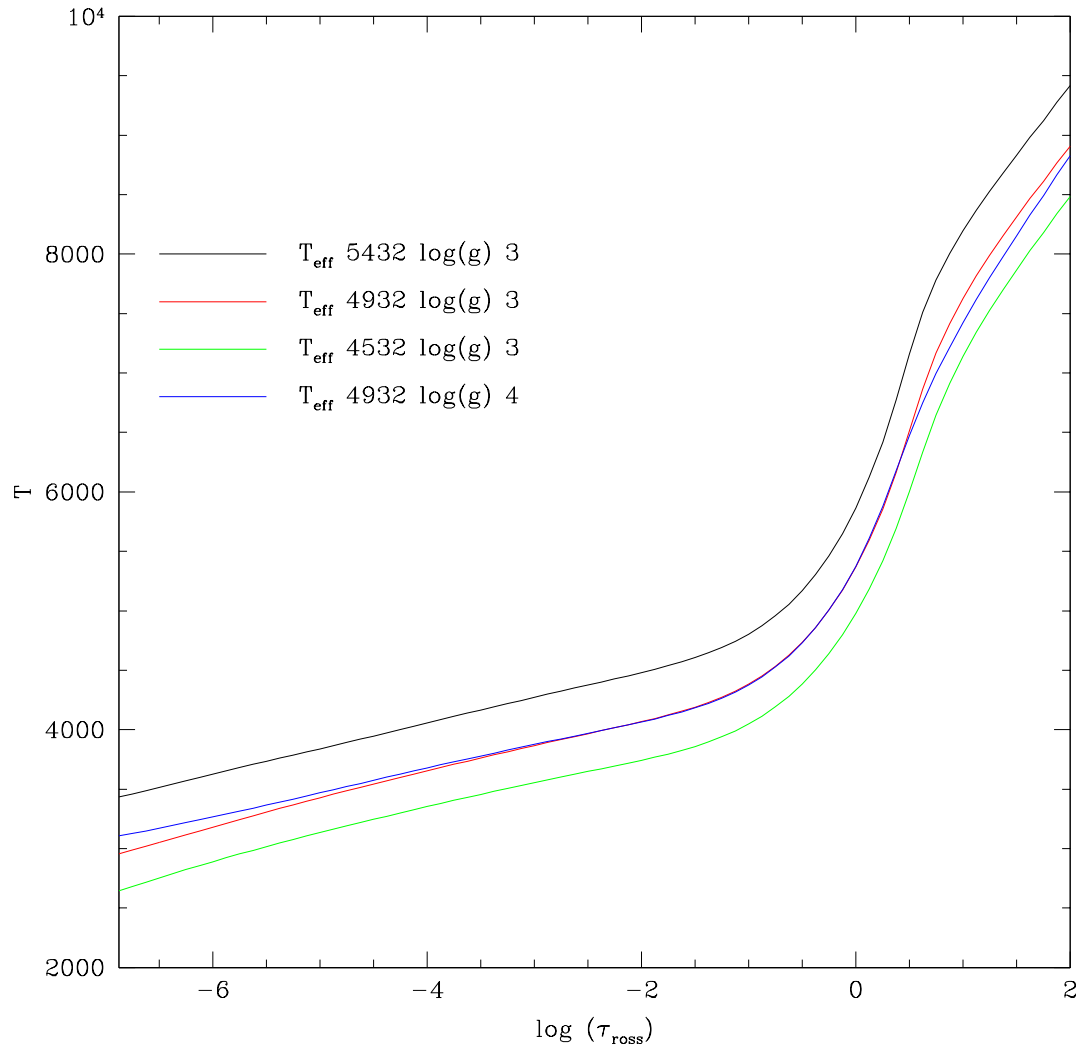


Figure 2.14: Confrontation between the temperatures in the four models, plotted against $\log(\tau_{ross})$.

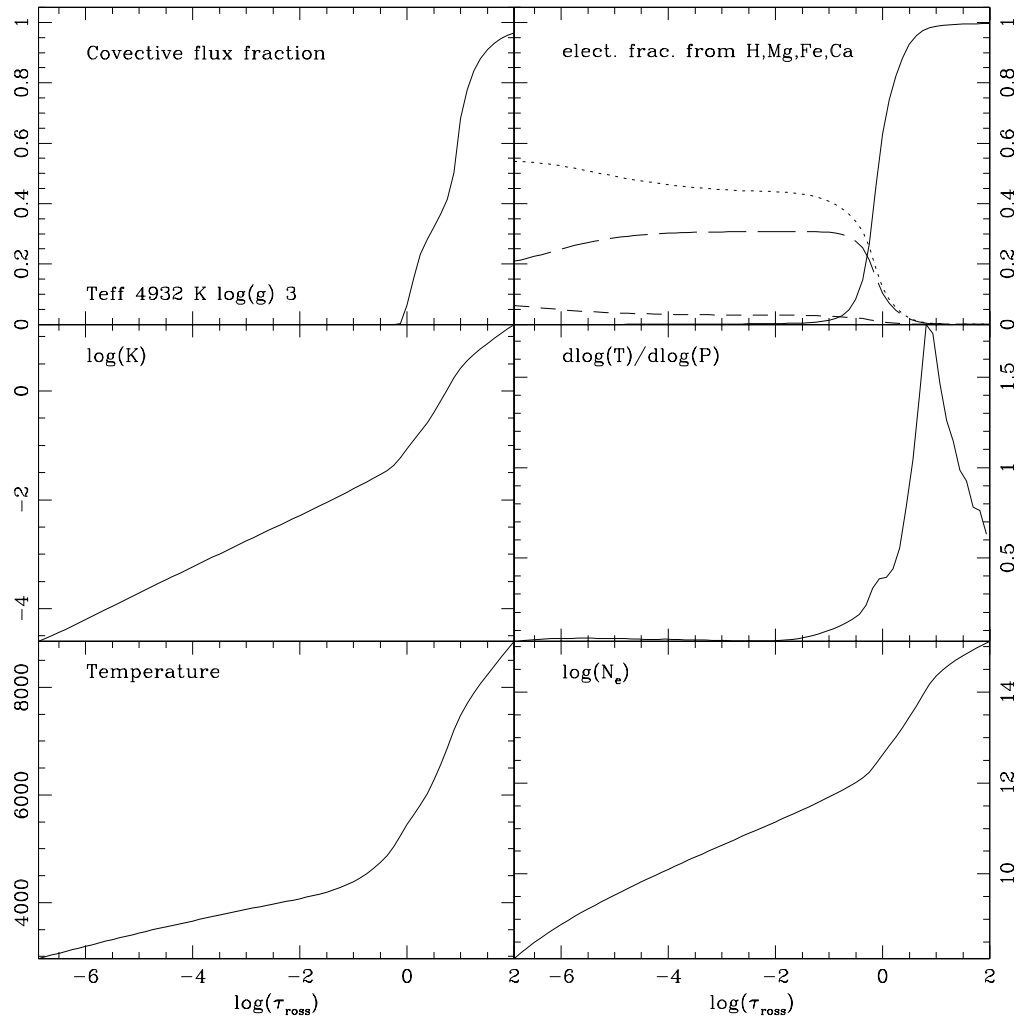


Figure 2.15: Same plots as in fig. 2.1, but for a model with T_{eff} 4932 K, $\log(g) = 3$ and overshooting.

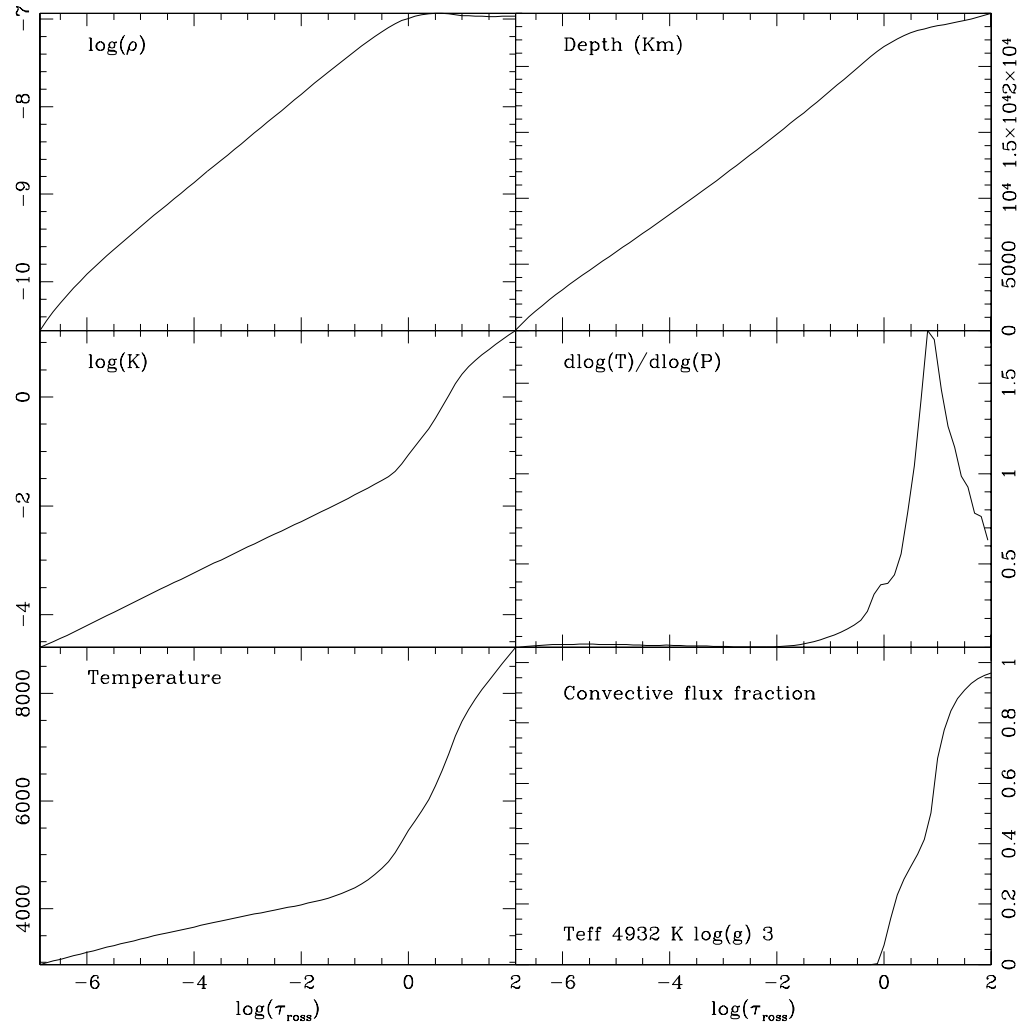


Figure 2.16: Same plots as in fig. 2.3, but for a model with T_{eff} 4932 K, $\log(g) = 3$ and *overshooting*.

Chapter 3

Porting the ATLAS suite to GNU Linux

Along some 40 years, ATLAS, WIDTH and SYNTH (to which we will generically refer as ATLAS suite) have been developed under many different systems (such as CDC, IBM and Cray machines), but in the last 20 years has been almost exclusively available under VMS operating system. Of course, this constitutes an important limit nowadays, since VMS is being dismissed, and is anyway now far less widespread than Linux. Moreover, relatively cheap PCs running Linux can now outperform most (if not all) VMS workstations, and anyway are powerful enough to be used in model atmosphere and synthetic spectra calculation. Some Unix ports of the ATLAS suite do exist, but they are of limited availability, and rarely maintained full compatibility with the original file formats. Besides that, they have not been kept up to date with the evolution of the “original” VMS code. As a consequence, we resolved to produce a “minimal” porting of the entire ATLAS suite, having in mind two main goals:

- To produce a Linux porting that maintained full compatibility with VMS models, linelists, opacities and input files. This, besides allowing the use of all the already existent model grids, ad-hoc ODFs and so on, would have allowed to do only minimal changes to any pre-existent input-output handling script, limiting the modifications to the need of “translate” VMS DCL scripts into UNIX shell ones;
- To limit to the minimum the number of changes inside the code, by looking for a compiler with the largest possible set of backward com-

patibility options, in order to minimize the effort necessary to port any new modification that may be done by the author on the “original” VMS code.

3.1 Porting Issues and solutions

The ATLAS suite has been developed along the years from an original core written in Fortran 4, and was never rewritten in more recent versions of the language, such as Fortran 77. As a consequence, four main classes of issues were to be expected:

1. The presence of obsolescent syntax (e.g. frequent use of Hollerith characters);
2. The presence of obsolescent language behavior, such as the “onetrup” behavior, standard in many compilers up to Fortran 66, causing any “do” loop to be always executed at least once;
3. Analogous to this second class of issues was the (possible) presence of behaviors typical of the standard VMS-Fortran compiler, which may be different from the ones encountered in the Linux compiler of choice;
4. Finally, we were aware of the fact that in many places VMS-Fortran specific library functions had been used, which may not exist or behave differently in other compilers.

Problems 2 and 3 were going to be the more challenging, since they do not generate compilation time errors, but emerge at runtime as inexplicable program behaviors, memory handling errors or unpredictable calculation results.

To minimize the insurgence of such problems, we needed a compiler with a vast set of backward compatibility options. The GNU Linux standard compiler (`g77`) resulted in the past to be ineffective for this purpose, so we decided from the beginning to look for a different solution. We choose to employ the Intel Fortran Compiler (IFC), a F90-95 (with proprietary extensions) compiler whose Linux version is licensed free of charge for research application. Versions 7.0 and 8.0 have been used in the porting (at the time of writing, version 8.1 is available). IFC has an excellent set of backward

compatibility options, as well as a set of VMS – compatibility libraries that can be called at link time.

The changes to the codes were actually minimal. We will now briefly cite the most significant. Most of the described changes had to be applied more or less to all the codes of the ATLAS suite, some of them are explicitly indicated as having been used for a specific code. In all the examples the **first** form presented is the one of the **Linux version** of the code, while the second refers to the old VMS code, unless differently stated.

- **Modified all the OPEN statements**, e.g.:

```
<      OPEN(UNIT=9,file='for009.dat'
<      &,FORM='UNFORMATTED',STATUS='OLD',READONLY,SHARED)
---
>      OPEN(UNIT=9,FORM='UNFORMATTED',STATUS='OLD',READONLY,SHARED)
```

Now, all the input-output files have fixed names: as we will see in 3.1.1, in the new c-shell execution scripts the input files are soft-linked to the proper names, and outputs moved to the final names. The attempt to open a file declaring only the unit number generates an error.

- **Modified all the exponential constant with exponent absolute value above 38 to (at least) double precision.** in IFC exponential representation using the E exponent definition are limited to exponents in the range ± 38 , above D or Q have to be used, e.g.:

```
<      1(-5.519E27+4.808q41/FREQ)/FREQ)/FREQ)/FREQ
---
>      1(-5.519E27+4.808E41/FREQ)/FREQ)/FREQ)/FREQ
```

In particular, Q definition is an IFC proprietary extension to Fortran 95, corresponding to REAL(KIND=16) definition, or 16 bit representation real.

- **Updated the syntax of some FORMAT statements.** IFC supports Hollerith constant representation, but requires the use of commas inside FORMAT statements, e.g.:

```
<      201 FORMAT(1H1/////36X,30HHMINUS STATISTICAL EQUILIBRIUM/10X,4HRHOX,
---
>      201 FORMAT(1H1/////36X30HHMINUS STATISTICAL EQUILIBRIUM/10X4HRHOX,
```

- **Updated unacceptable syntax into implicit iterative read**, e.g.:

```

<      READ(3,1171)  TEFF,GLOG,WLTE,TITLE,IFOP,A,MIXLTH,B,TRBFDG,
<      1TRBPOW,TRBSND,TRBCON,XSCALE,(IZ,ABUND(IZ1),IZ1=1,99)
---
>      READ(3,1171)  TEFF,GLOG,WLTE,TITLE,IFOP,A,MIXLTH,B,TRBFDG,
>      1TRBPOW,TRBSND,TRBCON,XSCALE,(IZ,ABUND(IZ),IZ=1,99)

```

The old statement allowed before to read `IZ` as a variable, and at the same time to use it as a loop counter while reading. This is no longer permitted in IFC, so we had to use another variable as a counter inside the implicit loop. For the sake of clarity: the `ABUND` vector contains the abundances read from the input model for elements of atomic number 1 to 99 (the ones ATLAS considers). In fact, `IZ` is dropped immediately, since is overwritten at every iteration of the implicit loop.

- **Inside ATLAS, passed to a file the iron peak (Ca → Ni) partition functions, before hard-coded inside a DATA block.** At the time the ATLAS suite was initially developed, hard-coding table values (assuming they were constant, of course) was a better solution than reading them in from a file, given the very slow input-output devices of the time. As a consequence, a huge amount of tables are present inside ATLAS, in the form of `DATA` blocks. Nevertheless, apparently IFC has some limitation on the maximum size admitted for `DATA` blocks, thus refusing to compile the code with the iron peak elements partition functions tabulated inside. We have thus moved them on a file (`PFIRON.DAT`) uncommenting a read-in block already present into ATLAS:

```

<      IF(PFTAB(1,1,1,1).EQ.0.)THEN
<      OPEN(UNIT=4,FILE='PFIRON.DAT',STATUS='OLD',SHARED,READONLY)
<      READ(4,1)PFTAB
<      1 FORMAT(26X,7F10.3)
<      ENDIF
---
> C      IF(PFTAB(1,1,1,1).EQ.0.)THEN
> C      OPEN(UNIT=4,FILE='KU2A:[KURUCZ.SYNTH]PFIRON.DAT',
> C      1STATUS='OLD',SHARED,READONLY)
> C      READ(4,1)PFTAB
> C      1 FORMAT(26X,7F10.3)
> C      ENDIF

```

- **Enforced alignment of COMMON blocks inside various subroutines.** When variables are passed between routines inside a `COMMON` block, the user must be aware that, at least in present time FORTRAN,

they are read and written to the block in strict byte order, so that if, for example, a variable is written to the block as a 8-bytes real, and then read in another routine as a 4-bytes real, no conversion is performed by the code (at variance to what happens when operating with variables of different kinds inside routines, or for variables passed as arguments). Instead, only 4 of the 8 bytes are read, producing unpredictable and generally wrong results, a problem known as “disalignment”. Moreover, all the subsequent variables are read sequentially, so that, in case of a disalignment, bytes “leak” from one variable to the next one after the disalignment point.

When compiling with IFC, many misalignment cases appeared in the common blocks inside ATLAS. The y did not show up in VMS - Fortran, is unclear if due to some alignment check that was performed by VMS - Fortran, or by the different behavior of some implicit kind definitions. We did not investigate the origin of the discrepancy, simply enforced coherence of the variables kind along the various routines.

- **In ATLAS, changed the structure of the BLOCKJ subroutine, to break up other big DATA blocks.** A problem analogous to the one above described for the read of iron peak distribution functions arose for the huge COMMON blocks, initialized by DATA instructions, present in the BLOCKJ and BLOCKH subroutines. To obtain IFC to compile this part of the code, we broke them up into three subroutines (BLOCKJ, BLOCKH and tre) and wrote a new subroutine BLOCKJH to “rebuild” the original COMMON block. In all the points where previously BLOCKJ or BLOCKH were called, now BLOCKJH is called instead¹. The *old* code was:

```

SUBROUTINE BLOCKJ
COMMON /MATX/CJ(2601),CH(2601),XTAU(51),NXTAU
DIMENSION CJ  1(36),CJ  2(36),CJ  3(36),CJ  4(36),CJ  5(36)

..... (abridged)

2-1.85281351E-05,-3.70871197E-04,-9.85146118E-03, 9.43947195E-02,
3 9.92892411E-01/
DATA XTAU/0.,.0000032,.0000056,.00001,.000018,
A.000032,.000056,.0001,.00018,.00032,
1.00056,.001,.0018,.0032,.0056,.01,.016,.025,.042,.065,
```

¹This is actually a sort of “quick and dirty” solution to the problem, we are presently aware that a better implementation should exist (F. Castelli, private communication) and will most likely adopt it in the future.

```

2.096,.139,.196,.273,.375,.5,.63,.78,.95,1.15,1.35,1.6,1.85,2.15,
32.45,2.75,3.15,3.65,4.25,5.0,6.,7.,8.,9.,10.,11.5,13.,14.5,16.,
4 18.,20./
DATA NXTAU/51/
END
SUBROUTINE BLOCKH
COMMON /MATX/CJ(2601),CH(2601),XTAU(51),NXTAU
DIMENSION CH 1(36),CH 2(36),CH 3(36),CH 4(36),CH 5(36)

..... (abridged)

2-4.66809104E-06,-1.85535655E-04,-4.04881136E-03, 8.50154847E-02,
3 1.69140724E-01/
END

```

While in the new one we passed to:

```

subroutine BLOCKJ
c implicit real(kind=16) (a-h,o-z)
implicit real*8 (a-h,o-z)
COMMON /MATX_J/CJv(2601)
c dimension cj(2601)
DIMENSION CJ1(36),CJ2(36),CJ3(36),CJ4(36),CJ5(36)

..... (abridged)

2-1.85281351E-05,-3.70871197E-04,-9.85146118E-03, 9.43947195E-02,
3 9.92892411E-01/
return
end
C *****
subroutine tre
c real(kind=16) xtauv,nxtauv
real*8 xtauv
integer nxtauv
common /ecche/xtauv(51),nxtauv
DATA XTAUv/0.,.0000032,.0000056,.00001,.000018,
A.000032,.000056,.0001,.00018,.00032,
1.00056,.001,.0018,.0032,.0056,.01,.016,.025,.042,.065,
2.096,.139,.196,.273,.375,.5,.63,.78,.95,1.15,1.35,1.6,1.85,2.15,
32.45,2.75,3.15,3.65,4.25,5.0,6.,7.,8.,9.,10.,11.5,13.,14.5,16.,
4 18.,20./
DATA NXTAUv/51/
return
end
C *****
subroutine blockh
c implicit real(kind=16) (a-h,o-z)
implicit real*8 (a-h,o-z)
COMMON /MATX_h/CHv(2601)
DIMENSION CH 1(36),CH 2(36),CH 3(36),CH 4(36),CH 5(36)

..... (abridged)

```

```

2-4.66809104E-06,-1.85535655E-04,-4.04881136E-03, 8.50154847E-02,
3 1.69140724E-01/
return
end
C *****
subroutine blockjh
implicit real*8 (a-h,o-z)
COMMON /MATX_J/CJ_p(2601)
COMMON /MATX_h/CH_p(2601)
common /ecche/XTAU_p(51),NXTAU_p
common /matx/CJ(2601),ch_X(2601),XTAU(51),NXTAU
call blockj
call blockh
call tre
do i=1,2601
  cj(i)=cj_p(i)
  ch_X(i)=ch_p(i)
enddo

do i=1,51
  xtau(i)=xtau_p(i)
enddo
nxtau=nxtau_p
return
end
C *****

```

- **IFC 7 only change:** added a definition for ABORT and EXIT library functions. VMS - Fortran EXIT and ABORT library functions had been used in the original codes. In the version ported to IFC 7.0, we needed to introduce INTERFACE blocks to make the corresponding compatibility library functions visible to the compiler, e.g.:

```

interface
  subroutine exit(status)
    integer(4),optional,intent(in)::status
  end subroutine
end interface

```

Together with an USE IFPORT instruction. Since IFC 8.0 this is no longer necessary, so the corresponding lines are commented.

3.1.1 Execution scripts

Execution scripts have been of course completely rewritten from scratch as tcsh shell script, so there's no point in citing here the individual changes. Suffice to say that now input files are soft-linked to the (fixed) filenames used by the codes, e.g.:

```
ln -s /usr/local/kurucz/lines/he1tables.dat fort.18
```

Similarly, the output files are moved from the fixed name to the desired one. Many codes in the ATLAS suite require to receive input directly from the standard input. This has solved in ways analogous to this one, an input to SYNBEQ inside the calculation of a synthetic spectrum:

```
/usr/local/kurucz/bin/synbeg.exe <<EOF
AIR      669.1    670.1    600000.    0.83    0    30    .0001    1    0
AIRorVAC  WLBEG     WLEND     RESOLU    TURBV   IFNLTE  LINOUT  CUTOFF      NREAD
EOF
```

3.1.2 Linelists, opacities and similar input data

Linelists format is completely unchanged, since these files are in ASCII. ODFs instead were read from *binary* files, which should in principle being readable on a Linux machine (being both little endian systems). Nevertheless, for some still unclear reason we were not able to read them directly, so we translated them from binary to ASCII on a VMS machine, passed the ASCII files on a Linux machine, and translated them back to Linux binary. ODFs are extremely bulky, so that binary form saves a lot of disk space. Apart from this, the content of the ODF files is totally unchanged. We have prepared versions able to read in bot the “old” (Kurucz, 1993) and “new” (Castelli & Kurucz, 2004) ODFs. Molecular linelists, which were typically binary in the VMS version of the codes, are instead read in ASCII form in the Linux version, and are read by an *ad hoc* version of the RMOLEC code (RMOLECCASC).

3.2 Results, performance and availability

The results obtained with the ported version of the codes are, as can be seen in fig. 3.1, 3.2 and 3.3, indistinguishable from the ones produced by the VMS version.

The porting leads to a dramatic increase in performance with respect to the VMS version. Examples of ATLAS and SYNTHE execution times (WIDTH is a very fast program, with execution times of about 1 - 2 seconds) are summarized in table 3.1. Listed execution times are indicative since they also depend on disk throughput. As can be seen, both atmosphere modeling and spectral synthesis can now be performed in very short times on a mainstream laptop computer (the system labeled as “Pentium M” in

	ATLAS	SYNTHE
	s	s
VMS	478 (3.54)	69
Pentium 4	177 (1.31)	10
Pentium M	122 (0.9)	10

Table 3.1: Execution time comparison for ATLAS 9, calculated on 135 iterations of a 72 layers model (time per iteration within parentheses), and for the calculation of a 5 nm synthetic spectrum at resolution 600000 with SYNTHE. Systems are: VMS: AlphaServer 800 5-500; Pentium 4: 1.9 GHz 768 Mb RAM kernel 2.4.18-3 (Red Hat 7.3) IFC 7.0; Pentium M: 1.6 GHz, 512 Mb RAM kernel 2.4.22-1.2115.nptl (Fedora Core 1) IFC 8.0. All times in seconds.

table 3.1 is actually a laptop). This would allow any user to calculate directly any atmosphere he needs, without having to rely on precalculated grids.

Moreover, together with the use of Linux supercomputer architectures such as Beowulf, this allows to use this programs in the framework of large automated spectral analysis codes (see for instance Bonifacio & Caffau, 2003) conceived to analyze semi-automatically the high amount of data produced by high multiplexity spectrographs such as VLT-FLAMES. The high speed at which both the atmosphere modeling and the spectral synthesis steps can be performed, allows to produce large amounts of Monte Carlo tests to assess the error budget of the derived abundances.

The suite, as the original Kurucz one, is intended to be freely available to everyone interested in it. The full disk space required is about 700 Mb, for a typical set of ODFs of the BIG type (for model computation), line lists and molecular data. For the time being, a restricted access area has been set to download the codes from at the web address <http://wwwuser.oat.ts.astro.it/bonifacio/web/>. Interested people are encouraged to contact us to obtain the password to access the codes, and any information related to them².

Anyone using the codes for scientific publications is only requested to cite Sbordone et al. (2004a) along with Kurucz (1993). Nevertheless, we plan to publish it on the Web as soon as possible, along with the proper

²by emailing lsbordone@eso.org or bonifaci@ts.astro.it

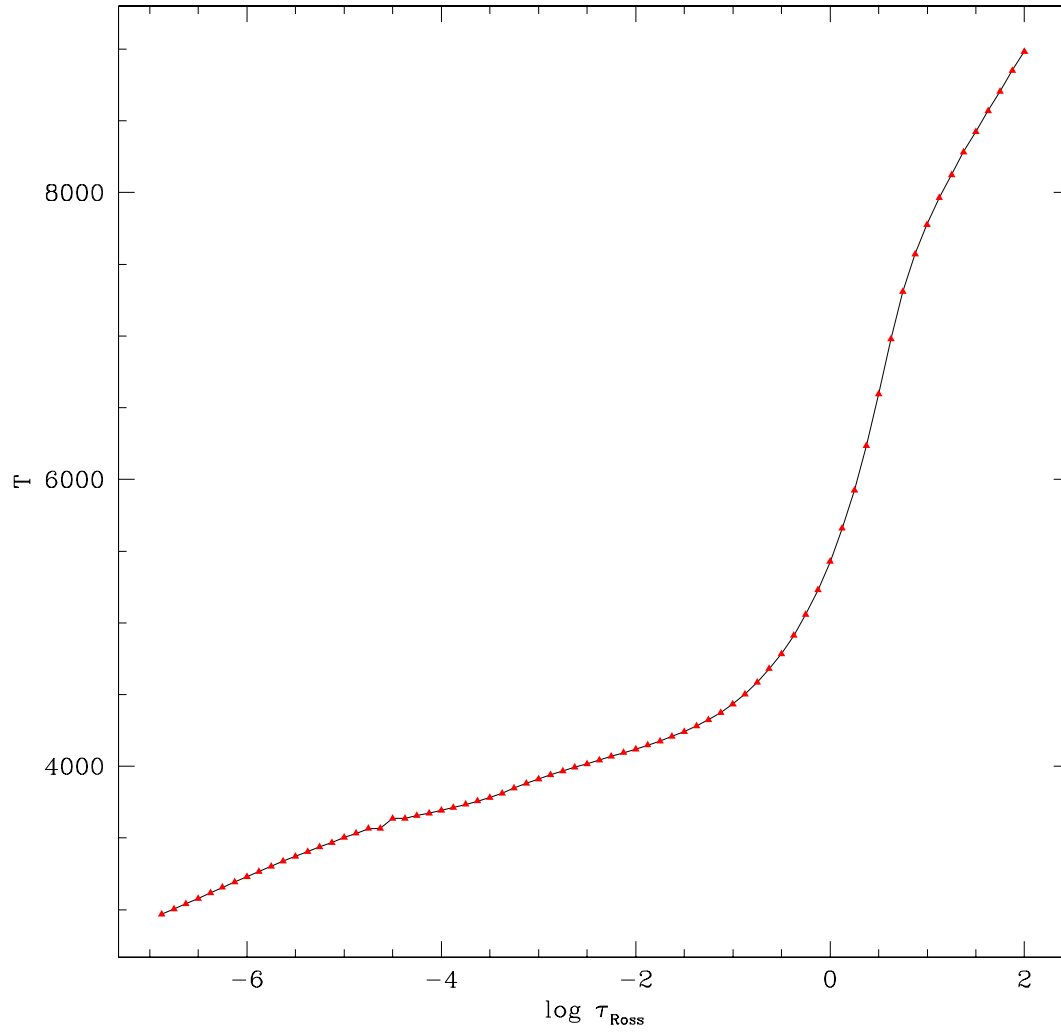


Figure 3.1: Plot of T against $\log(\tau_{Ross})$ along the atmosphere of a star of $T_{eff} = 5000$ K, $\log g = 2.5$, $[Fe/H] = -0.5$, as produced by the Linux ported code (solid line) and the original VMS code (triangles).

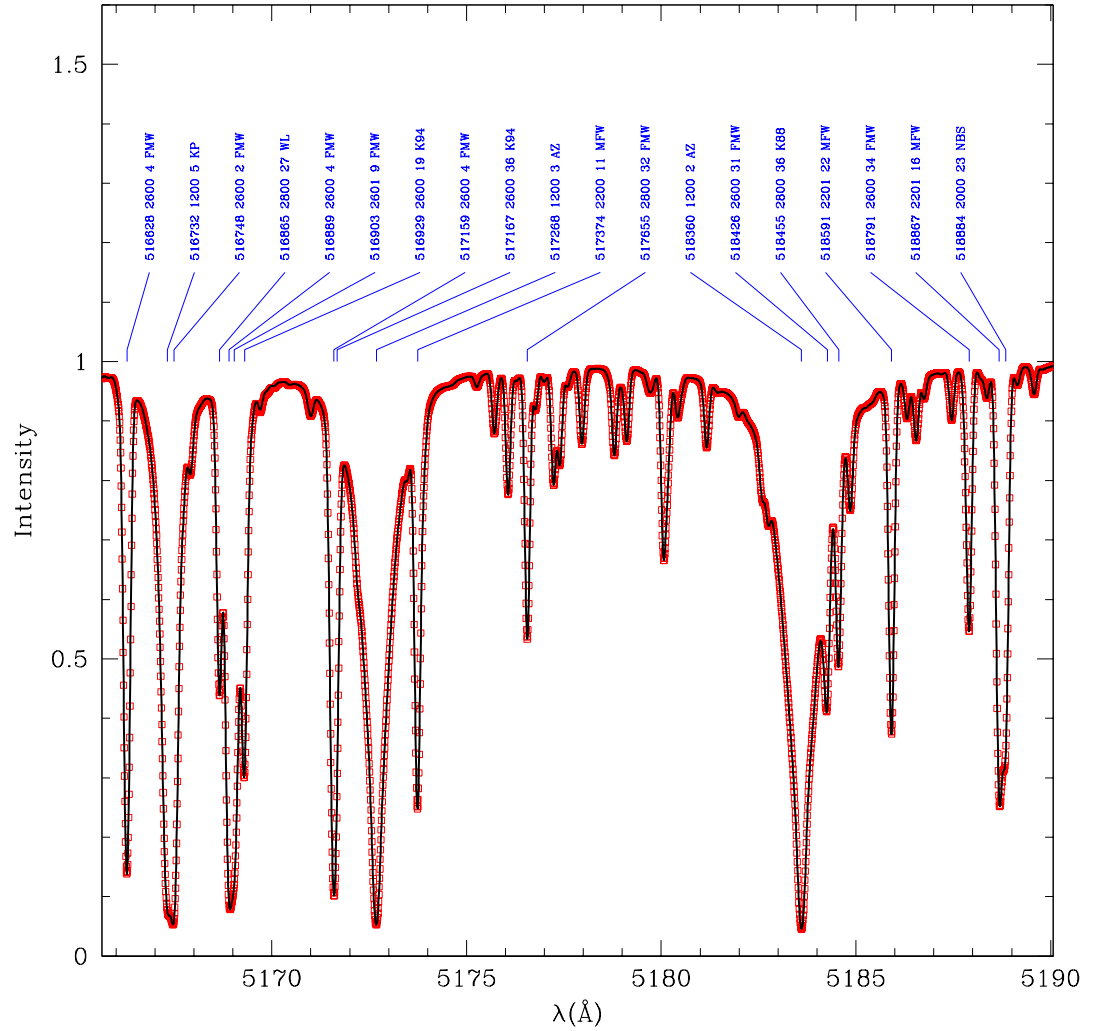


Figure 3.2: Synthetic spectrum for the above mentioned star around the Mg b triplet. Open squares is VMS original code, solid line Linux code. The resolution of the calculation is 600000, then a gaussian broadening (7 km/s FWHM) has been added to simulate the output of a spectrometer with resolution of about 43000. An example of line label: 518360 = 518.360 nm; 1200 = Mg (12 atomic number) neutral (00); 2 = 2% residual intensity at line center (unbroadened spectrum); AZ is a code for the line $\log(gf)$ source.

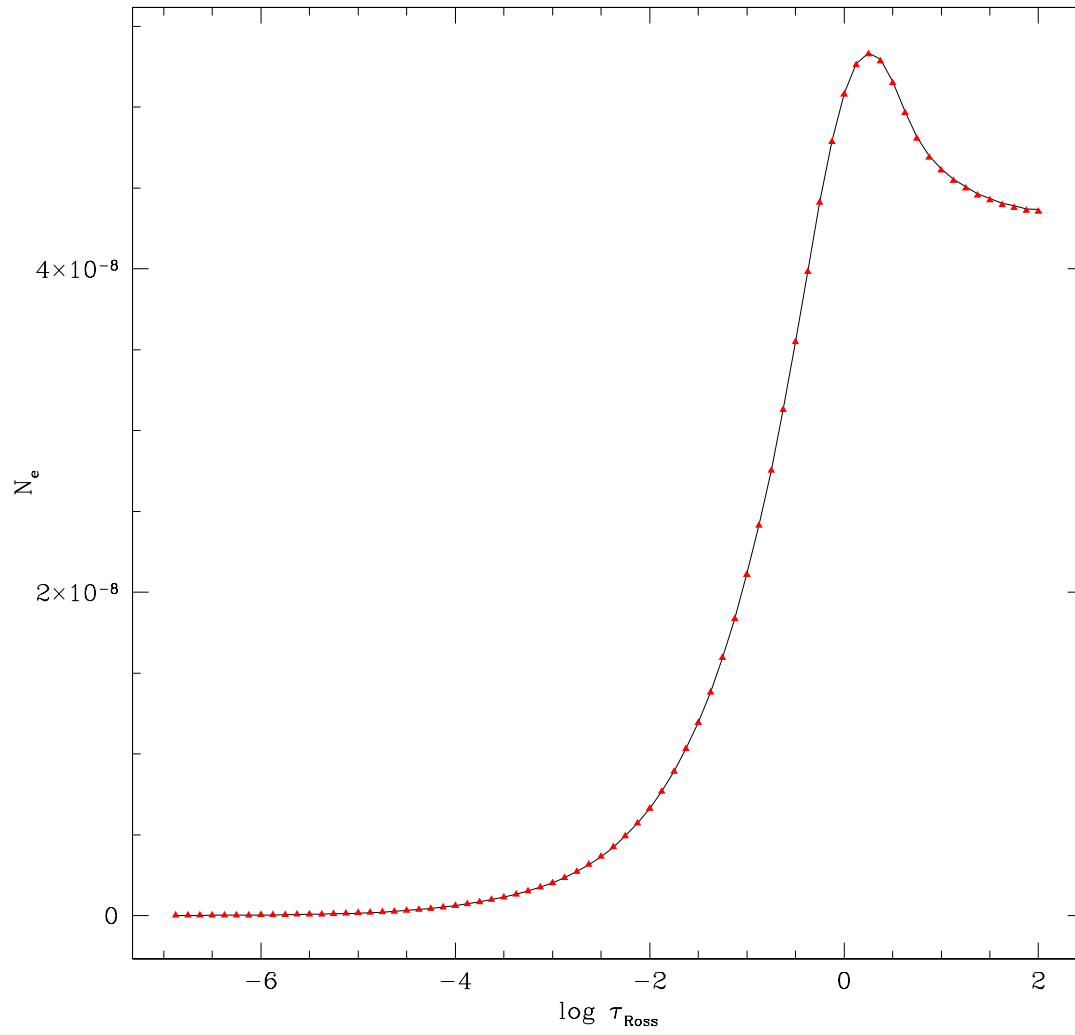


Figure 3.3: Same as in fig. 3.1, but now comparing electron number densities.

documentation.

Chapter 4

Abundances in Sgr dSph

4.1 Introduction

The Sagittarius Dwarf Spheroidal galaxy (Sgr dSph) is the nearest *confirmed* neighbor of the Milky Way. Should the Canis Major overdensity (see chapter 6) be confirmed as an actual dwarf galaxy, Sgr dSph would become the second nearest satellite of the MW.

Sgr dSph was discovered by Ibata et al. (1994, 1995) while studying MW Bulge cinematic. The authors discovered a subpopulation characterized by high radial velocity ($\sim 140 \pm 2 \text{ kms}^{-1}$) with small velocity dispersion ($\sim 10 \text{ kms}^{-1}$) the standard galactic models failed to account for. They interpreted it as a new dwarf galaxy, and derived, from the comparison of its (putative) horizontal branch with the Small Magellanic Cloud (SMC) a distance from the Sun of about 24 Kpc. They also plotted the spatial distribution of the peculiar population, which resulted to resemble an elongated object of about $10^\circ \times 5^\circ$, exactly centered on the globular cluster M54. As a consequence, the authors suggested that M54 may actually constitute the *nucleus* of the Sgr dSph. They also postulated the association to Sgr dSph of three more globular clusters, Terzan 7, Terzan 8 and Arp 2, basing this hypothesis on the fact that distances and radial velocities of these clusters were very similar to the ones derived for Sgr dSph. The new galaxy appeared to be comparable in mass with the most massive dwarf spheroidal in the local group (Fornax). The comparison of the main red giant branch of Sgr dSph with galactic globular clusters RGBs led to a rough estimate of $[\text{Fe}/\text{H}] \sim -1$.

The association of M54, Ter 7, Ter 8 and Arp 2 with the Sgr dSph was also

confirmed by Da Costa & Armandroff (1995). They measured Ca II triplet for a sample of halo GCs, included the four Sgr dSph clusters. The clusters showed an important spread in metallicity, between $[\text{Fe}/\text{H}] = -1.88$ (Ter 8) and $[\text{Fe}/\text{H}] = -0.36$ (Ter 7, a value significantly higher than the photometric estimates: we will consider this problem in chapter 5).

Many photometric studies tried to establish stellar content, age and star formation history of Sgr dSph (Mateo et al., 1995; Sarajedini & Layden, 1995; Marconi et al., 1998; Alard, 2001, among others). The galaxy was depicted as harboring stellar populations with significant age, or metallicity spread (as already suggested by the differences in metallicity among the associated globulars), with the older / more metal poor core constituted by M54, while the most metal rich populations detected were compatible with the high metallicity of Terzan 7.

To date, the largest published photometric study of the Sgr dSph has analyzed an area of about one square degree, with a total of about 500,000 stars (Monaco et al., 2002, 2003, 2004). This vast research led to the first detection of the RGB bump, allowing the authors to pose a stringent constraint to the metallicity and age of the main population of the galaxy, resulting to be of $[\text{Fe}/\text{H}] = -0.5$ and between 4 and 8 GYr respectively. It also allowed to give a new distance estimate based on the position of the RGB tip (heliocentric distance 26.3 Kpc, $(m-M)_0 = 17.10$). The authors also detected the presence of a blue horizontal branch in the galaxy main body, evidence of the existence of a metal poor ($[\text{Fe}/\text{H}] < -1.3$) and old (age > 10 GYr) population in the galaxy, which the authors estimate to account at least for the 10% of the total galactic population. It is important to notice, nevertheless, that even this very wide field study covers only a small fraction of the total area of Sgr dSph.

Since its discovery, it had been clear that Sgr dSph was moving along a very short period orbit and, consequently, was likely being tidally accreted by the MW. It was determined (Ibata et al., 1997; Helmi & White, 1999; Gómez-Flechoso et al., 1999) that the galaxy was moving on a quasi-polar, short period (less than 1 GYr) orbit inside the Milky Way Halo. The strong tidal interaction was actually leading Sgr dSph to “dissolve” in the MW Halo (Ibata & Lewis, 1998), a process thought to be fundamental for the Halo buildup (Helmi & White, 1999). This finding was in agreement with a number of observational evidences (Mateo et al., 1996; Alard, 1996) indicating that stellar populations related to Sgr dSph could be identified at great angular distances from the galaxy center. Among the most intriguing was

the suggestion by Ng (1997, 1998) that from this could come a solution to the so-called Bulge C stars problem (Blanco et al., 1978; Azzopardi et al., 1988). Carbon stars are present in the MW Bulge, but appear to be about 2.5 mag too faint to *actually* belong to the bulge, if they are assumed to be at RGB tip. Ng observed that Sgr dSph has a distance modulus 2.5 mag fainter than the bulge, so, by putting the Bulge C-stars at the distance of the Sgr dSph they would have the “right” luminosity. Although not dynamically compatible with a Sgr membership, these stars may have originated in the MW from the shock due to the interaction with the Sgr dSph (see 4.7).

The first detection of the Sgr dSph stream was also accomplished partly by detecting a C star overdensity inside the halo (Ibata et al., 2001, and references therein), but a comprehensive picture of the dSph and its stream was not available until a full-sky view of the system was obtained from 2MASS data (Majewski et al., 2003). The major axis of the main body resulted to extend over an impressive 30° , beyond which the density dropped sharply and the tidal stream developed, encompassing the entire MW. The Sgr dSph was recognized to contribute more than 75% of the high galactic latitude Halo M giants, thus confirming the importance of the galaxy in shaping the outermost part of the MW.

At the same time, evidences accumulated that many Halo globular clusters may have been accreted by the MW after having been formed elsewhere. A number of them have been tentatively associated to the Sgr dSph on the basis of dynamical considerations and the presence of extended tidal tails: among them Palomar 12, Palomar 5 and NGC 5634 (see e. g. Bellazzini et al., 2002, 2003; Martínez-Delgado et al., 2002). Later on, Palomar 5 has been dismissed as probable former Sgr dSph member (Odenkirchen et al., 2003), but the “best candidate”, Palomar 12, can now be safely considered as a former Sgr dSph cluster (Cohen, 2004, and this work, 4.4.6). It is worth noticing that this takes the number of globulars formed inside Sgr dSph at least to five, the highest number among local group dwarf galaxies, another strong hint of the great mass that the Sgr system should have possessed in the past.

When the present work was started, all the photometric studies indicated that the Sgr dSph was not interpretable as a single stellar population. The very different metallicities and ages in the associated globulars, the evidences of gradients in the populations, the excessively wide RGB and the puzzling presence of a blue plume (BP) detected by Marconi et al. (1998) were all hints that a significant spread in ages or in metallicities were present in

the galaxy. During the UVES commissioning, two stars in the RGB of Sgr dSph were observed and analyzed by Bonifacio et al. (2000a), who derived chemical abundances for 21 elements from Oxygen to Europium. Surprisingly enough, the two stars resulted to be exceptionally metal rich ($[\text{Fe}/\text{H}] = -0.21$ and -0.28), and displayed a truly unusual overall abundance pattern, with negative $[\alpha/\text{Fe}]$, underabundant Ni, Cu and Y and overabundant La and Nd. This raised different questions, first of all whether or not were these stars representative of the main population of Sgr dSph. Their high metallicity was indeed difficult to reconcile with the photometric data. The hypothesis that they were to represent the extreme metal rich wing of the metallicity distribution of Sgr dSph was statistically unlikely. But if an important metal rich (and presumably young) population existed in the galaxy, it should have appeared more clearly in the CMD. And, finally, it was unclear whether or not the anomalous abundance pattern observed was to be considered typical of the dSph.

4.2 Observations and data reduction

This study was started with the aim of obtaining a significant sample of the chemical abundances in the stellar population of Sgr dSph. Ten stars were selected in the RGB of the sample of Marconi et al. (1998), from which already came the two stars analyzed by Bonifacio et al. (2000a), thus taking the total sample to 12 stars. The sample was selected to cover the entire width in color of the RGB (see fig. 4.3). All the targets were confirmed radial velocity members of Sgr dSph. The stars were observed in June-July 2001 with VLT-UVES in good seeing conditions. The standard dichroic 1 setting of UVES (DIC1) was employed, providing both blue and red arm spectra. Due to the extremely low signal to noise in the blue spectra, red arm spectra only have been employed in this analysis. The standard 580 nm setting was used, covering (red arm) the wavelength range between 480 and 680 nm, at a resolution of about 43000 with 1" slit and 2×2 on-chip binning. For each star, three or four one-hour exposure has been taken.

The spectra of the 10 new stars were provided by ESO already extracted by means of the UVES pipeline. For each star, the three or four spectra were doppler corrected to rest wavelength and coadded. A sample of the final spectra for all the twelve stars, centered in the Mg b triplet region, is provided in 4.1.

Table 4.1: Position, photometry, S/N ratios 580 nm and atmosphere parameters for the 12 Sgr dSph stars.

Star	$\alpha(2000)^a$		$\delta(2000)^a$		V	$(V - I)_0^b$		S/N	T_{eff}	$\log g$	ξ	
432	18	53	50.75	-30	27	27.3	17.55	0.965	28	4818	2.30	1.35
628	18	53	47.91	-30	26	14.5	18.00	0.928	37	4904	2.30	1.95
635	18	53	51.05	-30	26	48.3	18.01	0.954	19	4843	2.50	1.80
656	18	53	45.71	-30	25	57.3	18.04	0.882	24	5017	2.50	1.65
709	18	53	38.73	-30	29	28.5	18.09	0.917	41	4930	2.70	1.40
716	18	53	52.97	-30	27	12.8	18.10	0.902	36	4967	2.50	2.00
717	18	53	48.05	-30	29	38.1	18.10	0.872	20	5042	2.70	1.30
772 ^c	18	53	48.13	-30	32	0.8	18.15	0.947	32	4932	2.50	1.50
867	18	53	53.02	-30	27	29.2	18.30	0.933	20	4892	2.30	2.40
879 ^d	18	53	48.59	-30	30	48.7	18.33	0.965	29	4902	2.50	1.40
894	18	53	36.84	-30	29	54.1	18.34	0.940	34	4876	2.50	1.40
927	18	53	51.69	-30	26	50.7	18.39	0.937	43	4880	2.75	1.30

^a accurate to 0".3 (Ferraro & Monaco 2002, private communication)

^b The adopted reddening is $E(V - I) = 0.22$

^c this is star [BHM2000] 143 of Bonifacio et al. (2000a)

^d this is star [BHM2000] 139 of Bonifacio et al. (2000a)

Equivalent widths have been measured by means of IRAF task SPLLOT for lines of species Na I, Mg I, Al I, Si I, Ca I, Sc II, Ti I, V I, Cr I, Fe I, Fe II, Ni I, Zn I, Y II, Ba II, La II, Ce II, Nd II. The measure has been performed either by fitting a single gaussian or by deblending multiple gaussians on weakly blended lines. The standard deviation of multiple measures on the same line was verified to be compatible with the estimate given by the Cayrel formula (Cayrel, 1988).

4.3 Abundance analysis

Abundance analysis was performed in a traditional way. Effective temperatures for the stars were derived from the $(V-I)_0$ color (adopting a reddening of $E(V - I) = 0.22$) following the calibration of Alonso et al. (1999, 2001). Gravities were initially estimated at $\log g = 2.5$ from the location of the stars in the $(V - I)_0, M_v$ diagram and the isochrones of Straniero et al. (1997) of ages between 8 and 10GYr, which is an age range compatible with the analysis of Marconi et al. (1998). Atmosphere modeling, abundance deriva-

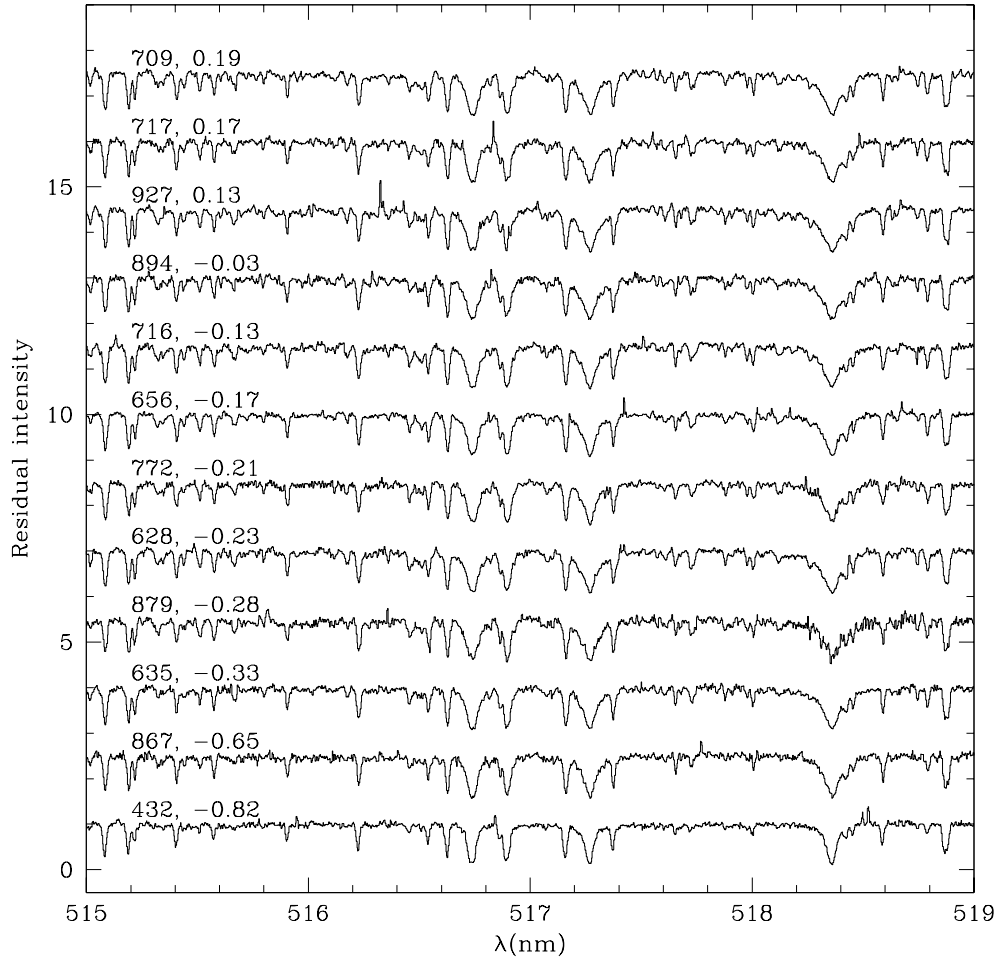


Figure 4.1: Sample from the Mg b triplet region for the 12 stars of Sgr dSph. Spectra are normalized to one on the continuum, but shifted vertically to make the figure readable. Each spectrum is shifted of 1.5 with respect to the one below it, such as the continuum of Sgr 432 is at residual intensity of 1, for Sgr 867 is at 2.5, for Sgr 635 is at 4 and so on. Spectra are ordered such that metallicity increases *ascending* in the plot, every one is labeled with the star number and the $[\text{Fe}/\text{H}]$ of the star.

tion and spectral synthesis have been performed by using our ported version of the ATLAS suite of codes (Kurucz, 1993, and this work, chapter 3). Monodimensional LTE models were computed by means of the ATLAS code. We employed solar-scaled, non-alpha-enhanced ODF of the set computed by Castelli & Kurucz (2004), convection has been treated without introducing overshooting (as recommended by Castelli et al., 1997). Abundances for the aforementioned species were derived from the measured EWs by means of WIDTH. In the course of the analysis, where necessary original estimated gravities have been modified to enforce equal abundances to be provided by Fe I and Fe II lines. Microturbulent velocity has been fixed by imposing no correlation between abundance and EWs for Fe I lines. Coordinates, photometry and derived atmospheric parameters for the 12 stars are summarized in table 4.1.

Available lines for species Mn I, Co I, Cu I and Eu II were known to be significantly affected by hyperfine splitting, so the abundance for these ions have been derived by computing grid of synthetic spectra (by using SYNTH) for the range surrounding each line, varying the abundance, and then interpolating the abundance providing the best fit with the observed line. Solar isotopic ratios have been used for the calculation of the lines.

For all the analyzed lines, measurements, results and sources of the atomic data are presented in table 4.6 through 4.9. The chosen linelist is essentially the same employed by Bonifacio et al. (2000a) and Bonifacio et al. (2004), but many atomic data has been upgraded. New Mg I $\log gf$ have been derived from Gratton et al. (2003), Ca I from Smith & Raggett (1981), La II from Lawler et al. (2001a), Nd II from Den Hartog et al. (2003) and Eu II HFS components from Lawler et al. (2001b).

Another improvement with respect to Bonifacio et al. (2000a, 2004) has been the adoption of the newer ODFs from Castelli & Kurucz (2004), which led to slight variations in gravity, microturbulence and metallicity for some stars. These changes did not exceed the stated uncertainties on the abundances, and the general picture was totally unchanged.

Adopted solar abundances, mean final abundances and related uncertainties are presented in tables 4.2 4.3. Ratios against iron and uncertainties are listed in tables 4.4 and 4.5. The adopted solar values are obtained from hydrostatic monodimensional solar models, and correspond essentially to the ones in Anders & Grevesse (1989), slightly updated (Grevesse, 2001, private communication). For Oxygen abundance, has been adopted the value derived from MARCS 1D models by Asplund et al. (2004a). Recently, As-

plund et al. (2004b) re-compiled solar abundances now obtained by means of 3D, hydrodynamical and (partly) NLTE models, finding important variations in the abundances of C, N, O (thus leading to an important variation of the overall solar metallicity Z), slighter (\sim -0.5 dex) variations in Fe and α elements. Some other element show significant change (e.g. Na, passing from 6.33 to 6.17, Al, from 6.47 to 6.37, Ti, from 5.02 to 4.90). We *did not* adopt this new solar abundance scale. As above stated, we employ LTE 1D hydrostatic models in our analysis, and the same is true for the totality of the abundances available in Disk, Halo, globular clusters or LG dwarf galaxies, against which our data are naturally compared. Systematic effects exist between 1D and 3D models (and statical against dynamical, and LTE against NLTE...), and all these effects are bound to be metallicity, gravity and temperature dependent. Besides that, no 3D hydrodynamical models of giant stars are available to date. Finally, adopted ODFs have been calculated with “old” solar abundances, and use the new solar values would thus be inconsistent. Is also worth saying how new Asplund et al. (2004b) abundances would not significantly change our results by any means: to make an example, due to similar changes in Iron and α elements abundances, $[\alpha/\text{Fe}]$ would not change more than \sim 0.01 dex, which is of course negligible.

4.4 Results: the signature of an exotic chemistry

The results obtained are definitively surprising considering what was expected from the photometric studies of Sgr dSph, but come to confirm that the two stars analyzed by Bonifacio et al. (2000a) were by no means exceptional. An overall picture of the chemistry of this population can be seen in fig. 4.2. By looking at the figure one has to keep in mind that such a plot is degenerate in $[\text{Fe}/\text{H}]$, and our analyzed stars span an order of magnitude in iron content.

This considered, the systematicity of all the abundance deviations with respect to the solar ratios is striking. This lead us to think that this abundance pattern should be in fact related to the peculiar chemical evolution of Sgr dSph, and thus to its star formation history, yields retention capability, and, potentially, initial mass function. The strong interaction (and possibly gas exchange) with the milky way is very likely to have played a key role also.

We will return on this later: what we want to stress here is that, whatever may be the evolutive history hiding behind the present time chemistry of the galaxy, Sgr dSph display a highly peculiar and well recognizable chemical signature, which has already proven valuable (see Cohen, 2004) to recognize stellar populations stripped from the dSph by the Milky Way.

We will now examine each group of elements in detail, trying to reconstruct a common and (possibly) coherent picture of Sgr dSph chemistry.

4.4.1 Iron: a young population

All the sample of stars is significantly metal rich, ranging from $[\text{Fe}/\text{H}] = -0.82$ (Sgr 432) to a marginally over-solar value of $[\text{Fe}/\text{H}] = 0.19$ (Sgr 709). The first interesting deduction that can be derived from this is that the stellar population we are sampling should be definitively very young. Assuming that C traces Fe, and being our measures indicating that O follows the other α elements, we can consider our sample as spanning the interval between $Z=0.004$ and $Z=0.02$. In fig. 4.3 we show the photometry of Field 1 of Marconi et al. (1998) where our stars were selected. The 12 program stars are indicated by larger filled dots. To this photometry we superimpose two isochrones covering this range of metallicity. Two things appear immediately evident:

- A very young age is required for the isochrone to match the position in the CMD of the observed stars. With any reasonable assumption on reddening, it's impossible reach ages beyond 2 GYr. with the assumed $E(V-I)$ and A_V the best age estimate is around 1 GYr.
- The upper ZAMS of these young age isochrones is exactly superimposed to the blue plume.

The most simple explanation of these findings is that Sgr dSph actually *hosts a metal rich, young population* (Bonifacio et al., 2004), of which the blue plume constitutes the upper ZAMS, with an age of the order of 1 GYr. Is worth noticing how, in fact, this age is coherent with the time of the last perigalacticon passage of the Sgr dSph. We will come back on this later on (see 4.7).

An histogram of the metallicity distribution of the 12 program stars is presented in fig. 4.4. The most reliable photometric estimates of the Sgr dSph metallicity (Cole, 2001; Monaco et al., 2002) point towards a typical

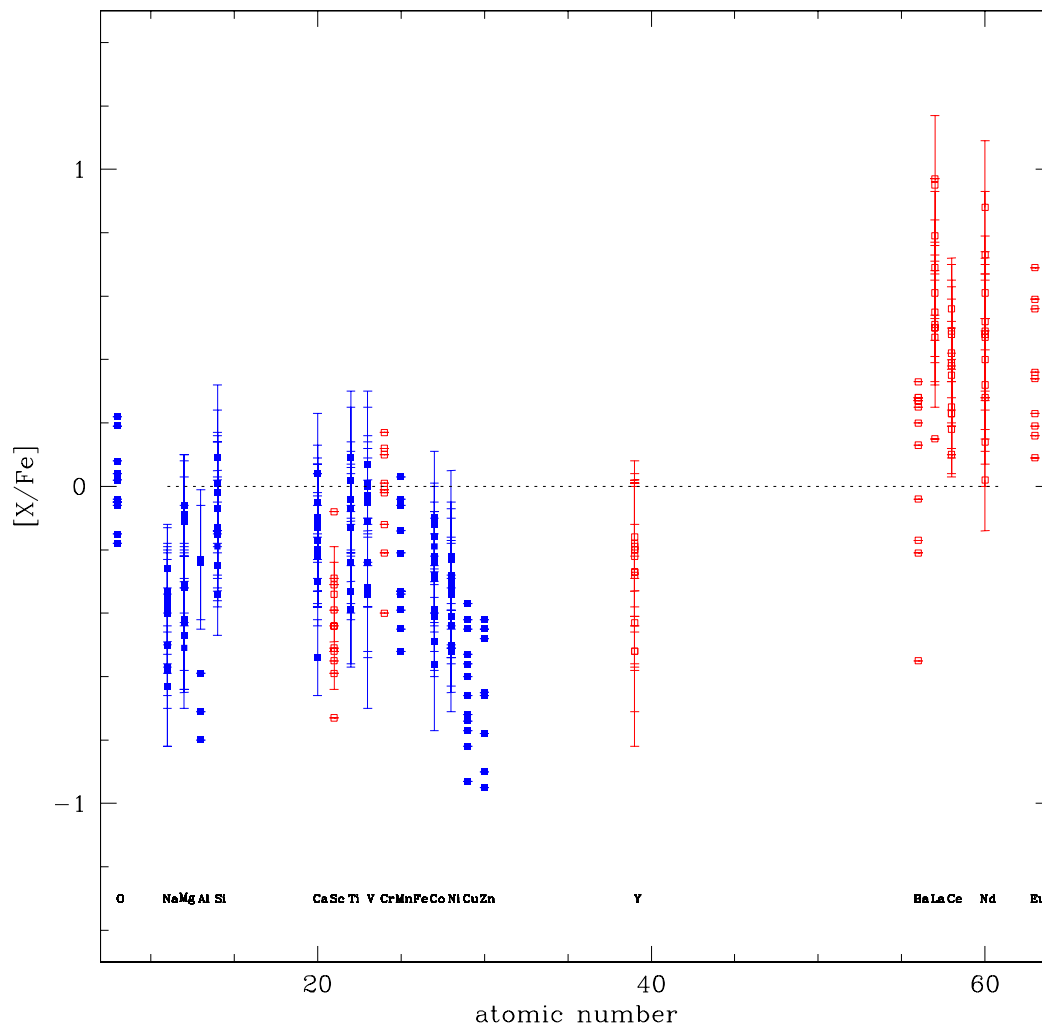


Figure 4.2: The overall plot of the chemical “signature” of the analyzed population in Sgr dSph. $[X/Fe]$ ratios are here plotted against atomic number. Blue symbols represent neutral elements for which $[X/FeI]$ is plotted, while red symbols represent ionized elements, for which $[X/FeII]$ is displayed.

Table 4.2: Abundances for the first 6 Sgr dSph stars.

Ion	solar ab.	Ab. 432	σ	Ab. 628	σ	Ab. 635	σ	Ab. 656	σ	Ab. 709	σ	Ab. 716	σ
O I	8.72	8.09	–	8.45	–	8.33	–	8.50	–	8.76	–	8.61	–
Na I	6.33	–	–	5.84	0.08	5.42	0.03	5.80	0.09	6.02	0.12	5.80	0.16
Mg I	7.58	6.67	0.02	7.24	0.15	7.14	0.17	7.10	0.07	7.26	0.16	7.14	0.07
Al I	6.47	–	–	–	–	–	–	–	–	–	–	5.75	–
Si I	7.55	6.74	0.11	7.30	0.11	7.09	0.11	7.31	0.07	7.40	0.08	7.27	0.13
Ca I	6.36	5.49	0.13	5.93	0.14	5.92	0.13	6.09	0.10	6.01	0.06	6.01	0.12
Sc II	3.17	2.00	–	2.32	–	2.42	–	2.55	–	2.77	–	2.51	–
Ti I	5.02	4.13	0.06	4.66	0.13	4.45	0.13	4.78	0.10	4.97	0.08	4.65	0.11
V I	4.00	–	–	3.72	0.16	3.43	0.08	3.80	0.07	3.85	0.17	3.88	0.01
Cr II	5.67	–	–	–	–	5.29	–	5.55	–	5.65	–	5.70	–
Mn I	5.39	4.24	–	5.19	–	4.67	–	5.08	–	5.24	–	5.20	–
Fe I	7.50	6.68	0.12	7.27	0.11	7.17	0.12	7.33	0.10	7.69	0.10	7.37	0.11
Fe II	7.50	6.64	0.13	7.38	0.14	7.14	0.19	7.39	0.13	7.69	0.21	7.37	0.11
Co I	4.92	3.82	0.14	4.57	0.06	4.30	0.07	4.59	0.05	4.55	0.18	4.60	0.02
Ni I	6.25	4.99	0.02	5.80	0.10	5.58	0.11	5.77	0.10	5.93	0.07	5.82	0.09
Cu I	4.21	2.46	–	3.21	–	3.22	–	3.44	–	3.68	–	3.34	–
Zn I	4.60	3.33	–	–	–	–	–	3.94	–	3.83	–	3.81	–
Y II	2.24	0.86	0.14	1.90	0.20	1.68	0.09	1.93	0.16	2.25	0.15	1.84	0.27
Ba II	2.13	1.22	–	2.29	–	1.56	–	2.28	–	2.59	–	1.82	–
La II	1.13	0.42	–	1.98	–	1.28	0.18	1.63	0.08	2.27	0.08	1.79	0.08
Ce II	1.58	0.82	–	1.84	0.02	1.61	0.07	1.65	0.07	2.19	0.10	2.01	0.12
Nd II	1.50	0.92	0.16	1.87	0.15	1.54	0.17	1.86	0.15	2.17	0.12	2.10	0.17
Eu II	0.51	0.34	–	–	–	0.74	–	–	–	1.04	–	0.54	–

Table 4.3: Abundances for the other 6 Sgr dSph stars.

Ion	solar ab.	Ab. 717	σ	Ab. 772	σ	Ab. 867	σ	Ab. 879	σ	Ab. 894	σ	Ab. 927	σ
O I	8.72	8.93	–	8.33	–	8.29	–	7.83	–	8.77	–	8.80	–
Na I	6.33	5.87	0.17	5.55	0.17	5.34	0.07	5.72	0.12	5.92	0.13	6.08	0.16
Mg I	7.58	7.44	0.03	6.94	0.09	6.87	0.08	6.98	0.20	7.13	0.17	7.24	0.16
Al I	6.47	5.84	–	6.03	0.12	–	–	5.95	0.08	–	–	5.89	–
Si I	7.55	7.53	0.11	7.27	0.09	6.99	0.18	7.20	0.26	7.53	0.04	7.43	0.07
Ca I	6.36	6.33	0.15	6.03	0.10	5.75	0.13	5.91	0.14	6.20	0.14	6.19	0.12
Sc II	3.17	3.22	–	2.50	0.20	2.11	–	2.50	0.05	2.63	–	2.92	–
Ti I	5.02	4.80	0.16	4.83	0.13	4.33	0.11	4.83	0.13	4.92	0.11	4.82	0.22
V I	4.00	3.85	0.18	3.79	0.16	–	–	3.79	0.16	3.86	0.23	3.79	0.35
Cr II	5.67	5.90	–	5.32	–	–	–	5.35	–	5.17	–	5.82	–
Mn I	5.39	5.11	–	4.85	–	–	–	5.07	–	5.15	–	5.00	–
Fe I	7.50	7.67	0.09	7.29	0.19	6.85	0.14	7.22	0.16	7.47	0.14	7.63	0.08
Fe II	7.50	7.64	0.16	7.27	0.04	6.99	0.13	7.17	0.14	7.40	0.13	7.54	0.15
Co I	4.92	4.60	0.03	4.30	0.04	4.17	0.15	4.42	0.15	4.65	0.08	4.66	0.10
Ni I	6.25	5.90	0.09	5.81	0.21	5.28	0.17	5.69	0.16	5.72	0.16	5.97	0.10
Cu I	4.21	3.56	–	3.47	–	3.11	–	3.37	–	3.81	–	3.92	–
Zn I	4.60	4.12	–	–	–	3.52	–	–	–	3.66	–	3.94	–
Y II	2.24	2.19	0.10	1.58	0.13	1.21	0.27	1.63	0.08	1.87	0.28	2.12	0.08
Ba II	2.13	2.54	–	2.03	–	1.07	–	2.05	–	2.36	–	2.36	–
La II	1.13	1.77	0.09	1.37	0.05	–	–	1.30	0.09	1.58	0.09	1.86	0.01
Ce II	1.58	1.95	0.11	1.58	0.13	1.32	0.03	1.73	0.06	1.83	0.07	2.11	0.14
Nd II	1.50	2.16	0.15	1.41	0.13	1.01	0.10	1.49	0.15	2.01	0.12	2.42	0.14
Eu II	0.51	0.74	–	0.64	–	–	–	0.74	–	0.64	–	0.74	–

Table 4.4: Ratios against Iron for the first 6 stars. $[X/FeI]$ is used for neutral ions, $[X/FeII]$ for the ionized ones. For Fe I and Fe II $[Fe/H]$ is displayed instead.

[p!] Ion	$[X/Fe]$ 432	σ	$[X/Fe]$ 628	σ	$[X/Fe]$ 635	σ	$[X/Fe]$ 656	σ	$[X/Fe]$ 709	σ	$[X/Fe]$ 716	σ
O I	0.18	–	-0.04	–	-0.06	–	-0.05	–	-0.15	–	0.02	–
Na I	–	–	-0.26	0.14	-0.58	0.12	-0.36	0.13	-0.50	0.16	-0.40	0.19
Mg I	-0.09	0.12	-0.11	0.19	-0.11	0.21	-0.31	0.12	-0.51	0.19	-0.31	0.13
Al I	–	–	–	–	–	–	–	–	–	–	-0.59	–
Si I	0.01	0.16	-0.02	0.16	-0.13	0.16	-0.07	0.12	-0.34	0.13	-0.15	0.17
Ca I	-0.05	0.18	-0.20	0.18	-0.11	0.18	-0.10	0.14	-0.54	0.12	-0.22	0.16
Sc II	-0.31	–	-0.73	–	-0.39	–	-0.51	–	-0.59	–	-0.52	–
Ti I	-0.07	0.13	-0.13	0.17	-0.24	0.18	-0.07	0.14	-0.24	0.13	-0.24	0.16
V I	–	–	-0.05	0.19	-0.24	0.14	-0.03	0.12	-0.34	0.20	0.01	0.11
Cr II	–	–	–	–	-0.02	–	-0.01	–	-0.21	–	0.17	–
Mn I	-0.33	–	0.03	–	-0.39	–	-0.14	–	-0.34	–	-0.06	–
Fe I	-0.82	0.12	-0.23	0.11	-0.33	0.12	-0.17	0.10	0.19	0.10	-0.13	0.11
Fe II	-0.86	0.13	-0.12	0.14	-0.36	0.19	-0.11	0.13	0.19	0.21	-0.13	0.11
Co I	-0.28	0.18	-0.12	0.13	-0.29	0.14	-0.16	0.11	-0.56	0.21	-0.19	0.11
Ni I	-0.44	0.12	-0.22	0.15	-0.34	0.16	-0.31	0.14	-0.51	0.12	-0.30	0.14
Cu I	-0.93	–	-0.77	–	-0.66	–	-0.60	–	-0.72	–	-0.74	–
Zn I	-0.45	–	–	–	–	–	-0.48	–	-0.95	–	-0.66	–
Y II	-0.52	0.19	-0.22	0.24	-0.20	0.21	-0.20	0.21	-0.18	0.26	-0.27	0.29
Ba II	-0.04	–	0.28	–	-0.21	–	0.27	–	0.28	–	-0.17	–
La II	0.15	–	0.97	–	0.51	0.26	0.61	0.15	0.95	0.22	0.79	0.14
Ce II	0.10	–	0.38	0.14	0.39	0.20	0.18	0.15	0.42	0.23	0.56	0.16
Nd II	0.28	0.21	0.49	0.21	0.40	0.25	0.47	0.20	0.48	0.24	0.73	0.20
Eu II	0.69	–	–	–	0.59	–	–	–	0.34	–	0.16	–

Table 4.5: Ratios against Iron for the other 6 stars. $[X/FeI]$ is used for neutral ions, $[X/FeII]$ for the ionized ones. For Fe I and Fe II $[Fe/H]$ is displayed instead.

Ion	$[X/Fe]$ 717	σ	$[X/Fe]$ 772	σ	$[X/Fe]$ 867	σ	$[X/Fe]$ 879	σ	$[X/Fe]$ 894	σ	$[X/Fe]$ 927	σ
O I	0.04	–	-0.18	–	0.22	–	-0.61	–	0.08	–	-0.05	–
Na I	-0.63	0.19	-0.57	0.25	-0.34	0.16	-0.33	0.20	-0.38	0.19	-0.38	0.18
Mg I	-0.31	0.09	-0.43	0.21	-0.06	0.16	-0.32	0.26	-0.42	0.22	-0.47	0.18
Al I	-0.80	–	-0.23	0.22	–	–	-0.24	0.18	–	–	-0.71	–
Si I	-0.19	0.14	-0.07	0.21	0.09	0.23	-0.07	0.31	0.01	0.15	-0.25	0.11
Ca I	-0.20	0.17	-0.12	0.21	0.04	0.19	-0.17	0.21	-0.13	0.20	-0.30	0.14
Sc II	-0.08	–	-0.44	0.20	-0.55	–	-0.34	0.15	-0.44	–	-0.29	–
Ti I	-0.39	0.18	0.02	0.23	-0.04	0.18	0.09	0.21	-0.07	0.18	-0.33	0.23
V I	-0.32	0.20	–	0.25	–	–	0.07	0.23	-0.11	0.27	-0.34	0.36
Cr II	0.10	–	-0.12	–	–	–	0.01	–	-0.40	–	0.12	–
Mn I	-0.45	–	-0.33	–	–	–	-0.04	–	-0.21	–	-0.52	–
Fe I	0.17	0.09	-0.21	0.19	-0.65	0.14	-0.28	0.16	-0.03	0.14	0.13	0.08
Fe II	0.14	0.16	-0.23	0.04	-0.51	0.13	-0.33	0.141	-0.10	0.13	0.04	0.15
Co I	-0.49	0.09	-0.41	0.19	-0.10	0.21	-0.22	0.22	-0.24	0.16	-0.39	0.13
Ni I	-0.52	0.13	-0.23	0.28	-0.32	0.22	-0.28	0.23	-0.50	0.21	-0.41	0.13
Cu I	-0.82	–	-0.53	–	-0.45	–	-0.56	–	-0.37	–	-0.42	–
Zn I	-0.65	–	–	–	-0.42	–	–	–	-0.90	–	-0.78	–
Y II	-0.19	0.19	-0.43	0.14	-0.52	0.30	-0.28	0.16	-0.27	0.31	-0.16	0.17
Ba II	0.27	–	0.13	–	-0.55	–	0.25	–	0.33	–	0.20	–
La II	0.50	0.18	0.47	0.06	–	–	0.50	0.17	0.55	0.16	0.69	0.15
Ce II	0.23	0.19	0.23	0.14	0.25	0.13	0.48	0.15	0.35	0.15	0.49	0.21
Nd II	0.52	0.22	0.14	0.14	0.02	0.16	0.32	0.21	0.61	0.18	0.88	0.21
Eu II	0.09	–	0.36	–	–	–	0.56	–	0.23	–	0.19	–

value of $[\text{Fe}/\text{H}]=-0.5$, so our subpopulation should constitute the metal rich tail of Sgr dSph. This arises the problem of how this metal rich tail may actually be *dominant* in our sample, and, conversely, of why does a metal poor population not show up in the sample. The problem is exacerbated by the apparent low density of the BP population, that may not seem rich enough to dominate along the RGB. That a metal poor population *should* exist is not debatable, given the fact that the metallicities of the globulars associated to Sgr actually go down at least to $[\text{Fe}/\text{H}]=-1.5$ (in M54, see Brown et al., 1999). McWilliam et al. (2003); McWilliam & Smecker-Hane (2004) also found three significantly metal poor stars ($[\text{Fe}/\text{H}]=-1.59$) by studying a different field of Sgr dSph with respect to ours, and sampling a brighter, redder part of the RGB. Given the small size of the sample, statistic could be invoked to explain the absence of metal poor stars from our sample, but, in fact, this is not necessary. As can be readily seen from fig. sgr:youngpop, the stars we observed should be intermediate mass objects, and we may have caught them in the so called “helium loop” phase of their post-ZAMS evolution (although some of them may be still ascending the RGB). Such phase is the only long-lived one in the post-ZAMS evolution of such objects, and preliminary population syntheses confirm (Girardi 2004 private communication) that, actually, evolved stars from such a young population tend to concentrate in that CMD area.

Conversely, is relatively easy to explain how could initial photometric estimates of Sgr dSph metallicity have been skewed towards such low iron content. Metallicity estimates based on the comparison against Galactic GC RGB fiducial lines (see e.g. Marconi et al., 1998), in fact, relied on the assumption that the “main” population of Sgr dSph should have an age comparable with the one of the clusters used to produce the fiducial lines: the considerably younger age of Sgr dSph skewed such measures towards lower metallicity.

4.4.2 α elements

Another striking characteristic of Sgr dSph appears to be its systematic low content of α elements. In the top-left panel of fig. 4.6 we plot the $[\alpha/\text{Fe}]$ trend with $[\text{Fe}/\text{H}]$, where $[\alpha/\text{Fe}]$ is defined as the weighted mean of $[\text{Mg}/\text{Fe}]$, $[\text{Si}/\text{Fe}]$ and $[\text{Ca}/\text{Fe}]$. The trends for the three elements are plotted in the other panels. We did not consider $[\text{O}/\text{Fe}]$ and $[\text{Ti}/\text{Fe}]$ in the mean: O measures are highly uncertain (they are based on a single weak line which is

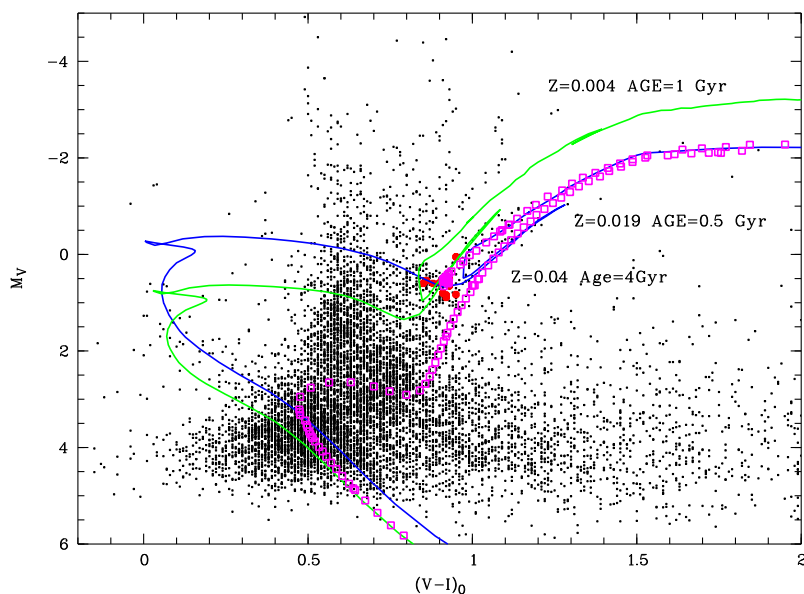


Figure 4.3: CMD of the Marconi et al. (1998) photometry of Field 1, with superimposed the program stars (filled dots) and three isochrones from the Padova series (Girardi et al., 2002) for the metallicities found in the sampled population. Adopted reddening $E(V-I)=0.22$, $A_V=0.55$, and distance modulus $(m-M)=16.95$ from Marconi et al. (1998).

at the detection limit in most cases with our S/N). Conversely, Ti is easily measured in such stars, but is generally considered as a sort of “transition” element between α elements and Fe-peak elements. Their trend with $[\text{Fe}/\text{H}]$ is presented in fig. 4.7. O appears to essentially follow the general α elements trend, while Ti displays a somewhat higher ratio with Fe with respect to the mean α elements value, but is nevertheless coherent with the general picture.

In fig 4.5 we plot the same quantities already presented in 1.1, but now employing the updated values for Sgr dSph iron and α elements abundances. As already noticed in 1, the $[\alpha/\text{Fe}]$ trend with $[\text{Fe}/\text{H}]$ in dwarf galaxies appears to be similar to the MW one, but set off by some -0.2 dex, at least at high metallicities. As said in 1.3.1, this is currently interpreted as being due to the combined effect of a slow/bursting star formation and of the loss of SN yields due to the onset of a galactic wind. Sgr dSph behaves similarly to

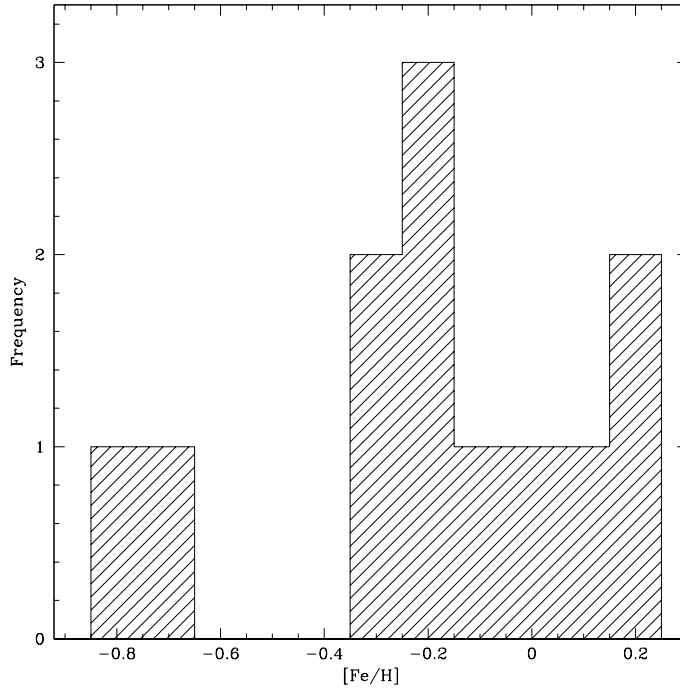


Figure 4.4: Distribution of metallicity for the 12 UVES stars in Sgr dSph.

other dSphs here, but appear to be outstanding for its very high metallicity (and consequent very low α elements content) which puts it at the Fe-rich extreme of the sequence of local group dwarf spheroidals.

α elements abundances also led Lanfranchi & Matteucci (2004) to infer a significant difference in the star formation (SF) and wind efficiency for Sgr dSph compared to other LG dwarf spheroidals. The authors had previously calculated (Lanfranchi & Matteucci, 2003) that, due to the low SF efficiency of dSphs (typically of the order of $0.02 - 0.5 \text{ GYr}^{-1}$), after the beginning of SN Ia explosions a sharp decrease should occur in $[\text{O}/\text{Fe}]$ and $[\text{Mg}/\text{Fe}]$ (which are almost pure SN II products) with respect to $[\text{Si}/\text{Fe}]$ or $[\text{Ca}/\text{Fe}]$, which are partly produced also by SN Ia. The $[\text{Mg}/\text{Ca}]$ ratio should reach at least -0.5 dex at solar metallicity. Nevertheless, Sgr is the *only* dSph for which solar metallicity stars have actually been found and analyzed, and appears to have galactic $[\text{Mg}/\text{Ca}]$ up to slightly over-solar metallicity (see fig. 4.9).

The only way to reproduce Sgr dSph metallicity and α elements content was to a much higher star formation efficiency (between 1 and 5 Gyr^{-1}) to produce a sufficient quantity of SN II to account for the Mg content, and a high enough metallicity. They had also to infer a relatively mild wind efficiency. Although the strong interaction between the MW and Sgr dSph fits well with an anomalously fast star formation (see 4.7), a weak wind may seem somewhat at odd with the prescription of a high SN explosion rate. Nevertheless, it has to be borne in mind that Lanfranchi & Matteucci (2003, 2004) models do not try to reproduce the aforementioned interaction with the MW, which is a specificity of Sgr.

Finally, Sgr dSph extends to high metallicities the similarities encountered between dSphs and DLAs $[\alpha/\text{Fe}]$ ratios. Nevertheless, Sgr dSph abundances also come to cast some doubt on the significance of this comparison, see 4.4.4

4.4.3 Light odd elements

Light odd elements Na I, Al I and Sc II have been measured in our sample stars. All show important underabundances with respect to iron (see fig. 4.10), although a caveat is in order for Sc, since is measured from a single line.

Na and Al underabundances of this entity (down to $[\text{Na}/\text{Fe}] \sim -0.3$) are unusual in the MW disk at such metallicity (Edvardsson et al., 1993; Fulbright, 2000; Prochaska & Wolfe, 2002). As also noted by McWilliam & Smecker-Hane (2004) this is not surprising in such metal rich population, since Na and Al production processes are, like the ones leading to α elements formation, mostly related to high-mass, short lived stars (see 1.2.1).

4.4.4 Iron peak elements

Iron peak elements also show a diverse and somewhat puzzling pattern of abundances in Sgr dSph. We measured abundances for V, Cr, Mn, Co, Ni, Cu, and Zn. All these elements show some degree of underabundance with respect to iron: for V this is significant only for the two most metal rich stars (which go down to $[\text{V}/\text{Fe}] \sim -0.2$), for Ni, Cu and Zn is strong and systematic. $[\text{X}/\text{Fe}]$ vs. $[\text{Fe}/\text{H}]$ are presented for V, Cr, Mn, and Co in fig. 4.11, while Ni, Cu and Zn are presented in 4.12

The most interesting results are the ones for Mn, Ni, Cu and Zn. The Mn abundance in Sgr dSph was first derived and interpreted by McWilliam

et al. (2003). Mn deficiencies with respect to iron were known in the MW at low metallicities since long time (Wallerstein, 1962). Gratton (1989) noticed that significant underabundance existed at low metallicity, but that $[\text{Mn}/\text{Fe}]$ started to climb above $[\text{Fe}/\text{H}]=-1$. He interpreted the fact as due to the onset of SN Ia explosions, thus inferring that SN Ia were a significant source of Mn. Nevertheless, Sgr dSph significant Mn depletion at high metallicity appear to be in contrast with this interpretation: α elements Na, Al and Sc underabundances are a clear sign of SN Ia over-efficiency (or SN II inefficiency), which should lead to an *overabundance* of Mn.

Nickel also shows a strong underabundance, roughly constant with $[\text{Fe}/\text{H}]$ at values of $[\text{Ni}/\text{Fe}]\sim-0.4$ on all the metallicity range. Again, in the galactic disk Ni is very consistently on solar values along a large metallicity range (Edvardsson et al., 1993; Gratton et al., 2003). A possible explanation of Ni underabundance is provided by Timmes et al. (2003), who suggest that Ni yield from SN Ia should be *metallicity dependent*.

Although represented by a single line, Cu shows a strong and consistent depletion, roughly constant with metallicity. Cu I 510.5 nm line has been synthesized by taking into account HF splitting, and the fit is generally robust due to the strength of the line. Some examples are presented in fig. 4.8. Cu is known to be heavily underabundant in low metallicity MW stars (Mishenina et al., 2002; Simmerer et al., 2003), but $[\text{Cu}/\text{Fe}]$ like the ones observed in Sgr dSph are not observed above $[\text{Fe}/\text{H}]=-1.5$. Like for Ni and Zn, Cu production channel are not clearly defined. At low metallicity they should (rather obviously) be produced by SN II (see e.g. Timmes et al., 1995), but their strong increase with metallicity is a clear hint of important SN Ia production at higher metallicity (Mishenina et al., 2002).

Finally, probably the most interesting of the abundance anomalies involving Fe-peak elements is the one of Zinc. Zn is consistently found on solar values on a broad range of metallicities in the MW (Mishenina et al., 2002; Bihain et al., 2004; Nissen et al., 2004), but is heavily underabundant in Sgr dSph. Zn abundance is solely based on the Zn I 481.0 nm line, a rather strong transition, although situated in a crowded part of the spectrum, and is available on 8 stars only. It is worth noting that this result is supported by Cohen (2004) who finds analogous Zn underabundance in Palomar 12, a globular cluster formerly associated with Sgr (see also 4.4.6). Taken at face value, it suggests that $[\text{Zn}/\text{Fe}]$ never rises above -0.4, with more than a hint of a *decreasing* trend with metallicity. As for copper, production channels for Zn are poorly known, so that it is difficult to deduct much from this result,

nevertheless, the main reason of interest in the Zn abundance is related to the Zn role in DLAs chemical analysis. DLAs $[\text{Zn}/\text{Fe}]$ show heavy enhancements (see e.g. Prochaska & Wolfe, 2002), which has been interpreted as due to incorporation of Fe (and some other Fe-peak elements as Cr and Ni) into dust grains, while Zn remains essentially undepleted. Vladilo (2002) developed an effective correction accounting for dust depletion, thus recovering $[\text{Zn}/\text{Fe}] \sim 0$ in DLAs; at the same time, Zn is routinely used as a proxy for Fe in DLAs (Centuri3n et al., 2003).

Dwarf galaxies are among the preferred models for explaining the nature of DLA absorption systems, an interpretation supported mainly by chemical considerations (Lanfranchi & Friaça, 2003), but also fitting conveniently in the hierarchical buildup model for the formation of giant galaxies. As already shown in fig. 4.5 and in Bonifacio et al. (2004), LG dwarf spheroidals show $[\alpha/\text{Fe}]$ trends with metallicity which are strongly resembling the ones seen in DLAs. Nevertheless, the very low Zn abundance in the Sgr dSph does not seem compatible with such an interpretation. Obviously, a plot of $[\alpha/\text{Zn}]$ is strongly enhanced in Sgr dSph: when actually looking at the same ratios, Sgr dSph does not look like a DLA.

Zn measurements in other dwarf galaxies are not widespread, but Shetrone et al. (2003) finds Zn depletion in one star in Fornax, one in Leo, two in Sculptor and four in Carina I Dwarf spheroidals. These underabundances are of smaller entity (typically of the order of $0.2 \sim 0.3$ dex), and occurring at much lower metallicity (typically $[\text{Fe}/\text{H}] \sim -1.5$) should the aforementioned trend in $[\text{Zn}/\text{Fe}]$ vs. $[\text{Fe}/\text{H}]$ be real, we would consistently expect higher $[\text{Zn}/\text{Fe}]$ at low metallicities. Sadly, no data are currently available to fill the gap among our Sgr data and Shetrone et al. (2003) abundances, nor to extend the Sgr sequence to lower metallicities: Brown et al. (1999) analysis of M 54 did not include Zn measurements.

All considered, Fe-peak elements may well provide clues to the star formation history of Sgr dSph (McWilliam et al., 2003; McWilliam & Smecker-Hane, 2004), although, due to the poor understanding of their production channels, their interpretation may prove to be tricky (see 4.7). We instead think that, for the time being, their main reason of interest may better lay in the highly peculiar values of these abundances, when compared with the values encountered in the MW. For this reason they may be considered among the prominent traits of the ‘‘Sgr signature’’ to be looked for in any MW population suspected to have been accreted from Sgr dSph.

4.4.5 Heavy neutron capture elements

We obtained abundances for heavy n-capture elements Y, Ba, La, Ce, Nd and Eu (all one time ionized). For all of them, EW measurements has been used, with the exception of Europium, for which spectral synthesis has been performed on the 664.5 nm line. Trends in $[X/FeII]$ against $[FeII/H]$ are presented in fig. 4.13 and 4.14

Yttrium show a general underabundance with respect to Fe II in all the stars, with hints of an *increasing* trend with Fe content. The trend is largely due to the two more metal poor stars, but is supported by Cohen (2004) who finds $[YII/FeII]=-0.48$ at $[Fe/H]=-0.78$ in Pal 12. Y is a produced essentially via r-process at lower metallicities but a s-process contribution arises at higher metallicity (see 1.2.4). Thus, an increase in Y abundance with metallicity is naively coherent with the general picture of a system with slow star formation over-polluted by the products of long lived stars (SN Ia and, in this case, AGB stars).

Largely s-process element Barium shows a somewhat mixed picture, where 8 stars out of 12 show enhanced $[BaII/FeII]$ while 4 stars, mostly but not exclusively metal poor show strong depletion. Since Ba is represented by a single, albeit strong, transition, it is possible that in these stars the Ba 649.6 nm line is somewhat altered. Cohen (2004) finds *enhanced* barium at $[Fe/H]=-0.78$ in Pal 12, and all the McWilliam & Smecker-Hane (2004) Sgr stars have enhanced Ba as well.

Lanthanum, Cerium and Neodymium, also significantly produced by s-process, show various degrees of enhancement with respect to solar values, most notably La and Nd, reaching up to 1 dex in enhancement, with sharp *increasing* trends with metallicity.

Finally, Eu, an almost entirely r-process element, consistently shows a *decrease* with metallicity, consistent with the aforementioned trends towards an increasing prevalence of the products of SN IIa and AGB nucleosynthesis at high metallicities.

4.4.6 Palomar 12, the lost son

Palomar 12 is a sparse Globular Cluster first photometrically studied by Gratton & Ortolani (1988) and Stetson et al. (1989). These photometric analyses suggested that Pal 12 should be significantly (25-30%) younger than the bulk of Halo GC. First CaII triplet metallicities were derived by Armandroff & Da

Costa (1991), deriving a surprisingly high metallicity ($[\text{Fe}/\text{H}]=-0.61$) given the large galactocentric distance of the cluster. Brown et al. (1997), from high resolution spectra, derived a significantly lower metallicity of $[\text{Fe}/\text{H}]\sim-1.0$. The high metallicity was consistent with a young age, which Rosenberg et al. (1999) set at about 70% of the bulk of the Galactic GC (or about 8.4 GYr). Buonanno et al. (1995) noted the fact that Pal 12 was similar to Terzan 7 (still not identified as a *de facto* Sgr dSph member and Ruprecht 106 in showing significant discrepancies between photometric and CaII triplet metallicities.

After the discovery of Sgr dSph and the first reliable estimates and simulations of its orbit, Martínez-Delgado et al. (2002) detected the Sgr dSph stream in the surroundings of Pal 12, and noticed that the cluster’s orbit was suggesting for it an origin inside the Sgr dSph system. Also Bellazzini et al. (2003), looking for phase space correlations among the orbit of Sgr dSph and the ones of MW globulars considered Pal 12 as the most likely candidate to have been stripped by the MW from the Sgr dSph system.

Cohen (2004) analyzed the detailed abundances of 21 elements on 4 Pal 12 giants by using Keck HIRES spectra, compared them with the (still limited) available abundances for Sgr dSph, and deduced that, based on the chemical similarities between the two objects, Pal 12 should actually have formed inside the Sgr dSph. The correctness of this deduction is made even more evident by the comparison of Cohen (2004) measurements with our sample.

In figures 4.15 through 4.18 we compare the mean ratios with iron from Cohen (2004) with our Sgr sample. The results do not need a lot of commentary: Palomar 12 appears to fit perfectly into the abundance pattern defined by our Sgr dSph main body stars, even in the abundances that are more strikingly at odds with the ones characteristic of MW globulars. In fact, Pal 12 stars appear to be indistinguishable from relatively metal poor Sgr dSph main body stars, bearing the same “signature”.

In our opinion, this constitute a conclusive evidence that actually Pal 12 *formed inside the Sgr dSph system* and was consequently stripped by the MW tidal force. Besides that, it constitutes a clear case of the importance that the “Sgr signature” may have in unambiguously recognize Sgr dSph debris inside the MW.

4.4.7 Comparison with other studies

Bonifacio et al. (2000a) sample of 2 stars was reanalyzed inside this work

by using slightly improved models. Bonifacio et al. (2004) presented part of these same results (namely Fe and α elements). The only competing set of data is the one by Smecker-Hane and McWilliam (still largely unpublished, Smecker-Hane & McWilliam, 2002; McWilliam et al., 2003; McWilliam & Smecker-Hane, 2004).

Their sample is constituted by 14 giants, observed by Keck-HIRES. At the moment, no coordinates or atmospheric parameters for the observed stars are available, but Smecker-Hane & McWilliam (2002) reports that they were observed in the neighborhood of M54, while our stars are picked from a field about 20 arcmin. east of M54. Moreover, from a CMD identifying the program stars it can be deduced that their targets are cooler and brighter than ours, and spread on a larger area of the Sgr dSph CMD. No details are provided about the lines and the atomic data used, while it is reported that the authors used MARCS grids of models.

Given the significant differences in the target selection and analysis methodology, it is surely comforting the fact that our results are strictly matching the ones by Smecker-Hane and McWilliam. The first very interesting result is that, although sampling a wider area of the high Sgr dSph RGB, the bulk of their sample appears as metal rich as our is. In 4.4.1 we tentatively explained the high concentration of the metal rich population in the Sgr dSph clump as due to a long-lived post-ZAMS phase of our stars: Nevertheless, this explanation does not seem to be applicable to Smecker-Hane & McWilliam (2002) stars. Nevertheless, the authors claim their stars to be considerably young too.

It is of great interest that Smecker-Hane & McWilliam (2002) also sampled three “truly” metal poor stars ($[\text{Fe}/\text{H}] \sim -1.5$) which are totally absent in our sample. The field they selected their target from lies very near to M54, and the similarities between these stars and the M54 giants studied by Brown et al. (1999), lead to consider them as likely M54 debris. This by the way creates another interesting problem: since recent studies (Monaco et al., 2005) show that M54 lies precisely in correspondence with the central density cusp of Sgr dSph its nature as the *de facto* nucleus of the galaxy appear now difficult to dispute. The evolutive relationship between M54 and the Sgr dSph body is not completely straightforward, and a sort of hiatus seem to exist between the two populations.

Aside the three “M54-like” stars, the abundance pattern displayed by Smecker-Hane & McWilliam (2002); McWilliam et al. (2003); McWilliam & Smecker-Hane (2004) stars is in almost perfect agreement with ours. The

main differences are:

- Their $[\alpha/\text{Fe}]$ appears to be systematically higher than our by about $0.1\sim 0.15$ dex;
- Their Yttrium content seem to be higher than our. The comparison is made on the base of the graphs in Shetrone et al. (2003), given that no abundances are explicitly tabulated in Smecker-Hane & McWilliam (2002).

Both these differences may be due to different linelists or atomic datasets, or be somewhat related to the position of the two sampled fields: Sgr dSph is likely to harbor some kind of population and abundance gradient.

4.5 Widening the view: an ongoing FLAMES study

The previous analysis should have made clear that Sgr dSph is a complex and extended system that the available spectroscopic studies have sampled in a largely insufficient way. Many questions remain unanswered that require a wide field spectroscopic analysis based on a statistically significant sample of stars. VLT-FLAMES is one of the best suited instruments to produce such a study. During the ITAL-FLAMES granted time of observation (GTO) we observed two Sgr dSph fields, one centered on M54 and the other corresponding again to Marconi et al. (1998) “field 1”. The targets were selected on the Monaco et al. (2002) photometry, chosen in such a way as to sample the whole width of the Sgr dSph RGB (see fig. 4.19). Two GIRAFFE high resolution settings were used, HR09 (centered at 525.8nm) and HR14 (centered at 651.5 nm, this grating has now been decommissioned).

Radial velocities were measured by cross-correlation against a synthetic spectrum template. T_{eff} was derived from Alonso et al. (1999) calibration against $(V-I)_0$ color, and gravity fixed to 2.0 for all the stars. Metallicities and α elements abundance were determined by means of the automatic analysis code described in Bonifacio & Caffau (2003). Given the very low S/N ratio, it was not possible to fit also the microturbulent velocity, which was fixed to 1.6 km kms^{-1} , the mean value found by Fulbright (2000), for stars of similar type and luminosity.

For the time being, we considered as Sgr dSph members all stars with radial velocities exceeding 100kms^{-1} . This is a rather crude assumption, and some (scarce) contamination should still be present in the sample. A finer selection is in progress. The histogram of the derived metallicities is presented in fig. 4.20. Three main results have been obtained:

- The main population of Sgr dSph appear to lie at $[\text{Fe}/\text{H}]\sim-0.5$;
- The (relatively) metal rich population *is still present inside the tidal radius of M54*. This was already observed photometrically by Monaco et al. (2005);
- Sgr dSph appear to possess a truly metal poor tail, with stars down to $[\text{Fe}/\text{H}]=-3.0$. Of course, given the small numerical consistence of this population, MW contamination is a crucial issue here. Nevertheless, is unlikely that the entire metal poor tail may be due to MW contaminants.

The use of FLAMES opens totally new possibilities to the study of the populations of this complex object. In particular, the identification of a metal poor population is very important since it can allow to trace back the chemical evolution of Sgr dSph presently sampled only from the most recent and metal rich populations. Also, to determine the percentage of Sgr dSph stars belonging to the metal poor tail would be of paramount importance to calibrate the evolutive models for the galaxy.

This is still a work in progress: Period 73 observations were plagued by bad weather, and we are looking forward to obtain new observations in period 75. Meanwhile, we are using the very high multiplexity of VLT-VIMOS to carry out a first survey on 11 fields across Sgr dSph main body, and also in the associated (or suspected so) globulars. Stars identified as likely Sgr dSph members in the pre-imaging photometry are going to be observed via low resolution spectroscopy to determine whether they are Sgr dSph members, and to derive Ca II triplet metallicities. This will allow us to produce both decontaminated CMDs for a different areas across all the extension of the galaxy, and to produce a large catalog of target for high resolution spectroscopy.

4.6 Looking for gas in Sgr dSph

To explain the presence of such a very young stellar population in Sgr dSph, we need to assume the survival of a significant supply of gas up to very recent times. Koribalski et al. (1994) and later Burton & Lockman (1999) detected no H I emission from Sgr dSph, determining an upper limit of $7000 M_{\odot}$ for the total neutral hydrogen mass over 18 square degrees, a mass largely insufficient to form the observed young population. We thus decided to use our sample stars as background sources to study the interstellar (IS) absorption features towards Sgr dSph (Monai et al., 2005). Two problems have to be kept in mind: looking for gas in Sgr dSph, we were interested in *high* velocity components, compatible with the radial velocities typical of Sgr dSph stars, but, although necessary, a suitable radial velocity is not sufficient to ensure a membership. Also, our stars are not ideal targets for such a study, for which hot objects are better choices. Cool metal rich giants show a large number of absorption features in their spectra, making the search and analysis of interstellar components problematic: in fact, the only reliable feature resulted to be the Na I D doublet. Nevertheless, the best targets in the Sgr dSph CMD, the Blue Plume stars, are about two magnitudes fainter than the giants we analyzed, making them very difficult targets for high resolution spectroscopy. The study of the Na I D doublet is in general complicated by the fact that the telluric Na I D emission is very strong and difficult to subtract, but this is not a problem in our case, since Sgr dSph features should have typical radial velocities above 100 km s^{-1} . A more serious problem is given by the stellar absorption feature, but, since detailed abundances are known for these objects, we could largely account for them by producing synthetic spectra in the region of interest.

By comparing with the syntheses, we rejected any possible IS line identification where severe blending was present with a stellar feature, claiming a detection of an IS feature only where it was detected beyond 3σ level over the synthetic spectrum, on both components. By means of the code `fitvoigtminuit` (E. Caffau, 2004, private communication) we fitted the central wavelength of the detected IS components. The line $\log gf$ was held fixed since is well known, and column density and b factor *were assumed*. This was done due to the low S/N ratio of the spectrum and the heavy contamination by the stellar Na I D features, making the simultaneous fit of interstellar and stellar spectrum an unreliable procedure. Given the exploratory nature of this study, in fact, we were mostly interested in the *detection* of high velocity

components.

We detected “local” absorption components (with radial velocities equal or less than 50 km s^{-1} thus incompatible with a Sgr dSph origin) in the spectra of all the 12 main body and the three $\hat{7}$ stars with DIC 1 spectra (# 1272, # 1282 and # 1515, see chapter 5). Around the two Sgr dSph main body stars # 635 and # 656 (see fig. 4.21) clear high velocity components were detected. Two components at 150 and 165 km s^{-1} were detected in the spectrum of star # 635, while a single 160 km s^{-1} component was observed for star # 656. Stars # 635 and # 656 (see fig. 4.22) are separated by about 95 arc seconds, while star # 927, the nearest one to star # 635, and star # 628, situated between the # 635 and # 656, do not show high velocity absorptions. Many explanations may exist for this:

1. The gas distribution may be very clumpy. At the distance of Sgr dSph, the separation between # 927 and # 635 is about 2.9 PC: in this hypothesis this should be the typical cloud scale.
2. More simply, one may notice that both # 628 and # 927 have radial velocities of about 145 km s^{-1} , thus most likely hiding a 150-160 km s^{-1} IS component below the stellar Na lines.
3. Star # 927 is also about a factor of two more metal rich than # 635, thus showing stronger absorption features, and making a IS component detection even more difficult.

If we consider the radial velocity for the observed IS components as typical, we see that point 2) should also hold for star # 432 (the second nearest to # 635), and # 867, and possibly for # 717 and # 772. At the same time, a clumpy gas distribution as inferred in point 1) may well explain the negative detection of Burton & Lockman (1999), since the 21' wide radio beam integrates on an area considerably larger than our entire field, all contained within 9 arc minutes. If we assume the detected gas to be inside Sgr dSph, it may actually be the residual of the last star formation epoch that produced the metal rich population we detected. It is reasonable to infer that it may be related to the gas discovered by Putman et al. (2004) along the Sgr stream. Anyway, it is clear that any conclusion we may draw from this observation should be regarded as preliminary: a larger sample, on hotter sources would be necessary.

4.7 On the star formation in Sgr dSph

Summing up the state of our knowledge of Sgr dSph chemistry and evolution, we apparently end up with more questions than answers. This should not be surprising: as already said, Sgr dSph is a large object, result of a complex evolution involving a close interaction with the MW, and the small samples of abundances we can count on cannot be possibly sufficient to draw a clear picture of it.

To try to summarize the available evidences:

- It is no longer questioned that Sgr dSph *hosts a metal rich, young population*, with a roughly solar iron content. This population is consistent enough to dominate both the available high resolution spectroscopic samples of giants. It also does not seem to be a local feature, since the two samples come from fields which are about 20 arc minutes apart. The population is detected also in the aforementioned FLAMES sample. Nevertheless, we completely lack informations on its large-scale distribution, since Sgr dSph is much larger than this;
- This metal rich population presents a highly characteristic abundance pattern, characterized by depletion of the elements produced by short lived, massive stars (type II SN), and a strong enhancement in the ones contributed by processes linked to low mass, long lived stars (type Ia SN, low mass AGB). This is rather easily interpreted as being sign of a prolonged, but slow (compared to the one of the MW) star formation;
- Less easy to interpret are the abundance anomalies of many Fe-peak elements due to poor theoretical constraints on their formation processes. Nevertheless some of these abundances are highly anomalous (Cu, Zn...) and surely hide some important clue on the Sgr dSph history;
- The dominant population of the Sgr dSph main body appears to have $[Fe/H] \sim -0.5$, but M54, which apparently resides in the nucleus of the galaxy, has a much lower metallicity;
- At the same time, Sgr dSph appear to possess a metal poor tail the metallicity (and, in a naive view, the age) of which is comparable with the one of the oldest stars in the MW;

- In the theoretical models, the only way to explain the Sgr dSph abundances seem to be to infer that it experienced a stronger star formation with respect to other LG dSphs (like, e.g., Sculptor or Carina). This is, naively seen, fitting with the strong harassment Sgr dSph is experiencing by the MW tidal field;
- Estimates of the Sgr dSph stream size and orbit simulations suggest that Sgr dSph should have been much larger in the past. This is also supported by the large number of GC associated to Sgr dSph. Given the evidence that Pal 12 had indeed formed inside Sgr dSph the number of GC related to Sgr dSph rises at least to 5, an impressive value considered that all the LG dSph do not possess any GC, with the exception of Fornax that has one (van den Bergh, 1998);
- The Sgr dSph globulars also appear to be of great interest. Not only, as above stated, they are in unusually great number for such a small object. They also span an order of magnitude in metallicity from the $[\text{Fe}/\text{H}] = -2.0$ of Terzan 8 (Montegriffo et al., 1998), and the $[\text{Fe}/\text{H}] = -0.5$ of Terzan 7 (see 5). Arp 2 ($[\text{Fe}/\text{H}] = -1.7$, Buonanno et al., 1994), M 54 ($[\text{Fe}/\text{H}] = -1.5$, Brown et al., 1999) and Pal 12 ($[\text{Fe}/\text{H}] = -0.8$, Cohen, 2004) are distributed in between, suggesting that Sgr dSph was able to form GC for a long period.
- Sgr dSph shows significant similarities with the Large Magellanic Cloud (LMC), namely an essentially identical RR Lyr population, and some abundance patterns (Bonifacio et al., 2000a, 2004, and references therein). This also supports the inference of a higher Sgr dSph mass in the past. It has to be noted nevertheless that the LMC does not host any globular cluster, nor is any MW globular believed to have been stripped from LMC.
- At odds with the discovery of a young population and a prolonged star formation history, attempts to detect a corresponding gas supply in Sgr dSph have been largely unfruitful. Burton & Lockman (1999) failed to detect any HI associated to Sgr dSph main body, which implies that the overall density of the gas should be very low, or perhaps, that its distribution must be very spotty (see Monai et al., 2005, and section 4.6 above). It is reasonable to assume that it may have been stripped by the interaction with the MW, and Putman et al. (2004) actually detected

HI likely associated with the Sgr stream. In any case, presently the main body of Sgr dSph does not host a significant amount of cold gas, which would be required to support further star formation;

The scenario these evidences suggest has some clear points: most likely, Sgr dSph was originally a large, gas rich nucleated dwarf galaxy, perhaps somewhat similar to the LMC. Given its small mass, analogously to other dwarf galaxies Sgr formed star at a lower rate compared to the MW, thus experiencing a stronger contamination from SN Ia and AGB nucleosynthesis products.

At a given point, Sgr dSph started interacting more and more heavily with the MW, losing a great fraction of its star and gas mass in the MW disk and halo. It is worth remembering that it is basically not possible to reconstruct the early orbital evolution of Sgr dSph without an accurate MW model taking into account a live Halo (as opposed to the statical one used in the available models) and the feedback of the interaction with Sgr dSph on the MW structure: as a consequence, the more the present Sgr dSph orbit is integrated back in time, the more uncertain the model becomes. In fact, the present models are unable to explain the Sgr dSph survival to more than a few MW Disk crossings.

Nevertheless, it seems sensible to assume that the young Sgr dSph stellar population is indeed the result of the starbursts triggered by the very last disk crossings. The derived age of the youngest and most metal rich stars in both our sample and the one of Smecker-Hane & McWilliam (2002) is, quite interestingly, coinciding with the last Disk-crossing shock. This of course raises the problem of where may Sgr dSph have found the necessary gas. One may assume that we are just looking at Sgr dSph in the special time following the very last starburst: the last gas may just have been stripped from the galaxy's main body. This is of course possible, but has the limit to constitute an *ad hoc* scenario.

Such a picture would become more acceptable if it were suggested by future analyses and simulations that Sgr dSph orbit decayed quickly in time from a relatively undisturbed one (i.e., one where Sgr may essentially keep its gas and enrich it) to the present one, losing almost entirely its gas supply in a very small number of close interaction episodes. In this case, MW interaction may have, in the early stages of the interaction, stimulated the star formation in Sgr dSph. Then, when the orbit decayed, it would have rapidly stripped away the Sgr dSph gas supply (which may also have been overheated by

ongoing starburst episodes), quickly stopping the star formation in the dwarf galaxy. In this case, we would not be observing a very special moment in a long interaction history, but simply a relatively fast tidal accretion episode, caught in becoming.

We may also speculate that, perhaps, Sgr dSph is (was) massive enough to “steal” some MW disk gas during the crossings, thus “refueling” to sustain its star formation. This scenario has two main limits: first, without a detailed hydrodynamical simulation of a Sgr dSph disk crossing episode, it is not even clear whether is physically sound or not. Second, it has the fundamental fault that stars produced by such a “refueling” would not display the characteristic Sgr dSph chemical signature, or would display a “diluted” version of it, in the case of a partial MW gas contribution. But we have seen that younger, more metal rich stars conversely display the most marked departures from the MW chemistry.

An interesting question posed by these findings is whether the “ancient” Sgr dSph was actually an object similar to the contemporary forms of the others LG dwarf spheroidals. Its likely past large mass, its strongly concentrated nucleus (M54) and large GC population suggest that it may have been significantly different. The way the interaction with the MW reshaped Sgr dSph is, for the time being, difficult to assess.

The above presented scenarios are, of course, highly speculative: we still have an incomplete knowledge of the *present* Sgr dSph orbit, and the modeling of the past one presents, as said, greater difficulties. At the same time, a detailed model of a disk crossing interaction is still lacking.

Another difficult task is to assess quantitatively the yields of the stellar evolution in such a system. As previously cited, Lanfranchi & Matteucci (2003, 2004) derived that Sgr dSph α elements yields are reproduced by their models, when a higher than usual star formation efficiency is coupled with a low galactic wind efficiency. Nevertheless, it would be more intuitive to assume that higher star formation rate induced a *more intense* galactic wind. At the same time, the interaction with the MW is likely to have favored rather than inhibited the yields dispersion. It remains clear that modeling the interaction with the MW was outside the scope of the models of Lanfranchi & Matteucci (2003, 2004), and that, in the case of Sgr dSph star formation and wind efficiency act mainly as parameters. Nevertheless it is indisputable that a model seeking to describe the Sgr dSph enrichment quantitatively should include in the future some kind of modeling of the effect of the MW - Sgr dSph interaction.

As already said, the Fe-peak elements abundances present the most difficult interpretative challenges. Smecker-Hane & McWilliam (2002); McWilliam et al. (2003); McWilliam & Smecker-Hane (2004) noticed that for many of these elements, although the actual production processes are still unclear, the yields are likely metallicity dependent. Consequently, they explain the depletion of some Fe-peak elements as due to an enrichment by a generation of very metal poor stars. Consequently, they infer that Sgr dSph may have experienced a period of very strong star formation in the distant past, after which the star formation almost stopped. The few stars born recently (as a consequence of the interaction with the MW) should have formed out of a gas that had been enriched by the products of metal poor type Ia SN, thus much more enriched in iron than, e.g., Manganese or Copper. This interpretation is nevertheless difficult to reconcile with the few clues we possess on the Sgr dSph star formation history. The most metal poor population found in Sgr dSph has $[\text{Fe}/\text{H}]=-3.0$, the most metal rich is slightly over-solar, the five globulars associated to Sgr dSph are scattered between $[\text{Fe}/\text{H}]=-1.8$ and $[\text{Fe}/\text{H}]=-0.5$. All this seems to point towards a continuous story of chemical enrichment rather than an interrupted one. Moreover, the FLAMES results indicate that the main Sgr dSph population has essentially the same metallicity as Terzan 7 (actually, this is an information that McWilliam and Smecker Hane did not possess). A lot of chemical processing is needed to increase the iron content of a large population of the order of magnitude existing between M 54 and the Sgr dSph main population.

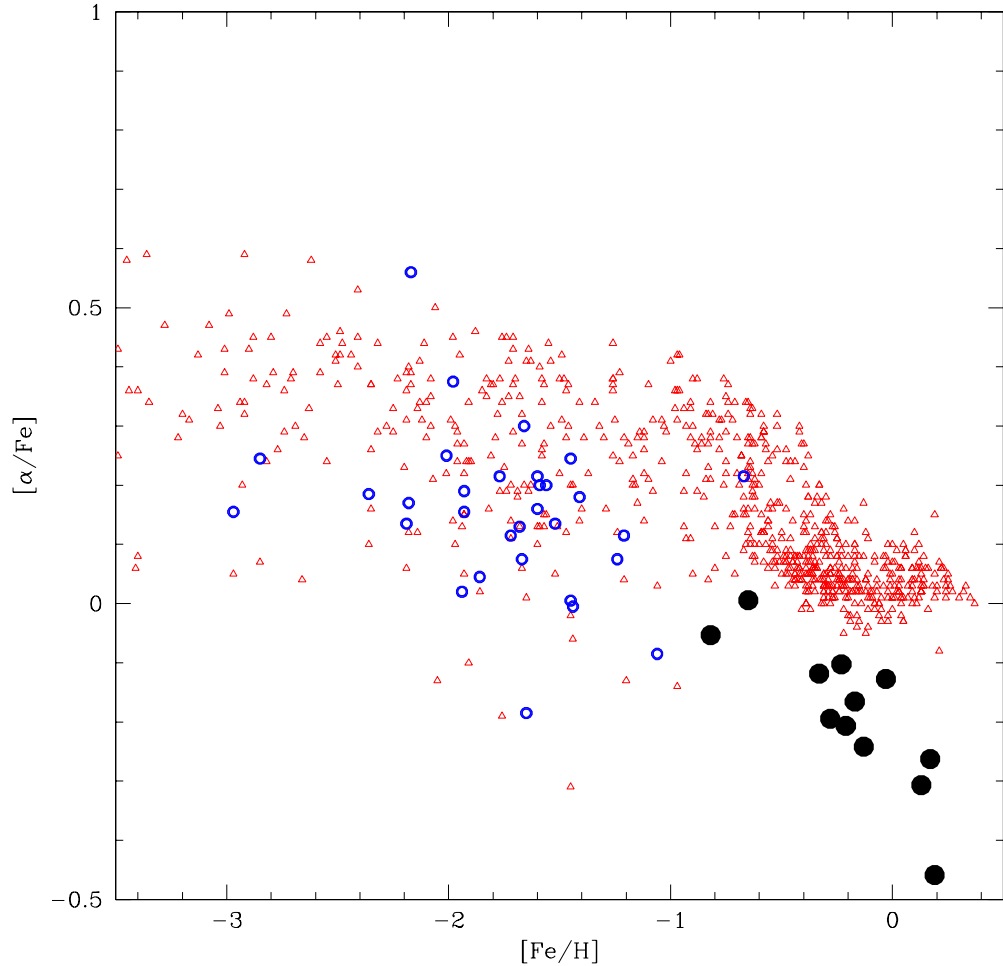


Figure 4.5: Updated version of fig. 1.1. Here the new Sgr dSph α elements values here presented (black filled dots). Blue open circles refer again to stars in the Local Group dwarf spheroidals, Draco, Ursa Minor, Sextans from Shetrone, Côté, & Sargent (2001), Carina, Sculptor, Fornax and Leo from Shetrone, Venn, Tolstoy, Primas, Hill, & Kaufer (2003). Red open triangles represent the MW sample of Venn et al. (2004), comprising the Gratton et al. (2003) sample already presented in fig. 1.1.

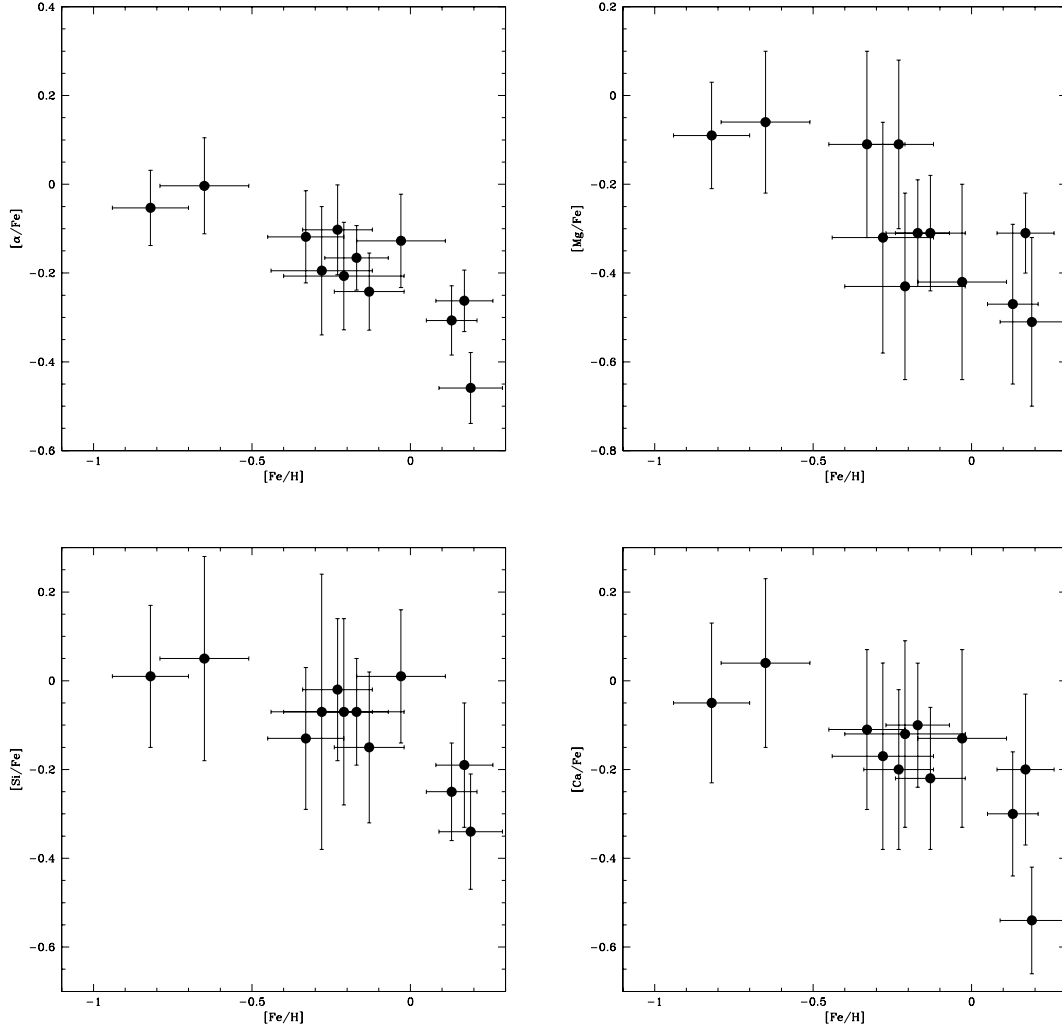


Figure 4.6: In top-left panel, $[\alpha/Fe]$ for the 12 Sgr dSph stars, plotted against $[Fe/H]$. Here we define $[\alpha/Fe]$ as the weighted mean of $[Mg/Fe]$, $[Si/Fe]$ and $[Ca/Fe]$, which are plotted, again versus $[Fe/H]$ in the remaining three panels. $[\alpha/Fe]$ appear to have a decreasing trend with increasing metallicity, and remains sub-solar or solar down to almost $[Fe/H]=-0.8$.

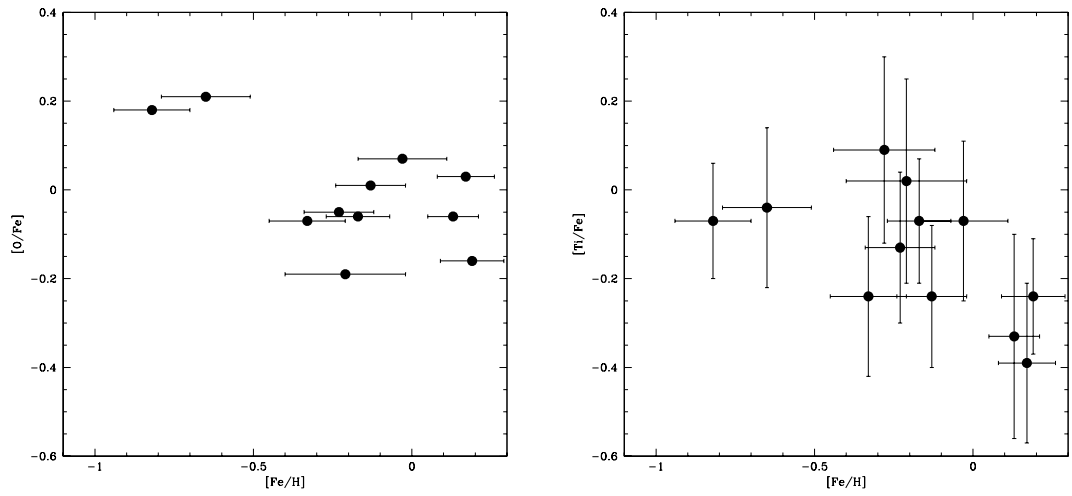


Figure 4.7: $[O/Fe]$ and $[Ti/Fe]$ ratios for the 12 stars of Sgr dSph plotted against $[Fe/H]$.

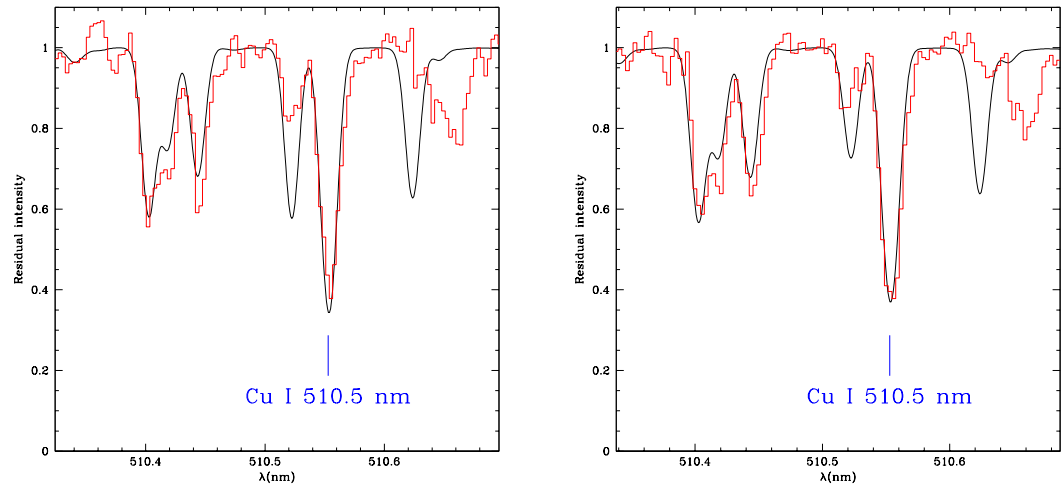


Figure 4.8: Spectral syntheses for the Cu I 510.5 nm line in stars 628 and 635.

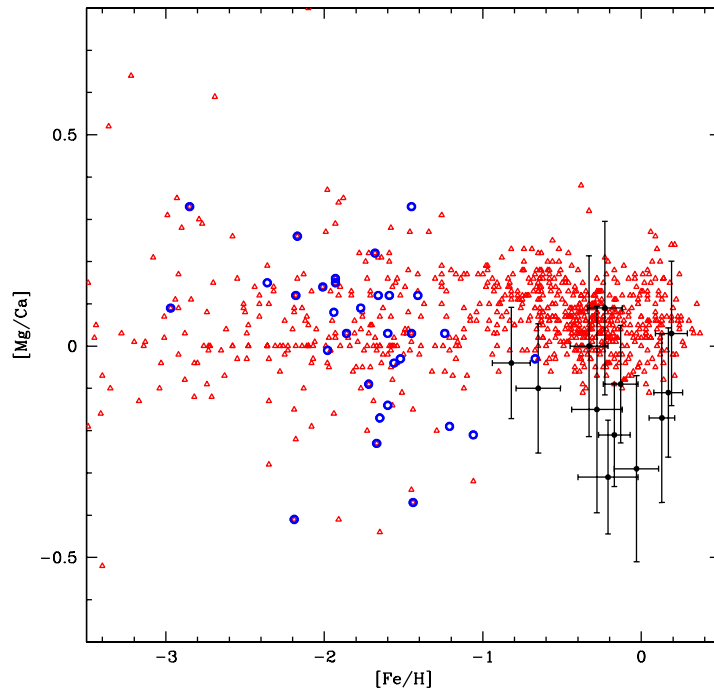


Figure 4.9: $[\text{Mg}/\text{Ca}]$ ratio for Sgr dSph, after the new measurements (black filled dots with error bars), for stars in the other LG dwarf spheroidals (blue open circles, same sample used in fig. 1.1 and 4.5, and for the sample of MW stars from Venn et al. (2004) (red open triangles).

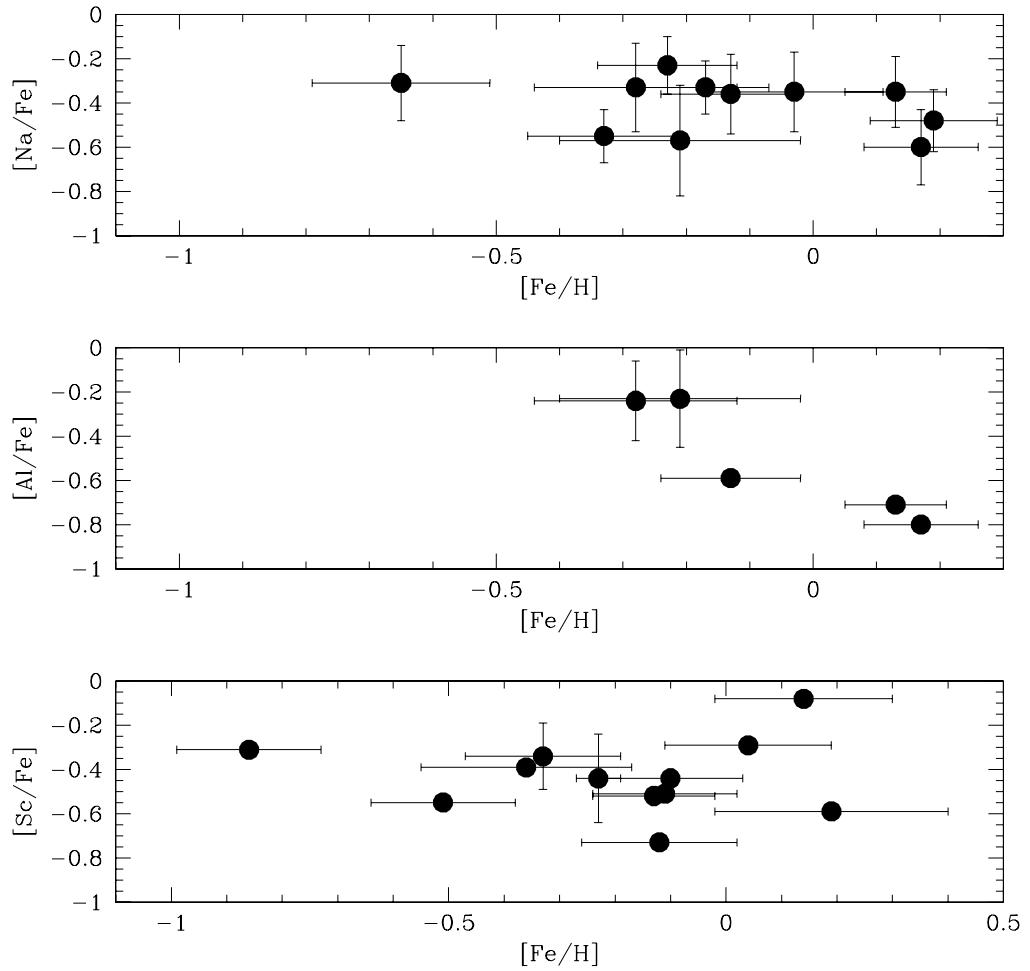


Figure 4.10: Na, Al and Sc ratios with Iron, against $[Fe/H]$, in the Sgr dSph sample. For Na and Al ratios against Fe I are plotted against $[FeI/H]$ while for Sc we plot $[ScII/FeII]$ vs. $[FeII/H]$. Notice the $[Fe/H]$ range is larger for the Sc plot.

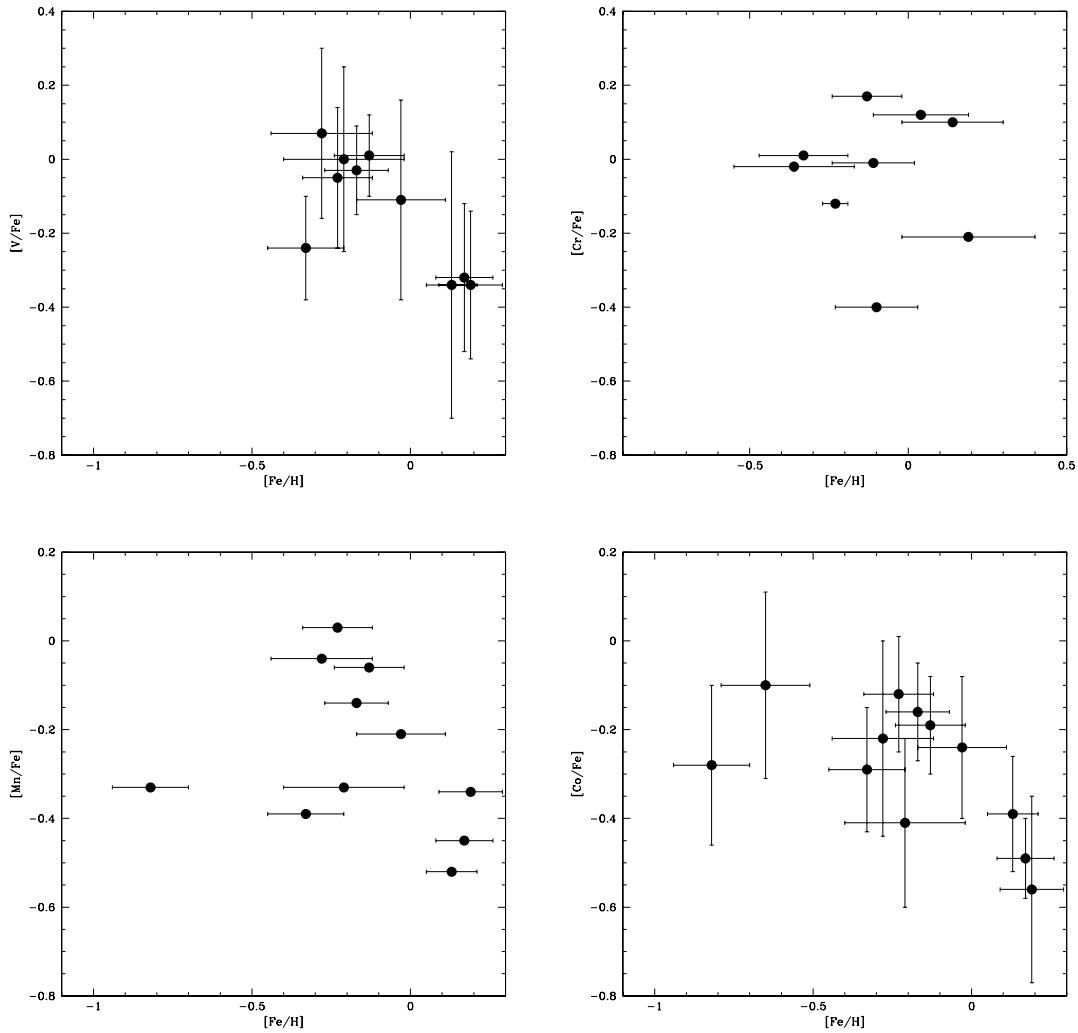


Figure 4.11: $[X/Fe]$ vs. $[Fe/H]$ for V, Cr, Mn and Co in the sampled stars. V, Mn and Co are neutral, Cr is ionized, so Fe II is used instead of Fe I and the $[Fe/H]$ range is different.

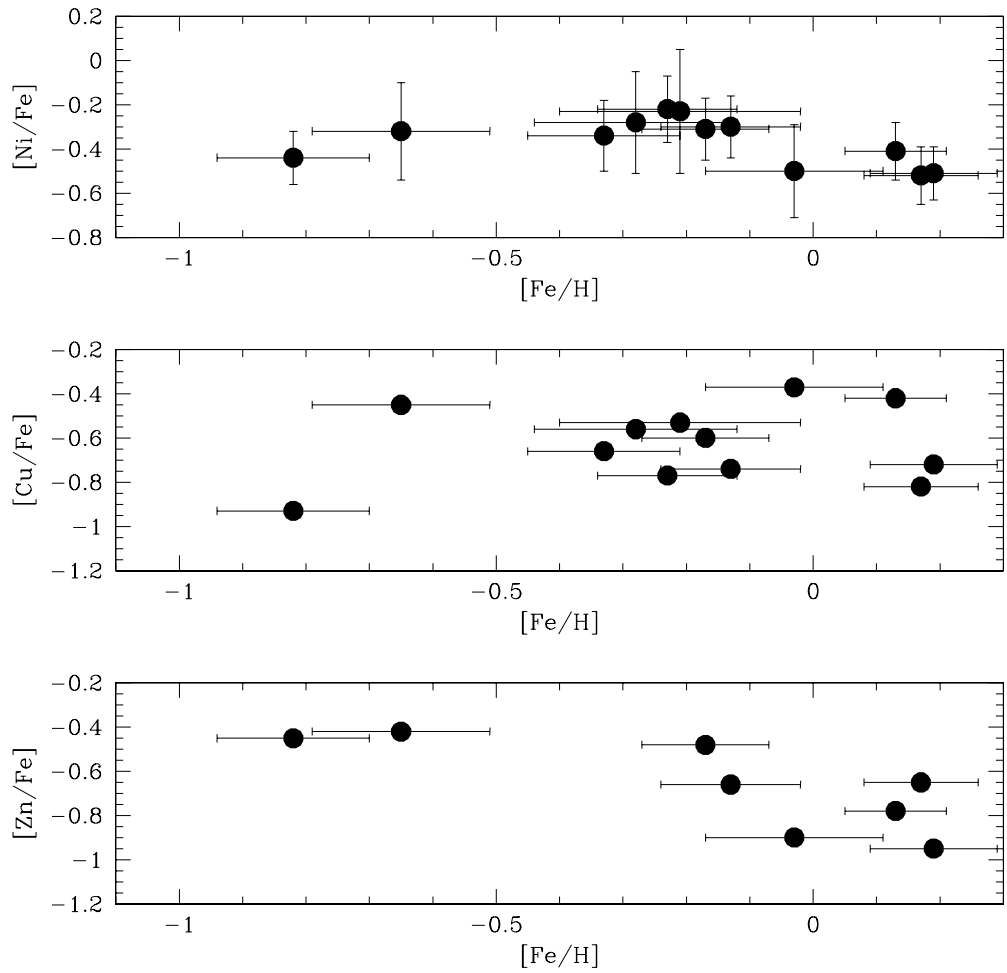


Figure 4.12: Same than in fig. 4.11, for Ni, Cu and Zn.

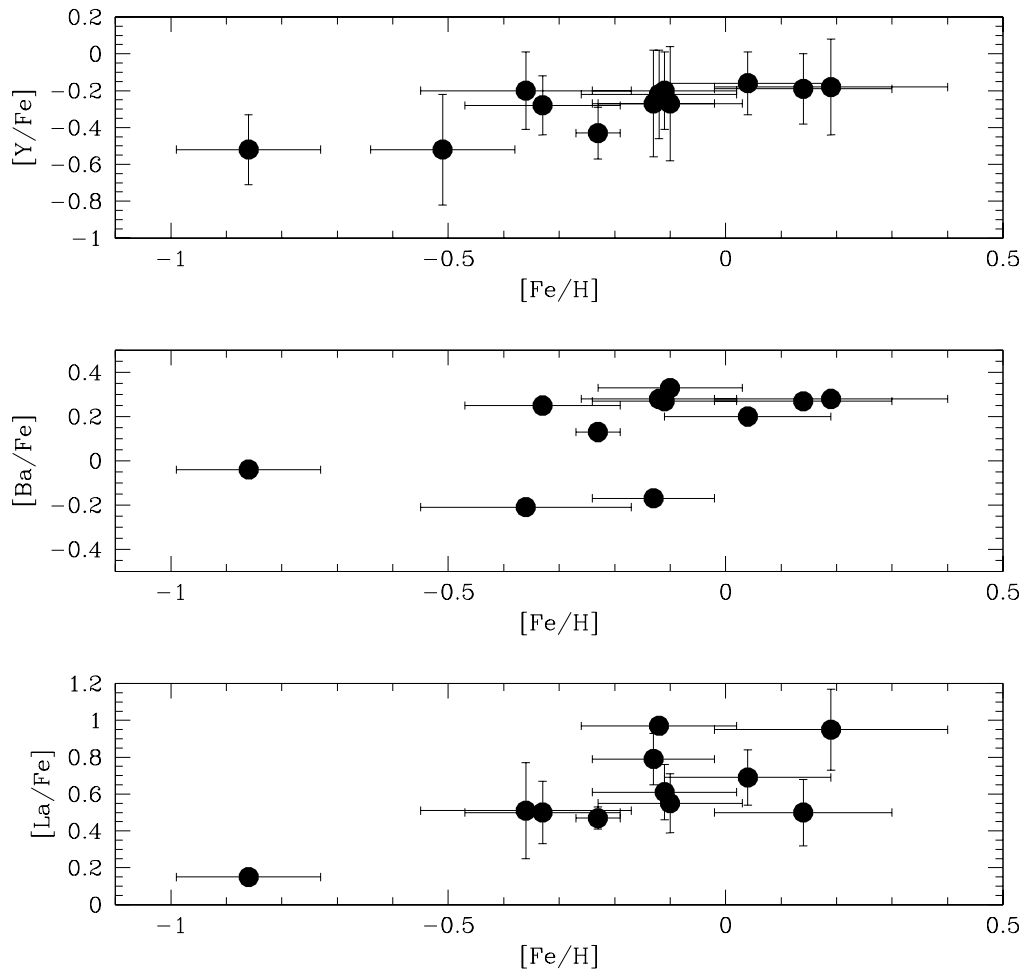


Figure 4.13: $[X/FeII]$ vs. $[FeII/H]$ for species Y II, Ba II and La II in Sgr dSph.

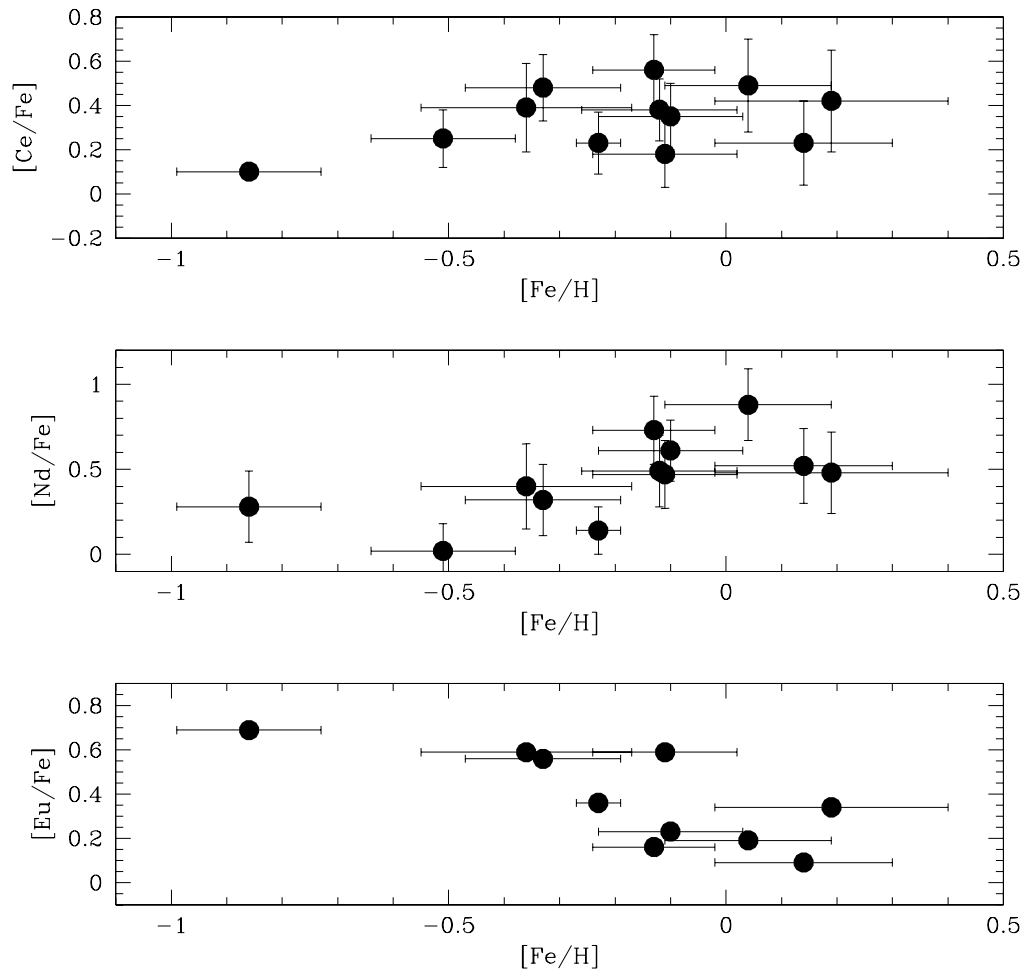


Figure 4.14: $[X/\text{FeII}]$ vs. $[\text{FeII}/\text{H}]$ for species Ce II, Nd II and Eu II in Sgr dSph.

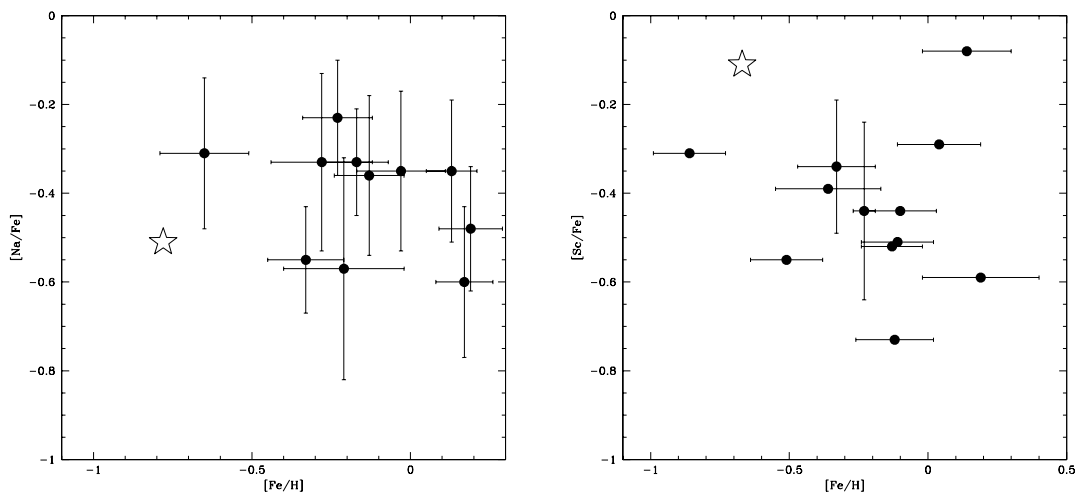


Figure 4.15: Comparison of Sgr dSph and Pal 12 on the $[X/Fe]$ vs. $[Fe/H]$ for light odd elements Na and Sc. Big star symbol is the mean value for four Pal12 giants from Cohen (2004).

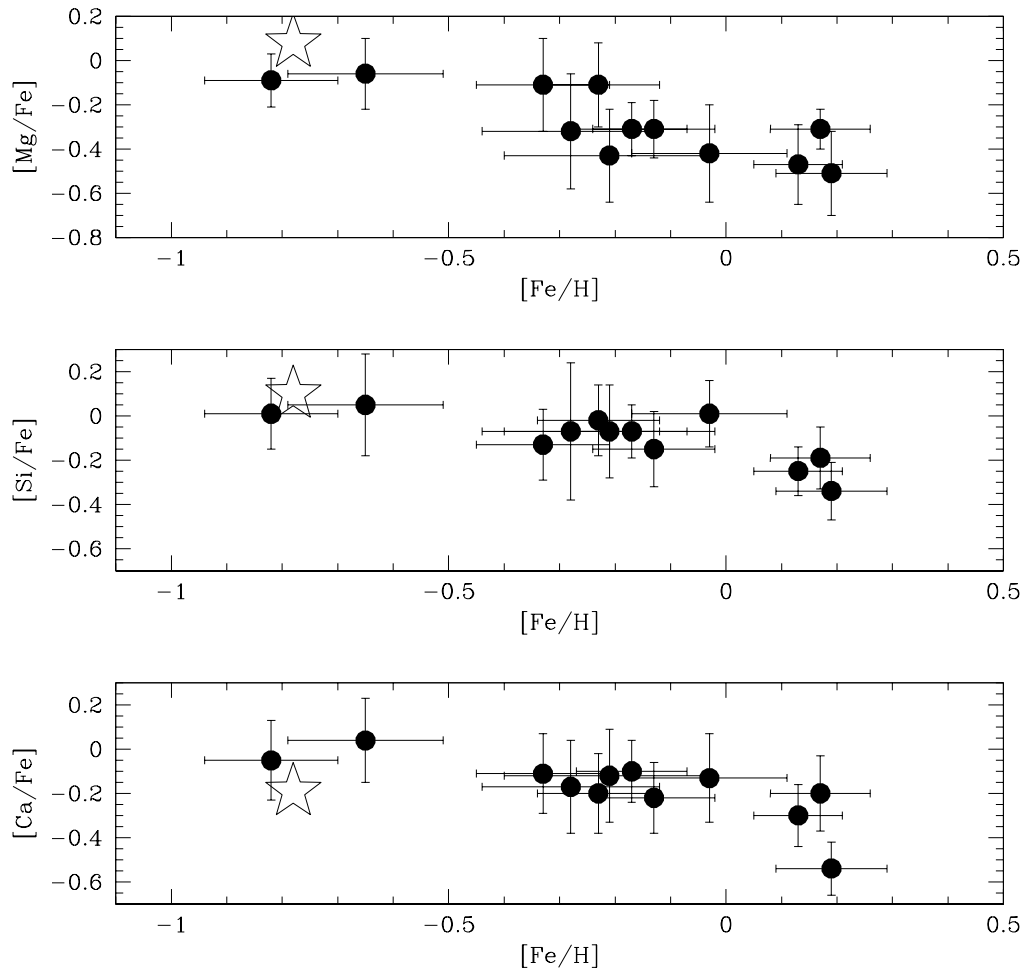


Figure 4.16: Like in fig. 4.15, but now for α elements Mg, Si and Ca.

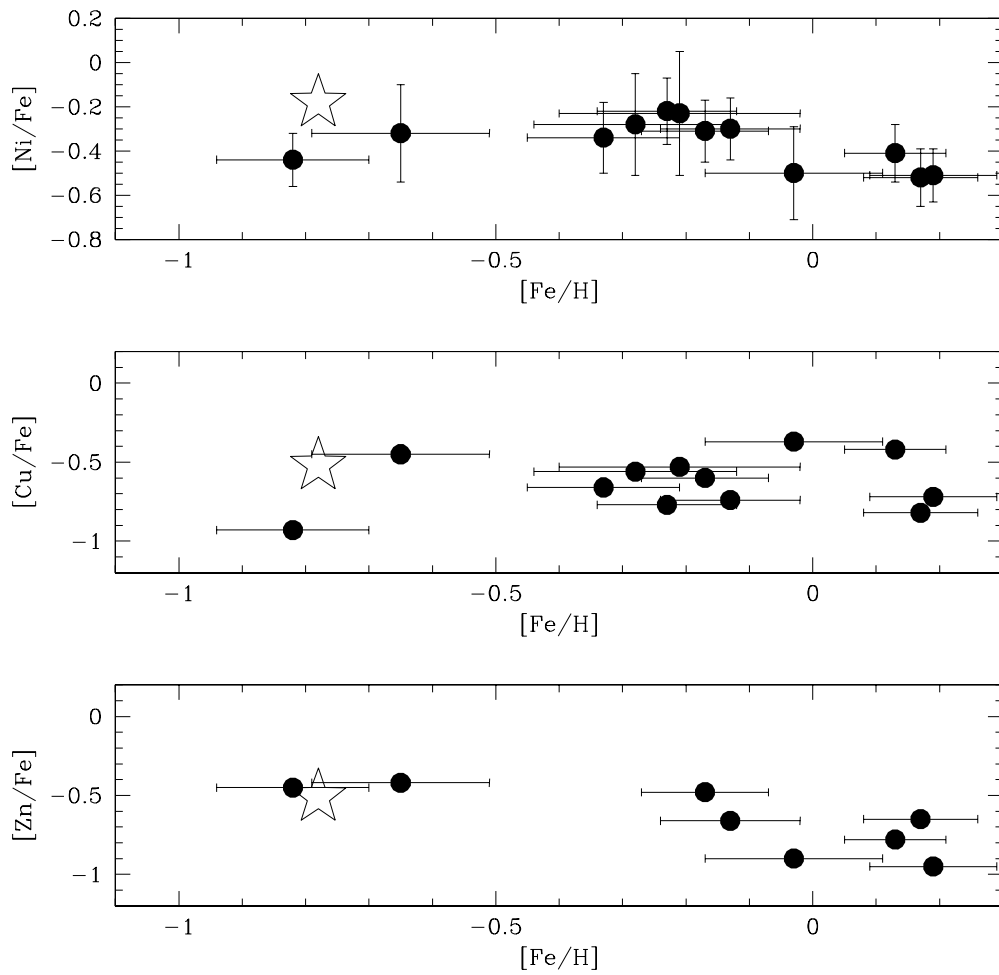


Figure 4.17: Like in fig. 4.15, but now for Fe-peak elements Ni, Cu and Zn.

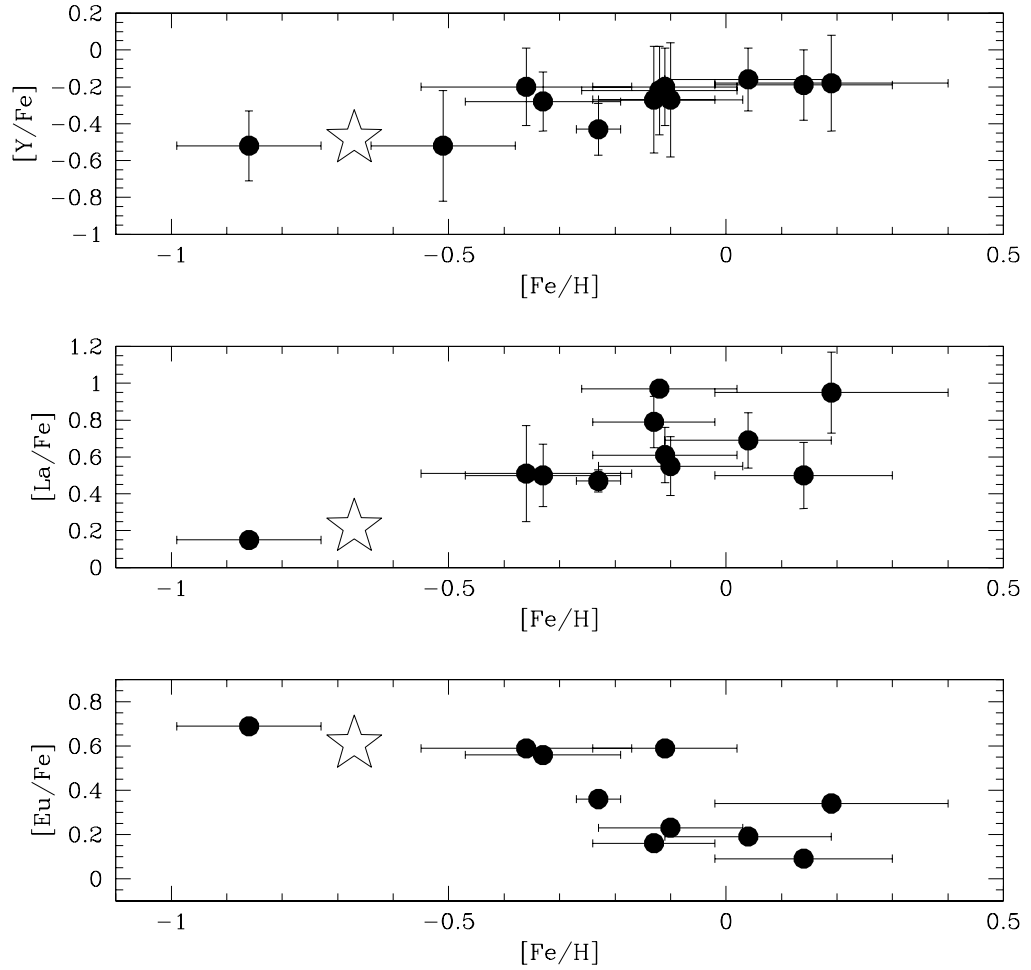


Figure 4.18: Like in fig. 4.15, but now for heavy n-capture elements Y, La, Eu.

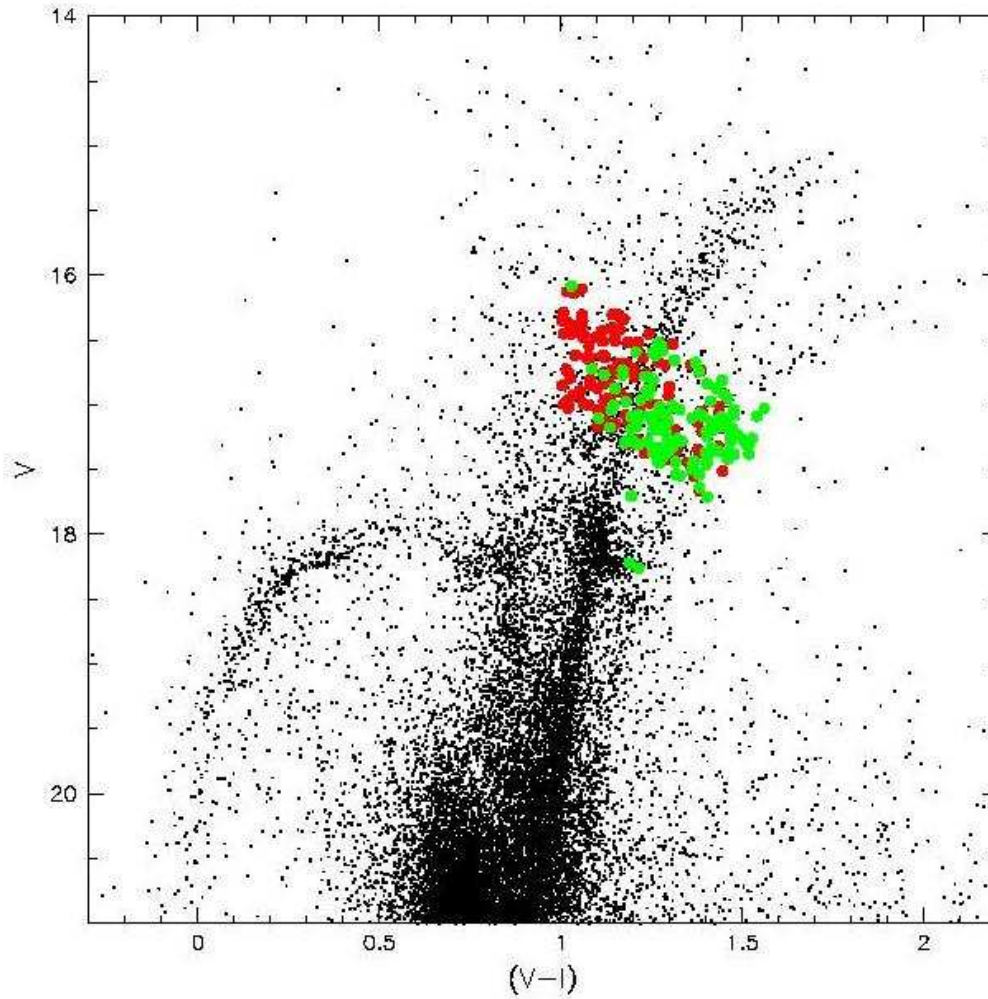


Figure 4.19: Selection of the targets for the FLAMES analysis. Dark dots represent the targets considered Sgr dSph members, light dots the ones that resulted to be non members.

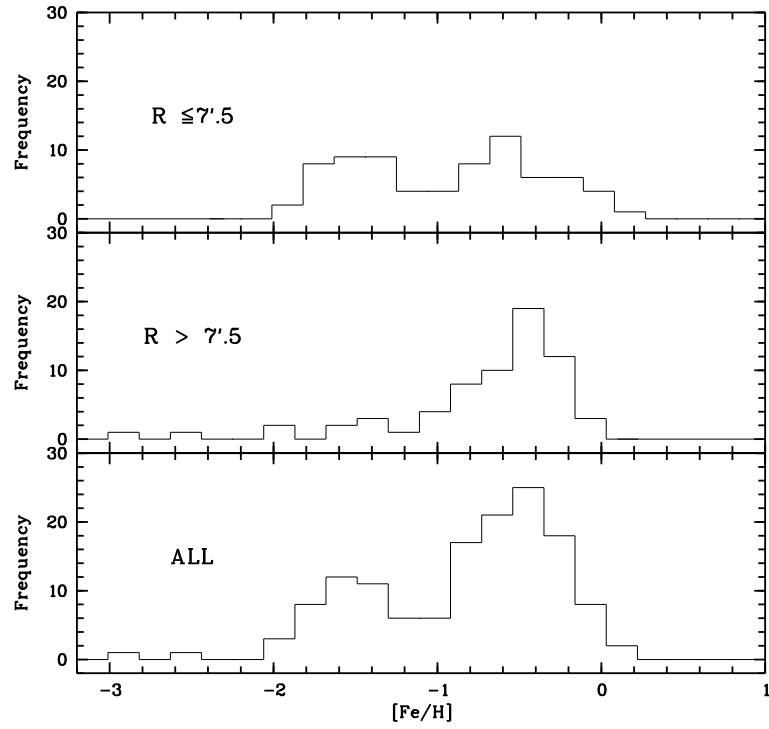


Figure 4.20: Histogram of the entire FLAMES sample presented in Zaggia et al. (2004). The peak of the distribution is around $[Fe/H] = -0.5$, the secondary peak around $[Fe/H] = -1.5$ is due to M54 stars. Separate histograms are presented for stars within and outside 7.5 arcmin from the M54 center.

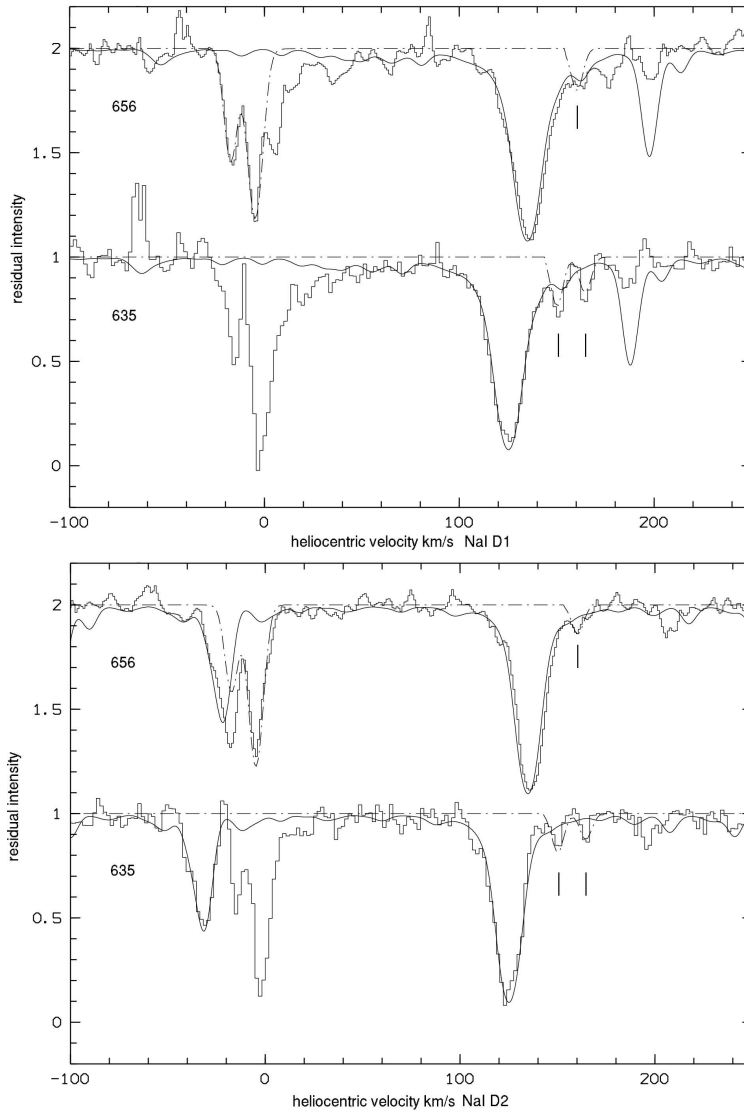


Figure 4.21: Spectra of stars showing high velocity Na I D absorptions. The dashed-dotted line is the synthetic IS fit whereas the continuous line is the synthetic stellar spectrum. The local components in star # 635 are severely contaminated by telluric lines and the fit was not reliable.

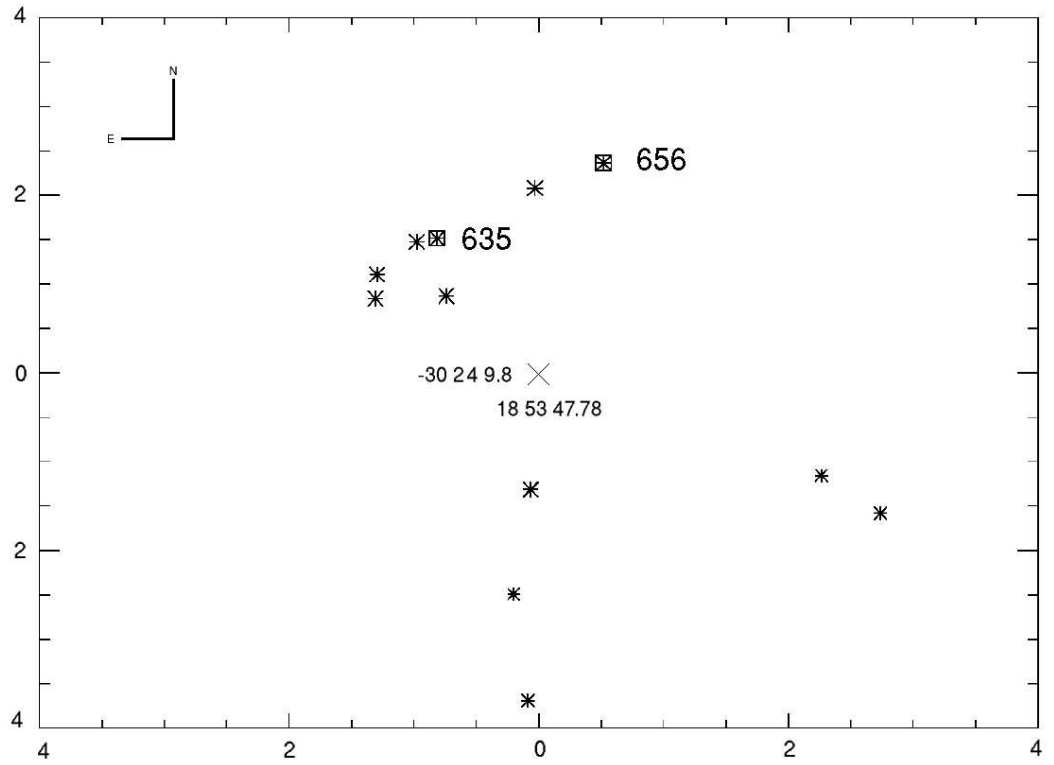


Figure 4.22: A map of the position in the sky of the 12 Sgr dSph main body stars, with indicated the two stars along which line of sight high velocity interstellar absorption components have been identified. The coordinates of the field center are indicated.

Table 4.6: Atomic data, measured EWs, sources of the atomic data and derived abundances for the measured lines, for stars 439, 628, 635 and 656. “Syn” means that the line has been measured by synthesis (no EW provided), “HFS” that hyperfine splitting has been taken into account in the synthesis, so no EW is given, and the log gf is of limited significance. For the meaning of the log gf source references see table 4.12.

Ion	λ (nm)	log gf	source of log gf (see notes)	EW (pm) 432	ϵ	EW (pm) 628	ϵ	EW (pm) 635	ϵ	EW (pm) 656	ϵ
O I	630.0304	-9.717	STZ	syn	8.09	syn	8.45	syn	8.33	syn	8.50
Na I	568.2633	-0.700	KP	–	–	10.67	5.893	7.56	5.454	9.61	5.899
Na I	615.4226	-1.610	ED	–	–	4.38	5.944	1.95	5.429	3.36	5.862
Na I	616.0747	-1.310	ED	–	–	5.26	5.771	3.60	5.474	4.34	5.729
Mg I	552.8405	-0.522	GC	–	–	21.74	7.041	22.55	6.987	19.77	7.006
Mg I	571.1088	-1.729	GC	7.98	6.656	12.46	7.194	10.81	6.967	11.05	7.169
Mg I	631.8717	-1.945	GC	2.08	6.701	5.04	7.279	5.83	7.367	3.59	7.120
Mg I	631.9237	-2.165	GC	–	–	4.77	7.460	3.66	7.252	–	–
Si I	594.8541	-1.230	GARZ	6.16	6.793	8.42	7.172	8.26	7.132	9.30	7.403
Si I	612.5021	-1.540	ED	1.80	6.834	–	–	–	–	–	–
Si I	614.2483	-1.480	ED	–	–	4.54	7.440	3.21	7.180	3.50	7.298
Si I	614.5016	-1.430	ED	1.39	6.589	–	–	3.28	7.140	3.34	7.213
Si I	615.5134	-0.770	ED	–	–	8.26	7.295	5.64	6.890	7.99	7.336
Ca I	551.2980	-0.447	SR	5.48	5.227	10.74	5.952	10.64	5.966	10.69	6.162
Ca I	560.1277	-0.523	SR	–	–	–	–	14.10	6.259	–	–
Ca I	585.7451	0.240	SR	–	–	15.85	6.028	14.22	5.857	14.22	6.053
Ca I	586.7562	-1.490	SR	1.49	5.380	3.86	5.958	3.22	5.798	4.26	6.130
Ca I	612.2217	-0.315	NIST	–	–	–	–	19.53	5.894	19.56	6.192
Ca I	616.1297	-1.266	SR	5.98	5.643	–	–	9.33	6.061	–	–
Ca I	616.6439	-1.142	SR	6.75	5.657	10.81	6.133	9.54	5.970	9.73	6.195
Ca I	616.9042	-0.797	SR	7.25	5.412	13.05	6.140	10.88	5.851	11.64	6.184
Ca I	643.9075	0.390	SR	13.16	5.393	18.30	5.761	17.94	5.786	17.69	5.987
Ca I	645.5598	-1.290	SR	5.86	5.632	8.98	5.990	8.05	5.868	8.16	6.063
Ca I	649.3781	-0.109	SR	11.35	5.543	15.17	5.745	15.03	5.838	13.98	5.867
Ca I	649.9650	-0.818	SR	7.69	5.511	10.77	5.773	10.91	5.856	–	–
Ca I	650.8850	-2.110	NBS	1.38	5.466	2.48	5.826	–	–	–	–
Ca I	679.8479	-2.320	K88	–	–	–	–	–	–	1.45	6.047
Sc II	552.6790	0.130	MFW	8.28	2.000	9.87	2.318	10.42	2.415	10.01	2.551
Ti I	488.5082	0.358	MFW	7.06	4.183	10.22	4.553	–	–	9.83	4.791
Ti I	491.5233	-1.019	MFW	–	–	–	–	–	–	1.91	4.677
Ti I	499.7098	-2.118	MFW	5.51	4.038	9.23	4.544	7.97	4.330	8.42	4.730
Ti I	508.7055	-0.780	MFW	–	–	7.95	4.740	5.73	4.365	6.16	4.688
Ti I	586.6452	-0.840	MFW	6.43	4.141	10.31	4.595	9.16	4.437	9.91	4.841
Ti I	612.6217	-1.425	MFW	3.45	4.156	8.28	4.869	6.99	4.665	7.18	4.958
V I	573.7059	-0.740	MFW	–	–	5.48	3.831	3.80	3.508	3.79	3.764
V I	613.5361	-0.746	MFW	–	–	3.49	3.496	3.14	3.355	3.92	3.748
V I	615.0157	-1.780	MFW	–	–	4.87	3.828	–	–	3.93	3.898
Cr II	488.4607	-2.080	MFW	–	–	–	–	3.59	5.291	4.55	5.555
Mn I	511.79**	-1.140	MFW	HFS	4.24	HFS	5.19	HFS	4.67	HFS	5.08

Table 4.7: Continued from table 4.6.

Ion	λ (nm)	log gf	source of log gf (see notes)	EW (pm) 432	ϵ	EW (pm) 628	ϵ	EW (pm) 635	ϵ	EW (pm) 656	ϵ
Fe I	489.2871	-1.290	FMW	4.42	6.69	8.28	7.33	—	—	7.78	7.44
Fe I	506.7151	-0.970	FMW	—	—	10.54	7.40	8.42	7.03	9.54	7.46
Fe I	510.4436	-1.690	FMW	2.46	6.73	—	—	4.51	7.14	4.81	7.35
Fe I	510.9650	-0.980	FMW	6.07	6.82	—	—	9.51	7.35	7.98	7.24
Fe I	552.5539	-1.330	FMW	3.51	6.52	7.17	7.15	8.14	7.31	7.92	7.46
Fe I	585.6083	-1.640	FMW	2.38	6.64	6.16	7.37	5.52	7.24	4.85	7.27
Fe I	585.8779	-2.260	FMW	—	—	2.56	7.29	2.88	7.30	2.00	7.24
Fe I	587.7794	-2.230	FMW	1.65	6.88	—	—	—	—	3.64	7.53
Fe I	588.3813	-1.360	FMW	5.80	6.70	10.41	7.37	—	—	8.48	7.27
Fe I	615.1617	-3.299	FMW	6.81	6.66	9.92	7.04	—	—	9.37	7.22
Fe I	616.5361	-1.550	FMW	4.19	6.76	—	—	6.22	7.07	6.39	7.27
Fe I	618.7987	-1.720	FMW	4.01	6.65	—	—	7.51	7.21	6.49	7.23
Fe I	649.6469	-0.570	FMW	3.56	6.39	9.10	7.28	7.73	7.08	7.81	7.25
Fe I	670.3568	-3.160	FMW	4.09	6.67	7.53	7.22	6.29	7.00	7.27	7.38
Fe II	483.3197	-4.780	FMW	1.20	6.67	—	—	—	—	3.18	7.53
Fe II	492.3927	-1.320	FMW	14.99	6.38	—	—	—	—	—	—
Fe II	499.3358	-3.650	FMW	4.10	6.50	8.35	7.46	6.35	7.09	7.05	7.35
Fe II	510.0664	-4.370	FMW	2.08	6.73	3.76	7.33	4.30	7.42	3.30	7.30
Fe II	513.2669	-4.180	FMW	2.57	6.67	4.43	7.27	4.01	7.17	4.72	7.41
Fe II	516.1184	-4.483	K88	—	—	—	—	—	—	2.17	7.19
Fe II	525.6938	-4.250	K88	2.57	6.83	5.44	7.62	3.36	7.20	4.66	7.56
Fe II	526.4812	-3.190	FMW	4.84	6.68	7.10	7.23	—	—	—	—
Fe II	614.9258	-2.724	K88	3.69	6.69	—	—	3.55	6.82	—	—
Co I	533.17**	-6.473	K88	HFS	3.92	HFS	4.61	HFS	4.24	HFS	4.62
Co I	553.07**	-2.060	FMW	HFS	3.72	HFS	4.52	HFS	4.35	HFS	4.55
Ni I	612.8963	-3.330	FMW	2.48	5.018	6.81	5.86	4.16	5.39	6.24	5.96
Ni I	613.0130	-0.960	FMW	—	—	3.14	5.92	2.22	5.66	1.96	5.72
Ni I	617.5360	-0.530	FMW	—	—	5.69	5.71	5.32	5.62	4.71	5.67
Ni I	617.6807	-0.260	FMW	3.27	4.96	7.10	5.66	6.32	5.52	6.75	5.75
Ni I	617.7236	-3.500	FMW	—	—	4.24	5.84	3.86	5.69	2.78	5.72
Cu I	510.55**	-1.516	BIEL	HFS	2.46	HFS	3.21	HFS	3.22	HFS	3.44
Zn I	481.0528	-0.170	BG	5.72	3.33	—	—	—	—	7.88	3.95
Y II	488.3684	0.070	HL	6.17	0.79	10.65	1.73	9.84	1.56	10.46	1.98
Y II	498.2129	-1.290	HL	—	—	5.81	2.17	3.65	1.72	4.06	2.00
Y II	508.7416	-0.170	HL	4.93	0.74	9.20	1.67	—	—	7.92	1.67
Y II	511.9112	-1.360	HL	1.71	1.05	4.82	2.02	3.82	1.77	4.41	2.08
Ba II	649.6897	-0.377	NBS	13.06	1.23	21.52	2.29	15.69	1.55	19.02	2.28
La II	480.4039	-1.490	LA	—	—	7.18	1.98	—	—	4.55	1.70
La II	511.4559	-1.030	LA	—	—	—	—	7.35	1.46	—	—
La II	632.0376	-1.610	ABH	1.34	0.42	—	—	2.95	1.10	4.00	1.54
Ce II	518.7458	0.130	H	1.64	0.82	5.00	1.85	4.45	1.68	2.78	1.56
Ce II	533.0556	-0.360	H	—	—	4.30	1.82	3.30	1.55	3.07	1.72
Ce II	546.8371	0.140	H	—	—	3.69	1.81	—	—	2.43	1.66
Ce II	604.3373	-0.430	MC	—	—	2.31	1.85	—	—	—	—
Nd II	491.4382	-0.700	HA	4.53	1.14	8.19	2.01	5.95	1.55	6.80	2.00
Nd II	495.9119	-0.800	HA	4.17	0.78	9.71	2.00	7.95	1.64	8.64	2.11
Nd II	496.1387	-0.710	MC'	—	—	5.31	1.82	4.78	1.65	4.14	1.78
Nd II	508.9832	-1.160	MC'	—	—	4.63	1.66	—	—	—	—
Nd II	529.3163	0.100	HA	3.65	0.84	—	—	5.53	1.37	7.60	1.82
Nd II	543.1516	-0.470	HA	—	—	—	—	2.51	1.51	2.24	1.64
Nd II	548.5696	-0.120	HA	—	—	—	—	—	—	3.79	1.79
Eu II	644.50**	0.120	LAW	HFS	0.34	—	—	—	0.74	—	—

Table 4.8: As in table 4.6 for stars 709, 716, 717, and 772

Ion	λ (nm)	log gf	source of log gf (see notes)	EW (pm) 709	ϵ	EW (pm) 716	ϵ	EW (pm) 717	ϵ	EW (pm) 772	ϵ
O I	630.0304	-9.717	STZ	syn	8.76	syn	8.61	syn	8.93	syn	8.33
Na I	498.2814	-0.950	KP	–	–	–	–	–	–	syn	5.44
Na I	568.2633	-0.700	KP	11.23	6.14	11.18	5.99	10.30	6.11	–	–
Na I	615.4226	-1.610	ED	–	–	2.47	5.64	2.95	5.81	3.32	5.74
Na I	616.0747	-1.310	ED	6.07	5.94	5.77	5.87	4.45	5.78	3.42	5.46
Mg I	552.8405	-0.522	GC	21.53	7.10	21.90	7.05	–	–	18.19	6.78
Mg I	571.1088	-1.729	GC	10.66	7.12	11.76	7.13	12.42	7.48	10.16	7.01
Mg I	631.8717	-1.945	GC	5.95	7.49	4.53	7.23	5.34	7.45	3.19	7.00
Mg I	631.9237	-2.165	GC	3.61	7.32	–	–	3.78	7.41	2.00	6.95
Al I	669.6023	-1.347	NBS	–	–	–	–	–	–	syn	5.77
Al I	669.6788	-1.420	??	–	–	–	–	–	–	syn	6.17
Al I	669.8673	-1.647	NBS	–	–	1.90	5.75	2.01	5.84	syn	6.27
Si I	577.2146	-1.750	GARZ	4.82	7.29	–	–	–	–	4.82	7.16
Si I	594.8541	-1.230	GARZ	8.84	7.43	10.26	7.45	10.14	7.66	8.84	7.28
Si I	612.5021	-1.540	ED	–	–	–	–	–	–	–	–
Si I	614.2483	-1.480	ED	4.34	7.52	3.31	7.24	3.64	7.38	4.34	7.40
Si I	614.5016	-1.430	ED	3.79	7.36	–	–	4.44	7.48	3.79	7.24
Si I	615.5134	-0.770	ED	7.87	7.42	7.01	7.12	8.88	7.59	7.87	7.27
Ca I	551.2980	-0.447	SR	10.09	6.08	11.31	6.07	11.47	6.46	10.09	6.08
Ca I	560.1277	-0.523	SR	–	–	–	–	–	–	12.43	6.24
Ca I	585.7451	0.240	SR	13.38	5.97	15.84	6.05	16.28	6.51	–	–
Ca I	586.7562	-1.490	SR	3.58	5.96	–	–	4.19	6.17	3.58	5.95
Ca I	612.2217	-0.315	NIST	17.26	5.92	22.15	6.22	22.05	6.54	17.26	5.87
Ca I	616.1297	-1.266	SR	–	–	9.85	6.16	–	–	9.20	6.25
Ca I	616.6439	-1.142	SR	–	–	9.91	6.04	10.05	6.44	8.01	5.90
Ca I	616.9042	-0.797	SR	10.93	6.10	11.75	5.97	11.00	6.28	10.93	6.10
Ca I	643.9075	0.390	SR	17.33	5.99	19.22	5.90	–	–	17.33	5.95
Ca I	645.5598	-1.290	SR	–	–	8.84	6.01	7.95	6.17	7.85	6.01
Ca I	649.3781	-0.109	SR	14.52	6.04	15.20	5.78	14.65	6.24	14.52	6.03
Ca I	649.9650	-0.818	SR	–	–	11.51	5.92	11.51	6.38	9.95	5.92
Ca I	650.8850	-2.110	NBS	–	–	3.29	6.03	3.21	6.12	–	–
Ca I	679.8479	-2.320	K88	–	–	–	–	–	–	–	–
Sc II	552.6790	0.130	MFW	9.97	2.77	10.74	2.52	12.08	3.22	10.91	2.66
Sc II	632.0851	-1.770	NBS	–	–	–	–	–	–	1.62	2.36
Ti I	488.5082	0.358	MFW	–	–	–	–	–	–	8.97	4.63
Ti I	491.5233	-1.019	MFW	3.13	4.87	–	–	–	–	–	–
Ti I	497.7719	-0.920	WOLN	–	–	–	–	–	–	syn	4.80
Ti I	497.8222	-0.388	WOLN	–	–	–	–	–	–	syn	4.60
Ti I	498.9131	-0.217	MFW	–	–	–	–	–	–	syn	4.44
Ti I	499.7098	-2.118	MFW	–	–	8.88	4.59	–	–	syn	4.70
Ti I	508.7055	-0.780	MFW	8.29	5.04	5.84	4.51	6.74	4.92	–	–
Ti I	586.6452	-0.840	MFW	10.26	4.92	10.61	4.72	7.41	4.58	8.41	4.57
Ti I	612.6217	-1.425	MFW	8.17	5.07	7.03	4.79	6.12	4.91	6.72	4.83
V I	573.7059	-0.740	MFW	4.87	3.85	5.28	3.89	2.72	3.61	3.28	3.57
V I	613.5361	-0.746	MFW	3.92	3.64	5.35	3.86	4.30	3.88	syn	3.50
V I	615.0157	-1.780	MFW	5.68	4.06	4.57	3.87	4.41	4.05	syn	3.60
Cr II	488.4607	-2.080	MFW	4.14	5.65	5.53	5.71	5.38	5.91	3.76	5.32
Mn I	511.07**	-2.901	K88	HFS	5.24	HFS	5.20	HFS	5.11	HFS	4.85

Table 4.9: Continued from table 4.9

Ion	λ (nm)	log gf	source of log gf (see notes)	EW (pm) 709	ϵ	EW (pm) 716	ϵ	EW (pm) 717	ϵ	EW (pm) 772	ϵ
Fe I	489.2871	-1.290	FMW	8.12	7.60	8.67	7.43	8.48	7.81	5.91	7.06
Fe I	506.7151	-0.970	FMW	10.08	7.70	11.31	7.56	—	—	8.34	7.24
Fe I	510.4436	-1.690	FMW	6.81	7.77	—	—	5.90	7.77	6.58	7.65
Fe I	510.9650	-0.980	FMW	10.57	7.90	—	—	9.39	7.78	7.90	7.24
Fe I	552.5539	-1.330	FMW	9.20	7.79	8.83	7.45	8.03	7.67	—	—
Fe I	585.5091	-1.760	FMW	4.70	7.74	—	—	—	—	4.24	7.61
Fe I	585.6083	-1.640	FMW	7.06	7.72	—	—	6.54	7.72	6.24	7.51
Fe I	585.8779	-2.260	FMW	—	—	2.89	7.40	3.19	7.57	2.37	7.27
Fe I	586.1107	-2.450	FMW	2.86	7.69	—	—	2.90	7.77	1.22	7.18
Fe I	587.7794	-2.230	FMW	4.48	7.68	3.73	7.48	—	—	3.34	7.25
Fe I	588.3813	-1.360	FMW	9.11	7.49	10.38	7.40	9.07	7.62	9.15	7.43
Fe I	615.1617	-3.299	FMW	—	—	10.86	7.24	—	—	8.02	6.98
Fe I	616.5361	-1.550	FMW	8.00	7.62	—	—	7.64	7.66	6.46	7.26
Fe I	618.7987	-1.720	FMW	8.83	7.72	8.21	7.37	7.32	7.53	6.34	7.17
Fe I	649.6469	-0.570	FMW	9.02	7.55	8.50	7.22	8.20	7.49	8.45	7.38
Fe I	670.3568	-3.160	FMW	—	—	7.80	7.32	7.95	7.66	7.16	7.33
Fe II	483.3197	-4.780	FMW	3.11	7.68	—	—	—	—	1.94	7.27
Fe II	492.3927	-1.320	FMW	—	—	—	—	—	—	—	—
Fe II	499.3358	-3.650	FMW	8.35	7.90	7.14	7.28	6.32	7.42	6.37	7.30
Fe II	510.0664	-4.370	FMW	5.32	7.94	4.64	7.55	4.13	7.63	—	—
Fe II	513.2669	-4.180	FMW	3.93	7.44	4.64	7.36	4.16	7.45	3.98	7.33
Fe II	516.1184	-4.483	K88	—	—	—	—	—	—	—	—
Fe II	525.6938	-4.250	K88	—	—	—	—	5.06	7.81	—	—
Fe II	526.4812	-3.190	FMW	6.36	7.46	—	—	7.55	7.68	6.09	7.24
Fe II	614.9258	-2.724	K88	—	—	5.80	7.30	7.29	7.85	—	—
Co I	533.17**	-6.473	K88	HFS	4.42	HFS	4.58	HFS	4.62	HFS	4.27
Co I	553.07**	-2.060	FMW	HFS	4.68	HFS	4.62	HFS	4.58	HFS	4.33
Ni I	585.7746	-0.636	K88	—	—	—	—	—	—	4.38	5.75
Ni I	612.8963	-3.330	FMW	5.60	5.88	6.49	5.89	5.34	5.94	5.60	5.81
Ni I	613.0130	-0.960	FMW	2.60	5.90	3.19	5.97	2.34	5.87	1.89	5.62
Ni I	617.5360	-0.530	FMW	6.47	6.05	5.63	5.74	4.79	5.78	5.74	5.64
Ni I	617.6807	-0.260	FMW	—	—	7.45	5.75	7.26	6.02	5.73	6.21
Ni I	617.7236	-3.500	FMW	3.71	5.88	3.24	5.75	—	—	3.69	5.82
Cu I	510.55**	-1.516	BIEL	HFS	3.68	HFS	3.34	HFS	3.56	HFS	3.47
Zn I	481.0528	-0.170	BG	6.50	3.84	7.87	3.81	7.73	4.12	—	—
Y II	488.3684	0.070	HL	11.80	2.47	10.34	1.72	10.60	2.33	9.37	1.67
Y II	498.2129	-1.290	HL	4.43	2.21	4.79	2.08	3.57	2.04	2.78	1.57
Y II	508.7416	-0.170	HL	8.65	2.04	7.48	1.44	8.86	2.17	7.13	1.40
Y II	511.9112	-1.360	HL	4.69	2.28	4.84	2.10	4.20	2.20	3.15	1.67
Ba II	649.6897	-0.377	NBS	22.13	2.60	17.03	1.83	20.33	2.54	18.92	2.03
La II	480.4039	-1.490	LA	6.82	2.35	6.03	1.88	3.61	1.67	3.53	1.32
La II	511.4559	-1.030	LA	—	—	—	—	—	—	—	—
La II	632.0376	-1.610	ABH	6.73	2.18	5.73	1.71	4.80	1.86	4.31	1.42
Ce II	518.7458	0.130	H	5.34	2.24	—	—	4.49	2.09	3.00	1.44
Ce II	533.0556	-0.360	H	4.74	2.19	3.94	1.85	3.35	1.93	3.26	1.59
Ce II	546.8371	0.140	H	3.51	2.03	4.49	2.04	3.31	2.00	—	—
Ce II	604.3373	-0.430	MC	3.21	2.28	3.30	2.15	1.37	1.78	2.04	1.71
Nd II	491.4382	-0.700	HA	7.53	2.37	7.01	1.89	5.72	2.02	3.82	1.24
Nd II	495.9119	-0.800	HA	—	—	10.88	2.30	8.27	2.39	6.73	1.57
Nd II	496.1387	-0.710	MC'	5.69	2.24	7.19	2.21	4.76	2.09	3.01	1.36
Nd II	508.9832	-1.160	MC'	5.13	2.05	—	—	—	—	2.94	1.30
Nd II	529.3163	0.100	HA	—	—	—	—	—	—	6.48	1.47
Nd II	543.1516	-0.470	HA	3.85	2.13	—	—	3.26	2.02	2.84	1.61
Nd II	548.5696	-0.120	HA	4.42	2.06	5.15	1.98	5.15	2.26	2.32	1.30
Eu II	644.50**	0.120	LAW	HFS	1.04	HFS	0.54	HFS	0.74	HFS	0.64

Table 4.10: As in table 4.6 for stars 867, 879 894 and 927

Ion	λ (nm)	log gf	source of log gf (see notes)	EW (pm) 867	ϵ	EW (pm) 879	ϵ	EW (pm) 894	ϵ	EW (pm) 927	ϵ
O I	630.0304	-9.717	STZ	syn	8.29	syn	7.83	syn	8.77	syn	8.80
Na I	498.2814	-0.950	KP	-	-	-	-	-	-	-	-
Na I	568.2633	-0.700	KP	6.37	5.27	-	-	10.83	6.05	12.21	6.27
Na I	615.4226	-1.610	ED	-	-	3.73	5.80	-	-	5.40	6.12
Na I	616.0747	-1.310	ED	3.50	5.47	4.48	5.63	5.58	5.84	6.19	5.93
Mg I	552.8405	-0.522	GC	-	-	17.80	6.78	19.47	6.95	20.90	7.03
Mg I	571.1088	-1.729	GC	10.73	6.85	11.48	7.17	10.49	7.07	11.73	7.27
Mg I	631.8717	-1.945	GC	2.40	6.79	4.00	7.14	5.32	7.36	5.95	7.48
Mg I	631.9237	-2.165	GC	2.28	6.98	1.50	6.79	-	-	2.96	7.18
Al I	669.6023	-1.347	NBS	-	-	syn	5.87	-	-	-	-
Al I	669.6788	-1.420	??	-	-	syn	6.04	-	-	-	-
Al I	669.8673	-1.647	NBS	-	-	2.88	5.95	-	-	2.64	5.89
Si I	577.2146	-1.750	GARZ	-	-	6.67	7.48	-	-	4.82	7.32
Si I	594.8541	-1.230	GARZ	6.71	6.79	7.12	7.00	9.24	7.48	8.98	7.50
Si I	614.2483	-1.480	ED	3.87	7.23	2.36	7.05	4.80	7.58	3.63	7.41
Si I	614.5016	-1.430	ED	3.30	7.08	4.99	7.47	4.83	7.53	4.21	7.47
Si I	615.5134	-0.770	ED	5.99	6.84	5.80	6.95	8.67	7.54	7.88	7.47
Ca I	551.2980	-0.447	SR	8.98	5.58	-	-	10.24	6.08	-	-
Ca I	560.1277	-0.523	SR	12.63	5.71	-	-	-	-	-	-
Ca I	585.7451	0.240	SR	16.00	5.85	12.48	5.85	15.39	6.24	14.65	6.17
Ca I	586.7562	-1.490	GC	4.00	5.94	4.38	6.09	5.12	6.20	4.98	6.18
Ca I	612.2217	-0.315	NIST	-	-	17.26	5.88	-	-	22.54	6.39
Ca I	615.6023	-2.180	NIST	-	-	1.81	5.74	-	-	-	-
Ca I	616.1297	-1.266	SR	8.16	5.78	7.99	6.03	10.72	6.48	8.64	6.13
Ca I	616.6439	-1.142	SR	7.21	5.54	-	-	10.42	6.30	9.61	6.19
Ca I	616.9042	-0.797	SR	11.18	5.71	9.44	5.84	10.45	5.96	11.73	6.25
Ca I	643.9075	0.390	SR	-	-	18.95	6.15	18.43	6.12	17.53	6.02
Ca I	645.5598	-1.290	SR	8.75	5.87	6.37	5.75	9.46	6.24	9.08	6.22
Ca I	649.3781	-0.109	SR	-	-	12.84	5.78	-	-	14.43	6.04
Ca I	649.9650	-0.818	SR	-	-	-	-	11.53	6.15	12.37	6.38
Ca I	650.8850	-2.110	NBS	-	-	3.28	6.01	-	-	-	-
Ca I	679.8479	-2.320	K88	-	-	-	-	-	-	1.79	6.05
Sc II	552.6790	0.130	MFW	10.54	2.10	9.94	2.53	9.67	2.63	10.31	2.92
Sc II	632.0851	-1.770	NBS	-	-	1.92	2.46	-	-	-	-
Ti I	488.5082	0.358	MFW	9.24	4.24	9.92	4.88	10.63	4.98	8.50	4.53
Ti I	491.5233	-1.019	MFW	-	-	-	-	4.72	5.10	2.52	4.68
Ti I	497.7719	-0.920	WOLN	-	-	syn	4.66	-	-	-	-
Ti I	497.8222	-0.388	WOLN	-	-	syn	4.76	-	-	-	-
Ti I	498.9131	-0.217	MFW	-	-	syn	4.76	-	-	-	-
Ti I	499.7098	-2.118	MFW	7.73	4.24	syn	5.05	-	-	-	-
Ti I	508.7055	-0.780	MFW	6.16	4.41	-	-	7.77	4.86	8.42	5.06
Ti I	586.6452	-0.840	MFW	8.29	4.23	10.14	4.91	10.48	4.88	10.74	5.01
Ti I	612.6217	-1.425	MFW	5.79	4.50	6.40	4.76	7.06	4.79	-	-
V I	573.7059	-0.740	MFW	-	-	-	-	6.22	3.99	5.38	3.88
V I	613.5361	-0.746	MFW	-	-	syn	3.68	3.76	3.54	2.63	3.33
V I	615.0157	-1.780	MFW	-	-	syn	3.91	6.26	4.06	6.73	4.17
Cr II	488.4607	-2.080	MFW	-	-	3.76	5.35	2.51	5.17	4.56	5.83
Mn I	511.07**	-2.901	K88	-	-	HFS	5.07	HFS	5.15	HFS	5.00

Table 4.11: Continued from table 4.10

Ion	λ (nm)	log gf	source of log gf (see notes)	EW (pm) 867	ϵ	EW (pm) 879	ϵ	EW (pm) 894	ϵ	EW (pm) 927	ϵ
Fe I	489.2871	-1.290	FMW	6.89	6.97	7.09	7.32	8.21	7.58	8.59	7.75
Fe I	506.7151	-0.970	FMW	—	—	7.46	7.06	8.82	7.38	—	—
Fe I	510.4436	-1.690	FMW	—	—	5.89	7.27	—	—	—	—
Fe I	510.9650	-0.980	FMW	8.06	6.91	—	—	9.39	7.60	9.18	7.64
Fe I	552.5539	-1.330	FMW	6.75	6.97	6.25	7.13	7.06	7.31	8.53	7.69
Fe I	585.5091	-1.760	FMW	—	—	4.12	7.56	4.65	7.69	—	—
Fe I	585.6083	-1.640	FMW	—	—	3.85	7.04	6.89	7.65	6.87	7.71
Fe I	585.8779	-2.260	FMW	—	—	1.97	7.14	2.68	7.35	3.39	7.53
Fe I	586.1107	-2.450	FMW	—	—	1.81	7.35	2.47	7.56	2.81	7.77
Fe I	587.7794	-2.230	FMW	1.77	6.96	2.74	7.25	—	—	4.55	7.69
Fe I	588.3813	-1.360	FMW	—	—	7.88	7.18	9.33	7.49	—	—
Fe I	615.1617	-3.299	FMW	8.04	6.64	9.59	7.28	—	—	—	—
Fe I	616.5361	-1.550	FMW	4.27	6.72	5.98	7.17	6.58	7.29	—	—
Fe I	618.7987	-1.720	FMW	4.92	6.75	7.36	7.37	6.74	7.26	7.99	7.57
Fe I	649.6469	-0.570	FMW	5.75	6.68	6.26	6.97	9.06	7.52	8.59	7.51
Fe I	670.3568	-3.160	FMW	7.00	7.04	7.72	7.42	7.61	7.39	8.22	7.58
Fe II	483.3197	-4.780	FMW	—	—	2.72	7.34	—	—	—	—
Fe II	492.3927	-1.320	FMW	—	—	—	—	—	—	—	—
Fe II	499.3358	-3.650	FMW	6.96	6.93	5.97	7.10	5.78	7.26	6.25	7.54
Fe II	510.0664	-4.370	FMW	3.63	7.11	—	—	4.34	7.66	—	—
Fe II	513.2669	-4.180	FMW	4.66	7.10	—	—	4.67	7.54	4.87	7.74
Fe II	516.1184	-4.483	K88	—	—	—	—	2.46	7.36	2.14	7.40
Fe II	525.6938	-4.250	K88	—	—	—	—	2.93	7.29	4.17	7.74
Fe II	526.4812	-3.190	FMW	6.11	6.80	6.00	7.11	6.32	7.38	5.45	7.35
Fe II	614.9258	-2.724	K88	—	—	—	—	4.80	7.32	4.75	7.47
Co I	533.17**	-6.473	K88	HFS	4.28	HFS	4.31	HFS	4.59	HFS	4.73
Co I	553.07**	-2.060	FMW	HFS	4.06	HFS	4.53	HFS	4.71	HFS	4.58
Ni I	585.7746	-0.636	K88	—	—	2.74	5.41	—	—	—	—
Ni I	612.8963	-3.330	FMW	3.43	5.25	5.60	5.75	5.88	5.85	5.71	5.90
Ni I	613.0130	-0.960	FMW	—	—	1.89	5.61	1.66	5.60	2.52	5.89
Ni I	617.5360	-0.530	FMW	4.96	5.49	5.74	5.81	4.10	5.55	—	—
Ni I	617.6807	-0.260	FMW	3.98	5.07	5.73	5.81	5.98	5.64	7.96	6.13
Ni I	617.7236	-3.500	FMW	—	—	3.69	5.75	4.49	5.95	4.13	5.95
Cu I	510.55**	-1.516	BIEL	HFS	3.11	HFS	3.37	HFS	3.81	HFS	3.92
Zn I	481.0528	-0.170	BG	7.82	3.52	—	—	10.54	2.18	6.70	3.95
Y II	488.3684	0.070	HL	8.15	0.94	5.84	0.95	10.54	2.18	9.95	2.20
Y II	498.2129	-1.290	HL	2.93	1.45	3.35	1.71	3.51	1.93	4.01	2.16
Y II	508.7416	-0.170	HL	6.34	0.91	7.58	1.55	6.12	4.41	8.06	1.99
Y II	511.9112	-1.360	HL	3.09	1.50	2.91	1.63	3.56	1.95	3.75	2.12
Ba II	649.6897	-0.377	NBS	15.22	1.07	18.80	2.06	18.96	2.36	18.25	2.37
La II	480.4039	-1.490	LA	—	—	3.76	1.38	4.18	1.66	4.53	1.87
La II	511.4559	-1.030	LA	—	—	—	—	—	—	—	—
La II	632.0376	-1.610	ABH	—	—	3.20	1.21	3.65	1.49	4.78	1.84
Ce II	518.7458	0.130	H	3.06	1.29	4.30	1.74	3.42	1.73	4.50	2.10
Ce II	533.0556	-0.360	H	—	—	3.53	1.66	3.67	1.88	4.46	2.18
Ce II	546.8371	0.140	H	2.44	1.35	3.60	1.78	3.19	1.87	4.36	2.26
Ce II	604.3373	-0.430	MC	—	—	—	—	—	—	1.63	1.89
Nd II	491.4382	-0.700	HA	4.51	1.15	5.89	1.71	7.33	2.23	6.94	2.30
Nd II	495.9119	-0.800	HA	4.67	0.90	—	—	6.98	2.04	9.28	2.59
Nd II	496.1387	-0.710	MC'	—	—	2.80	1.26	4.81	1.95	5.53	2.26
Nd II	508.9832	-1.160	MC'	—	—	3.79	1.49	—	—	—	—
Nd II	529.3163	0.100	HA	5.46	0.97	5.70	1.07	6.30	1.86	9.47	2.54
Nd II	543.1516	-0.470	HA	—	—	—	—	—	—	—	—
Nd II	548.5696	-0.120	HA	—	—	3.53	1.59	3.58	1.97	—	—
Eu II	644.50**	0.120	LAW	—	—	HFS	0.74	HFS	0.64	HFS	0.74

Table 4.12: Bibliographic reference for the log gf sources cited in tables 4.6 through 4.11, 5.2 through 5.4 and 6.5 through 6.7.

ABH	Arnesen et al. (1977)
BIEL	Bielski (1975)
BG	Biemont & Godefroid (1980)
ED	Edvardsson et al. (1993)
FMW	Fuhr et al. (1988a)
GARZ	Garz (1973)
GC	Gratton et al. (2003)
H	Hill et al. (1995)
HA	Den Hartog et al. (2003)
HL	Hannaford et al. (1982)
K88	Kurucz (1988)
KP	Kurucz & Peytremann (1975)
LA	Lawler et al. (2001a)
LAW	Lawler et al. (2001b)
MC	Meggers, Corliss & Scribner (1975)
MC'	Meggers, Corliss & Scribner (1975)
MFW	Fuhr et al. (1988b)
NBS	S I - Wiese et al. (1969)
	Ca I - Wiese et al. (1969)
	Ba II - Miles & Wiese (1969)
NIST	NIST online database
SR	Smith & Raggett (1981)
STZ	Storey & Zeippen (2000)
WOLN	Wolnik & Berthel (1973)

Chapter 5

Abundances in Terzan 7

5.1 Introduction

Terzan 7 (Terzan, 1968; Buonanno et al., 1995) is a sparse, young and metal rich globular cluster, one of the four believed to be physically associated to Sgr dSph (see 4).

Terzan 7 has long been known to be a somewhat peculiar globular cluster. Even before the Sgr dSph discovery (Ibata et al., 1994, 1995), it has been associated with a small group of other objects due to their anomalous characteristics. It was shown to share with Arp 2, Ruprecht 106 and Pal 12 the young age and a significant discrepancy between the photometric metallicities and those based on the Ca II IR triplet (Buonanno et al. 1995 and references therein). The fact that all these clusters, with the exception of Ru 106, appear now to be somehow linked to the Sgr dSph lead to interpret their anomalies as linked to their origin in the Sgr dSph system.

Given the peculiar chemical composition displayed by Sgr dSph the chemistry of Terzan 7 (and of the other globular clusters associated to the Sgr dSph) is of particular importance: since it belongs to the Sgr dSph system, we expect to find the same chemical peculiarities we observed in the main body of the galaxy.

Detailed abundances on Terzan 7 stars are presented in literature only by Tautvaišienė et al. (2004), where authors analyzed three low gravity, cool giants (one of which could also be an AGB star given its proximity to RGB tip), finding a rather high mean metallicity ($[Fe/H] \sim -0.6$), very slight α enhancement and a marginally significant Ni under-abundance with respect to

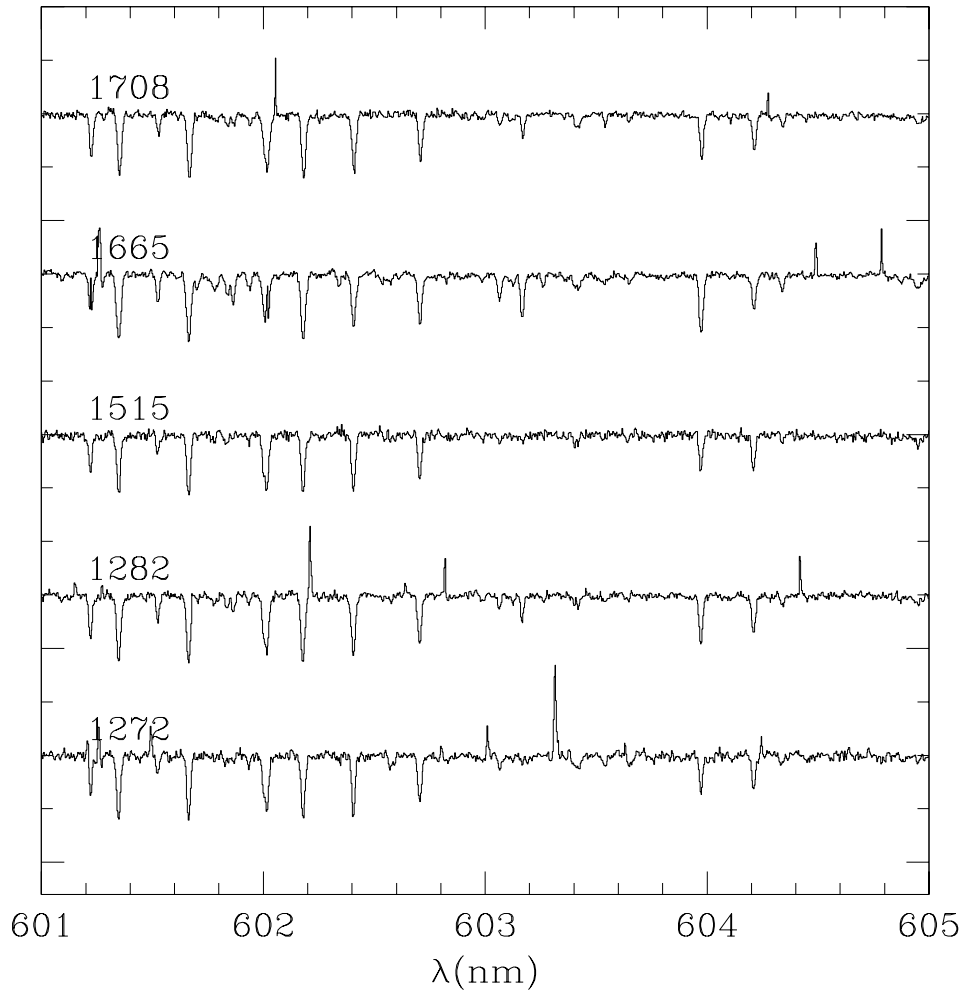


Figure 5.1: A sample of the spectra of the five stars in the wavelength range 601 to 605 nm, where many used Fe I features are. For star # 1282 the DIC1 spectrum is shown.

Table 5.1: Photometry and physical parameters for the five stars.

Number ^a	V mag	(B-V) ₀ mag	T _{eff} K	log g cgs	ξ kms ⁻¹	α(J2000) hms	δ(J2000) °, ', ''	v _r ^b kms ⁻¹
1272	16.62	1.15	4421	1.2	1.45	19 17 37.1	-34 39 11.9	158.9
1282 ^c	16.08	1.30	4203	1.3	1.60	19 17 39.4	-34 39 06.4	158.2
1515	16.76	1.12	4468	2.0	1.45	19 17 38.2	-34 39 16.8	157.8
1665 ^d	15.04	1.50	3945	0.7	1.55	19 17 43.2	-34 39 43.2	159.6
1708 ^e	16.08	1.28	4231	1.2	1.70	19 17 43.5	-34 39 12.4	160.6

^a Referred to the catalog of Buonanno et al. (1995), available via CDS at <http://cdsweb.u-strasbg.fr/cgi-bin/qcat?J/AJ/109/663/>.

^b The presented v_r is the heliocentric value.

^c This is star S34 in Tautvaišienė et al. (2004)

^d This is star S16 in Tautvaišienė et al. (2004)

^e This is star S35 in Tautvaišienė et al. (2004)

iron. A strong La and Eu overabundance is also noticeable in their results.

Along with the Sgr dSph main body stars described in chapter 4, we also observed three giants in Terzan 7 (see also Sbordone et al. 2004b). One of the stars of Tautvaišienė et al. (2004) has also been observed by us although with a slightly different instrumental setting. Here we present a methodologically coherent analysis of all the five Terzan 7 stars observed at high resolution, looking in particular for the presence of a “family signature” linking Terzan 7 with the Sgr dSph and the other globular clusters associated to the system (Sbordone et al., 2005a).

5.2 Observations and data reduction

The five stars studied in this paper have all been observed at the VLT/UVES high resolution spectrograph. Their coordinates, photometry and atmospheric parameters are listed in Table 5.1.

The first three stars (# 1272, # 1515, # 1282) have been observed in the course of our programme in dichroic 1 (DIC1) mode during the same session devoted to the Sgr dSph main body described in chapter 4. Both blue and red arm were used, but only red arm data is presented here. The integration time was 3600 s on each star, splitted into two 1800 s exposures. The pipeline extracted, radial velocity corrected spectra have been coadded to reach a S/N \simeq 50 at 600 nm, increasing at longer wavelengths.

The spectra for the three stars described in Tautvaišienė et al. (2004) have been retrieved from the ESO archive. They are dichroic 2 spectra (DIC2), with both blue and red arm data (blue chip 375 to 500 nm, red CCD mosaic 593 to 960 nm). Each star received a single 3600 s exposure. We have extracted the spectra by means of the UVES pipeline, obtaining a S/N of about 70 at 600 nm. Blue DIC 2 chip has not been in fact used: some lines in that wavelength range were initially included in the linelist, but in metal rich, low gravity stars that area of the spectrum is subject to such crowding that proper continuum estimate was exceedingly difficult.

A sample of the spectra is shown in Fig. 5.1. The star identified as S34 in Tautvaišienė et al. (2004) is star # 1282 and has also been observed independently by us.

For Terzan 7 stars, abundances have been determined for the same species examined in the Sgr dSph main body, but, due to the different wavelength coverage of DIC2, stars # 1665 # 1798 lack Mn, Cu, Zn, Ba, Ce and Nd measurements. Also, Cr I has been measured instead of Cr II. The lines employed are essentially the same used in chapter 4 for # 1515 and # 1272, while a completely different linelist has been prepared for stars # 1665 and # 1708, due to the different spectral coverage. Star # 1282, having both DIC1 and DIC2 spectra available, had the two linelists merged. For this star, in the (sporadic) case of a line being measured in both spectra, the mean of the two EWs has been used. The lines employed, the atomic data used and the abundances derived are listed in tables 5.2 to 5.4

5.3 Abundance analysis

The analysis method is essentially identical to the one described for Sgr dSph main body stars in section 4.3, with only minor differences. First, we used the Alonso et al. (1999) calibration for (B-V) color instead than the (V-I) one employed in the case of Sgr dSph, since we had B and V photometry. This calibration, at variance with the (V-I) one, is mildly dependent on metallicity. We thus used the Tautvaišienė et al. (2004) metallicity as a first guess, computed the temperatures, derived the iron content and recomputed the metallicity: the variation was of the order of few degrees, absolutely negligible.

Tautvaišienė et al. (2004) used a different approach to T_{eff} determination and relied on an excitation temperature, nevertheless their estimates result

Table 5.2: Iron lines for the five Terzan 7 stars. For other elements see tables 5.3 and 5.4, please refer to table 4.12 for the reference of the log gf sources.

Ion	λ (nm)	log gf	source of log gf (see notes)	EW (pm) 1272	ϵ	EW (pm) 1282	ϵ	EW (pm) 1515	ϵ	EW (pm) 1665	ϵ	EW (pm) 1708	ϵ
Fe I	466.1535	-1.270	FMW	–	–	4.21	6.68	–	–	6.53	7.07	–	–
Fe I	479.4354	-4.050	FMW	–	–	5.90	6.94	–	–	6.25	6.77	–	–
Fe I	484.9668	-2.680	FMW	–	–	–	–	–	–	–	–	–	–
Fe I	489.2859	-1.290	FMW	7.11	6.923	7.15	6.82	6.51	6.90	–	–	–	–
Fe I	489.6439	-2.050	FMW	–	–	7.20	7.15	–	–	7.80	7.16	–	–
Fe I	491.8013	-1.360	FMW	–	–	6.41	6.75	–	–	6.77	6.73	–	–
Fe I	510.9652	-0.980	FMW	8.24	6.94	–	–	8.24	7.03	–	–	–	–
Fe I	552.5544	-1.330	FMW	7.32	6.95	8.05	6.99	6.66	6.93	–	–	–	–
Fe I	585.6087	-1.640	FMW	4.11	6.71	5.84	6.96	4.20	6.84	–	–	–	–
Fe I	585.8779	-2.260	FMW	2.26	6.84	3.55	7.05	1.95	6.86	–	–	–	–
Fe I	586.1109	-2.450	FMW	1.44	6.87	–	–	–	–	–	–	–	–
Fe I	587.7794	-2.230	FMW	–	–	–	–	3.24	7.09	–	–	–	–
Fe I	588.3817	-1.360	FMW	7.83	6.71	9.72	6.98	7.89	6.85	–	–	–	–
Fe I	595.2717	-1.440	FMW	–	–	9.04	6.95	–	–	8.37	6.70	9.59	6.98
Fe I	601.2210	-4.200	FMW	–	–	8.38	7.14	–	–	–	–	7.83	6.99
Fe I	601.5245	-4.680	FMW	–	–	–	–	–	–	–	–	3.44	6.76
Fe I	601.9366	-3.360	FMW	–	–	–	–	–	–	3.09	7.05	1.93	6.92
Fe I	602.4058	-0.120	FMW	–	–	11.97	6.95	–	–	11.65	6.82	11.97	6.86
Fe I	602.7051	-1.210	FMW	–	–	9.66	6.96	–	–	10.18	6.95	9.66	6.87
Fe I	605.6005	-0.460	FMW	–	–	7.92	6.74	–	–	8.29	6.76	9.24	6.92
Fe I	607.9008	-1.120	FMW	–	–	6.07	6.94	–	–	–	–	7.02	7.06
Fe I	609.6663	-1.930	FMW	–	–	6.65	6.96	–	–	7.28	6.97	6.79	6.94
Fe I	610.5128	-2.050	FMW	–	–	2.28	6.99	–	–	3.19	7.11	2.38	6.99
Fe I	612.0246	-5.950	FMW	–	–	–	–	–	–	–	–	6.37	6.67
Fe I	615.1616	-3.299	FMW	10.45	6.75	–	–	9.99	6.85	–	–	–	–
Fe I	615.9375	-1.970	FMW	–	–	–	–	–	–	–	–	2.93	7.11
Fe I	616.5360	-1.550	FMW	6.11	6.78	7.06	6.87	6.24	6.92	8.08	6.96	7.26	6.85
Fe I	618.7989	-1.720	FMW	6.77	6.81	8.20	6.98	–	–	8.64	6.95	7.72	6.83
Fe I	622.6734	-2.220	FMW	–	–	6.21	7.03	–	–	7.19	7.09	6.31	7.00
Fe I	649.6465	-0.570	FMW	7.25	6.836	6.99	6.73	7.39	6.97	–	–	7.49	6.76
Fe I	651.8366	-2.750	FMW	–	–	11.40	7.02	–	–	13.03	7.10	10.42	6.77
Fe I	659.7559	-1.070	FMW	–	–	5.86	7.02	–	–	6.54	7.10	5.99	7.00
Fe I	670.3565	-3.160	FMW	7.81	6.83	9.42	6.95	8.20	7.07	–	–	–	–
Fe I	672.5356	-2.300	FMW	–	–	4.39	7.06	–	–	5.29	7.11	–	–
Fe I	673.9521	-4.950	FMW	–	–	8.63	6.90	–	–	10.55	6.91	–	–
Fe I	674.6954	-4.350	FMW	–	–	3.42	6.92	–	–	4.84	6.94	3.52	6.92
Fe I	679.3258	-2.470	FMW	–	–	3.78	7.08	–	–	3.97	7.01	2.77	6.86
Fe I	684.2685	-1.320	FMW	–	–	6.36	7.14	–	–	6.71	7.14	6.12	7.05
Fe I	684.3655	-0.930	FMW	–	–	8.33	6.98	–	–	8.74	6.99	8.40	6.93
Fe I	685.7250	-2.150	FMW	–	–	–	–	–	–	–	–	4.10	6.79
Fe I	686.2492	-1.570	FMW	–	–	5.15	7.06	–	–	5.92	7.13	4.90	6.98
Fe I	691.6680	-1.450	FMW	–	–	8.68	7.02	–	–	10.25	7.20	8.96	7.00
Fe I	697.6922	-1.850	FMW	–	–	2.44	6.85	–	–	3.71	7.04	2.72	6.89
Fe I	698.8524	-3.660	FMW	–	–	–	–	–	–	12.04	7.12	10.40	7.02
Fe I	702.2952	-1.250	FMW	–	–	9.64	7.04	–	–	10.62	7.11	8.96	6.84
Fe I	706.9531	-4.340	FMW	–	–	4.00	6.93	–	–	5.03	6.87	–	–
Fe I	721.9682	-1.690	FMW	–	–	8.16	7.05	–	–	9.27	7.14	8.74	7.08
Fe I	747.6375	-1.680	FMW	–	–	2.71	7.00	–	–	–	–	3.73	7.17
Fe I	749.8530	-2.250	FMW	–	–	3.87	6.94	–	–	5.50	7.12	4.23	6.97
Fe I	758.3787	-1.990	FMW	–	–	14.44	6.90	–	–	15.74	6.90	15.71	7.00
Fe I	794.1087	-2.580	FMW	–	–	9.04	6.91	–	–	10.19	6.92	9.24	6.87
Fe I	883.8427	-1.980	FMW	–	–	17.12	6.92	–	–	–	–	18.18	6.97
Fe II	483.3197	-4.780	FMW	2.22	6.84	–	–	–	–	–	–	–	–
Fe II	499.3358	-3.650	FMW	–	–	6.27	7.12	4.65	6.88	–	–	–	–
Fe II	510.0664	-4.370	FMW	3.54	6.96	–	–	–	–	–	–	–	–
Fe II	513.2669	-4.180	FMW	–	–	3.50	7.01	3.01	7.01	–	–	–	–
Fe II	525.6937	-4.250	K88	3.08	6.82	2.90	7.03	–	–	–	–	–	–
Fe II	526.4812	-3.190	FMW	5.71	6.79	4.55	6.81	4.56	6.90	–	–	–	–
Fe II	599.1376	-3.557	K88	–	–	3.23	6.80	–	–	3.90	7.04	3.91	6.85
Fe II	608.4111	-3.808	K88	–	–	2.74	6.98	–	–	2.23	6.87	–	–
Fe II	614.9258	-2.724	K88	–	–	3.16	6.86	2.75	6.79	3.58	7.10	4.17	7.00
Fe II	624.7557	-2.329	K88	–	–	4.50	6.83	–	–	4.32	6.92	5.80	6.98
Fe II	636.9462	-4.253	K88	–	–	2.28	6.92	–	–	2.43	7.01	2.84	6.97
Fe II	643.2680	-3.500	H92	–	–	4.60	6.76	–	–	4.50	7.02	–	–
Fe II	645.6383	-2.075	K88	–	–	5.87	6.91	–	–	4.90	6.84	–	–
Fe II	651.6080	-3.380	H92	–	–	6.08	6.95	–	–	5.65	7.02	6.81	7.02

Table 5.3: Other elements lines for the five stars (see also tab. 5.2, 5.4). For the three Sulphur lines, in each star equal abundances are given for all the lines, since they have been fitted together (see 5.3.1).

Ion	λ (nm)	log gf	source of log gf	EW (pm) 1272	ϵ	EW (pm) 1282	ϵ	EW (pm) 1515	ϵ	EW (pm) 1665	ϵ	EW (pm) 1708	ϵ
O I	630.0304	-9.717	STZ	syn	8.17	syn	8.22	syn	-	syn	8.20	syn	8.24
Na I	498.2814	-0.950	KP	6.21	5.32	7.92	5.36	5.81	5.26	-	-	-	-
Na I	615.4227	-1.560	KP	2.75	5.28	3.50	5.22	2.98	5.35	4.87	5.22	2.60	5.08
Na I	616.0747	-1.260	KP	4.36	5.27	5.67	5.26	4.43	5.30	8.02	5.36	4.81	5.16
Mg I	552.8405	-0.522	GC	20.79	6.88	22.72	6.86	-	-	-	-	-	-
Mg I	571.1087	-1.729	GC	12.14	7.03	12.75	6.96	12.37	7.12	-	-	-	-
Mg I	631.8716	-1.945	GC	2.89	6.68	-	-	3.81	6.91	-	-	4.49	6.88
Mg I	631.9237	-2.165	GC	3.04	6.93	3.30	6.91	2.79	6.93	3.54	6.92	3.31	6.90
Mg I	738.7689	-1.020	KP	-	-	-	-	-	-	4.81	6.82	-	-
Mg I	871.7825	-0.772	GC	-	-	5.40	6.85	-	-	6.41	7.10	4.76	6.73
Mg I	892.3568	-1.659	GC	-	-	4.28	6.84	-	-	-	-	-	-
Al I	669.6022	-1.347	NBS	3.41	5.44	4.64	5.46	-	-	5.98	5.45	4.33	5.43
Al I	669.8673	-1.647	NBS	3.03	5.66	3.00	5.48	2.90	5.66	3.67	5.40	-	-
Si I	594.8541	-1.230	GARZ	-	-	7.32	7.04	8.15	7.23	-	-	-	-
Si I	612.5021	-1.540	ED	3.49	7.16	3.05	7.19	2.76	7.15	-	-	-	-
Si I	613.1852	-1.140	KP	-	-	-	-	-	-	3.68	7.02	-	-
Si I	614.2482	-1.480	ED	2.37	6.87	1.97	6.88	2.70	7.10	1.97	6.92	-	-
Si I	614.5015	-1.430	ED	2.05	6.73	-	-	2.85	7.08	2.17	6.93	-	-
Si I	615.5134	-0.770	ED	5.99	6.89	6.30	7.09	6.43	7.12	5.60	7.06	-	-
Si I	703.4902	-0.880	GARZ	-	-	4.22	7.14	-	-	-	-	5.05	7.22
Si I	725.0627	-1.042	SG	-	-	-	-	-	-	3.45	6.90	3.84	6.83
Si I	727.5292	-1.003	SG	-	-	4.07	6.90	-	-	4.79	7.14	3.99	6.82
Si I	728.9176	-0.197	SG	-	-	-	-	-	-	7.36	6.81	7.96	6.71
Si I	793.2349	-0.470	GARZ	-	-	5.33	7.05	-	-	-	-	5.67	7.03
Si I	874.2446	-0.630	KP	-	-	6.17	7.20	-	-	5.51	7.21	6.88	7.23
S I	921.2863	0.420	NBS	-	-	syn	6.62	-	-	syn	6.62	syn	6.59
S I	922.8093	0.260	NBS	-	-	syn	6.62	-	-	syn	6.62	syn	6.59
S I	923.7538	0.040	NBS	-	-	syn	6.62	-	-	syn	6.62	syn	6.59
Ca I	551.2980	-0.447	SR	11.00	5.90	11.72	5.72	9.85	5.69	-	-	-	-
Ca I	585.7451	0.240	SR	14.37	5.76	-	-	14.75	5.83	-	-	-	-
Ca I	586.7562	-1.490	GC	4.87	5.79	4.73	5.54	4.71	5.78	-	-	-	-
Ca I	616.1296	-1.266	SR	10.22	5.98	-	-	-	-	-	-	-	-
Ca I	616.6438	-1.142	SR	-	-	12.19	5.87	10.97	6.05	13.90	5.90	-	-
Ca I	616.9042	-0.797	SR	12.91	6.05	13.46	5.76	11.89	5.88	15.87	5.93	13.23	5.68
Ca I	643.9075	0.390	SR	18.79	5.80	21.41	5.73	18.69	5.76	-	-	20.87	5.64
Ca I	645.5597	-1.290	SR	-	-	10.88	5.75	9.57	5.90	11.94	5.63	10.31	5.63
Ca I	649.3781	-0.109	SR	16.15	5.87	17.72	5.72	15.70	5.84	19.39	5.71	17.09	5.57
Ca I	649.9650	-0.818	SR	12.17	5.87	13.96	5.81	12.22	5.94	15.41	5.77	13.59	5.70
Sc II	552.6790	0.130	MFV	10.45	2.15	11.21	2.30	10.23	2.43	-	-	-	-
Sc II	624.5637	-0.980	NBS	6.76	2.14	7.90	2.39	6.04	2.36	8.86	2.34	8.76	2.44
Sc II	632.0852	-1.770	NBS	2.69	2.16	3.35	2.39	2.49	2.46	3.70	2.26	2.46	2.14
Ti I	488.5078	0.358	MFV	-	-	-	-	10.72	4.46	-	-	-	-
Ti I	491.5229	-1.019	MFV	5.14	4.58	-	-	4.06	4.44	8.68	4.45	5.49	4.30
Ti I	499.7096	-2.118	MFV	11.51	4.35	14.81	4.58	11.41	4.48	-	-	-	-
Ti I	508.7058	-0.780	MFV	9.36	4.53	-	-	9.19	4.57	-	-	-	-
Ti I	586.6450	-0.840	MFV	11.85	4.37	15.65	4.57	12.41	4.61	-	-	-	-
Ti I	606.4626	-1.944	MFV	-	-	9.61	4.50	-	-	13.38	4.70	9.79	4.53
Ti I	609.2792	-1.379	MFV	-	-	4.73	4.40	-	-	6.88	4.31	3.81	4.28
Ti I	612.6215	-1.425	MFV	9.80	4.52	13.75	4.71	9.32	4.56	-	-	-	-
Ti I	631.2236	-1.552	MFV	-	-	7.91	4.41	-	-	10.52	4.36	6.76	4.27
Ti I	633.6098	-1.743	MFV	-	-	7.34	4.50	-	-	10.38	4.52	6.98	4.47
Ti I	655.6061	-1.074	MFV	-	-	12.51	4.62	-	-	16.40	4.86	10.88	4.35
Ti I	659.9105	-2.085	MFV	-	-	-	-	-	-	15.41	4.83	9.88	4.38
Ti I	686.1447	-0.740	MFV	-	-	4.95	4.27	-	-	7.42	4.25	5.03	4.31
Ti I	718.8565	-1.760	MFV	-	-	7.04	4.37	-	-	-	-	5.73	4.22
Ti I	744.0578	-0.700	MFV	-	-	5.15	4.20	-	-	-	-	4.88	4.19
Ti I	802.4843	-1.140	MFV	-	-	-	-	-	-	-	-	7.61	4.42
Ti I	835.3161	-2.677	MFV	-	-	9.82	4.61	-	-	14.72	4.75	7.99	4.42
Ti I	867.5372	-1.669	MFV	-	-	14.80	4.58	-	-	-	-	14.29	4.49
Ti I	868.2980	-1.941	MFV	-	-	11.91	4.46	-	-	17.32	4.72	11.89	4.46
Ti I	869.2331	-2.295	MFV	-	-	10.48	4.63	-	-	-	-	10.25	4.61
Ti I	873.4712	-2.384	MFV	-	-	9.15	4.56	-	-	14.40	4.74	8.18	4.47
V I	573.7059	-0.740	MFV	7.92	3.56	-	-	6.78	3.45	-	-	-	-
V I	613.5361	-0.746	MFV	6.88	3.32	10.01	3.38	6.63	3.38	13.32	3.50	9.12	3.23
V I	653.1414	-0.840	MFV	4.20	3.18	7.81	3.32	5.37	3.45	11.05	3.36	6.62	3.17

Table 5.4: Other elements lines for the five stars (see also tab. 5.2, 5.3)

Ion	λ (nm)	log gf	source of log gf	EW (pm) 1272	ϵ	EW (pm) 1282	ϵ	EW (pm) 1515	ϵ	EW (pm) 1665	ϵ	EW (pm) 1708	ϵ
Cr I	633.0090	-2.920	MFW	9.45	4.97	12.41	4.99	8.77	4.98	16.05	5.24	–	–
Cr I	663.0010	-3.560	MFW	5.23	5.02	8.22	5.05	4.95	5.06	11.23	5.05	7.40	4.95
Cr I	735.5960	-0.285	MFW	–	–	12.62	5.09	–	–	15.26	5.22	13.02	5.12
Mn I	511.79**	-1.140	MFW	HFS	4.47	HFS	4.58	HFS	4.45	–	–	–	–
Co I	533.17**	-6.473	K88	HFS	4.19	HFS	4.28	HFS	4.32	–	–	–	–
Co I	553.07**	-2.060	FMW	HFS	4.02	HFS	4.35	HFS	4.27	–	–	–	–
Co I	609.34**	-4.568	K88	–	–	HFS	4.16	HFS	4.15	HFS	4.10	HFS	4.01
Ni I	493.5830	-0.350	FMW	–	–	7.40	5.49	–	–	–	–	7.33	5.40
Ni I	585.7746	-0.636	K88	4.37	5.43	5.36	5.61	4.47	5.60	–	–	–	–
Ni I	600.7306	-3.330	FMW	–	–	8.42	5.48	–	–	–	–	9.12	5.54
Ni I	608.6276	-0.530	FMW	–	–	4.01	5.37	–	–	4.67	5.45	4.83	5.48
Ni I	611.1065	-0.870	FMW	–	–	–	–	–	–	–	–	3.47	5.33
Ni I	612.8963	-3.330	FMW	–	–	9.04	5.58	6.28	5.44	–	–	–	–
Ni I	613.0130	-0.960	FMW	1.43	5.16	–	–	2.25	5.55	–	–	–	–
Ni I	617.5360	-0.530	FMW	5.01	5.33	5.32	5.39	5.35	5.55	5.34	5.33	5.93	5.44
Ni I	617.6807	-0.260	WL	6.42	5.33	7.04	5.44	6.77	5.56	–	–	–	–
Ni I	617.7236	-3.500	FMW	4.99	5.37	5.66	5.36	4.96	5.57	7.39	5.41	–	–
Ni I	618.6708	-0.960	FMW	–	–	–	–	–	–	–	–	3.30	5.41
Ni I	620.4600	-1.100	WL	–	–	2.46	5.38	–	–	2.84	5.39	2.83	5.43
Ni I	632.7592	-3.150	FMW	–	–	–	–	–	–	–	–	11.26	5.69
Ni I	648.2796	-2.630	FMW	–	–	10.77	5.51	–	–	12.10	5.51	10.99	5.46
Ni I	658.6307	-2.810	FMW	–	–	–	–	–	–	12.39	5.76	11.33	5.72
Ni I	659.8592	-0.980	FMW	–	–	–	–	–	–	–	–	2.88	5.50
Ni I	677.2313	-0.980	FMW	–	–	6.62	5.47	–	–	7.12	5.47	7.59	5.57
Ni I	700.1534	-3.660	FMW	–	–	–	–	–	–	–	–	5.49	5.55
Ni I	706.2951	-3.500	FMW	–	–	5.77	5.50	–	–	7.98	5.61	6.18	5.52
Ni I	778.8936	-2.420	FMW	–	–	–	–	–	–	–	–	14.92	5.71
Cu I	510.55**	-1.516	BIEL	HFS	3.14	HFS	2.91	HFS	3.22	–	–	–	–
Zn I	481.0528	-0.170	BG	6.20	3.39	7.83	3.88	6.94	3.81	–	–	–	–
Y II	488.3683	0.070	HL	–	–	–	–	9.58	1.64	–	–	–	–
Y II	498.2130	-1.290	HL	3.91	1.27	5.79	1.66	4.81	1.79	–	–	–	–
Y II	508.7417	-0.170	HL	7.63	1.02	8.56	1.18	8.51	1.57	–	–	–	–
Y II	511.9113	-1.360	HL	3.74	1.24	3.93	1.31	3.06	1.44	–	–	–	–
Y II	679.5413	-1.190	CC	–	–	1.72	1.54	–	–	3.48	1.79	1.67	1.47
Ba II	649.6897	-0.377	NBS	17.99	1.81	21.05	2.01	18.53	2.09	–	–	21.01	1.90
La II	480.4039	-1.500	LA	4.65	0.93	5.69	1.08	4.39	1.22	–	–	–	–
La II	511.4558	-1.030	LA	–	–	9.77	1.45	–	–	–	–	–	–
La II	632.0377	-1.610	ABH	4.89	0.87	7.14	1.21	3.71	1.00	9.46	1.27	6.21	0.98
La II	639.0477	-1.410	LA	4.33	0.75	5.07	0.86	3.78	1.00	7.31	0.90	4.95	0.78
Ce II	518.7457	0.130	H	4.19	1.14	5.53	1.41	4.84	1.62	–	–	–	–
Ce II	533.0556	-0.360	H	2.98	0.92	4.00	1.13	3.59	1.40	–	–	–	–
Nd II	491.4382	-0.700	HA	6.39	1.15	8.90	1.61	6.15	1.44	–	–	–	–
Nd II	496.1387	-0.710	MC'	5.26	1.22	7.25	1.58	5.83	1.69	–	–	–	–
Nd II	498.9950	-0.500	MC'	–	–	10.13	2.03	7.26	1.82	–	–	–	–
Nd II	499.8540	-1.100	MC'	3.36	1.00	4.96	1.28	3.20	1.31	–	–	–	–
Nd II	508.9832	-1.160	MC'	4.42	0.93	5.96	1.15	4.77	1.35	–	–	–	–
Nd II	543.1515	-0.470	HA	2.87	1.05	3.54	1.22	2.19	1.23	–	–	–	–
Nd II	548.5097	-1.640	HA	–	–	3.28	1.57	–	–	–	–	–	–
Eu II	644.50**	0.120	LAW	HFS	0.04	HFS	0.34	HFS	0.64	HFS	0.34	HFS	0.21

in good agreement our T_{eff} 's, differing at most of 50K.

As in the case of Sgr dSph, we estimated surface gravity from isochrones and then adjusted it to match the iron ionization equilibrium. This led to marginal changes to the isochrones gravities, with the notable exception of star 1272 that, with magnitude and color very near to star 1515, has a gravity coherent with stars (like for example 1282) which are almost 0.5 mags brighter in V, and 0.15 mags redder in (B-V). For star 1272 $\log g \sim 0.7$ lower than the one suggested by the isochrones. At the moment we lack an explanation for this. The easiest explanation would be some kind of error in the photometry affecting more the V magnitude than the B one. This may have fortuitously kept the star along its isochrone. We can also speculate that star # 1272 may be a long period variable. We will also see in section 5.4 that this star shows also a metallicity slightly differing from the one of the other 4 stars, a fact suggestive of the possibility that something wrong may exist in its parameters. We will look deeper into the problem.

For one star, # 1665, significant inconsistencies emerged between the abundances computed with WIDTH and the corresponding synthetic spectra computed with SYNTH. Examination of the results showed that this was due to the fact that SYNTH read as input a model in which the elemental abundances had been changed according to the results of WIDTH, whereas WIDTH read a copy of the model in which all abundances were solar scaled. This is common practice in abundance analysis using ODF-based model atmospheres: one computes a model-atmosphere with a given ODF and the corresponding set of abundances, then with this model atmosphere one computes the detailed line transfer (with SYNTH, WIDTH or similar codes), varying the elemental abundances until a match is found between computed and observed spectra/EWs. This practice is legitimate inasmuch the abundance variation from the set assumed in the model computation have little or no influence on the model structure. While this true for trace elements it is in general not true for α elements, as pointed out by Bonifacio & Caffau (2003). Indeed, both the WIDTH and SYNTH suite, upon reading the input model atmosphere and abundances, compute the number densities of atomic species at all depths. Thus while a change in Fe abundance will have a negligible effect on the model structure, a change in Mg abundance will result in a change in the model ionization structure, since Mg is the main electron donor. It must be stressed that in such cases the results obtained by computing synthetic spectra from a model computed with a *different* chemical composition are inconsistent. On the other hand in the

cases in which e.g. a computation of abundance with WIDTH, yields the same result both when solar scaled abundances are used as input (and thus in the computation of number densities) and when the abundances so derived are used as input, it is justified to assume that the abundance of the given element has no significant effect on the model structure.

This is indeed the case for all the stars in our sample *except* star # 1665. For this star we computed an ad-hoc opacity sampling model with observed abundances by using ATLAS 12 (Kurucz, 1993). In figure 5.2 we show the temperature and ionization structure for models appropriate for star # 1665 in three cases:

1. ATLAS 12 opacity sampling model with abundances given in Table 5.5;
2. ATLAS 9 ODF-based model with solar scaled abundances;
3. ATLAS 9 ODF-based model with abundances given in Table 5.5.

It is obvious that changing the abundances in the ATLAS 9 model alters the ionization structure, which is, however, different from the one consistently computed with ATLAS 12 when all the final abundances are taken into account during the model computation. The process is clearly iterative, one starts from abundances derived from a model with solar-scaled abundances, then uses these to compute an ATLAS 12 model and determines new abundances, to be used for a new ATLAS 12 model, and so on, until the derived abundances coincide with the abundances used in the model computation. In our case two iterations were sufficient. We want to stress that the need for computing an ATLAS 12 model for this star is due to its extremely low gravity, nevertheless, the derived abundances appear in reassuring concordance with the ones derived for the other stars.

5.3.1 Sulphur abundances

As repeatedly stated above, the most commonly measured α elements in stars are O, Mg, Si, Ca and Ti. This is essentially due to the fact that these elements present a good number of suitable transitions in their optical spectra (with the exception of O). It is thus customary to assume that these elements may act as “proxies” for the other α elements, although both theoretical (e.g. Lanfranchi & Matteucci, 2003) and observational (Venn et al., 2004) hints exist that α elements may not vary in lockstep. Sulphur is one of

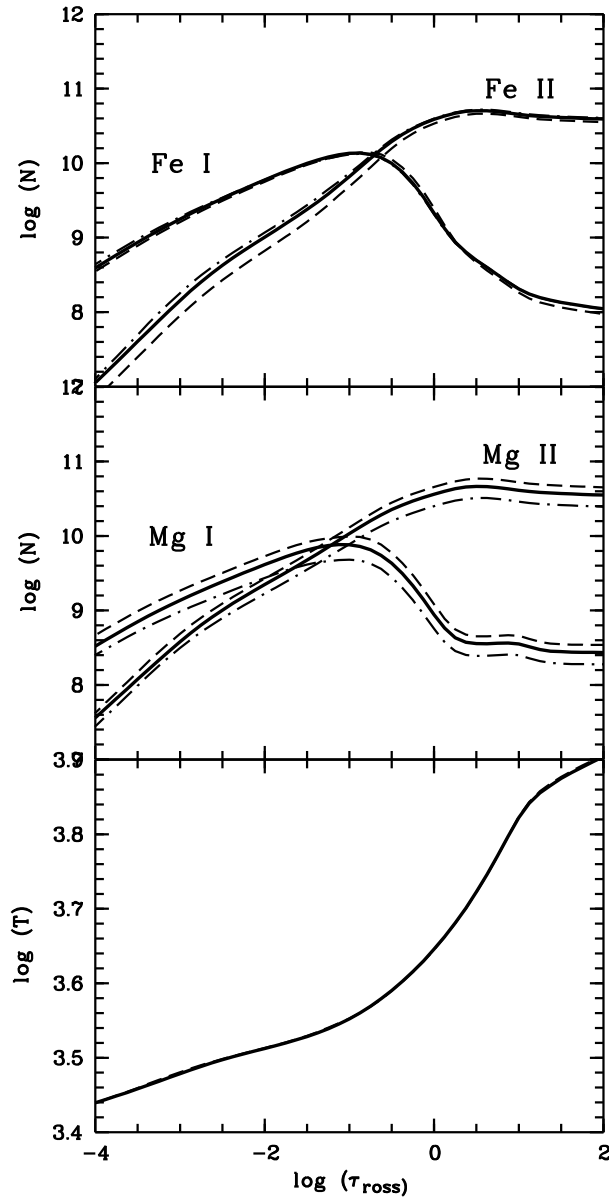


Figure 5.2: Atmospheric models for star # 1665. All models correspond to $T_{eff} = 3945$ K $\log g = 0.70$. The solid lines refer to an opacity sampling ATLAS 12 model with abundances as provided in table 5.5. The dashed lines refer to an ATLAS 9 model computed with a solar-scaled ODF with $[M/H] = -0.5$ and a microturbulence of 1 km s^{-1} . The dash-dotted lines refer to the ionization structure of the above ATLAS 9 model computed by WIDTH when the abundances of table 5.5 are provided as input. The top panel shows the Fe I and Fe II ions, the middle panel the Mg I and Mg II ions, while the bottom panel displays the temperature structure of the model. The neutral ions show a peak in number densities around $\log \tau_{ross} \sim -1.5$.

the α elements most rarely measured in galactic stars (and up to now never measured in extragalactic stars), but is frequently measured in HII regions (Garnett, 1989; Torres-Peimbert et al., 1989), in the warm ISM (Savage & Sembach, 1996), and in external Blue Compact Galaxies (Garnett, 1989; Izotov & Thuan, 1999) and DLAs (Centuri3n et al., 2000). One of its big advantages in ISM measurements, in comparison with other α elements, is that S is not affected by dust depletion (Savage & Sembach, 1996). This makes the comparison between ISM and stellar measurements potentially misleading, similarly to the Zinc - Iron one described in 4.4.4.

We were able (see Caffau et al., 2005b) to measure Sulphur abundances in three of our Terzan 7 stars, namely the ones for which DIC 2 spectra were available (# 1282, # 1665 and # 1708). In this setting, the S I multiplet 1 (921.2, 922.8, 923.8 nm) is within the observed range. A fast rotator spectrum was used to identify and subtract the superimposed telluric features. The 922.8 nm feature was not blended with telluric lines, thus allowing to check the success of the subtraction procedure. Due to the low temperature and gravity of these stars, some significant contamination from CN features may exist in the spectrum. The 923.8 nm line is, in fact, blended with a relatively strong CN line, while for the other two lines of the multiplet the CN absorption affects the continuum placement. The main problem in taking into account the CN contamination arises from the fact that neither element has been measured in these stars. Therefore, we first fitted the CN abundance in the 921.2 - 923.8 nm region, then used the best fitting CN abundance to compute the synthetic spectra used to fit the S abundance. The fits have been performed by χ^2 minimization, in the same way employed in Caffau et al. (2005a).

The associated errors have been estimated by means of a Monte Carlo simulation, performed only on the star # 1282, due to the similarity of the parameters of the three stars. Sets of synthetic spectra have been prepared by injecting noise so that S/N=50, each set comprising 10000 events. The simulated spectra (with $T_{eff}=4203$ K, $\log g=1.30$, $\xi=1.60$ kms $^{-1}$, $[Fe/H]=-0.54$ and $[Si/Fe]=0.01$) are fitted as they were observed spectra, and the standard deviation from the mean fitted abundance is taken as error estimate. The synthetic spectra used in the fitting have either equal T_{eff} , $\log g$ or ξ as the input spectrum, to estimate the random error due to the noise, or different atmospheric parameters to estimate the joint effect of noise and systematic errors in the atmospheric parameters estimate. A random error of 0.04 dex is derived. A change of 0.2 dex in metallicity induces a variation

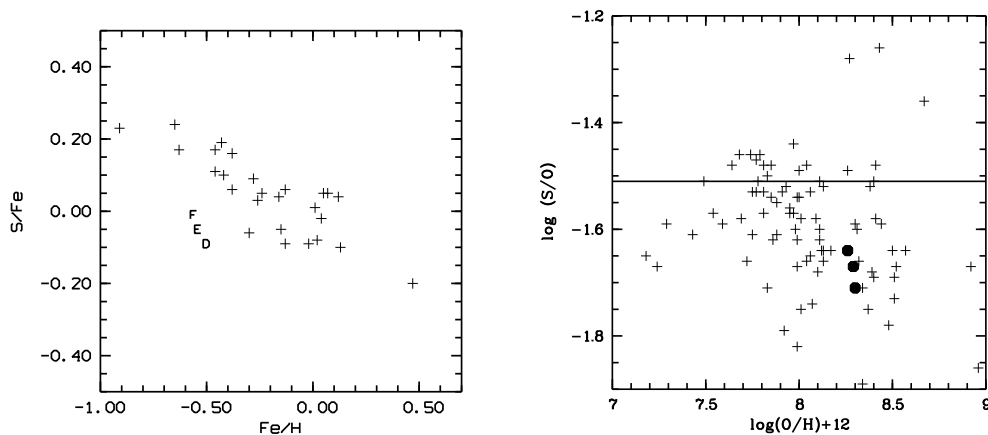


Figure 5.3: On the left, $[S/Fe]$ vs. $[Fe/H]$ for the three stars of Terzan 7 and the sample of galactic stars of Ecuivillon et al. (2004). The three stars are indicated by letters: # 1665 is D, # 1282 is E and # 1708 is F. On the right, S/O vs. Oxygen content for the three Terzan 7 stars and for the galactic and extragalactic HII regions from the samples of Garnett (1989) and Izotov & Thuan (1999). The solid line represents the solar value, where $A(S)_{\odot}=7.21$ (Lodders, 2003) and $A(O)_{\odot}=8.72$ (Asplund et al., 2004a).

of about 0.1 dex in Sulphur abundance; a variation of $\log g$ of ± 0.5 dex leads to a variation of ± 0.18 dex in $A(S)$; a variation in of ± 100 K in T_{eff} changes $A(S)$ of ∓ 0.18 dex.

In figure 5.4 the best fitting synthesis for the 922.8 nm line in the three stars is presented. The derived $[S/Fe]$ versus $[Fe/H]$ is displayed in fig. 5.3, left panel. $[S/Fe]$ appears to be essentially solar, thus significantly lower than the sample of galactic stars of Ecuivillon et al. (2004). This is coherent with the behavior of the other α elements measured in Terzan 7 and in Sgr dSph.

We also compared (see fig. 5.3, right panel) this result with the S/O values derived by Garnett (1989) and Izotov & Thuan (1999) for galactic and extragalactic HII regions. Here the three Terzan 7 stars show slightly undersolar S/O values, coherent with the bulk of the HII regions, although a large scatter in their S/O values can be observed. It is nevertheless interesting to notice how most of the sampled HII regions show subsolar S/O values. Of course, this result is strongly dependent from the still somewhat uncertain solar O content: this prevalence of undersolar values was not apparent in the previous works on the HII regions, where the “old” Anders & Grevesse

5.3. ABUND.

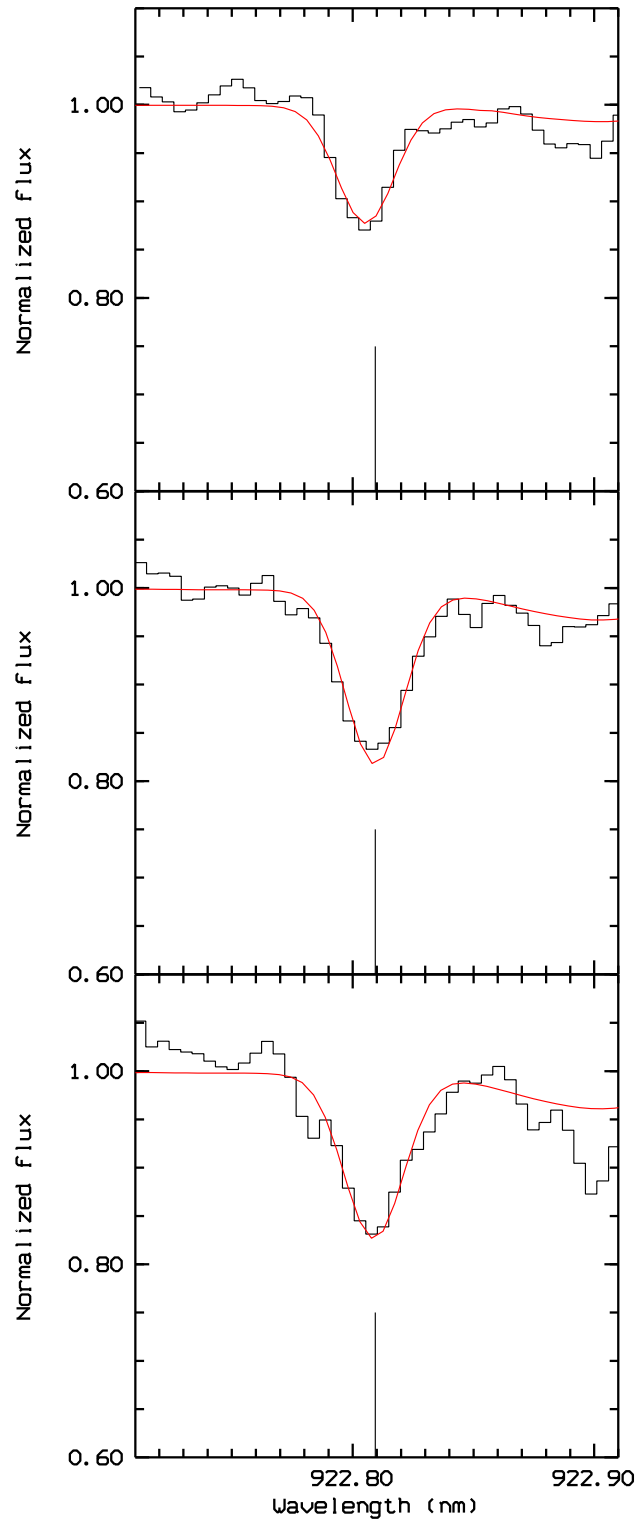


Figure 5.4: Best fit of the 922.8 nm S I line for the stars # 1665, # 1282 and # 1708 (top to bottom). This is the only of the three line to be not contaminated by telluric or CN features.

(1989) value of $A(O)_{\odot}=8.93$ was adopted.

The success of this measurement suggests that it should be possible to derive S abundances from multiplet 1 lines, at least down to $[S/H]\sim-1.5$, for stars in globular clusters and LG galaxies.

5.4 Results

Abundances for the five Terzan 7 stars are listed in table 5.5, the ratios against iron are presented in table 5.6. The same ratios against iron are compared with the corresponding Sgr dSph results in figures 5.5 through 5.8. As can be clearly see, the correspondence between Sgr dSph and Terzan 7 abundances is total, and no significant distinction can be made: as happened in the case of Palomar 12 (see section 4.4.6), Terzan 7 stars appear totally indistinguishable from the ones in Sgr dSph main body. The only minor difference can be seen in a slightly smaller Europium enhancement, but it has to be remembered that most Terzan 7 stars have much lower gravity than the one characteristic of the Sgr dSph sample, and Eu is sensitive to ionization (thus gravity) being observed in the ionized form. Moreover, the modeling of stars of such a low gravity naturally presents larger than average uncertainties, as the case of star # 1665 (albeit extreme) suggests. so we are not inclined to put too much weight on this single discrepancy.

Interestingly, Barium abundance in Terzan 7 stars is high, and no star joins the “low barium” subsample found in Sgr dSph. This is in agreement with the similar result found in Palomar 12 by Cohen (2004). This leads to consider the “low barium” stars in Sgr dSph as some kind of exception, and to think that the typical Sgr dSph population indeed has enhanced barium with no significant trend with metallicity.

Our iron abundances appear to be in very good agreement with the results in Tautvaišienė et al. (2004), leading to a mean value of $[Fe/H]\sim-0.6$. Our analysis provides $[Mg/Fe]= -0.12$ for star # 1665 and -0.10 for # 1708, coherent with the values we found for the first three stars. However this is significantly at odds with the Tautvaišienė et al. (2004) results. Left aside the case of star # 1665 due to its very low gravity and temperature, mean Mg and Ti abundances in Tautvaišienė et al. (2004) are about 0.25 dex higher than ours, while their Si abundance is 0.17 dex *lower* than the one we obtain.

Other elements are also at odd, as can also be seen from the figures 5.5 to 5.8: Aluminum, for example, is about .28 dex more abundant in Tautvaišienė

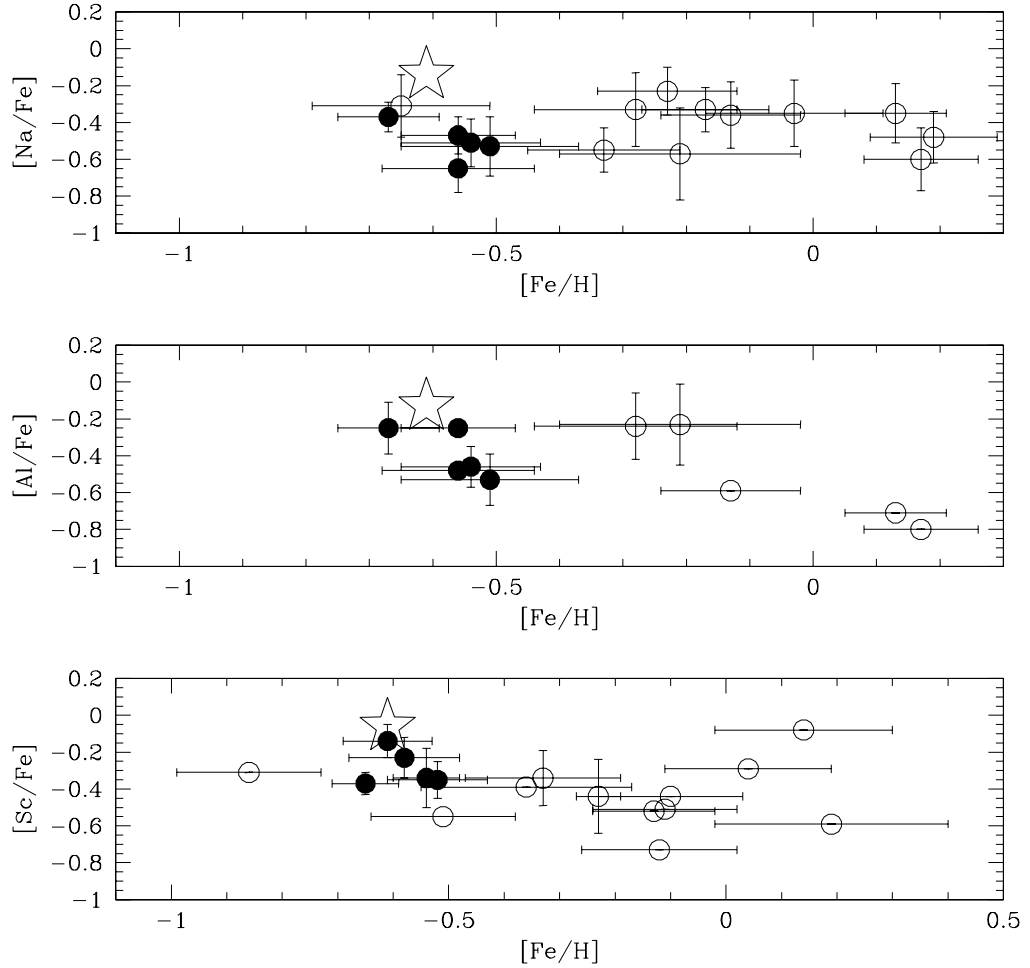


Figure 5.5: $[X/Fe]$ against $[Fe/H]$ for the light odd atomic number elements in Terzan 7 (filled dots), compared to the ones presented in chapter 4 for Sgr dSph main body (open dots). Also, for comparison we include the mean value of the three stars from Tautvaišienė et al. (2004) (large open star). As usual, ratios against Fe I are presented for neutral species, while for ionized species the comparison is made against Fe II.

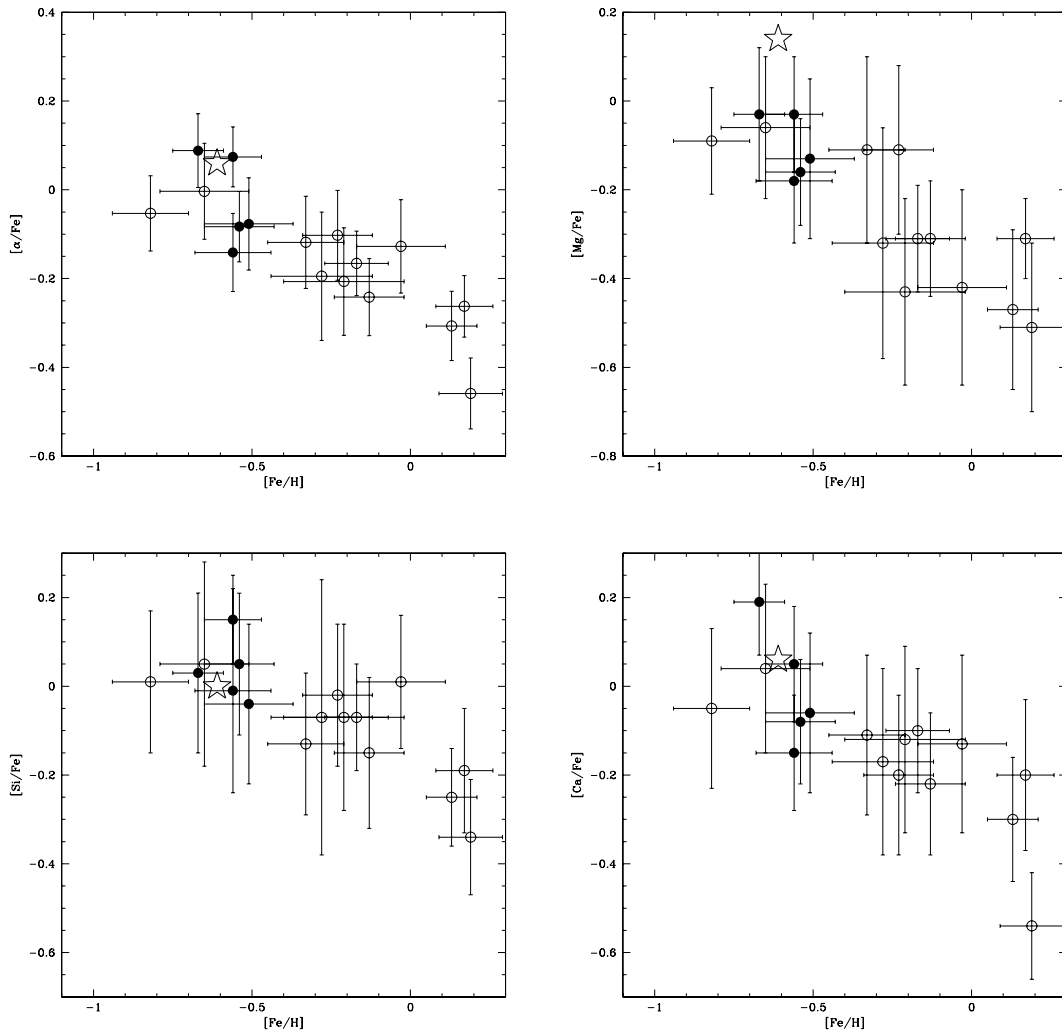


Figure 5.6: As in figure 5.5 but now for mean α elements and Mg, Si and Ca: this figure resembles directly fig. 4.6.

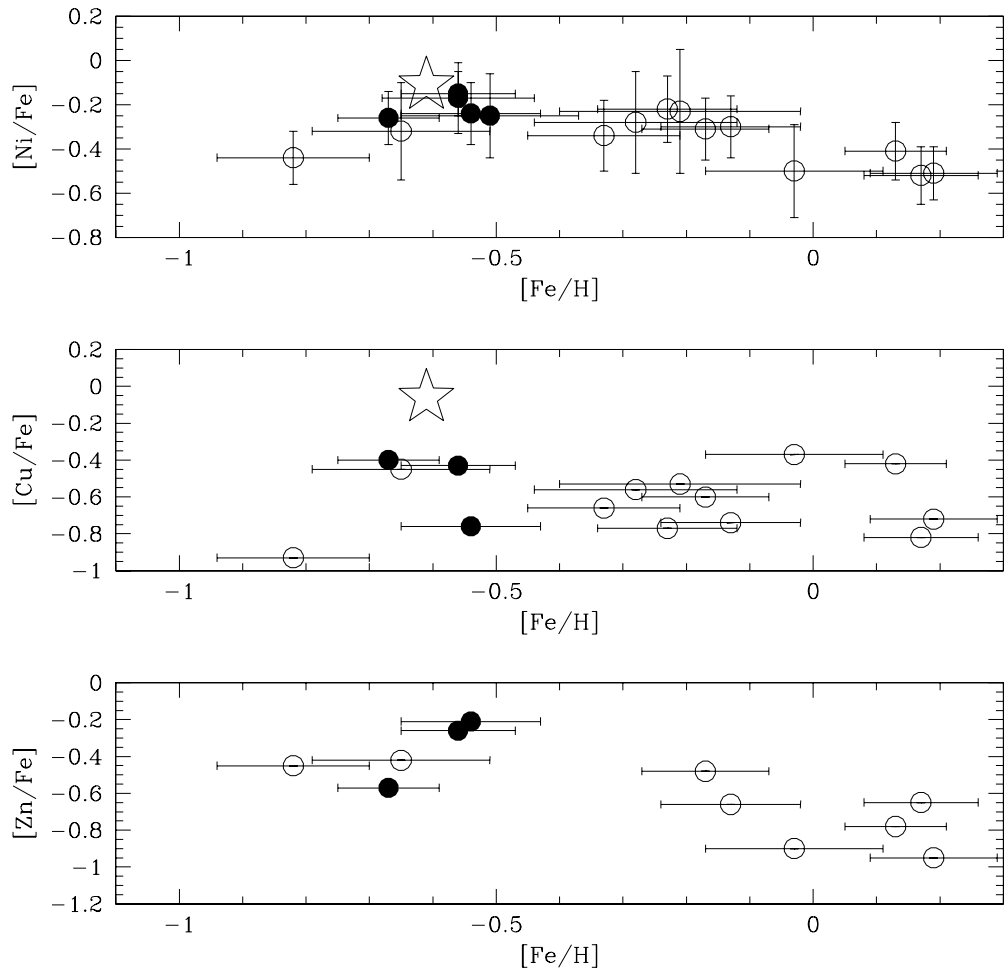


Figure 5.7: As in figure 5.5 but now for Fe-peak elements Ni, Cu and Zn.

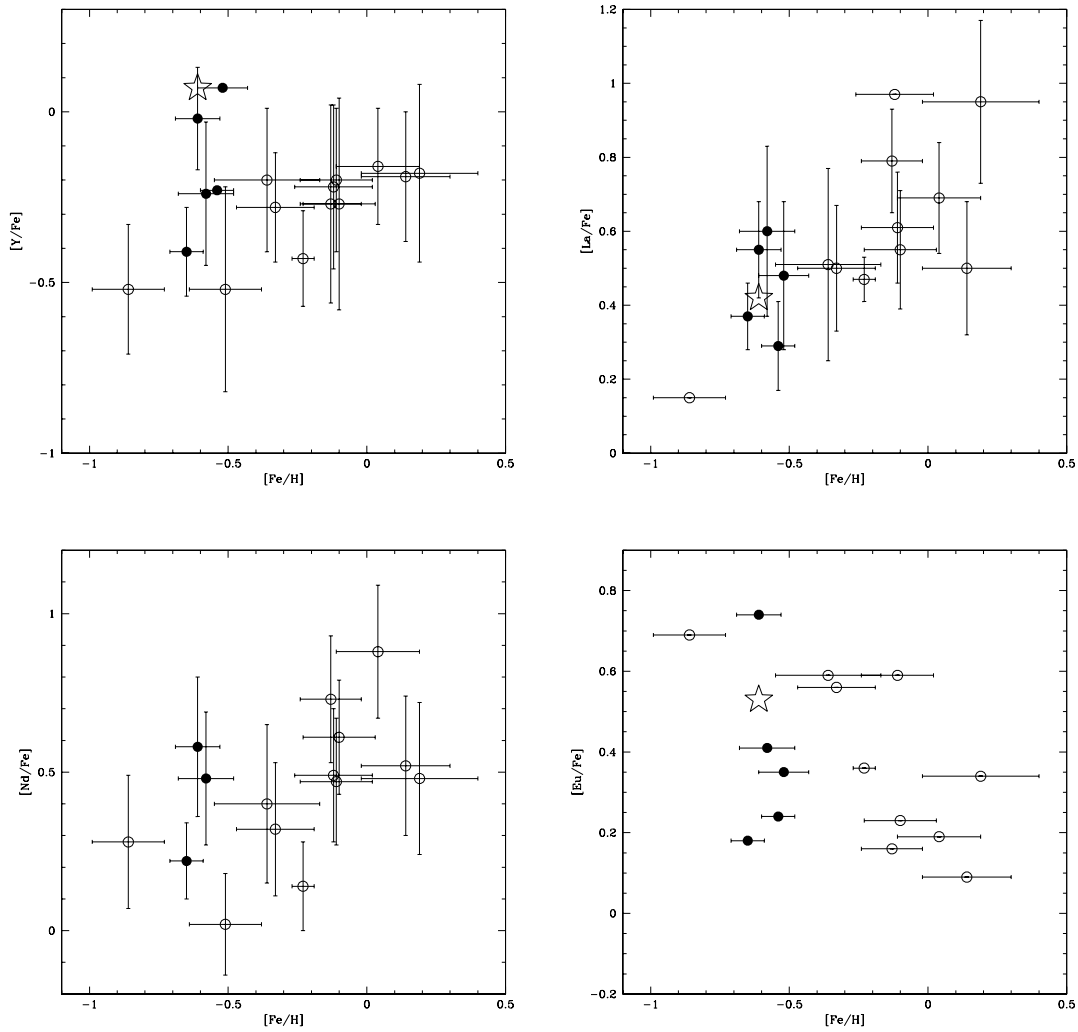


Figure 5.8: As in figure 5.5 but now for heavy n-capture elements Y, La, Nd and Eu.

Table 5.5: Abundances for the Terzan 7 stars, and assumed solar abundances.

Ion	solar ab.	Ab. 1272	σ	Ab. 1282	σ	Ab. 1515	σ	Ab. 1665	σ	Ab. 1708	σ
O I	8.72	8.17	–	8.22	–	–	–	8.20	–	8.24	–
Na I	6.33	5.29	0.02	5.28	0.06	5.30	0.04	5.29	0.07	5.12	0.04
Mg I	7.58	6.88	0.13	6.88	0.05	6.99	0.09	6.94	0.12	6.84	0.08
Al I	6.47	5.55	0.11	5.47	0.01	5.66	–	5.43	0.02	5.43	–
Si I	7.55	6.91	0.16	7.06	0.11	7.14	0.05	7.00	0.12	6.98	0.20
S I	7.21	–	–	6.62	0.04	–	–	6.62	0.04	6.59	0.04
Ca I	6.36	5.88	0.09	5.74	0.09	5.85	0.10	5.79	0.11	5.65	0.05
Sc II	3.17	2.15	0.01	2.36	0.04	2.42	0.04	2.30	0.04	2.29	0.15
Ti I	5.02	4.47	0.09	4.50	0.13	4.52	0.07	4.59	0.21	4.39	0.11
V I	4.00	3.35	0.16	3.35	0.03	3.43	0.04	3.43	0.07	3.20	0.03
Cr II	5.67	4.99	0.02	5.05	0.04	5.02	0.04	5.17	0.08	5.03	0.09
Mn I	5.39	4.47	–	4.58	–	4.45	–	–	–	–	–
Fe I	7.50	6.83	0.08	6.96	0.11	6.94	0.09	6.99	0.14	6.94	0.12
Fe II	7.50	6.85	0.06	6.92	0.10	6.89	0.08	6.98	0.09	6.96	0.06
Co I	4.92	4.11	0.12	4.27	0.09	4.25	0.09	4.10	–	4.01	–
Ni I	6.25	5.32	0.09	5.47	0.08	5.54	0.05	5.49	0.13	5.52	0.11
Cu I	4.21	3.14	–	2.91	–	3.22	–	–	–	–	–
Zn I	4.60	3.39	–	3.88	–	3.81	–	–	–	–	–
Y II	2.24	1.18	0.11	1.42	0.19	1.61	0.13	1.79	–	1.47	–
Ba II	2.13	1.81	–	2.01	–	2.09	–	–	–	1.90	–
La II	1.13	0.85	0.07	1.15	0.21	1.07	0.10	1.09	0.18	0.88	0.10
Ce II	1.58	1.03	0.11	1.27	0.14	1.51	0.11	–	–	–	–
Nd II	1.50	1.07	0.10	1.40	0.19	1.47	0.21	–	–	–	–
Eu II	0.51	0.04	–	0.34	–	0.64	–	0.34	–	0.21	–

et al. (2004), Scandium is about .18 dex more abundant, an Copper, in the only star in common where we measure it (# 1282), is about .50 dex more abundant according to Tautvaišienė et al. (2004) measurements.

The three stars in common testify that no significant offset is introduced by the different T_{eff} calibration methods. The (almost) identical gravities derived starting with (almost) identical iron abundances lead to infer that little difference should exist between the structure of our ATLAS model and of the MARCS ones used in Tautvaišienė et al. (2004). A comparison of EWs for lines in common suggests that there is no significant offset in EW measurements either: a linear regression provides slope of about 1 and no significant offset with an RMS which is of the order of our measurement error (a graphical comparison of our EW measurements with the ones of Tautvaišienė et al. (2004) is presented in fig. 5.9). Therefore probably the cause of this discrepancy resides in the choice of lines used and atomic data.

It is worth noticing that Tautvaišienė et al. (2004) analysis, at variance with our, is *differential*: once chosen a set of atomic data, *ad hoc* solar

Table 5.6: Ratios against Iron for the Terzan 7 stars. $[X/FeI]$ is used for neutral ions, $[X/FeII]$ for the ionized ones. For Fe I and Fe II $[FeI/H]$ and $[FeII/H]$ is presented.

Ion	$[X/Fe]$ 1272	σ	$[X/Fe]$ 1282	σ	$[X/Fe]$ 1515	σ	$[X/Fe]$ 1665	σ	$[X/Fe]$ 1708	σ
O I	0.10	–	0.08	–	–	–	0.00	–	0.06	–
Na I	-0.37	0.08	-0.51	0.13	-0.47	0.10	-0.53	0.16	-0.65	0.13
Mg I	-0.03	0.15	-0.16	0.12	-0.03	0.13	-0.13	0.18	-0.18	0.14
Al I	-0.25	0.14	-0.46	0.11	-0.25	–	-0.53	0.14	-0.48	–
Si I	0.03	0.18	0.05	0.16	0.15	0.10	-0.04	0.18	-0.01	0.23
S I	–	–	-0.05	0.12	–	–	-0.08	0.15	-0.06	0.13
Ca I	0.19	0.12	-0.08	0.14	0.05	0.13	-0.06	0.18	-0.15	0.13
Sc II	-0.37	0.06	-0.23	0.11	-0.14	0.09	-0.35	0.10	-0.34	0.16
Ti I	0.12	0.12	0.02	0.17	0.06	0.11	0.08	0.25	-0.07	0.16
V I	0.02	0.18	-0.11	0.11	-0.01	0.10	-0.06	0.16	-0.24	0.12
Cr II	-0.03	0.06	-0.04	0.11	-0.04	0.09	0.02	0.12	-0.10	0.11
Mn I	-0.25	–	-0.27	–	-0.38	–	–	–	–	–
Fe I	-0.67	0.08	-0.54	0.11	-0.56	0.09	-0.51	0.14	-0.56	0.12
Fe II	-0.65	0.06	-0.58	0.10	-0.61	0.08	-0.52	0.09	-0.54	0.06
Co I	-0.14	0.14	-0.11	0.14	-0.11	0.13	-0.31	–	-0.35	–
Ni I	-0.26	0.12	-0.24	0.14	-0.15	0.10	-0.25	0.19	-0.17	0.16
Cu I	-0.40	–	-0.76	–	-0.43	–	–	–	–	–
Zn I	-0.54	–	-0.18	–	-0.23	–	–	–	–	–
Y II	-0.41	0.13	-0.24	0.21	-0.02	0.15	0.07	–	-0.23	–
Ba II	0.33	–	0.46	–	0.57	–	–	–	0.31	–
La II	0.37	0.09	0.60	0.23	0.55	0.13	0.48	0.20	0.29	0.12
Ce II	0.10	0.13	0.27	0.17	0.54	0.14	–	–	–	–
Nd II	0.22	0.12	0.48	0.21	0.58	0.22	–	–	–	–
Eu II	0.18	–	0.41	–	0.74	–	0.35	–	0.24	–

abundances were calculated with this atomic data set, and then used to determine the $[X/H]$ ratio for the program stars, on which the same lines had been measured and the same atomic data set used to derive the abundances. Since Tautvaišienė et al. (2004) do not publish the solar abundances they used to calculate their published $[X/H]$ ratios, we cannot verify whether some of these discrepancies are due to offsets in the sets of solar abundances, i.e. in atomic line data.

5.5 Conclusions

Since we do not detect any significant difference between Sgr dSph and Terzan 7 abundances, there's not much left to say *specifically* about Terzan 7.

Terzan 7 apparently evolved from Sgr dSph enriched gas of which inher-

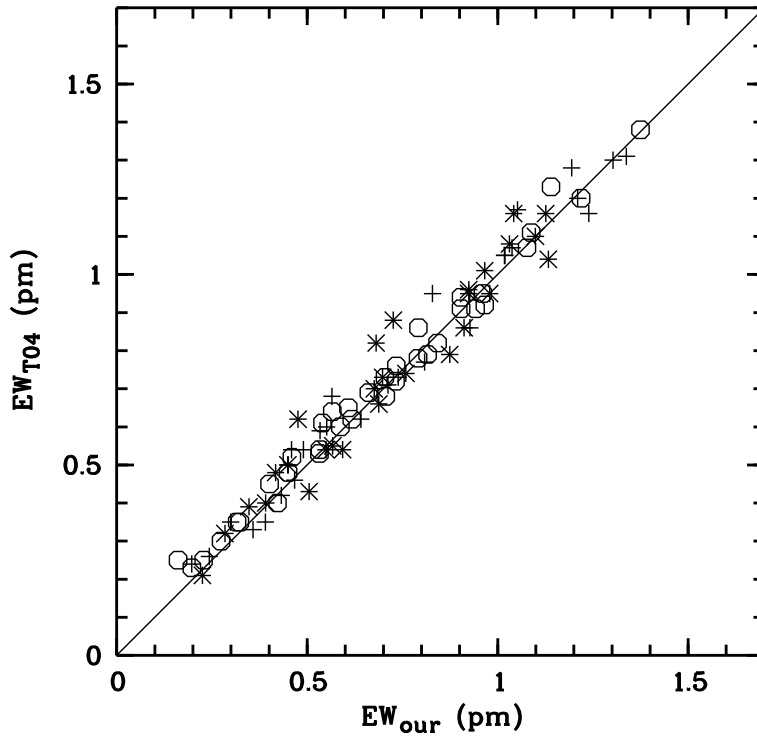


Figure 5.9: Comparison of our measured EWs with the ones of Tautvaišienė et al. (2004), for Fe, Mg, Si and Ca lines. Open hexagons refer to star 1282, crosses to star 1665, asterisks star 1708. The line is not a fit, but simply the bisector.

ited the entire abundance pattern without showing any sign of self-pollution (not surprising, given its small mass). Together with the aforementioned Palomar 12 case, this goes to show how clearly defined can be the “Sgr signature” in a population originated inside this galaxy.

Perhaps the most puzzling (and interesting) consequence of our results, regarding Terzan 7, is that apparently Sgr dSph, while forming its main population (which has essentially the same iron content as Terzan 7), was still an environment where a globular cluster (albeit a low mass one) could form.

Chapter 6

The Canis Major overdensity

6.1 Introduction

Since its discovery, Sgr dSph has been considered to be the nearest dwarf galaxy. In the subsequent years wide field surveys discovered many tidal structures in the halo of the MW, the most well known of them being the one variously known as “Monoceros ring” (Newberg et al., 2002), “ring” Ibata et al. (2003), and GASS (Galactic Anticenter Stellar Structure, Crane et al., 2003; Frinchaboy et al., 2004).

Recently Martin et al. (2004a) claimed the discovery of the core of a tidally disrupted dwarf galaxy, still recognizable as an overdensity in the external Galactic disc in Canis Major (Canis Major Overdensity or CMa from now on). In a subsequent paper (Bellazzini et al., 2004) they recognized the same population also in the background of the Galactic open cluster NGC 2477 at $\simeq 13^\circ$ from the CMA center. The authors situate the structure at about 7 Kpc from the Sun and about 16 Kpc from the Galactic Center, and estimate a mass of about $10^7 M_\odot$, which would make it the nearest known external galaxy. Martin et al. (2004a) inferred from dynamical similarities that CMa should be related with the GASS, and also inferred a link with some Galactic GC, among others NGC 2808. Shortly afterward, Momany et al. (2004) questioned the effective existence and size of CMa, claiming that the anomaly could be explained, to a large extent, by properly taking into account the Galactic disc warp, which is maximum in the CMa direction. Bellazzini et al. (2004) examined and rejected this hypothesis, and so did Martin et al. (2004b), deriving for the center of the structure a radial velocity

Table 6.1: Photometry and physical parameters for the three stars.

Star	α (J2000.0) hms	δ °, ', ''	V mag	$(V-I)_0$ mag	T_{eff} K	$\log g$ cgs	[Fe/H] dex	ξ kms $^{-1}$	V_{rad} kms $^{-1}$
EIS 6631	07 51 36.2	-38 31 10	16.35	0.75	5367	3.5	+0.15	1.80	135.4
EIS 7873	07 52 37.1	-38 28 01	16.26	0.89	4990	2.3	-0.42	1.80	111.1
EIS 30077	07 51 41.0	-38 38 39	16.51	0.89	4994	2.8	-0.04	1.45	97.0

of 109 kms $^{-1}$, with a low velocity dispersion of 13 kms $^{-1}$, both difficult to reconcile with the dynamics of the local disc.

6.2 Observations and data reduction

Shortly after the announcement of the discovery of CMa, we obtained Director's Discretionary Time (DDT) (program 272-B.5017) at VLT-FLAMES with the aim of probing the dynamics and chemical composition of the newly discovered structure. Bellazzini et al. (2004) detected the CMa population in the background of NGC 2477 using the EIS pre-FLAMES photometry and astrometry of Momany et al. (2001) which is publicly available. We therefore observed this field selecting in the EIS photometry Red Giant/Clump stars possible CMa members (Sbordone et al., 2005b). The target selections in the EIS (ESO Imaging Survey) CMD of the NGC 2477 area are plotted in fig. 6.1.

Observations were performed between January and March 2004 and consisted of 4×3045 seconds exposures, using the HR09 (centered at 515 nm) setting for the 114 GIRAFFE targets, providing a typical S/N of about 30, adequate for our abundance analysis needs. The standard setting centered at 580 nm has been used for the seven UVES fibers.

The analysis procedure was different between the GIRAFFE and the UVES stars. For the GIRAFFE fibers, the radial velocities for all the targets were determined by autocorrelation against a template synthetic spectrum. Subsequently, the radial velocity corrected spectra have been coadded and their metallicity derived by using the automatic code developed by Bonifacio & Caffau (2003), in the same fashion described in 4.5.

The pipeline extracted spectra of the seven UVES stars have been corrected to heliocentric radial velocity and then coadded. Given the very low

Table 6.2: Abundances and assumed solar abundances for the three likely CMa members.

Ion	solar ab.	Ab. 6631	σ	Ab. 7873	σ	Ab. 30077	σ
Na I	6.33	6.66	0.14	6.09	0.03	6.19	0.07
Mg I	7.58	7.24	0.01	6.98	0.21	7.53	0.07
Al I	6.47	6.41	0.08	5.91	0.08	6.19	0.04
Si I	7.55	7.49	0.08	7.23	0.05	7.24	0.10
Ca I	6.36	6.29	0.12	5.96	0.12	6.24	0.12
Sc II	3.17	3.26	–	2.52	0.06	2.90	0.18
Ti I	5.02	5.35	0.12	4.58	0.10	5.11	0.10
V I	4.00	4.48	0.16	3.89	0.06	4.45	0.06
Mn I	5.39	5.52	–	4.84	–	5.46	–
Fe I	7.50	7.65	0.11	7.08	0.10	7.46	0.13
Fe II	7.50	7.62	0.17	7.13	0.13	7.43	0.08
Co I	4.92	5.32	0.18	4.33	–	4.94	0.03
Ni I	6.25	6.42	0.14	5.74	0.16	6.00	0.08
Cu I	4.21	4.61	–	–	–	4.40	–
Y II	2.24	2.55	0.12	1.72	0.01	1.56	0.10
Ba II	2.13	2.46	–	2.13	–	2.13	–
La II	1.13	1.86	0.17	1.02	0.05	1.73	0.06
Ce II	1.58	2.29	0.02	1.14	–	1.40	0.13
Nd II	1.50	2.21	0.10	1.12	0.13	1.79	0.10
Eu II	0.51	0.84	–	0.34	–	0.54	–

S/N, they have been convolved with a 5 km s^{-1} FWHM gaussian, thus degrading the resolution to about 33000, but raising the S/N to about 40 per pixel at 580 nm.

During this phase we came to reject two stars from the UVES sample (EIS 4383 and EIS 31581), showing near-to-zero radial velocity (the CMa overdensity is supposed to show a radial velocity of about 130 km s^{-1} , see 6.4 or fig. 6.11).

6.3 UVES stars abundance analysis

The rest of the analysis was at all similar to the ones described in chapters 4 and 5 for Sgr dSph and Terzan 7. Equivalent widths have been measured (by means of IRAF task `splot`) for lines of Na I, Mg I, Al I, Si I, Ca I, Sc

Table 6.3: Abundance ratios for the three stars. $[X/Fe I]$ is used for neutral elements, $[X/Fe II]$ for ionized species, and $[Fe/H]$ for Fe I and Fe II. For Fe I and Fe II, $[FeI/H]$ and $[FeII/H]$ are presented.

Ion	$[X/Fe]$ 6631	σ	$[X/Fe]$ 7873	σ	$[X/Fe]$ 30077	σ
Na I	0.18	0.18	0.18	0.10	-0.10	0.15
Mg I	-0.49	0.11	-0.18	0.23	-0.01	0.15
Al I	-0.21	0.14	-0.14	0.13	-0.24	0.14
Si I	-0.21	0.14	0.10	0.11	-0.27	0.16
Ca I	-0.22	0.16	0.02	0.16	-0.08	0.18
Sc II	-0.03	–	-0.28	0.14	-0.20	0.20
Ti I	0.18	0.16	-0.02	0.14	0.13	0.16
V I	0.33	0.19	0.31	0.12	0.49	0.14
Mn I	-0.02	0.11	-0.12	–	0.12	–
Fe I	0.15	0.12	-0.42	0.10	-0.04	0.13
Fe II	0.12	0.24	-0.37	0.13	-0.07	0.08
Co I	0.25	0.21	-0.17	–	0.06	0.13
Ni I	0.02	0.18	-0.09	0.19	-0.21	0.15
Cu I	0.25	–	–	–	0.23	–
Y II	0.19	0.21	-0.15	0.13	-0.61	0.13
Ba II	0.21	–	0.37	–	0.07	–
La II	0.61	0.24	0.26	0.14	0.67	0.10
Ce II	0.59	0.17	-0.07	–	-0.11	0.15
Nd II	0.59	0.20	-0.01	0.18	0.36	0.13
Eu II	0.21	–	0.20	–	0.10	–

II, Ti I, V I, Cr I, Mn I¹, Fe I, Fe II, Ni I, Y II, Ba II, La II, Ce II and Nd II. The linelist used was obtained by merging the DIC1 linelist used in Sgr dSph main body stars and the DIC2 linelist used for Terzan 7 stars (for the lines falling inside the DIC1 range). Details are provided in tables 6.5 through 6.7. With respect to Sbordone et al. (2005b), new log gf values have employed for the Ce II lines.

In this phase we noticed that lines in the star EIS 7873 appear somewhat broader than the instrumental resolution. The low S/N does not allow to investigate the problem much further.

Effective temperatures were determined by using the Alonso et al. (1999) calibration for $(V-I)_0$; $E(V-I)$ color excesses were derived from Schlegel et al.

¹We employed the same Mn I line (511.7 nm) already measured in Sgr dSph and Terzan 7. Nevertheless, we used here the simple EW measurement instead of a HFS spectral synthesis, due to the poor quality of the line in the CMa stars. We consequently warn that the Mn measurement should be considered as significantly uncertain in these stars.

(1998) absorption maps, as corrected by Bonifacio et al. (2000b).

The same models and procedures already described in 4.3 were employed here: initial gravities were determined from isochrones, then corrected to enforce iron ionization equilibrium. In this phase, two more stars (EIS 2812 and EIS 5429) proved to be dwarfs ($\log g > 4.0$), and thus incompatible with a heliocentric distance of the order of 7 Kpc. The coordinates, photometry and atmospheric parameters for the three remaining stars are detailed in Table 6.1, which provides also heliocentric radial velocities.

Atmosphere models have been calculated by using ATLAS 9, and abundances derived from EWs by means of WIDTH. For species Co I, Cu I and Eu II, which employed lines are affected by HFS, synthetic spectra have been computed by using SYNTHE. The derived mean abundances are listed in table 6.2, while the ratios against iron are showed in 6.3

Some of the resulting abundances are presented in fig. 6.3 through 6.6. differently from what we saw in Sgr dSph and Terzan 7, we do not seem to have a strictly coherent picture here. The three stars are all significantly metal rich.

EIS 6631, the most metal rich, shows significant α elements depletion together with a strong overabundance of some s-process affected n-capture elements (Ba, La, Ce, Nd). Conversely, Eu shows only poor enhancement, which should be considered not significant, given the fact that Eu II 664.5 nm is very weak on this (relatively) high gravity star. Also significantly enhanced appear to be V, Co and Cu. Cu in particular is interesting: although based on a single line, its enhancement is clear and the line fit (presented in fig. 6.7) appears clean.

EIS 7873, conversely, the most metal poor of the three stars, shows no significant α elements depletion. V, Ba, La and Ce appear somewhat enhanced, but Ce abundance is based on a single, weak line and has to be considered not too reliable.

EIS 30077 appears more similar to EIS 6631, although somewhat less “extreme”: slight α elements depletion, significant Cu enhancement, important overabundance of n-capture elements. Nevertheless, it also shows some peculiarities, most notably a strong underabundance of Y.

To interpret these abundances we will find useful the broader view provided by the GIRAFFE stars.

6.4 GIRAFFE results: metallicity and V_{rad}

About 20% of the GIRAFFE targets were classified by the abundance analysis code as foreground dwarfs, and consequently removed from the sample. An histogram of the observed metallicities in the sample is shown in fig. 6.8. It appears to have two peaks, at $[\text{Fe}/\text{H}]=-0.4$ and $[\text{Fe}/\text{H}]=-0.7$. The higher metallicity peak is probably due to local thick disk stars (as can be seen, the galactic component of the model peaks at $[\text{Fe}/\text{H}]=-0.4$), while the one at $[\text{Fe}/\text{H}]=-0.7$ is likely due to CMa: only less than 50% of the observed stars at that metallicity are actually predicted by the model. Also absent from the model are the two objects at $[\text{Fe}/\text{H}]=-2.0$.

In figure 6.9 the distribution in V_{rad} is presented. Here, an overdensity with respect to the model above 90 km s^{-1} is striking, and only 50% or less of the observed stars above 125 km s^{-1} is accounted for by the model. This is in fairly good agreement with the Martin et al. (2004b) estimation of a $V_{rad} \sim 110 \text{ km s}^{-1}$ in the center of CMa. However, the second peak claimed by Martin et al. (2004b) is likely due to foreground dwarf stars: as can be seen in fig. 6.9, the dwarfs we previously removed from our sample appear to have a velocity distribution peaked at about 40 km s^{-1} .

In fig. 6.10 we show the combined radial velocity-metallicity distribution for the sample giants, together with the isodense curves of the distribution predicted by the Besancon model. As we can see, most of the GIRAFFE stars fall within the Besancon predictions, but a clear overdensity exist above $V_{rad}=120 \text{ km s}^{-1}$: we can tentatively center it at $V_{rad}=132 \text{ km s}^{-1}$, with $\sigma=12 \text{ km s}^{-1}$ (on a sample of 20 stars). It's interesting to notice that this structure has a very extended metallicity spread, containing bot the most metal rich of the UVES stars (EIS 6631, the most metal rich of the sample in fact, with $[\text{Fe}/\text{H}]=0.2$) and the most metal poor of the GIRAFFE targets, at $[\text{Fe}/\text{H}]=-2.0$. Even here, a residual contamination should exist and can be estimated to be around 30%.

Finally we plot (fig. 6.11) the aforementioned overdensity in the V_{rad} vs. galactic longitude plane. In the figure one can see our (putative) CMa identification in the background of NGC 2477 along with a sample of globular and open clusters, and the Yanny et al. (2003) measurements of the radial velocity of the Monoceros ring, and the CMa center measures from Martin et al. (2004b). As can be clearly seen from fig. 6.11, our putative overdensity lies within the locus of a galactic component in circular motion at 220 km s^{-1} at a distance of 16 Kpc from the galactic center, and appear most likely

linked to the Monoceros ring.

6.5 Discussion

The above section showed that an unexplained structure appear clearly to exist in the background of NGC 2477, but shows also that, of the three stars forming our UVES sample, only one falls within the $1-\sigma$ interval of our (tentative) identification of the CMa structure. Actually, all the three stars fall within $3-\sigma$, but, of course, the likelihood of being interlopers increases.

In order to see whether the chemical abundances of these three stars show any differences from Galactic stars let us compare with the large sample compiled by Venn et al. (2004). This catalog contains also a probability of each star to belong to the Halo, Thick disc or Thin disc. We selected only stars for which the population membership probability exceeds 85%. The mean values and dispersion for some significant abundance ratios are given in Table 6.4.

Table 6.4: Abundance ratios in different Galactic components, from Venn et al. (2004).

	(1)	(2)	(3)	(4)	(5)
N	16	11	35	31	4
$[\alpha/\text{Fe}]$	0.14	0.06	0.06	0.02	0.08
$[\alpha/\text{Fe}]_\sigma$	0.09	0.03	0.04	0.03	0.05
$[\text{Na}/\text{Fe}]$	0.06	0.03	0.05	0.00	–
$[\text{Na}/\text{Fe}]_\sigma$	0.04	0.08	0.04	0.07	–
$[\text{Y}/\text{Fe}]$	0.00 ^a	–0.11 ^b	0.11 ^c	0.04	–0.06
$[\text{Y}/\text{Fe}]_\sigma$	0.24	0.14	0.58	0.10	0.03

(1) Thick disc $-0.5 \leq [\text{Fe}/\text{H}] < -0.2$

(2) Thick disc $-0.2 \leq [\text{Fe}/\text{H}]$

(3) Thin disc $-0.5 \leq [\text{Fe}/\text{H}] < -0.2$

(4) Thin disc $-0.2 \leq [\text{Fe}/\text{H}]$

(5) Halo $-0.5 \leq [\text{Fe}/\text{H}]$

^a 8 stars; ^b 5 stars; ^c 28 stars

From this comparison we may see that star EIS 7873 appears to be indistinguishable from Galactic stars of similar metallicity. In this regime the three components are very similar, differing from each other by not more than 1σ . EIS 30077 and EIS 6631, instead, display a significant underenhancement of α elements (except for Ti) and a significant enhancement over the solar values of La, Ce and Nd. Unfortunately there is very little data available on these elements for Galactic stars in this metallicity regime. The situation is better for Y, for this element EIS 6631 shows $[Y/Fe] \approx 0$, while EIS 30077 shows a strong deficiency $[Y/Fe] \approx -0.6$; note that also Galactic stars display a large scatter in Y abundances. EIS 6631 and EIS 30077 display another remarkable abundance anomaly: a significant overabundance of Cu ($[Cu/Fe] \approx +0.25$). As above mentioned, the single line used to determine this abundance appears clean and the fitting straightforward, although all the usual *caveats* on speculating on an abundance derived from a single line apply. Galactic stars in the high metallicity regime show $[Cu/Fe] \sim 0$ (Bihain et al., 2004). Moreover, this resemblance strengthens the hypothesis that these two stars have a common origin.

It is worth noticing that, while α elements underabundance and n-capture elements enhancement appear to be characteristics shared by these stars (EIS 6631 in particular) with Sgr dSph (and obviously Terzan 7), the Cu enhancement, the essentially solar $[Ni/Fe]$ and $[Zn/Fe]$ and the solar (or slightly enhanced) $[Na/Fe]$ are absolutely at odds with Sgr dSph abundances.

The conclusions that may be drawn from our observations are not very compelling. EIS 7873 appears to be indistinguishable from Galactic stars. For EIS 30077 and EIS 6631 there are some clues for an extra-galactic origin, and these are stronger for EIS 6631, the most metal-rich star of the sample. This is surprising, since CMa is a highly “degraded” structure, at variance with the Sgr dSph, most of the (hypothetical) galaxy has already dissolved, and its gas content, whatever it may have been, has likely mixed with that of the MW. Colors and metallicity of EIS 6631 imply a young age (about 2 GYr according to isochrones). It should then have formed from gas in which possible chemical signatures may have been already diluted. If EIS 6631 actually belongs to an external galaxy, its high metallicity requires that the mass of this galaxy should be as large as that of Sgr ($M \geq 10^9 M_\odot$ Ibata et al. 1997), or larger. This is consistent with the high end of the mass estimate of the Ring by Ibata et al. (2003) ($2 \times 10^8 M_\odot \leq M \leq 10^9$).

Larger samples are required in order to shed more light on the origin and nature of the CMa overdensity. We undertook a larger FLAMES program,

based on new ESO-WFI pre-imaging (thus also producing a new photometrical dataset), to sample the central part of the structure in much larger detail. The observations are currently being executed.

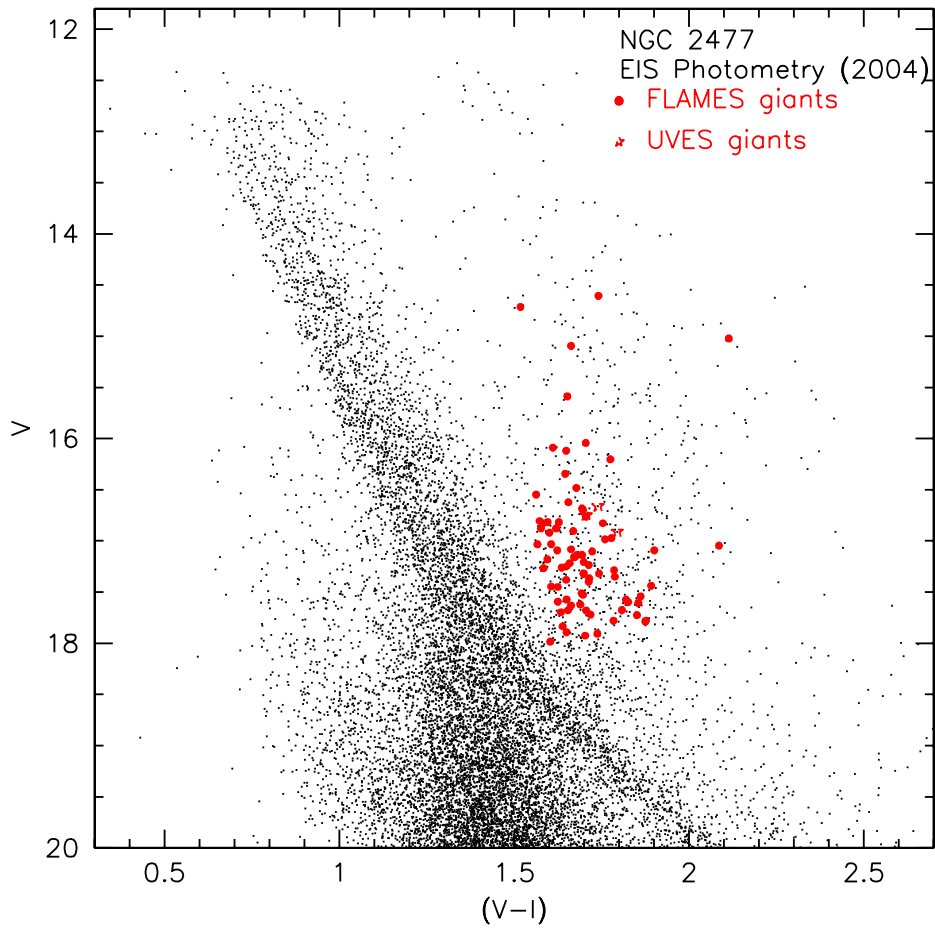


Figure 6.1: The EIS CMD of NGC 2477 inside which Bellazzini et al. (2004) identified the CMa population. The selected FLAMES targets are indicated by large dots, the three likely CMa members UVES stars (see 6.3) are indicated by open stars.

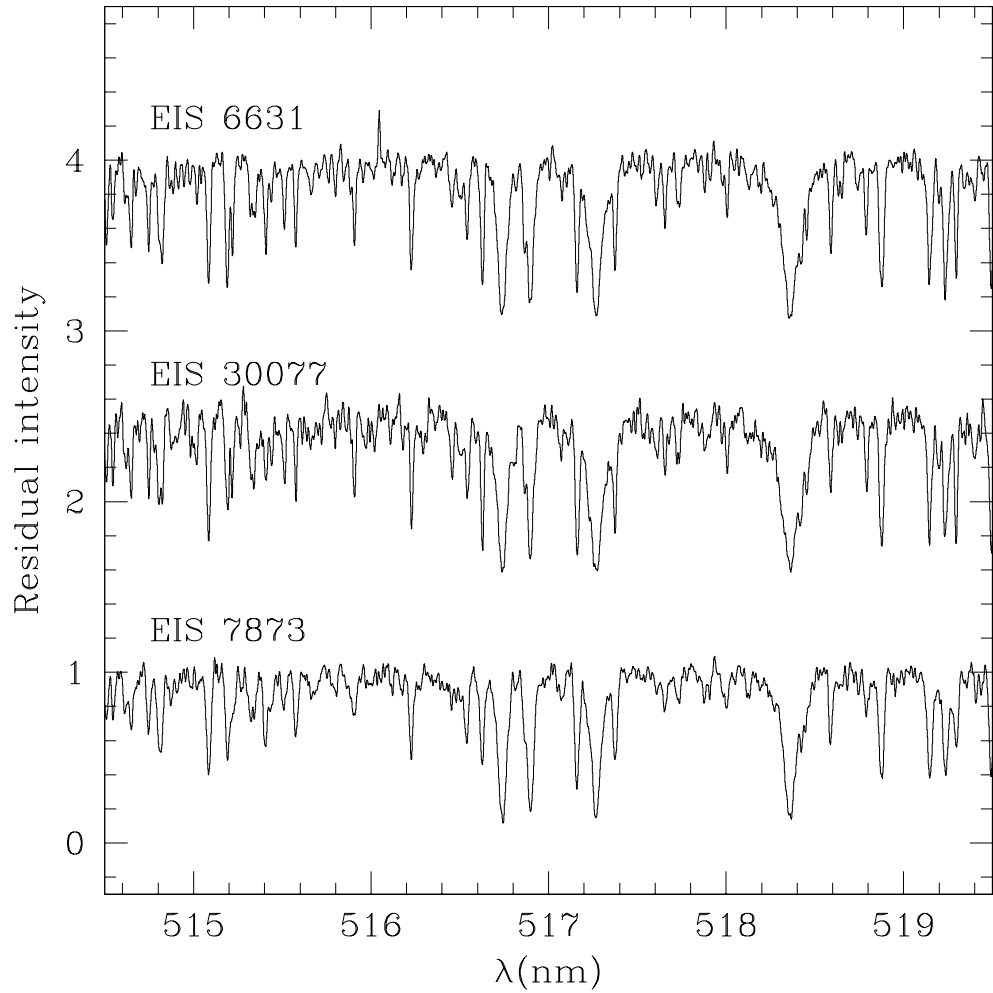


Figure 6.2: Spectra of the three most probable CMA stars, in the region of the Mg b triplet. $[\text{Fe}/\text{H}]$, $\log(g)$ and T_{eff} all increase from bottom to top. The spectra are normalized to one, stars 30077 and 6631 are shifted vertically for display purposes (continuum is at 2.5 for 30077 and at 4 for 6631).

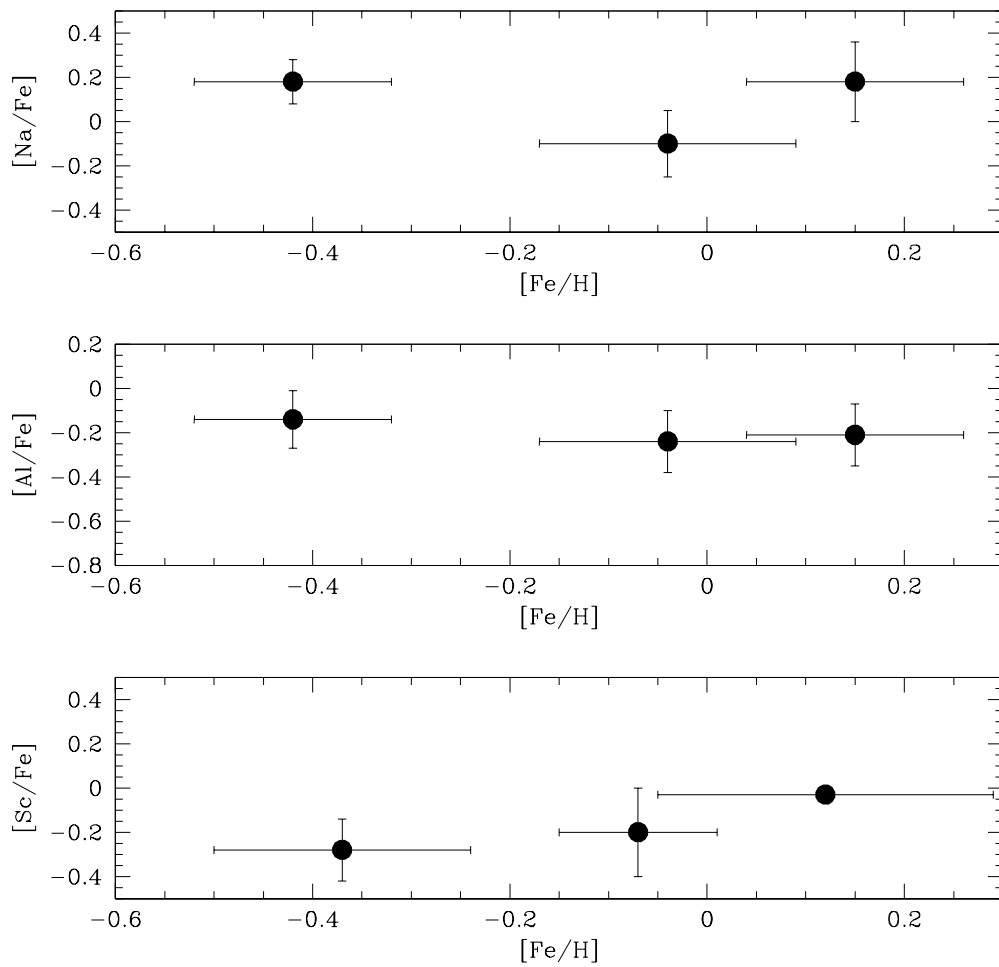


Figure 6.3: Abundance ratios against iron plotted vs. $[Fe/H]$ for the light odd elements Na, Al and Sc in the three possible CMA members.

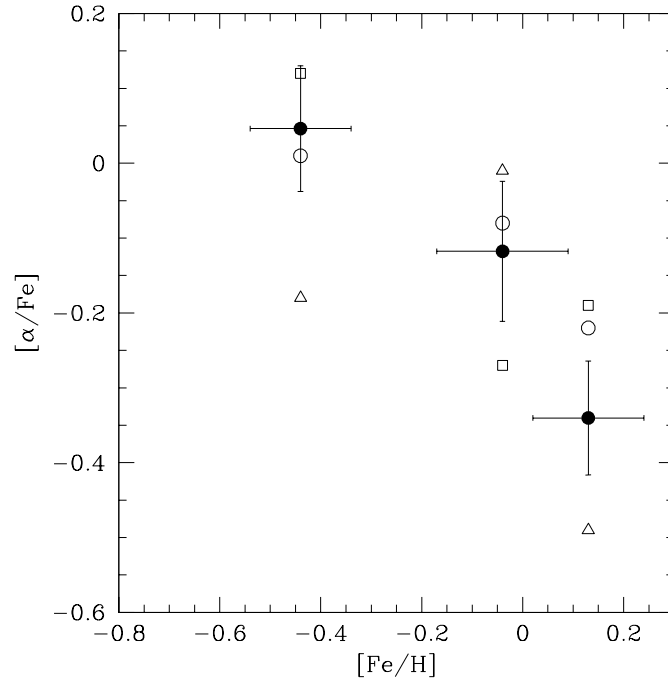


Figure 6.4: Like in fig. 6.3, for mean α elements abundance and Mg, Si and Ca. Here we use a single figure due to the small number of stars. The filled circles with error bars represent the mean α elements abundance similar to the one in the up-left panel of fig. 4.6, while triangles, squares and open circles represent Mg, Si and Ca respectively. Error bars for the single elements removed for clarity.

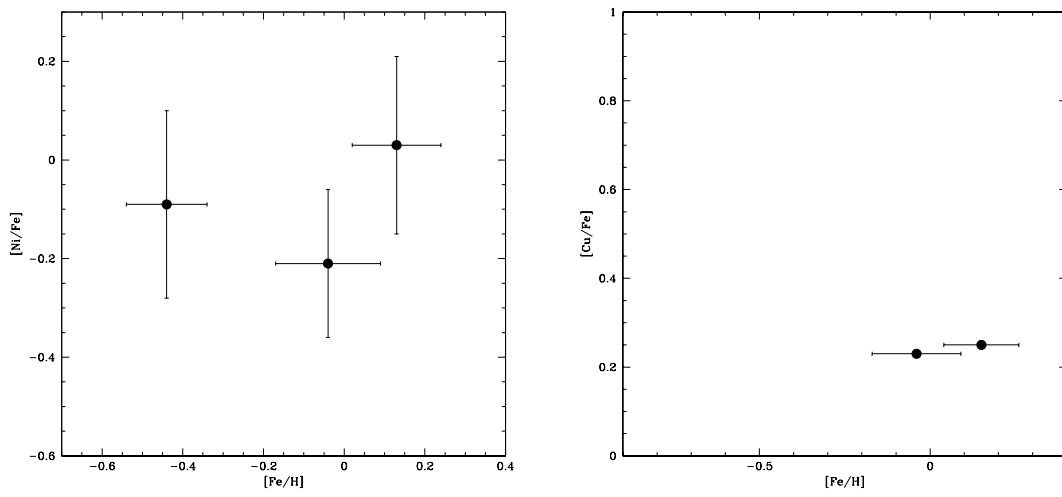


Figure 6.5: Like in fig. 6.3, for Fe-peak elements Ni and Cu.

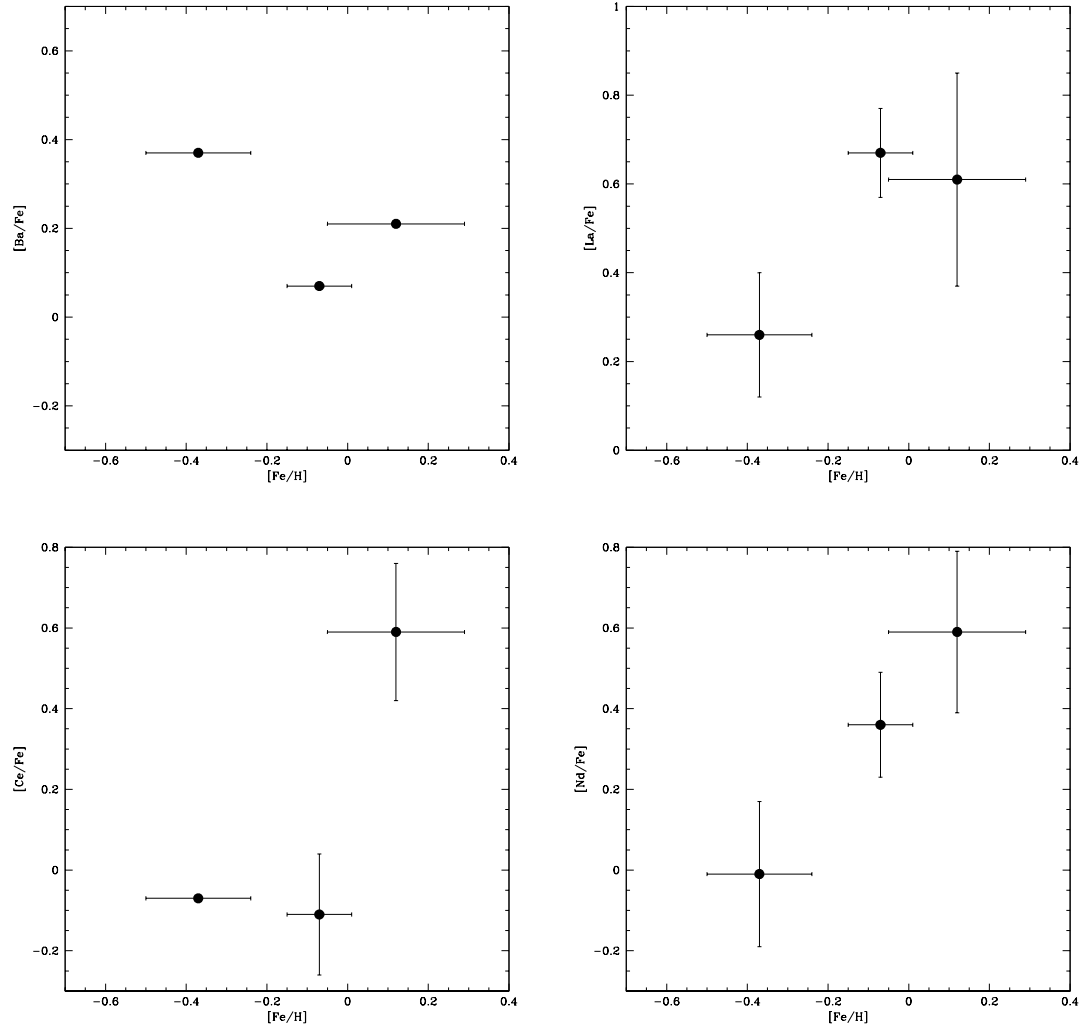


Figure 6.6: Like in fig. 6.3, for heavy n-capture elements Ba, La, Ce and Nd.

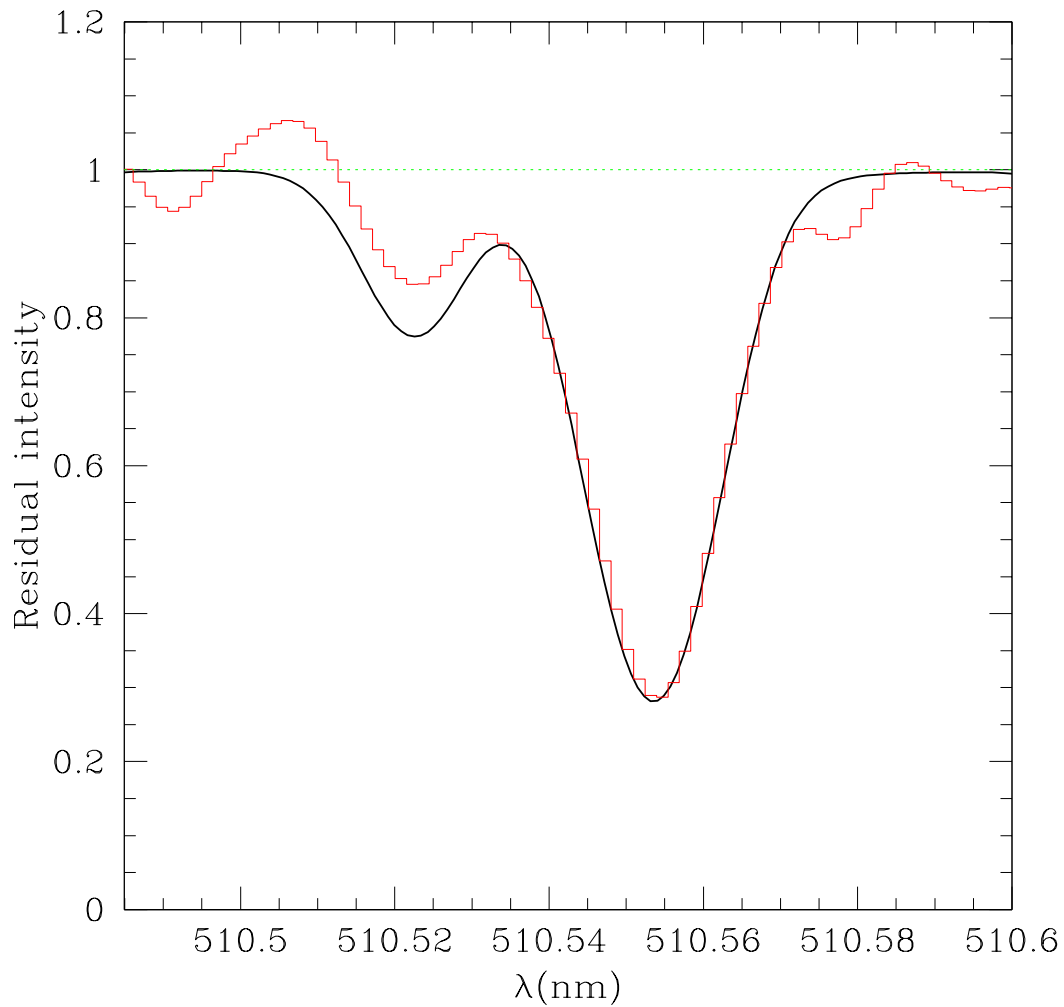


Figure 6.7: Synthesis for the Cu I 510.5 nm line in EIS 6631 (thick line) with superimposed the observed spectrum. Hyperfine splitting is taken into account, $[\text{Cu}/\text{Fe}] = +0.25$ in the synthesis.

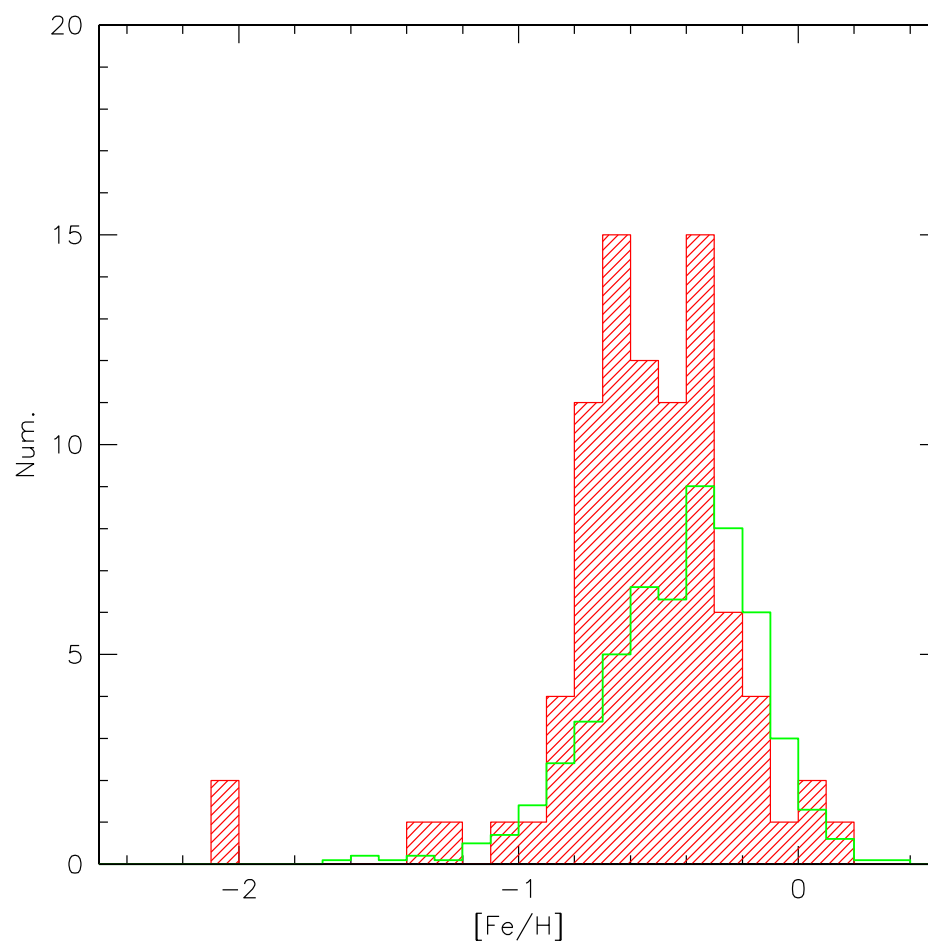


Figure 6.8: Metallicity distribution of the giants in the GIRAFFE sample (red shaded histogram). The green histogram is a realization of the Besançon model of the Galaxy, rescaled to the observed number of objects.

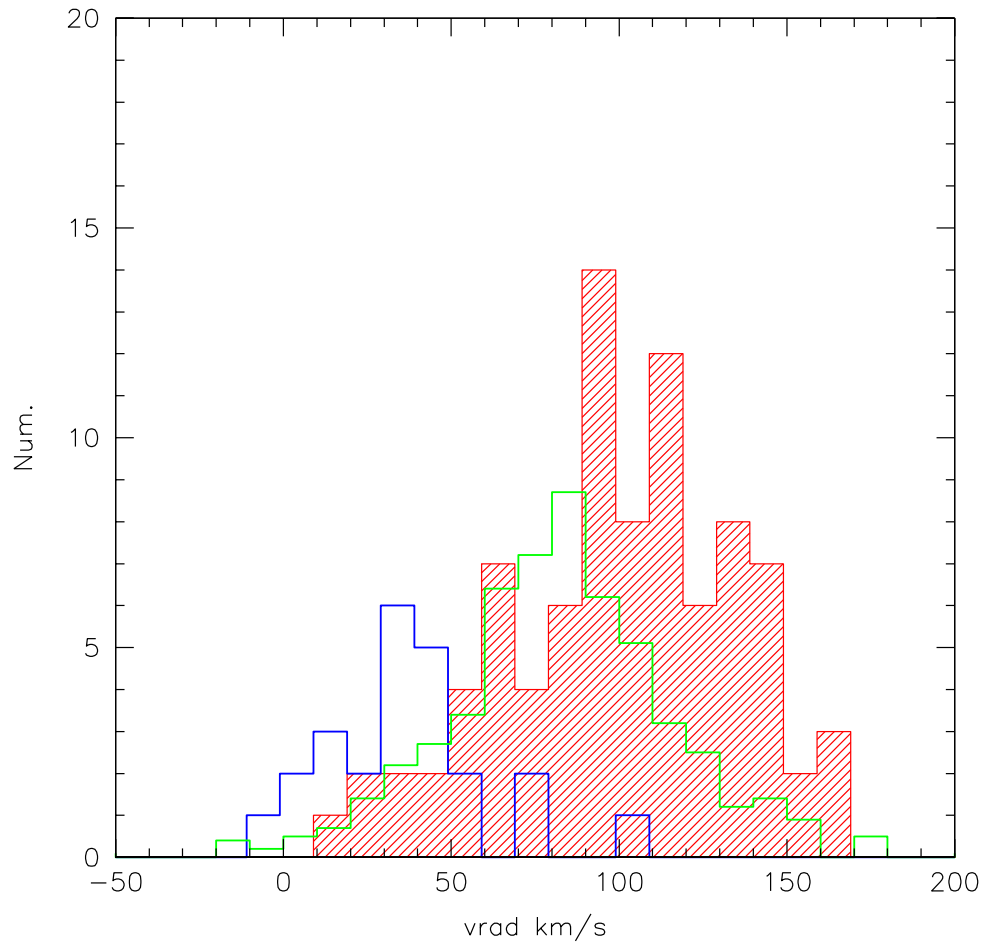


Figure 6.9: Radial velocity distribution of the sample giant stars (red shaded histogram), of the predicted stars of the Besancon model (green) and of the sample dwarf stars (blue).

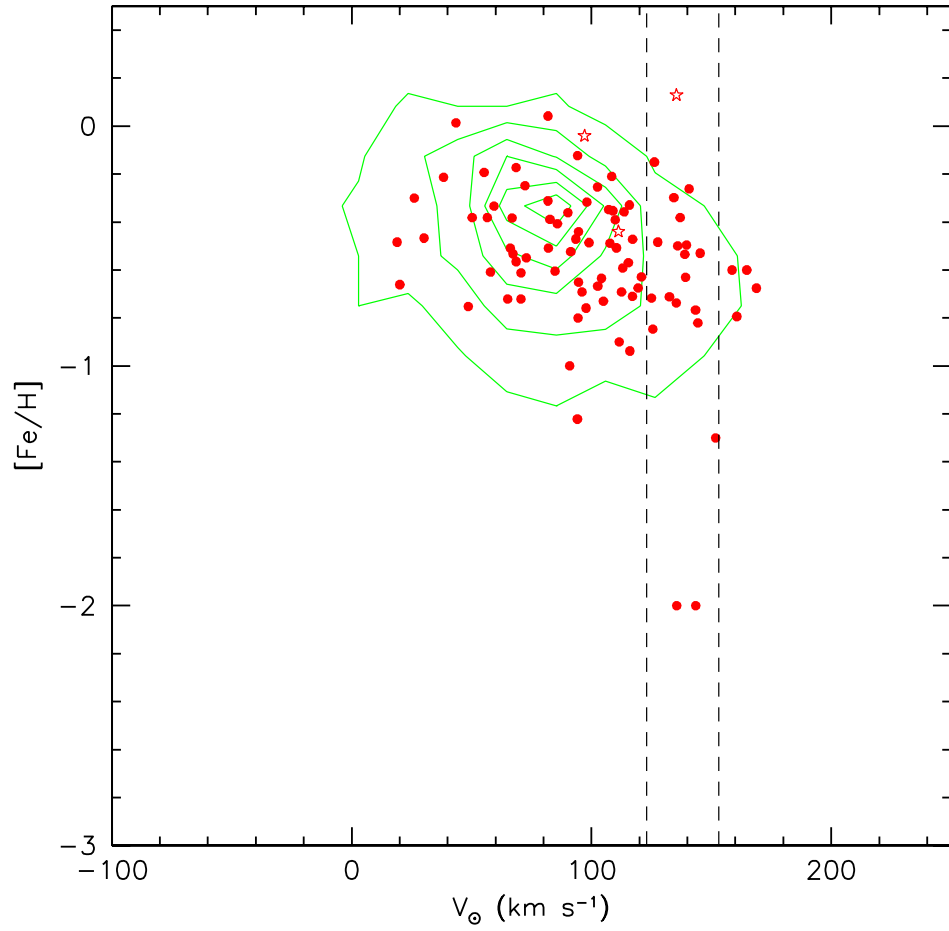


Figure 6.10: The $[Fe/H]$ vs. V_{rad} distribution of the observed FLAMES giants. The red dots are the GIRAFFE targets, the three stars represent the UVES candidate CMA members, the green contour lines are the isodensity curves of the Besancon MW model. The two vertical dashed lines include the radial velocities within which we estimate that MW contamination to the CMA population should be below 30%.

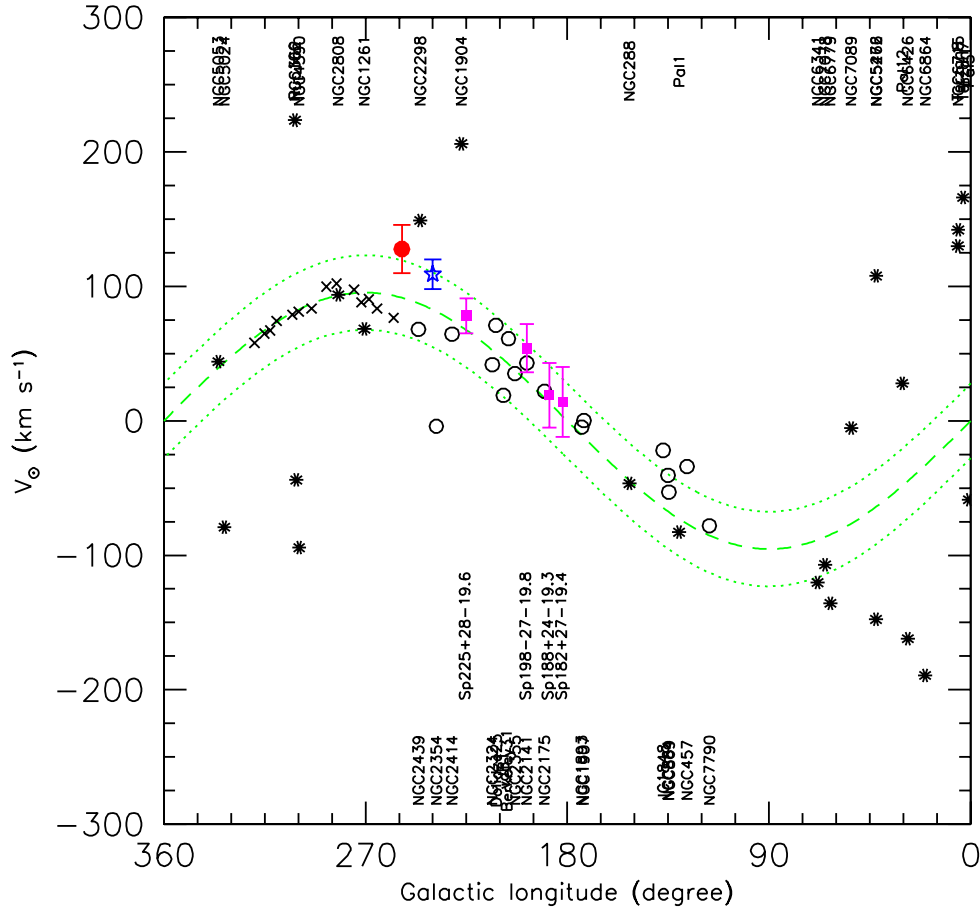


Figure 6.11: Radial velocity vs. galactic longitude plot for different objects of interest. Open dots mark open clusters, asterisks are globular clusters, crosses mark the velocity measurements for the recently discovered H I outer spiral arm (McClure-Griffiths et al., 2004); magenta squares represent the Yanny et al. (2003) measurements of the Monoceros Ring, the blue star is the last CMA measurements by Martin et al. (2004b), the red dot is our possible CMA component. The green lines show the expected velocity for a component in circular motion at 220 km s^{-1} at 15 Kpc from the center of the Galaxy.

Table 6.5: Employed iron lines, atomic data, EWs and resulting abundances for the three likely CMa overdensity members. Other ions, see tables 6.6 and 6.7. For the log gf references see table 4.12.

Ion	λ (nm)	log gf	source of log gf	EW (pm) 6631	ϵ	EW (pm) 7873	ϵ	EW (pm) 30077	ϵ
Fe I	484.9668	-2.680	FMW	–	–	–	–	4.88	7.624
Fe I	489.2859	-1.290	FMW	6.88	7.469	–	–	7.22	7.418
Fe I	489.6439	-2.050	FMW	5.72	7.681	–	–	–	–
Fe I	491.7230	-1.180	FMW	8.53	7.629	–	–	9.03	7.669
Fe I	491.8013	-1.360	FMW	–	–	–	–	7.45	7.548
Fe I	506.7151	-0.970	FMW	–	–	–	–	9.02	7.468
Fe I	510.4438	-1.690	FMW	–	–	–	–	4.92	7.414
Fe I	510.9652	-0.980	FMW	10.76	7.742	–	–	–	–
Fe I	552.5545	-1.330	FMW	9.01	7.841	6.27	7.085	–	–
Fe I	585.5076	-1.760	FMW	3.77	7.758	–	–	3.65	7.563
Fe I	585.6087	-1.640	FMW	5.54	7.619	3.72	7.019	6.13	7.565
Fe I	585.8779	-2.260	FMW	–	–	1.58	7.060	–	–
Fe I	586.1109	-2.450	FMW	–	–	–	–	1.34	7.304
Fe I	587.7794	-2.230	FMW	2.63	7.555	–	–	4.66	7.743
Fe I	588.3817	-1.360	FMW	9.75	7.691	–	–	8.98	7.458
Fe I	595.2717	-1.440	FMW	9.28	7.711	8.37	7.252	7.82	7.326
Fe I	601.2210	-4.200	FMW	–	–	4.34	7.311	–	–
Fe I	602.4058	-0.120	FMW	11.95	7.441	0.85	7.023	–	–
Fe I	602.7051	-1.210	FMW	–	–	7.30	6.937	9.51	7.537
Fe I	605.6005	-0.460	FMW	10.17	7.667	–	–	–	–
Fe I	607.9008	-1.120	FMW	7.46	7.783	3.87	6.917	–	–
Fe I	609.6663	-1.930	FMW	5.90	7.626	5.36	7.227	5.83	7.429
Fe I	610.5128	-2.050	FMW	2.11	7.624	–	–	2.04	7.411
Fe I	615.1616	-3.299	FMW	8.62	7.477	–	–	9.43	7.337
Fe I	616.5360	-1.550	FMW	–	–	5.45	7.039	7.18	7.480
Fe I	618.7990	-1.720	FMW	7.30	7.596	5.99	7.068	–	–
Fe I	622.6734	-2.220	FMW	5.07	7.670	3.50	7.078	5.31	7.502
Fe I	649.6465	-0.570	FMW	–	–	7.00	7.039	7.66	7.304
Fe I	651.8366	-2.750	FMW	9.12	7.693	8.00	7.104	7.91	7.247
Fe I	659.7559	-1.070	FMW	7.13	7.792	4.14	7.055	5.43	7.384
Fe II	499.3358	-3.650	FMW	5.72	7.367	6.62	6.975	–	–
Fe II	510.0664	-4.370	FMW	5.30	8.006	–	–	3.38	7.506
Fe II	513.2669	-4.180	FMW	4.61	7.686	4.81	7.162	4.10	7.483
Fe II	516.1184	-4.483	K88	3.40	7.799	–	–	–	–
Fe II	525.6937	-4.250	K88	3.62	7.646	–	–	3.01	7.388
Fe II	526.4812	-3.190	FMW	6.70	7.511	–	–	–	–
Fe II	599.1376	-3.557	K88	5.96	7.652	6.01	7.125	–	–
Fe II	608.4111	-3.808	K88	5.20	7.812	4.66	7.179	–	–
Fe II	614.9259	-2.724	K88	6.23	7.623	7.50	7.382	5.91	7.597
Fe II	624.7557	-2.329	K88	8.06	7.553	8.13	7.100	6.74	7.377
Fe II	636.9462	-4.253	K88	3.26	7.562	–	–	2.94	7.380
Fe II	643.2680	-3.708	K88	6.01	7.529	5.80	6.934	5.33	7.360
Fe II	645.6383	-2.075	K88	8.17	7.323	–	–	7.86	7.349
Fe II	651.6080	-3.450	K88	–	–	8.77	7.186	–	–

Table 6.6: Employed lines, atomic data, EWs and resulting abundances for ions from Na I to Mn I, for the three likely CMa overdensity members. For iron lines see table 6.5, for ions between Co I and Eu II see table 6.7.

Ion	λ (nm)	log gf	source of log gf	EW (pm) 6631	ϵ	EW (pm) 7873	ϵ	EW (pm) 30077	ϵ
Na I	498.2814	-0.950	KP	11.01	6.50	–	–	9.79	6.26
Na I	568.2633	-0.700	KP	15.77	6.84	11.32	6.14	11.62	6.25
Na I	615.4227	-1.560	KP	7.14	6.55	5.20	6.08	5.68	6.18
Na I	616.0747	-1.260	KP	10.79	6.74	7.17	6.06	7.02	6.08
Mg I	552.8405	-0.522	GC	22.18	7.24	22.12	7.19	28.99	7.58
Mg I	571.1087	-1.729	GC	–	–	10.31	7.04	13.63	7.61
Mg I	631.8716	-1.945	GC	3.53	7.24	–	–	5.43	7.43
Mg I	631.9237	-2.165	GC	2.31	7.22	1.17	6.70	4.58	7.51
Al I	669.6022	-1.347	NBS	5.61	6.33	4.57	5.99	5.44	6.15
Al I	669.8673	-1.647	NBS	4.64	6.49	2.15	5.83	4.04	6.22
Si I	612.5021	-1.540	ED	3.57	7.47	3.51	7.27	3.10	7.33
Si I	614.2482	-1.480	ED	4.12	7.52	3.39	7.19	2.60	7.16
Si I	614.5015	-1.430	ED	4.90	7.59	4.26	7.29	2.63	7.12
Si I	615.5134	-0.770	ED	7.88	7.37	7.73	7.18	7.44	7.33
Ca I	551.2980	-0.447	SR	9.98	6.17	9.52	5.92	10.56	6.19
Ca I	585.7451	0.240	NBS	17.07	6.52	–	–	14.50	6.16
Ca I	586.7562	-1.490	GC	3.55	6.20	3.76	6.01	–	–
Ca I	616.1296	-1.266	SR	8.72	6.36	8.49	6.08	10.14	6.45
Ca I	616.6438	-1.142	SR	10.06	6.44	8.16	5.90	–	–
Ca I	616.9042	-0.797	SR	11.66	6.35	9.70	5.81	12.45	6.40
Ca I	643.9075	0.390	SR	18.52	6.15	17.29	5.88	19.02	6.21
Ca I	645.5597	-1.290	SR	8.54	6.35	6.81	5.82	8.09	6.09
Ca I	649.3781	-0.109	SR	15.60	6.28	16.25	6.21	–	–
Ca I	649.9650	-0.818	SR	10.94	6.27	10.70	5.98	11.17	6.17
Ca I	650.8850	-2.110	NBS	2.25	6.11	–	–	–	–
Sc II	552.6790	0.130	MFW	–	–	11.84	2.57	11.56	3.09
Sc II	632.0852	-1.770	NBS	2.99	3.26	2.33	2.46	1.77	2.72
Ti I	491.5229	-1.019	MFW	–	–	–	–	4.37	5.17
Ti I	499.7097	-2.118	MFW	–	–	6.99	4.44	–	–
Ti I	508.7058	-0.780	MFW	7.60	5.29	–	–	8.40	5.13
Ti I	606.4627	-1.944	MFW	3.88	5.38	2.39	4.63	5.29	5.17
Ti I	609.2792	-1.379	MFW	1.48	5.17	–	–	2.04	4.96
Ti I	612.6215	-1.425	MFW	7.29	5.39	4.50	4.52	7.01	4.95
Ti I	633.6098	-1.743	MFW	3.33	5.49	–	–	–	–
Ti I	655.6061	-1.074	MFW	5.70	5.20	4.26	4.56	8.19	5.21
Ti I	659.9105	-2.085	MFW	4.94	5.49	3.21	4.74	5.95	5.19
V I	573.7059	-0.740	MFW	4.26	4.26	–	–	–	–
V I	613.5361	-0.746	MFW	6.32	4.53	4.67	3.829	8.58	4.51
V I	615.0157	-1.780	MFW	5.63	4.65	4.52	3.957	7.12	4.39
Mn I	511.7934	-1.140	MFW	HFS	5.52	HFS	4.84	HFS	5.46

Table 6.7: Employed lines, atomic data, EWs and resulting abundances for the three likely CMa overdensity members, for ions between Co I and Eu II. See also tables 6.5 and 6.6.

Ion	λ (nm)	log gf	source of log gf	EW (pm) 6631	ϵ	EW (pm) 7873	ϵ	EW (pm) 30077	ϵ
Co I	533.14**	-1.960	FMW	HFS	5.45	–	–	HFS	4.96
Co I	553.07**	-2.060	FMW	HFS	5.19	HFS	4.33	HFS	4.91
Ni I	493.5830	-0.350	FMW	9.52	6.49	6.85	5.67	6.85	5.67
Ni I	585.7747	-0.636	K88	5.35	6.19	–	–	–	–
Ni I	600.7307	-3.330	FMW	7.33	6.54	5.17	5.69	5.17	5.69
Ni I	608.6276	-0.530	FMW	6.54	6.37	5.36	5.88	5.36	5.88
Ni I	611.1065	-0.870	FMW	6.55	6.52	5.02	5.97	5.02	5.97
Ni I	612.8963	-3.330	FMW	8.50	6.72	5.93	5.80	5.93	5.80
Ni I	617.5360	-0.530	FMW	7.92	6.42	7.15	5.98	7.15	5.98
Ni I	617.6807	-0.260	WL	8.57	6.27	6.89	5.67	6.89	5.67
Ni I	617.7236	-3.500	FMW	5.00	6.50	2.41	5.53	2.41	5.53
Ni I	618.6708	-0.960	FMW	3.97	6.20	3.77	5.85	3.77	5.85
Ni I	620.4600	-1.100	WL	4.24	6.37	–	–	–	–
Ni I	632.7592	-3.150	FMW	–	–	5.52	5.54	5.52	5.54
Ni I	648.2796	-2.630	FMW	9.11	6.37	6.64	5.48	6.64	5.48
Ni I	658.6307	-2.810	FMW	9.02	6.54	7.16	5.75	7.16	5.75
Ni I	659.8592	-0.980	FMW	5.28	6.56	–	–	–	–
Ni I	677.2313	-0.980	FMW	7.49	6.29	6.76	5.84	6.76	5.84
Cu I	510.55**	-1.516	BIEL	HFS	4.71	–	–	HFS	4.40
Y II	488.3683	0.070	HL	11.70	2.60	10.65	1.73	10.65	1.73
Y II	498.2130	-1.290	HL	3.83	2.38	–	–	–	–
Y II	508.7417	-0.170	HL	–	–	9.64	1.71	9.64	1.71
Y II	511.9113	-1.360	HL	5.24	2.65	–	–	–	–
La II	511.4558	-1.030	LA	6.44	2.03	4.89	0.98	4.89	0.98
La II	632.0377	-1.610	ABH	2.30	1.68	3.08	1.07	3.08	1.07
Ce II	518.7457	0.130	H	4.38	2.31	2.20	1.14	2.09	1.53
Ce II	533.0556	-0.360	H	3.48	2.26	–	–	1.05	1.27
Nd II	491.4382	-0.700	HA	–	–	3.21	1.01	3.21	1.01
Nd II	495.9119	-0.800	HA	–	–	4.85	1.04	4.85	1.04
Nd II	496.1387	-0.710	MC'	4.52	2.31	–	–	–	–
Nd II	499.8540	-1.100	MC'	–	–	–	–	–	–
Nd II	508.9832	-1.160	MC'	3.54	2.12	–	–	–	–
Nd II	529.3162	-0.060	WVA	–	–	5.69	1.30	5.69	1.30
Nd II	543.1515	-0.470	HA	–	–	–	–	–	–
Eu II	644.50**	0.120	LAW	HFS	0.84	HFS	0.34	HFS	0.54

Bibliography

- Alard, C. 1996, *ApJ Letters*, 458, L17+
- . 2001, *A&A*, 377, 389
- Alonso, A., Arribas, S., & Martínez-Roger, C. 1999, *A&A Supplement*, 140, 261
- . 2001, *A&A*, 376, 1039
- Anders, E., & Grevesse, N. 1989, *GeCoA*, 53, 197
- Armandroff, T. E., & Da Costa, G. S. 1991, *AJ*, 101, 1329
- Arnesen, A., Bengtsson, A., Hallin, R., Lindskog, J., Nordling, C., & Noreland, T. 1977, *Phys. Scr*, 16, 31
- Asplund, M., Grevesse, N., Sauval, A. J., Allende Prieto, C., & Kiselman, D. 2004a, *A&A*, 417, 751
- Asplund, M., Grevesse, N., & Sauval, J. 2004b, *ArXiv Astrophysics e-prints*, astro-ph/0410214
- Azzopardi, M., Lequeux, J., & Rebeiro, E. 1988, *A&A*, 202, L27
- Bekki, K., Couch, W. J., Drinkwater, M. J., & Shioya, Y. 2003, *MNRAS*, 344, 399
- Bellazzini, M., Ferraro, F. R., & Ibata, R. 2002, *AJ*, 124, 915
- . 2003, *AJ*, 125, 188
- Bellazzini, M., Ibata, R., Monaco, L., Martin, N., Irwin, M. J., & Lewis, G. F. 2004, *MNRAS*, 354, 1263

- Bielski, A. 1975, *J. Quant. Spectrosc. Radiat. Transfer*, 15, 463
- Biemont, E., & Godefroid, M. 1980, *A&A*, 84, 361
- Bihain, G., Israelian, G., Rebolo, R., Bonifacio, P., & Molaro, P. 2004, *A&A*, 423, 777
- Blanco, B. M., Blanco, V. M., & McCarthy, M. F. 1978, *Nature*, 271, 638
- Bonifacio, P., & Caffau, E. 2003, *A&A*, 399, 1183
- Bonifacio, P., Hill, V., Molaro, P., Pasquini, L., Di Marcantonio, P., & Santin, P. 2000a, *A&A*, 359, 663
- Bonifacio, P., Monai, S., & Beers, T. C. 2000b, *AJ*, 120, 2065
- Bonifacio, P., Sbordone, L., Marconi, G., Pasquini, L., & Hill, V. 2004, *A&A*, 414, 503
- Brown, J. A., Wallerstein, G., & Gonzalez, G. 1999, *AJ*, 118, 1245
- Brown, J. A., Wallerstein, G., & Zucker, D. 1997, *AJ*, 114, 180
- Buonanno, R., Corsi, C. E., Pecci, F. F., Fahlman, G. G., & Richer, H. B. 1994, *ApJ Letters*, 430, L121+
- Buonanno, R., Corsi, C. E., Pulone, L., Pecci, F. F., Richer, H. B., & Fahlman, G. C. 1995, *AJ*, 109, 663
- Burton, W. B., & Lockman, F. J. 1999, *A&A*, 349, 7
- Busso, M., Gallino, R., & Wasserburg, G. J. 1999, *A&A Annual Review*, 37, 239
- Caffau, E., Bonifacio, P., Faraggiana, R., François, P., Gratton, R. G., & Barbieri, M. 2005a, *A&A*, submitted
- Caffau, E., Bonifacio, P., Faraggiana, R., & Sbordone, L. 2005b, *A&A Letters*, submitted
- Carbon, D. F. 1979, *A&A Annual Review*, 17, 513
- Cassisi, S., Salaris, M., Castelli, F., & Pietrinferni, A. 2004, *ApJ*, 616, 498

- Castelli, F. 1988, Kurucz's models, Kurucz's fluxes and the ATLAS code. Models and fluxes available at OAT, Pubblicazione oat n. 1164, Osservatorio Astronomico di Trieste
- Castelli, F., Gratton, R. G., & Kurucz, R. L. 1997, *A&A*, 318, 841
- Castelli, F., & Kurucz, R. L. 2004, ArXiv Astrophysics e-prints, astro-ph/0405087
- Cayrel, R. 1988, in IAU Symp. 132: The Impact of Very High S/N Spectroscopy on Stellar Physics, ed. G. Cayrel de Strobel & M. Spite
- Centurión, M., Bonifacio, P., Molaro, P., & Vladilo, G. 2000, *ApJ*, 536, 540
- Centurión, M., Molaro, P., Vladilo, G., Péroux, C., Levshakov, S. A., & D'Odorico, V. 2003, *A&A*, 403, 55
- Chieffi, A., & Limongi, M. 2003, *Publications of the Astronomical Society of Australia*, 20, 324
- . 2004, *ApJ*, 608, 405
- Cohen, J. G. 2004, *AJ*, 127, 1545
- Cole, A. A. 2001, *ApJ Letters*, 559, L17
- Crane, J. D., Majewski, S. R., Rocha-Pinto, H. J., Frinchaboy, P. M., Skrutskie, M. F., & Law, D. R. 2003, *ApJ Letters*, 594, L119
- Da Costa, G. S., & Armandroff, T. E. 1995, *AJ*, 109, 2533
- Dekker, H., D'Odorico, S., Kaufer, A., Delabre, B., & Kotzlowski, H. 2000, in *Proc. SPIE Vol. 4008*, p. 534-545, *Optical and IR Telescope Instrumentation and Detectors*, Masanori Iye; Alan F. Moorwood; Eds., 534–545
- Den Hartog, E. A., Lawler, J. E., Sneden, C., & Cowan, J. J. 2003, *ApJ Supplement*, 148, 543
- Drinkwater, M. J., Gregg, M. D., Hilker, M., Bekki, K., Couch, W. J., Ferguson, H. C., Jones, J. B., & Phillipps, S. 2003, *Nature*, 423, 519
- Ecuvillon, A., Israelian, G., Santos, N. C., Mayor, M., Villar, V., & Bihain, G. 2004, *A&A*, 426, 619

- Edvardsson, B., Andersen, J., Gustafsson, B., Lambert, D. L., Nissen, P. E., & Tomkin, J. 1993, *A&A*, 275, 101
- Frinchaboy, P. M., Majewski, S. R., Crane, J. D., Reid, I. N., Rocha-Pinto, H. J., Phelps, R. L., Patterson, R. J., & Muñoz, R. R. 2004, *ApJ Letters*, 602, L21
- Fuhr, J. R., Martin, G. A., & Wiese, W. L. 1988a, Atomic transition probabilities. Iron through Nickel (New York: American Institute of Physics (AIP) and American Chemical Society, 1988)
- . 1988b, Atomic transition probabilities. Scandium through Manganese (New York: American Institute of Physics (AIP) and American Chemical Society, 1988)
- Fulbright, J. P. 2000, *AJ*, 120, 1841
- Gómez-Flechoso, M. A., Fux, R., & Martinet, L. 1999, *A&A*, 347, 77
- Garnett, D. R. 1989, *ApJ*, 345, 282
- Garz, T. 1973, *A&A*, 26, 471
- Gilmore, G., & Wyse, R. F. G. 1991, *ApJ Letters*, 367, L55
- Girardi, L., Bertelli, G., Bressan, A., Chiosi, C., Groenewegen, M. A. T., Marigo, P., Salasnich, B., & Weiss, A. 2002, *A&A*, 391, 195
- Gratton, R. G. 1989, *A&A*, 208, 171
- Gratton, R. G., Carretta, E., Claudi, R., Lucatello, S., & Barbieri, M. 2003, *A&A*, 404, 187
- Gratton, R. G., & Ortolani, S. 1988, *A&A Supplement*, 73, 137
- Hannaford, P., Lowe, R. M., Grevesse, N., Biemont, E., & Whaling, W. 1982, *ApJ*, 261, 736
- Helmi, A., & White, S. D. M. 1999, *MNRAS*, 307, 495
- Hill, V., Andrievsky, S., & Spite, M. 1995, *A&A*, 293, 347
- Ibata, R., Irwin, M., Lewis, G. F., & Stolte, A. 2001, *ApJ Letters*, 547, L133

- Ibata, R. A., Gilmore, G., & Irwin, M. J. 1994, *Nature*, 370, 194
- . 1995, *MNRAS*, 277, 781
- Ibata, R. A., Irwin, M. J., Lewis, G. F., Ferguson, A. M. N., & Tanvir, N. 2003, *MNRAS*, 340, L21
- Ibata, R. A., & Lewis, G. F. 1998, *ApJ*, 500, 575
- Ibata, R. A., Wyse, R. F. G., Gilmore, G., Irwin, M. J., & Suntzeff, N. B. 1997, *AJ*, 113, 634
- Izotov, Y. I., & Thuan, T. X. 1999, *ApJ*, 511, 639
- Kobayashi, C. 2003, *Elemental Abundances in Old Stars and Damped Lyman- α Systems*, 25th meeting of the IAU, Joint Discussion 15, 22 July 2003, Sydney, Australia, 15
- Kobayashi, C., Tsujimoto, T., Nomoto, K., Hachisu, I., & Kato, M. 1998, *ApJ Letters*, 503, L155+
- . 2000, *Memorie della Societa Astronomica Italiana*, 71, 461
- Koribalski, B., Johnston, S., & Otrupcek, R. 1994, *MNRAS*, 270, L43+
- Kurucz, R. 1993, *ATLAS9 Stellar Atmosphere Programs and 2 km/s grid*. Kurucz CD-ROM No. 13. Cambridge, Mass.: Smithsonian Astrophysical Observatory, 1993., 13
- Kurucz, R. L. 1979, *ApJ Supplement*, 40, 1
- Kurucz, R. L., & Peytremann, E. 1975, *SAO Special Report*, 362
- Lanfranchi, G. A., & Friaça, A. C. S. 2003, *MNRAS*, 343, 481
- Lanfranchi, G. A., & Matteucci, F. 2003, *MNRAS*, 345, 71
- . 2004, *MNRAS*, 351, 1338
- Lawler, J. E., Bonvallet, G., & Sneden, C. 2001a, *ApJ*, 556, 452
- Lawler, J. E., Wickliffe, M. E., den Hartog, E. A., & Sneden, C. 2001b, *ApJ*, 563, 1075

- Le Brun, V., Bergeron, J., Boisse, P., & Deharveng, J. M. 1997, *A&A*, 321, 733
- Limongi, M., & Chieffi, A. 2003, *Memorie della Societa Astronomica Italiana Supplement*, 3, 58
- Lodders, K. 2003, *ApJ*, 591, 1220
- Majewski, S. R., Skrutskie, M. F., Weinberg, M. D., & Ostheimer, J. C. 2003, *ApJ*, 599, 1082
- Marconi, G., Buonanno, R., Castellani, M., Iannicola, G., Molaro, P., Pasquini, L., & Pulone, L. 1998, *A&A*, 330, 453
- Marconi, G., Matteucci, F., & Tosi, M. 1994, *MNRAS*, 270, 35
- Martin, N. F., Ibata, R. A., Bellazzini, M., Irwin, M. J., Lewis, G. F., & Dehnen, W. 2004a, *MNRAS*, 348, 12
- Martin, N. F., Ibata, R. A., Conn, B. C., Lewis, G. F., Bellazzini, M., Irwin, M. J., & McConnachie, A. W. 2004b, *MNRAS*, 355, L33
- Martínez-Delgado, D., Zinn, R., Carrera, R., & Gallart, C. 2002, *ApJ Letters*, 573, L19
- Mateo, M., Mirabal, N., Udalski, A., Szymanski, M., Kaluzny, J., Kubiak, M., Krzeminski, W., & Stanek, K. Z. 1996, *ApJ Letters*, 458, L13+
- Mateo, M., Udalski, A., Szymanski, M., Kaluzny, J., Kubiak, M., & Krzeminski, W. 1995, *AJ*, 109, 588
- McClure-Griffiths, N. M., Dickey, J. M., Gaensler, B. M., & Green, A. J. 2004, *ApJ Letters*, 607, L127
- McWilliam, A., Rich, R. M., & Smecker-Hane, T. A. 2003, *ApJ Letters*, 592, L21
- McWilliam, A., & Smecker-Hane, T. A. 2004, *ArXiv Astrophysics e-prints*, astro-ph/0409083
- Miles, B. M., & Wiese, W. L. 1969, *Atomic Data*, Vol. 1, p.1, 1, 1

- Mishenina, T. V., Kovtyukh, V. V., Soubiran, C., Travaglio, C., & Busso, M. 2002, *A&A*, 396, 189
- Momany, Y., Vandame, B., Zaggia, S., Mignani, R. P., da Costa, L., Arnouts, S., Groenewegen, M. A. T., Hatziminaoglou, E., Madejsky, R., Rit e, C., Schirmer, M., & Slijkhuis, R. 2001, *A&A*, 379, 436
- Momany, Y., Zaggia, S. R., Bonifacio, P., Piotto, G., De Angeli, F., Bedin, L. R., & Carraro, G. 2004, *A&A*, 421, L29
- Monaco, L., Bellazzini, M., Ferraro, F. R., & Pancino, E. 2003, *ApJ Letters*, 597, L25
- . 2004, *MNRAS*, 353, 874
- . 2005, *MNRAS*, 356, 1396
- Monaco, L., Ferraro, F. R., Bellazzini, M., & Pancino, E. 2002, *ApJ Letters*, 578, L47
- Monai, S., Bonifacio, P., & Sbordone, L. 2005, *ArXiv Astrophysics e-prints*, astro-ph/0501010
- Montegriffo, P., Bellazzini, M., Ferraro, F. R., Martins, D., Sarajedini, A., & Fusi Pecci, F. 1998, *MNRAS*, 294, 315
- Nakamura, T., Umeda, H., Iwamoto, K., Nomoto, K., Hashimoto, M., Hix, W. R., & Thielemann, F. 2001, *ApJ*, 555, 880
- Navarro, J. F., Frenk, C. S., & White, S. D. M. 1995, *MNRAS*, 275, 56
- Newberg, H. J., Yanny, B., Rockosi, C., Grebel, E. K., Rix, H., Brinkmann, J., Csabai, I., Hennessy, G., Hindsley, R. B., Ibata, R., Ivezi c, Z., Lamb, D., Nash, E. T., Odenkirchen, M., Rave, H. A., Schneider, D. P., Smith, J. A., Stolte, A., & York, D. G. 2002, *ApJ*, 569, 245
- Ng, Y. K. 1997, *A&A*, 328, 211
- . 1998, *A&A*, 338, 435
- Nissen, P. E., Chen, Y. Q., Asplund, M., & Pettini, M. 2004, *A&A*, 415, 993

- Odenkirchen, M., Grebel, E. K., Dehnen, W., Rix, H., Yanny, B., Newberg, H. J., Rockosi, C. M., Martínez-Delgado, D., Brinkmann, J., & Pier, J. R. 2003, *AJ*, 126, 2385
- Prochaska, J. X., & Wolfe, A. M. 2002, *ApJ*, 566, 68
- Putman, M. E., Thom, C., Gibson, B. K., & Staveley-Smith, L. 2004, *ApJ Letters*, 603, L77
- Rao, S. M., & Turnshek, D. A. 1998, *ApJ Letters*, 500, L115+
- Rosenberg, A., Saviane, I., Piotto, G., & Aparicio, A. 1999, *AJ*, 118, 2306
- Sarajedini, A., & Layden, A. C. 1995, *AJ*, 109, 1086
- Savage, B. D., & Sembach, K. R. 1996, *ApJ*, 470, 893
- Sbordone, L., Bonifacio, P., Castelli, F., & Kurucz, R. L. 2004a, *Memorie della Societa Astronomica Italiana Supplement*, 5, 93
- Sbordone, L., Bonifacio, P., Marconi, G., & Buonanno, R. 2004b, *Memorie della Societa Astronomica Italiana*, 75, 396
- Sbordone, L., Bonifacio, P., Marconi, G., Buonanno, R., & Zaggia, S. 2005a, *A&A*, accepted
- Sbordone, L., Bonifacio, P., Marconi, G., Zaggia, S., & Buonanno, R. 2005b, *A&A*, 430, L13
- Schlegel, D. J., Finkbeiner, D. P., & Davis, M. 1998, *ApJ*, 500, 525
- Shetrone, M., Venn, K. A., Tolstoy, E., Primas, F., Hill, V., & Kaufer, A. 2003, *AJ*, 125, 684
- Shetrone, M. D., Bolte, M., & Stetson, P. B. 1998, *AJ*, 115, 1888
- Shetrone, M. D., Côté, P., & Sargent, W. L. W. 2001, *ApJ*, 548, 592
- Simmerer, J., Sneden, C., Ivans, I. I., Kraft, R. P., Shetrone, M. D., & Smith, V. V. 2003, *AJ*, 125, 2018
- Smecker-Hane, T. A., & McWilliam, A. 2002, *ArXiv Astrophysics e-prints*, astro-ph/0410214

- Smith, G., & Raggett, D. S. J. 1981, *Journal of Physics B Atomic Molecular Physics*, 14, 4015
- Snedden, C. 2004, *Memorie della Societa Astronomica Italiana*, 75, 267
- Snedden, C., Johnson, H. R., & Krupp, B. M. 1976, *ApJ*, 204, 281
- Stetson, P. B., Hesser, J. E., Smith, G. H., Vandenberg, D. A., & Bolte, M. 1989, *AJ*, 97, 1360
- Storey, P. J., & Zeippen, C. J. 2000, *MNRAS*, 312, 813
- Straniero, O., Chieffi, A., & Limongi, M. 1997, *ApJ*, 490, 425
- Tautvaišienė, G., Wallerstein, G., Geisler, D., Gonzalez, G., & Charbonnel, C. 2004, *AJ*, 127, 373
- Terzan, A. 1968, *C.R. Acad. Sci. Ser. B1*, 267, 1245
- Timmes, F. X., Brown, E. F., & Truran, J. W. 2003, *ApJ Letters*, 590, L83
- Timmes, F. X., Woosley, S. E., & Weaver, T. A. 1995, *ApJ Supplement*, 98, 617
- Tinsley, B. M. 1979, *ApJ*, 229, 1046
- Torres-Peimbert, S., Peimbert, M., & Fierro, J. 1989, *ApJ*, 345, 186
- Trentham, N. 1998, *MNRAS*, 294, 193
- Tsuchiya, T., Korchagin, V. I., & Dinescu, D. I. 2004, *MNRAS*, 350, 1141
- Tsujimoto, T., Nomoto, K., Yoshii, Y., Hashimoto, M., Yanagida, S., & Thielemann, F.-K. 1995, *MNRAS*, 277, 945
- van den Bergh, S. 1998, *ApJ Letters*, 505, L127
- Venn, K. A., Irwin, M., Shetrone, M. D., Tout, C. A., Hill, V., & Tolstoy, E. 2004, *AJ*, 128, 1177
- Vladilo, G. 2002, *A&A*, 391, 407
- Wallerstein, G. 1962, *ApJ Supplement*, 6, 407

- White, S. D. M., & Frenk, C. S. 1991, *ApJ*, 379, 52
- Wiese, W. L., Smith, M. W., & Miles, B. M. 1969, Atomic transition probabilities. Vol. 2: Sodium through Calcium. A critical data compilation (NSRDS-NBS, Washington, D.C.: US Department of Commerce, National Bureau of Standards, —c 1969)
- Wolfe, A. M., Turnshek, D. A., Smith, H. E., & Cohen, R. D. 1986, *ApJ Supplement*, 61, 249
- Wolnik, S. J., & Berthel, R. O. 1973, *ApJ*, 179, 665
- Yanny, B., Newberg, H. J., Grebel, E. K., Kent, S., Odenkirchen, M., Rockosi, C. M., Schlegel, D., Subbarao, M., Brinkmann, J., Fukugita, M., Ivezić, Ž., Lamb, D. Q., Schneider, D. P., & York, D. G. 2003, *ApJ*, 588, 824
- Zaggia, S., Bonifacio, P., Bellazzini, M., Caffau, E., Di Marcantonio, P., Ferraro, F., Marconi, G., Monaco, L., Monai, S., Santin, P., & Sbordone, L. 2004, *Memorie della Societa Astronomica Italiana Supplement*, 5, 291
- Zucca, E., Zamorani, G., Vettolani, G., Cappi, A., Merighi, R., Mignoli, M., Stirpe, G. M., MacGillivray, H., Collins, C., Balkowski, C., Cayatte, V., Maurogordato, S., Proust, D., Chincarini, G., Guzzo, L., Maccagni, D., Scaramella, R., Blanchard, A., & Ramella, M. 1997, *A&A*, 326, 477